A NOVEL NUMERICAL ANALYSIS OF HALL EFFECT THRUSTER AND ITS APPLICATION IN SIMULTANEOUS DESIGN OF THRUSTER AND OPTIMAL LOW-THRUST TRAJECTORY

A Dissertation
Presented to
The Academic Faculty

by

Kybeom Kwon

In Partial Fulfillment
of the Requirements for the Degree
Doctor of Philosophy in the
School of Aerospace Engineering

Georgia Institute of Technology
August 2010

A NOVEL NUMERICAL ANALYSIS OF HALL EFFECT THRUSTER AND ITS APPLICATION IN SIMULTANEOUS DESIGN OF THRUSTER AND OPTIMAL LOW-THRUST TRAJECTORY

Approved by:

Dr. Dimitri N. Mavris
Advisor (Committee Chair), Professor
School of Aerospace Engineering
Director of Aerospace Systems Design
Laboratory
Georgia Institute of Technology

Dr. Justin Koo
Propulsion Directorate
Air Force Research Laboratory
Edwards AFB

Dr. Mitchell L. R. Walker
Co-Advisor, Assistant Professor
School of Aerospace Engineering
Director of High Power Electric
Propulsion Laboratory
Georgia Institute of Technology

Dr. Taewoo Nam
Research Engineer II
School of Aerospace Engineering
Aerospace Systems Design Laboratory
Georgia Institute of Technology

Dr. Ryan P. Russell
Co-Advisor, Assistant Professor
School of Aerospace Engineering
Space Systems Design Laboratory
Georgia Institute of Technology

Date Approved: [July 2, 2010]

To the space pioneers and my wife

ACKNOWLEDGEMENTS

TABLE OF CONTENTS

LIST OF TABLES

xii

LIST OF FIGURES

xvi

LIST OF SYMBOLS

A	Thruster channel area
a	Semi-major axis
$\vec{B}$	Magnetic field vector
B_{cath}	Radial magnetic field strength at the cathode
$B_{\max}$	Maximum radial magnetic field strength
ΔB	Magnetic field strength difference between B_{max} and B_{cath}
$d_{\text{lower limit}}$	Lower bound of support vector machine constraint
dt	Time interval
dz	Length of one computational grid cell
$\vec{E}$	Electric field vector
e	Electrical charge or eccentricity
$\vec{F}$	Force vector
f	Particle distribution function
g	Constraint function
g_e	Magnitude of gravitational acceleration at Earth's surface
I_b	Beam current
I_d	Discharge current
I_{sp}	Specific impulse
$I_{sp,ano}$	Anode specific impulse
$I_{sp,tot}$	Total specific impulse
i	Orbit Inclination

$\vec{j}$	Electric current density vector
$\vec{j}_{hall}$	Hall current density vector
Kn	Knudsen number
K	Radial magnetic field shape coefficient
k	Boltzmann constant
L	Thruster channel length
L_{cath}	Distance from thruster exit to cathode location
L_s	Smooth transition distance for the anomalous coefficients
$M_{thruster}$	Thruster mass
M_i	Ion Mach number
m	Mass of particle
$\dot{m}$	Propellant mass flow rate
$\dot{m}_a$	Anode mass flow rate
$\dot{m}_c$	Cathode mass flow rate
m_{final}	Final space vehicle mass
$m_{initial}$	Initial space vehicle mass
$\dot{m}_{tot}$	Total mass flow rate
$N(t)$	Unit normal distribution at time t
$\vec{n}$	Unit vector
n_0	Plasma number density
n_{e_0}	Electron number density at the matching point
n_e	Electron number density or plasma number density

$n_{e,m}$	Plasma number density at the matching point
$n_{n,ave}$	Average neutral number density in the presheath region
n_s	Species number density
P	Required Power
$P_{available}$	Available Power
P_{coll}	Collision probability
P_d	Discharge Power
P_{tot}	Total Power
P_{cath}	Power used by the cathode
P_{mag}	Power used by the electric magnet
$\tilde{P}_s$	Stress tensor
p_e	Electron pressure
$\vec{q}$	Heat transfer vector
R_1	Thruster inner radius
R_2	Thruster outer radius
R^2	Coefficient of determination
R^2_{adj}	Adjusted coefficient of determination
RR	Reaction Rate
r	Radial direction coordinate
r_c	Cyclotron radius
r_e	Electron gyro radius
r_i	Ion gyro radius

$S(z)$	Source generation function
T	Thrust
T_{anode}	Anode temperature
T_{cp}	Charged particle temperature
$T_{e,m}$	Electron temperature at the matching point
T_{eV}	Electron temperature in eV
T_p	Plasma temperature
t	Time variable
Δt	Time step
$u_{e,c}$	Electron mean velocity at the cathode
$u_{e,th}$	Mean electron thermal velocity
$u_{e,\theta}$	Azimuthal electron mean velocity
$\vec{u}_s$	Species mean velocity
u_{i_a}	Ion acoustic velocity
$u_{i,c}$	Ion mean velocity at the cathode
u_{i_0}	Ion mean velocity at the matching point
u_{n_0}	Constant neutral mean velocity
ΔV	Total required velocity change
$V(t)$	Velocity random variable at time t
V_d	Discharge voltage
V_x	Velocity random variable in the direction of x
V_y	Velocity random variable in the direction of y

$\vec{v}$	Velocity vector
$v_{\perp}$	Cross field velocity magnitude
v_{exit}	Exit velocity of Thruster
v_{th}	Thermal velocity
W	Thruster channel width
X	x position random variable
Xe	Abbreviation of Xenon
$\vec{x}$	Space coordinate
Y	y position random variable
z	Thruster axial coordinate
z_{cath}	Axial coordinate of cathode location from thruster exit
z_m	Axial coordinate of matching point
Subscript e, i, n	Electron, ion, and neutral, respectively
α_{ano}	Anomalous coefficient
$\hat{\alpha}_{ano}$	Inverse of anomalous coefficient
α_{relax}	Relaxation coefficient
β	Velocity space diffusion constant
$\Delta\varepsilon$	Energy loss
ε_0	Freespace permittivity
ε_e	Electron energy
ε_{exc}	Threshold energy of first excitation level for Xenon
ε_{ion}	Threshold energy of first ionization for Xenon

Γ	Flux
η	Efficiency
η_a	Acceleration efficiency
η_{ano}	Anode efficiency
η_b	Beam efficiency
η_e	Electrical efficiency
η_i	Ionization efficiency
η_{tot}	Total efficiency
η_u	Utilization efficiency
φ	Electric potential
φ_{edge}	Electric potential at the Tonks-Langmuir edge
φ_d	Electric potential at the anode
φ_m	Electric potential at the matching point
λ	Debye length
μ	Reduced mass
$\mu_{e,\perp}$	Electron cross field mobility
ν	Collision frequency or true anomaly
ν_B	Bohm collision frequency
ν_{coll}	Total collision frequency
ν_d	Effective frequency for the electron axial diffusion
ν_e	Electron momentum collision frequency
$\nu_{e,eff}$	Effective electron momentum collision frequency

$\nu_{e,\varepsilon}$	Electron energy loss frequency
$\nu_{e,m}$	Electron momentum collision frequency
$\nu_{e,w}$	Electron wall collision frequency
ν_{ei}	Coulomb collision frequency
ν_{en}	Electron neutral momentum collision frequency
ν_{exc}	Excitation collision frequency
ν_i	Ionization collision frequency
$\nu_{i,ave}$	Averaged ionization collision frequency
ν_{mt}	Momentum collision frequency
ν_{recom}	Recombination collision frequency
σ	Reaction cross section
θ	Azimuthal direction coordinate
Ω	Longitude of ascending node
Ω_e	Electron Hall parameter
ω	Argument of periapsis
ω_c	Cyclotron frequency
ω_e	Electron gyro frequency
ω_p	Plasma frequency

LIST OF ABBREVIATIONS

AFRL	Air Force Research Laboratory
ASDL	Aerospace Systems Design Laboratory
BN	Boron Nitride
BOL	Beginning Of Life
CCD	Central Composite Design
CDT	Closed Drift Thrusters
C-EOR	Chemical-Electric Orbit Raising
CFD	Computational Fluid Dynamics
CSR	Charge Saturation Regime
DC	Direct Current
DDP	Differential Dynamic Programming
DOE	Design of Experiment
DSE	Design Space Exploration
DSMC	Direct Simulation Monte Carlo
EDL	Entry, Descent and Landing
EOR	Electric Orbit Raising
EP	Electric Propulsion
FET	Finite Element in Time
GD-SPS	General Dynamics Space Propulsion Systems
GEO	Geosynchronous Earth Orbit
GTO	Geosynchronous Transfer Orbit
GRC	Glenn Research Center

HDDP	Hybrid Differential Dynamic Programming
HET	Hall Effect Thruster
IPS	Ion Propulsion System
ITAR	International Traffic in Arms Regulations
LEO	Low Earth Orbit
LHS	Latin Hypercube Sampling
LMSSC	Lockheed Martin Space Systems Company
LS	Least-Squares
LTE	Local Thermodynamic Equilibrium
MC	Monte Carlo
MCC	Monte Carlo Collision
MFE	Model Fit Error
MDO	Multidisciplinary Design Optimization
MLT	Magnetic Layer Thruster
MPD	Magnetoplasmadynamic Thruster
MRE	Model Representation Error
NLP	Nonlinear Programming
NMP	New Millennium Program
NN	Neural Network
NSSK	North South Stationkeeping
ODE	Ordinary Differential Equation
ORM	Orbit Raising Mission
O-U	Ornstein-Uhlenbeck
PIC	Particle-In-Cell
PM	Particle-Mesh

PPT	Pulsed Plasma Thruster
pmc	Percentage of mass flow rate at the cathode
ppc	Percentage of power consumed by the cathode
ppm	Percentage of power consumed by electrical magnets
QP	Quadratic Programming
RMSE	Root Mean Square Error
RSM	Response Surface Methodology
SEE	Secondary Electron Emission
SEP	Solar Electric Propulsion
SMO	Sequential Minimal Optimization
SPT	Stationary Plasma Thruster
SSDL	Space Systems Design Laboratory
SVM	Support Vector Machine
TAL	Thruster with Anode Layer
TPBVP	Two Point Boundary Value Problem
TRL	Technology Readiness Level

SUMMARY

Hall Effect Thrusters (HETs) are a form of electric propulsion device which uses external electrical energy to produce thrust. When compared to various other electric propulsion devices, HETs are excellent candidates for future orbit transfer and interplanetary missions due to their relatively simple configuration, moderate thrust capability, higher thrust to power ratio, and lower thruster mass to power ratio.

Due to the short history of HETs, the current design process of a new HET is a largely empirical and experimental science, and this has resulted in previous designs being developed in a narrow design space based on experimental data without systematic investigations of parameter correlations. In addition, current preliminary low-thrust trajectory optimizations, due to inherent difficulties in solution procedure, often assume constant or linear performances with available power in their applications of electric thrusters. The main obstacles come from the complex physics involved in HET technology and relatively small amounts of experimental data. Although physical theories and numerical simulations can provide a valuable tool for design space exploration at the inception of a new HET design and preliminary low-thrust trajectory optimization, the complex physics makes theoretical and numerical solutions difficult to obtain.

Numerical implementations have been quite extensively conducted in the last two decades. An investigation of current methodologies reveals that to date, none provide a proper methodology for a new HET design at the conceptual design stage and the coupled low-thrust trajectory optimization.

Thus, in the first half of this work, an efficient, robust, and self-consistent numerical method for the analysis of HETs is developed with a new approach. The key idea is to divide the analysis region into two regions in terms of electron dynamics based on physical intuition. Intensive validations are conducted for existing HETs from 1 kW to 50 kW classes.

The second half of this work aims to construct a simultaneous design optimization environment though collaboration with experts in low-thrust trajectory optimization where a new HET and associated optimal low-thrust trajectory can be designed simultaneously. A demonstration for an orbit raising mission shows that the constructed simultaneous design optimization environment can be used effectively and synergistically for space missions involving HETs.

It is expected that the present work will aid and ease the current expensive experimental HET design process and reduce preliminary space mission design cycles involving HETs.

CHAPTER 1

INTRODUCTION

1.1 Space Propulsion

Space propulsion basically has two objectives; one is obviously transportation, the other is for in-orbit usage. The space transportation objective is the same as other means of transportation; deliver payload from some initial point to a destination, which can be intermediate or final. For example, if a communication satellite were to be placed in Geosynchronous Earth Orbit (GEO), a launch vehicle might be used to deliver it from the Earth's surface to an intermediate destination in Low Earth Orbit (LEO). Another space propulsion device such as the upper stage rocket might then deliver it from LEO to a final destination of GEO. For planetary landing missions, another form of space propulsion is required for capturing the planet's orbit and Entry, Descent and Landing (EDL). In-orbit usage stems from the requirements for specific mission needs such as attitude requirements of the spacecraft or solar panel array (spacecraft attitude control) and space orbital perturbation compensation (orbital maintenance). A typical metric for the energetic requirements of these tasks is often expressed as the amount of total required velocity change or ΔV.

There are several space propulsion options available to accomplish various space mission ΔV requirements. Some of these options are commercially available while others are considered feasible based on laboratory research or in the state of future

concepts. Table 1.1 shows general performance, advantages and disadvantages for each of the space propulsion technology options, which are currently available [1] - [3].

Table 1.1: Available Space Propulsion Technology Options [1] - [3]

Space Propulsion Technology		Specific Impulse (I_{sp}) [sec]	Thrust [N]	Advantages	Disadvantages
Cold Gas		50 – 250	0.05 – 200	• Simplicity • Reliability • Safety	• Low I_{sp} • Heaviest for given performance
Chemical	Liquid	140 – 460	0.1 – 10^6	• Moderate I_{sp} • Can be restarted	• Toxic propellants • Intense combustion heat
	Solid	260 – 300		• Simplicity • No propellant management	• Susceptible to cracks in the grain • Can't restart • Difficult to stop
	Hybrid	290 – 350		• Safer and more flexible that solids • Can be restarted	• Short historical development
Electric		150 – 8,000	10^{-5} – 5	• Very high I_{sp}	• Short historical development • Complex system • Need for relatively high power • Low thrust level

The options which are feasible in the near future include nuclear and magnetoplasmadynamic propulsion systems. While nuclear propulsion can provide I_{sp} ranging from 800 up to 6000 sec and thrust up to 1.2×10^7 N, the technology has not been well proven, relatively expensive, and has encountered political and environmental issues. Magnetoplasmadynamic propulsion is a form of electric propulsion and within this class can provide the highest thrust (up to 100 N) as well as high I_{sp}. With this performance capability it is anticipated that it will be used for primary propulsion for large space vehicles.

Other concepts are massless propulsion devices which do not require propellants to obtain thrust. Examples are solar sails, tethers, gravity assists, and aerobrakes.

Each propulsion system in Table 1.1 has a specific operation mechanism. Cold gas propulsion simply uses the mechanical energy of a compressed gas propellant by expansion through a nozzle. Chemical propulsion relies on the bond energy of propellants through combustion. Electric propulsion uses electrical energy to accelerate the propellant.

Referring to Table 1.1, the propulsion systems which operate in the low thrust regime are often used for orbit maintenance, minor in-orbit maneuvers, and attitude control. On the other hand, high thrust propulsion systems are primarily used for launch, orbit insertion, and orbit transfers.

Specific impulse measures the efficiency of propellant usage since it is defined as thrust divided by the propellant weight flow rate (relative to the Earth's surface) as shown in Equation (1.1). A high specific impulse is desirable since it gives more thrust with given propellant mass flow rate.

$$I_{sp} = \frac{T}{\dot{m}g_e} \tag{1.1}$$

where, T is the thrust magnitude, $\dot{m}$ is the propellant mass flow rate, and g_e is the magnitude of the gravitational acceleration at the Earth's surface. In the mission perspective, specific impulse plays an important role in determining allowable payload fractions as seen in the ideal rocket equation [2],

$$\frac{m_{final}}{m_{initial}} = \exp\left(-\frac{\Delta V}{v_{exit}}\right) = \exp\left(-\frac{\Delta V}{I_{sp}g_e}\right) \tag{1.2}$$

where, m_{final} is the final space vehicle mass, $m_{initial}$ is the initial space vehicle mass, v_{exit} is the exit or exhaust velocity of the thruster, and ΔV is the required velocity change to complete the given mission. Equation (1.2) implies that if specific impulse is high, then for a given required velocity change, a high final mass fraction can be obtained. This is a significant benefit since less propellant is required for the given mission.

In terms of high I_{sp}, electric propulsion seems to lie at the leading edge for space propulsion. However, this is not the whole story. Due to their high thrust capability, chemical propulsion systems are the only current viable option for launch. In addition, orbit transfer missions have historically been performed almost exclusively by chemical propulsion systems. However, chemical propulsion systems for other operations, such as orbit maintenance, orbit maneuver and attitude control, are no longer the exclusive propulsion option. Such operations do not require a large thrust capability. Rather, they need to have the propulsion system controlled easily for precise maneuvers. Cold gas is a good candidate for these tasks, but it has low specific impulse which implies low payload mass fraction or short mission duration.

Electric propulsion is a leading candidate for orbit control due to its high specific impulse capability. Furthermore, a recent study shows that if these advanced propulsion technologies with their high specific impulse were used for general orbit transfer missions, e.g., from LEO to GEO, significant cost savings could be realized when compared to a conventional launch vehicle and a chemical upper stage configuration [4]. As a result, electric propulsion might be very promising for virtually all future space propulsion except for launch. In the next section, an overview of electric propulsion will be given.

1.2 Electric Propulsion (EP)

Since EP uses electrical energy to obtain thrust, the exhaust velocity produced is not restricted by the bond energy in the propellant. Thus, exhaust velocity is not limited in a theoretical sense, except by the speed of light. This results in a unique characteristic of very high specific impulse. What matters is how much power can be provided to accelerate the propellant. Therefore, a tradeoff between thrust or specific impulse and available power is always considered.
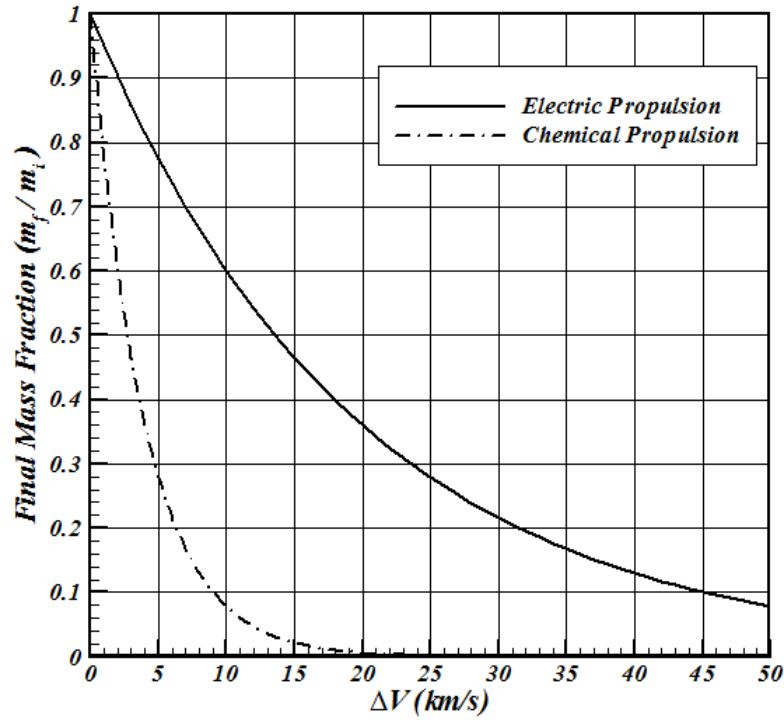
Figure 1.1: Final Mass Fraction Comparison (I_{sp} of EP = 2000 sec, I_{sp} of CP = 400 sec)

High specific impulse can expand current space mission capabilities and even create new possibilities for future missions. This fact is more clearly shown in Figure 1.1, which compares the final mass fractions between spacecraft using EP and chemical propulsion using Equation (1.2). The specific impulse of EP is assumed to be 2000 sec and that of chemical propulsion to be 400 sec.

5
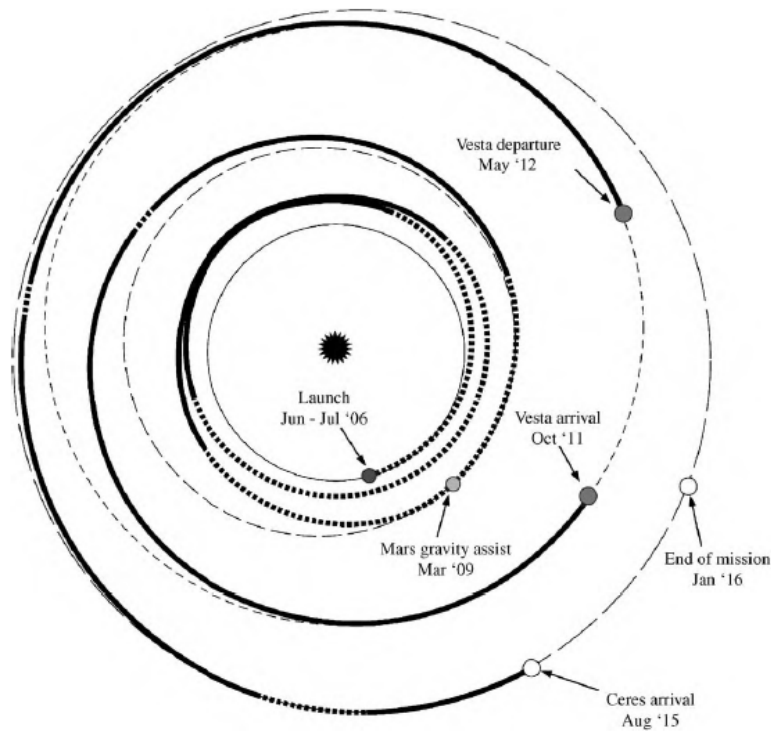
Figure 1.2: Baseline Dawn Mission [4]

This advantage, however, doesn't come without cost. In any mission analysis, there are always competing factors such as mission time and required velocity change. Usually, as smaller mission time is required, more overall velocity change is needed. However, in the sense of realizing impossible missions by other propulsion systems, higher specific impulse definitely provides overwhelming benefits. For example, in the Dawn Project, where the mission is to explore two large asteroids, Ceres and Vesta, an ion propulsion system is being used (Figure 1.2). The mission would not be possible under the given constraints if a chemical propulsion system were used [4]. This example demonstrates the use of EP very promising.

Of course, there also exist some disadvantages of EP that should be addressed. As seen in Table 1.1, its low thrust level discriminates against its use for a controlled landing operation. The primary reason why the Dawn project could not plan a landing mission on

6

either Ceres or Vesta was the inability of the propulsion system to provide the 200 N required to land on Ceres [4]. This thrust level is far beyond the capability of the current EP devices. Furthermore, its low thrust characteristics may cause significant gravity losses due to gradual and spiral acceleration; however this fact alone does not completely negate its relative advantage over the chemical propulsion in terms of payload mass fraction. Another drawback comes from its propellant acceleration mechanism. Because electric propulsion requires an external electrical energy, additional mass for power generation, processing and management is required, which results in a payload penalty. Another drawback is its short development history. In spite of EP's obvious advantages, spacecraft designers usually prefer to use proven and highly reliable technologies rather than those with significant uncertainties.

Table 1.2: Available Electric Propulsion Options and Their Characteristics [1] - [3]

Class	Thruster	I_{sp} [sec]	Thrust [N]	Efficiency [%]	Thrust /Power [mN/kW]	Specific Mass [kg/kW]	Propellant
Electrothermal	Arcjet	400 – 800	0.05 – 5	25 – 45	110 – 135	2.5 – 3.5	NH_3 / N_2H_4
Electrothermal	Resistojet	300	0.005 – 0.5	65 – 90	740 – 910	1 – 1.6	N_2H_4
Electrostatic	Ion	2000 – 8000	5×10^{-6} – 0.5	40 – 80	25 – 41	9.1 – 23.7	Xe
Electrostatic	Hall	1500 – 3250	5×10^{-6} – 3	35 – 60	55	6 – 7	Ar / Xe
Electromagnetic	PPTs	850 – 1200	5×10^{-6} – 0.005	7 - 13	16 – 21	85 – 195	Teflon

Interest in EP for space propulsion started in the early 1960's, although the possibility had been suggested earlier [6]. Since then, a wide variety of EP devices have been studied and developed. EP devices are classified into three categories based on their main mechanism of accelerating propellant; electrothermal, electrostatic, and electromagnetic. Table 1.2 shows EP classes, currently available representative thrusters, and their characteristics.

Electrothermal Propulsion

This category of EP has the most similar mechanism to conventional chemical propulsion. The primary difference is that the energy required to heat the working fluid comes from an electrical source. Conversion from heat to kinetic energy is accomplished by a conventional nozzle as in chemical propulsion. Whereas in chemical propulsion, heat is generated from the chemical reaction of the propellant and oxidizer, in electrothermal propulsion, the heat is directly deposited into the working fluid by either direct contact with resistively-heated elements (resistojet) or by passing the electric current directly through the fluid (arcjet). Because of the limited power available, their geometric characteristics result in small size and short nozzle length, which in turn make the residence time of the working fluid in the nozzle small. This causes frozen flow loss as the internal energy cannot be fully released into kinetic energy.

Electrostatic propulsion

As implied in the name, this category of propulsion uses electrostatic fields to accelerate the working fluid. This mechanism of obtaining thrust is quite different from those in other space propulsion options. Since electrostatic acceleration requires at least a partially ionized gas, the device must somehow provide the means of ionization. In

HETs, electron bombardment ionization is usually employed, i.e., ionization through collisions between neutral particles and electrons. The ionization results in a plasma consisting of atoms, electrons, and positively charged ions. Once charged particles are generated, the ions are extracted and accelerated by an applied electrostatic field. Then a cathode neutralizer emitting additional electrons neutralizes the accelerated ions to prevent the spacecraft from leaving the charge equilibrium.

The ion engine has distinct regions and elements for these three processes; ionization, ion acceleration, and ion neutralization. The ionization is done by a discharge chamber, ion acceleration is accomplished by a series of electrically biased grids, and ion neutralization is achieved by an additional cathode neutralizer located outside the thruster. In contrast with the ion engine, an HET does not have distinct regions, but rather continuous processes. Furthermore, ionization, acceleration, and neutralization are done by a relatively simple geometric configuration when compared to ion engines. The HET employs a magnetic field to trap electrons long enough for sufficient ionization. Traditionally, the magnetic field has been the ubiquitous means for plasma confinement in nuclear fusion plasma research. This is why HETs are sometimes classified as electromagnetic propulsion. However, because the main acceleration mechanism is electrostatic force, it seems more appropriate to classify HETs as electrostatic. Although the efficiency of an ion thruster is the highest in terms of power conversion to useful thrust, it suffers from a thrust density limitation (space charge constraint). In addition, typical ion engines have a lower thrust to power ratio and higher specific mass than HETs. In this sense, HETs are the most promising electrostatic EP device for near term in-space propulsion. HETs will be discussed in the next section in more detail.

Electromagnetic propulsion

This category of EP uses the Lorentz force, $\vec{j} \times \vec{B}$, where $\vec{j}$ is the applied current density and $\vec{B}$ is the magnetic field which can be self-generated or applied, to generate thrust. Magnetoplasmadynamic thrusters (MPDs) use self-generated magnetic fields and Pulsed Plasma Thrusters (PPTs) use an applied magnetic field. In MPDs, a large current flow is required to generate the magnetic field. Thus, although it can produce the highest thrust among EP devices, the amount of power usage is large. PPTs use solid propellant, usually Teflon, which doesn't need a complicated propellant management system. An arc through the Teflon propellant surface ablates and ionizes it, and any ionized propellant is then accelerated by the Lorentz force created by the arc current interacting with the applied magnetic field. Since PPTs have very low thrust capabilities, they have been used for stationkeeping, which require only a small thrust and impulse-bit thruster operation.

1.3 Hall Effect Thruster

HETs are electrostatic EP devices first studied by the USA and the former Soviet Union in the early 1960's. The USA rapidly shifted its research focus to ion thrusters at that time since the efficiency of HETs was less than that of ion thrusters. The former Soviet Union continued to research HETs, thus, many current technologies of HETs are attributed to their efforts. In 1972, the former Soviet Union completed the first on-orbit test with HET and has continued to use them for stationkeeping and orbit maintenance missions. After the Cold War, the HET technology was released to other countries, which spurred research and development, especially in USA and France. Additional details on HET history can be found in Ref. [7].

Simple schematics of an HET are shown in Figure 1.3 and Figure 1.4. Specifically, Figure 1.3 and Figure 1.4 show a Stationary Plasma Thruster (SPT) which is one kind of two types of HETs. The classes of HETs will be discussed later.
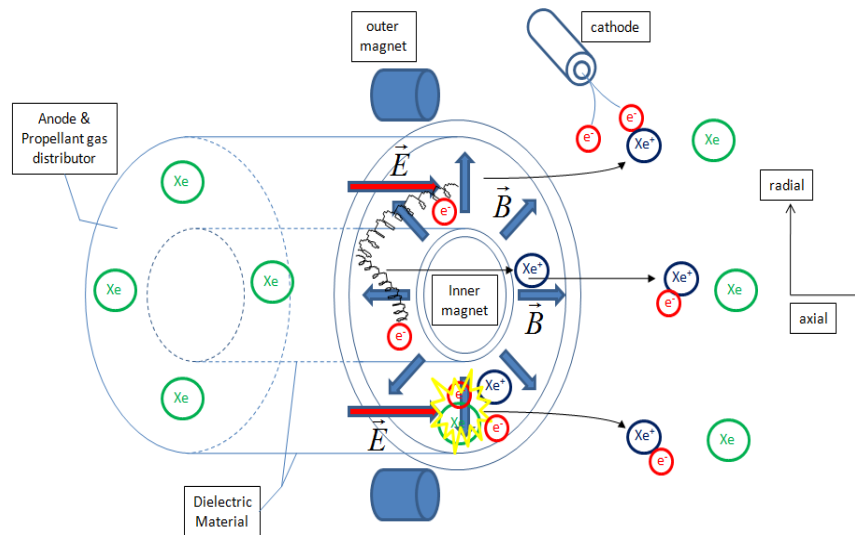
Figure 1.3: The Schematic of Hall Effect Thruster (SPT)
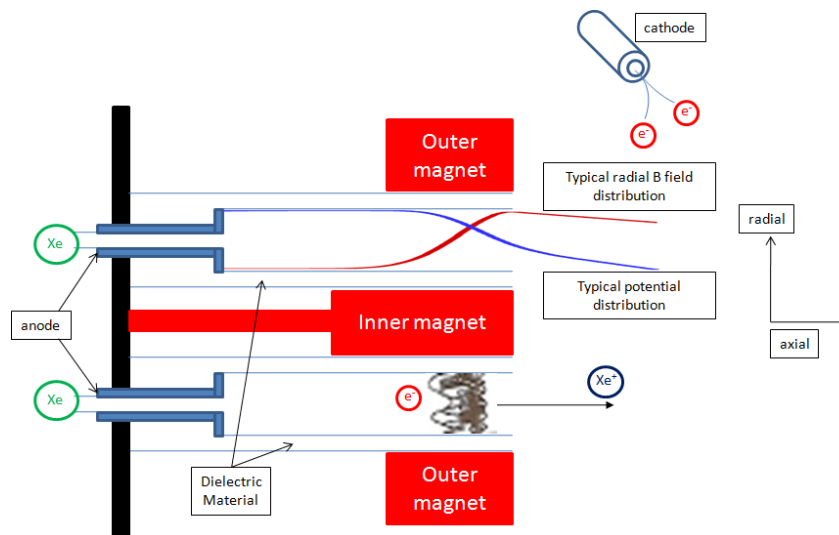
Figure 1.4: The Sectional View of a Hall Effect Thruster (SPT)

The electrons emitted from the cathode flow toward the anode due to the potential difference between the anode and the cathode. The electrons are collected at the anode and the electrical current is formed due to phenomenon called electrical discharge. This

discharge is shaped by the presence of a radial magnetic field which prohibits the electrons from moving directly toward the anode. This is because the magnetic field has the property of trapping the charged particles around its field lines.

Because of the axial electric field from the potential distribution between the anode and the cathode, the Lorentz force causes the electrons to drift in the direction of $\vec{E} \times \vec{B}$, which generates an azimuthal current. This phenomenon is called the Hall effect and the azimuthal current is called the Hall current in honor of Edwin Hall's discovery of this phenomenon [8]. The azimuthal current also inspired another name for HETs, Closed Drift Thrusters (CDTs). In order to have a discharge in the device, some form of electron transport mechanism must be present to allow the electrons to travel from the cathode to the anode. Collisions with neutrals and other anomalous transport mechanisms provide the mechanisms for this transport.

If a magnetic field does not exist, electrons are purely accelerated in the opposite direction of electric field. Because the electron mass is very small, the acceleration by the electric field causes electrons to obtain very high velocities in a very short time period. Thus, it is expected that electrons would be transported to the anode with very high velocity in a very short time scale, which makes it difficult to give the electrons enough time to ionize neutrals. Through electron trapping by the magnetic field, electrons have enough time to ionize the neutrals, i.e., raising the Damköhler number, which is the ratio of flow times to chemical time in combustion literature. The ionization process generates ions, which are then accelerated by the axial electric field and produce useful thrust. Ions are nearly unaffected by the magnetic field in the distance scale of the device because of their relatively large mass. The different responses of ions and electrons to the magnetic

field lead to an interesting plasma behavior in HETs. The fact that the applied DC voltage is almost the same potential difference between the anode and the cathode is largely attributed to this mechanism.

In the perspective of a force transferring mechanism to ions, although ions seem to be accelerated by the axial electric field, this force is approximately equal to the Lorentz force exerted on electrons from the quasi-neutrality of mixed ion and electron bulk plasma. Since the Lorentz force on the electrons is $\vec{j}_{hall} \times \vec{B}$, HETs are sometimes classified as the electromagnetic devices as stated in the previous section.

Basically, there are two types of HET; the Stationary Plasma Thruster (SPT) and the Thruster with Anode Layer (TAL). SPT is a translated name from the Russian literature. Another name for SPT is Magnetic Layer Thruster (MLT). The word "stationary" does not represent the physical characteristics of the SPT, rather it is intended to distinguish this type of thruster from PPTs. In general, SPT and TAL have similar performance and physical characteristics except for the length and composition of their acceleration channels. The SPT has a longer acceleration zone than the TAL. This physical difference comes from the different material used in the SPT and TAL. SPT uses dielectric materials which are typically a kind of ceramic, e.g., Boron Nitride (BN). TAL uses metallic wall materials which are usually stainless steel. These materials have different Secondary Electron Emission (SEE) properties, which in turn have an effect on the electron temperature in the plasma. Dielectric materials have large SEE coefficients when electrons collide with the channel wall, which lowers the overall electron temperature inside the channel. The reverse effect holds for TAL since a metallic wall

emits very few secondary electrons. This causes TALs to have very short acceleration regions.

The extensive discussions on HET technologies are provided in Ref. [9] - [10]. The fundamental differences between SPT and TAL are discussed in depth in Ref. [11].

1.4 Interim Summary

A Top-down approach has been used to introduce background for the general space propulsion options to the HETs. Since the current study specifically concerns HETs in the context of its conceptual design process regarding HET performances and its impacts on space mission trajectory optimization, the design activities for HETs and associated low-thrust trajectory optimizations requires review. The following sections will be devoted to these topics.

1.5 General Remarks on a New HET Design

The general design process used for aircraft or other products will apply to HETs; conceptual, preliminary and detailed. However, in the context of the design process, how to initiate the design process for a new HET is not an easy question due to its short history and lack of proper design tools. The current design process of a new HET is accomplished by empirical and experimental science. This means that specifications of required design variables, parameters and important metrics must rely thoroughly on previous experimental data and experience. If only historical and empirical data were to be used, the design space to be sought would be very narrow. What makes matters worse is that the reliance on empirical designs presents a risk for a new design which might not be explained by previous empirical results. This risk generally comes from design trials for either a configuration or highly nonlinear physical processes involved. The

configuration being designed may have major differences from what can be described by empirical data. Highly nonlinear physical processes may also cause an unexpected and undesirable design even though the configuration may be very similar to an existing design. As invoked recently in the design community [12] - [13], the design processes for a new HET must have the properties adapted into this design paradigm shift because of the limited historical experiences, particular difficulties arising from ground test of space propulsion devices, and highly nonlinear physical processes involved in HETs. An important property is to bring a physics-based analysis to early design stage.

Although there are some HETs which have a Technology Readiness Level (TRL) of 9, if one were to construct a new HET, its TRL drops significantly because of reasons stated in the previous paragraph. General information about TRL can be found in Ref. [14]. The performance characteristics are the most important metrics during this stage in the design of a new HET. Their variations with the input parameters are of interests as shown in Table 1.3.

Table 1.3: Metrics and Parameters of Interest in HET Design

Metrics	Parameters
Thrust	Available Power
Specific Impulse	Geometric Configuration
Efficiency	Magnetic Field Configuration
Specific Mass	Applied Discharge Voltage
Specific Power	Propellant Type and Mass Flow Rate

1.6 Previous Design Activities for HET

As mentioned in section 1.3, many current design rules for the HET have been established by the efforts of the former Soviet Union. Effective HETs could only be achieved after a great deal of experimental efforts requiring substantial investment. This

seems quite ineffective compared to the current aircraft design processes. However, this trial and error approach has been the typical process for newly proposed concepts which are in an initial development stage.

Typical design efforts for a new HET are as follows:

1) *Narrow the design space based on so called scaling laws established in the form of graphs or empirical equations. A large number of parameters are already determined at this step.*

2) *Experimental trial and error is then applied to obtain an effective HET.*

Scaling laws have been proposed to aid the conceptual design process and reduce experimental efforts. They are basically extracted from the experimental data of existing HETs [15]-[19]. Experimental results on existing HETs can be applied to determine the variation trend of concerned metrics for specific parameters. For example, the discharge voltage or propellant mass flow rate can be varied for a given configuration and their effects on metrics can be investigated. The costly parts of the design process are the investigations necessary to determine the effects of geometric changes due to the need of manufacturing parts of different sizes. Thus, the scaling laws for some important geometric dimensions such as the diameter of the discharge chamber also results from those existing HETs. Some of the detailed geometrical dimensions can be obtained directly from the Russian Hall Thruster designers [20].

The following two sub-sections are devoted to case studies of design processes which have been completed or proposed. The intent in presenting these case studies is to aid in understanding the state of the art in design process of the HET.

1.6.1 Case Study I – University of Michigan / AFRL P5 5 kW class HET Design

University of Michigan and Air Force Research Laboratory (AFRL) designed and built a 5kW class laboratory model HET, the UM-AFRL P5 [21]. The design process of the P5 is summarized here [22]. Designers began by narrowing down the design using simple equations and data from 8 existing HETs. With the targeted starting point of 5 kW nominal power level for the target thruster, the following conceptual design process was used.

Step 1: Determine Expected Specific Impulse

An exponential scaling law from existing thrusters was used to determine the expected specific impulse as shown in Figure 1.5.
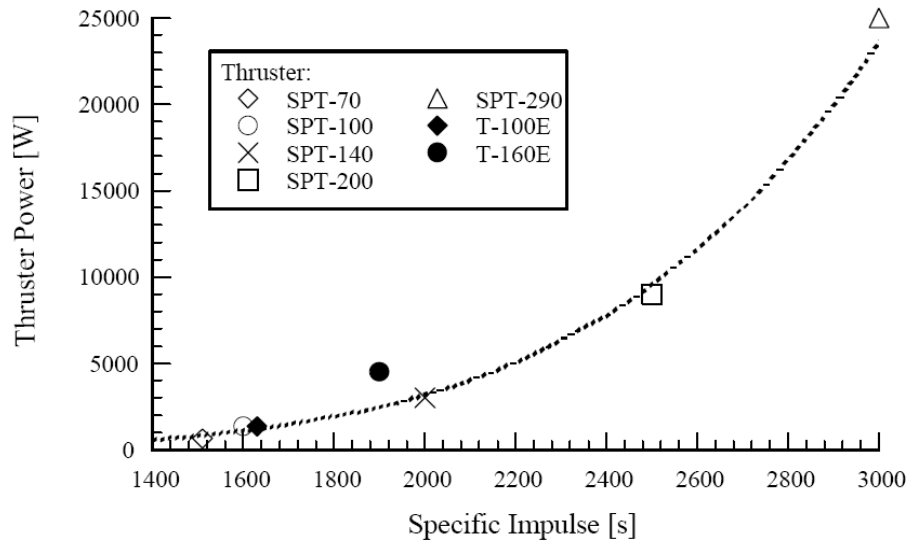
Figure 1.5: Relation between Thruster Power and Specific Impulse [22]

Step 2: Determine Expected Efficiency

The relation between expected efficiency and specific impulse was borrowed from one that had been proposed for ion engines with different coefficients [23]. The form of the equation is given by,

17

$$\eta = \frac{a}{1+\dfrac{b}{(g_e I_{sp})^2}}$$

(1.3)

where, a and b were estimated to be 0.8 and 1.42×10^8.

The resultant curve-fit is shown in Figure 1.6.
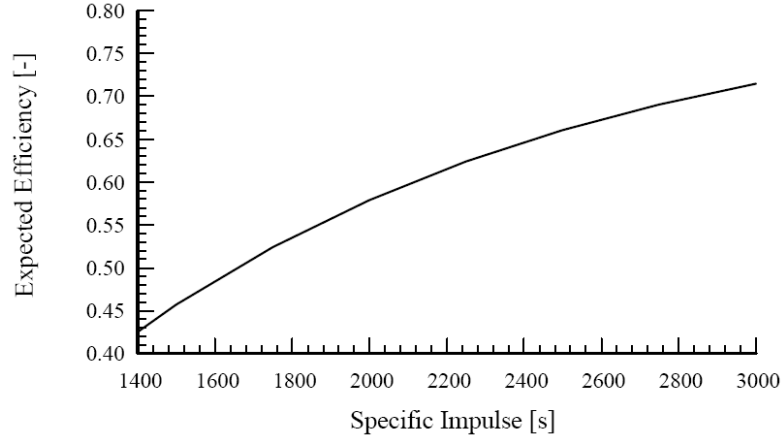
Figure 1.6: Relation between Expected Efficiency and Specific Impulse [22]

Step 3: Determine Expected Propellant Mass Flow Rate

The following relationship was used for the given nominal power level with determined efficiency and specific impulse in the previous steps.

$$\dot{m}_p = \frac{2\eta P_d}{(I_{sp} g_e)^2}$$

(1.4)

Step 4: Determine Expected Discharge Chamber Diameter

A linear scaling law from existing thrusters was used to determine the expected discharge chamber diameter as shown in Figure 1.7.
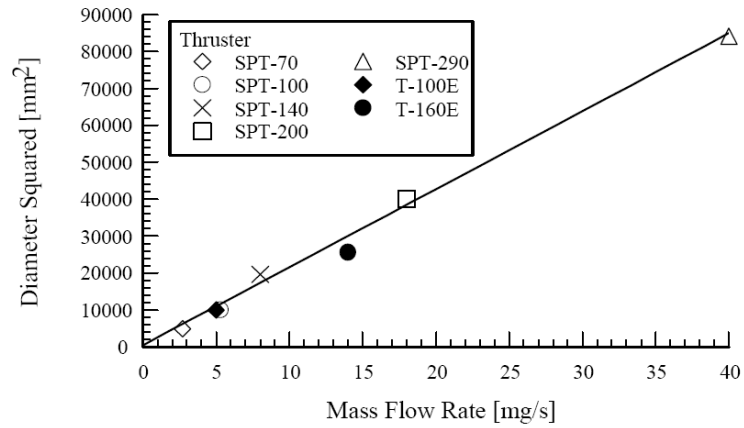
Figure 1.7: Relation between Expected Discharge Chamber Diameter Squared and Propellant Mass Flow Rate [22]

Step 5: Determine Other Geometrical Lengths

Other geometries to be determined are shown in Figure 1.8.
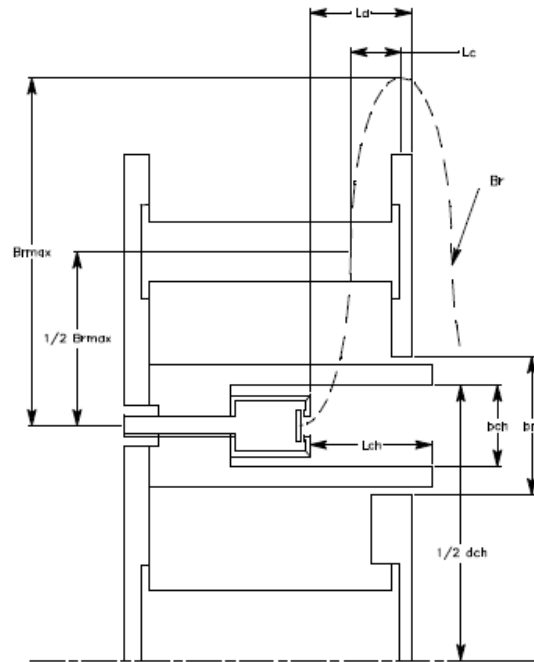
Figure 1.8: Lengths to be Determined [22]

These geometrical lengths were obtained from a set of design equations that had been given by Russian Hall Thruster designers presented in Ref. [20] as follows.

19

$$b_m = 0.3d_{ch} \ [mm]$$

$$b_{ch} = 6 + 0.375b_m \ [mm]$$

$$L_e = 0.32b_m \ [mm] \qquad\qquad (1.5)$$

$$L_a = 2L_e \ [mm]$$

$$L_{ch} \leq 1.1L_a \ [mm]$$

where, d_{ch} is the discharge chamber diameter, b_m is the distance between the front magnetic pole pieces, b_{ch} is the channel width, L_e is the axial distance between the point of maximum magnetic field and the point of half maximum magnetic field, L_a is the distance from the anode to the front magnetic pole and L_{ch} is the channel length.

As seen in the design procedure, starting from the specified nominal power level, the required parameters are determined step by step in a very deterministic way. There is no design space exploration or optimization process with consideration of a specific mission to obtain a proper basis for the concerned HET. From this case study, the following is observed:

1) The conceptual design process to find a basis for the target thruster was done completely by relying on previous experimental data (scaling laws).

2) The scaling laws for certain parameters were crude due to the small amount of available data.

3) There appears to be a lack of a proper tool for design space exploration or optimization in the early stage of design.

1.6.2 Case Study II – More Recently Suggested Scaling Laws and Design Process

In this case study, the scaling laws were extracted from a relatively large database on HET operation characteristics and suggestions of a design process are introduced. Most of the contents come from Ref. [24], where more than 1100 operating points of various Hall thrusters were collected to construct a database. Based on this database, metrics and parameters were correlated. For example, the following scaling laws were suggested.

$$T = 0.0785 \, P_d^{0.9515}, \quad I_d = 1.0709 \, \dot{m}, \quad M_{thruster} = 0.0334 \, P_d^{0.6415}$$

where, T is the thrust, P_d is the discharge power, I_d is the discharge current and $M_{thruster}$ is the thruster mass. From these types of scaling laws, the following preliminary design steps for 10 kW class thrusters were proposed. Two different scaling procedures, based on either an optimal efficiency scaling path or an optimal thrust-to-power ratio scaling path, were applied. The following are the detailed design steps:

Step 1: Determine Expected Thrust and Propellant Mass Flow Rate
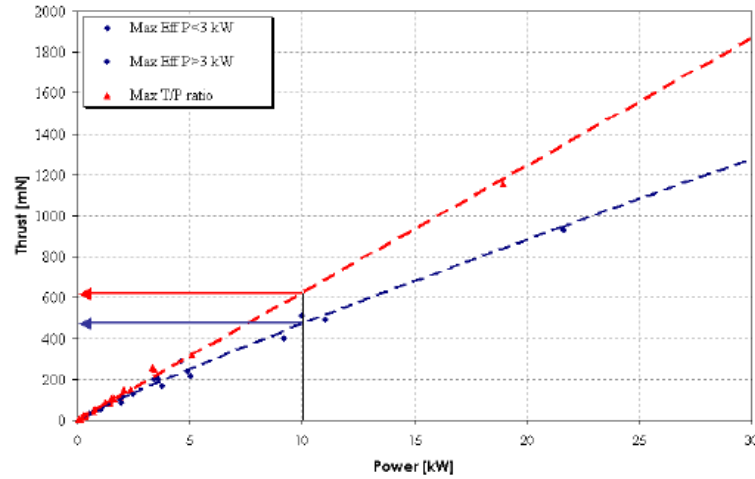
Figure 1.9: Relation between Expected Thrust and Nominal Discharge Power [24]

Expected thrust and propellant mass flow rate were obtained from correlations with nominal discharge power which are shown in Figure 1.9 and Figure 1.10. Two points are selected. One is from the optimal efficiency path; the other is from the optimal thrust-to-power ratio path.
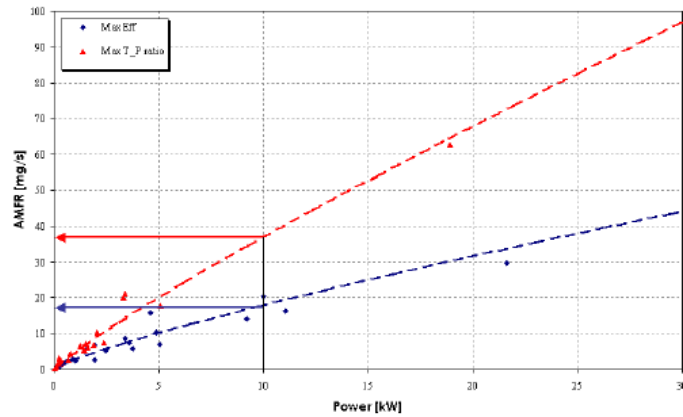
Figure 1.10: Relation between Expected Propellant Mass Flow Rate and Nominal Discharge Power [24]

Step 2: Determine Expected Discharge Current

The relation between expected discharge current and propellant mass flow rate is used to determine the expected discharge current as shown in Figure 1.11.
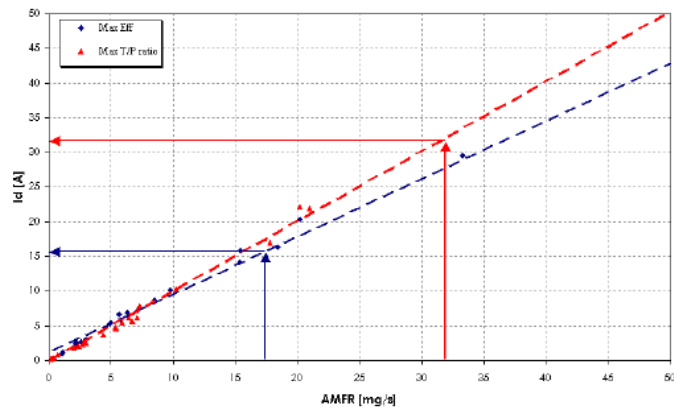
Figure 1.11: Relation between Expected Discharge Current and Propellant Mass Flow Rate [24]

Step 3: Determine Expected Specific Impulse

The study indicated that the expected specific impulse could be correlated in various ways. The correlation between expected specific impulse and nominal discharge power was chosen as shown in Figure 1.12.
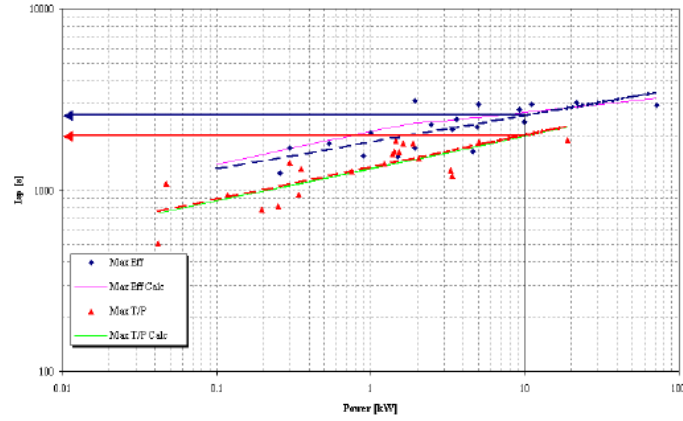
Figure 1.12: Relation between Expected Specific Impulse and Nominal Discharge Power [24]

Step 4: Determine Expected Efficiency

Expected efficiency is determined by the model suggested in Ref. [25]. The form of the model is the same as the one that was used for determining expected efficiency for the P5 in case study I. The curve of model is shown in Figure 1.13.
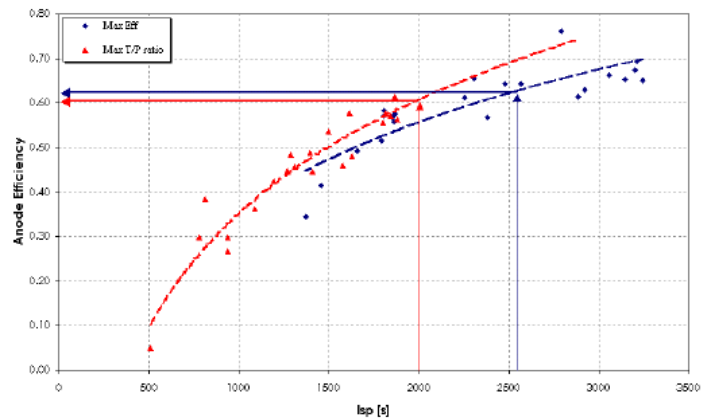
Figure 1.13: Relation between Expected Efficiency and Specific Impulse [24]

23

Step 5: Determine Expected Channel Diameter and Thruster Mass

They derived expected channel diameter and thruster mass from the correlations with nominal discharge power as shown in Figure 1.14 and Figure 1.15.
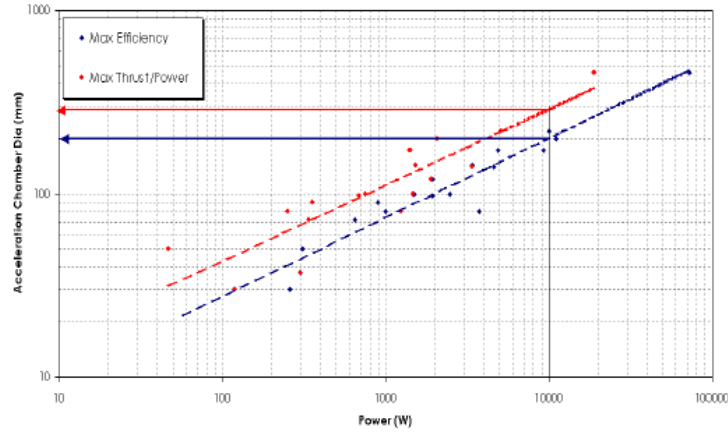
Figure 1.14: Relation between Expected Channel Diameter and Nominal Discharge Power [24]
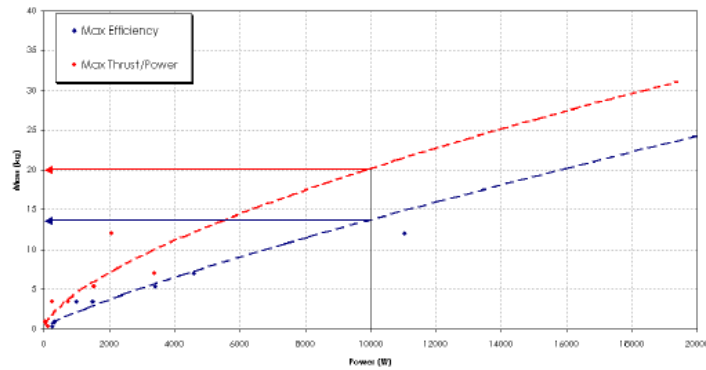
Figure 1.15: Relation between Expected Thruster Mass and Nominal Discharge Power [24]

As seen in the design procedure, starting from a specified nominal power level as for the P5, the required parameters were determined by applying sequential correlations with previously determined parameters. From this case study, the following are identified:

1) The same process as the P5 was used based on empirical scaling laws.

2) As seen in Step 3, there could be other possibilities for correlations among the given parameters. This could make the proposed process ambiguous.

1.6.3 Concluding Remarks on Case Studies

Overall, it can be concluded that the current design of a new HET is quite empirical and experimental as identified in the case studies. No physical considerations are given in the conceptual design process. The risk in this approach is magnified by the lack of historical data. When one takes into account that complicated, nonlinear physics are involved in the HET, total reliance on scaling laws for a new design might result in a suboptimal device. For example, MIT designed a 50 W miniaturized HET based on the scaling theory similar to those discussed in case studies [26]. This mini-thruster has only 6% efficiency and manufacturing problems. Although there is an effort to improve the scaling theory MIT used [27], it still relies on empirical data and simple physical relationships. Thus, there is a demand for a more reliable physics-based approach in the early stage of design.

1.7 Low-Thrust Trajectory Optimization

The advent of the EP technology brought a new dimension to space mission design, especially in trajectory optimization. In spite of its clear advantages, it has presented large challenge to space mission trajectory designers. This is because the traditional trajectory design based on chemical rockets and impulsive thrusting no longer applies to this low-thrust environment. In turn, a new mathematical approach of dealing with the low-thrust trajectory optimization is required, which results in a new field of space flight dynamics.

The first realized mission designed by this new method of low-thrust trajectory optimization was NASA's Deep Space 1 mission under the NASA New Millennium Program (NMP) [28]. The goal of this mission was to validate high-risk, advanced technologies for future missions. The major technology to be validated was Solar Electric Propulsion (SEP), which was the Ion Propulsion System (IPS) in this specific mission. The results from this mission were very successful and yielded extensive data which will be useful for future applications of involved technologies [29]. From a low-thrust trajectory design perspective, the tools for analyzing low-thrust trajectories were premature. In addition, there were several challenges in trajectory design with the SEP compared to conventional trajectory designs using chemical propulsion system; 1) a large number of unknowns should be determined and a considerable amount of tradeoff studies should be conducted, 2) spacecraft power consumption is highly coupled with the SEP thrusting cycle, and 3) spacecraft attitude requirement is also competing with the SEP thrusting.

Therefore, it is expected that the low-thrust trajectory optimization requires consistent updates with the spacecraft design evolution. Further sophisticated tools to optimize the low-thrust trajectory are imperative to handle the large sets of unknown parameters and properly deal with the unique characteristics of the SEP.

The next mission which successfully applied the SEP was European SMART-1's flight to the Moon [30]. In this mission, the HET type of the EP was used rather than the IPS. Note that the selection of the appropriate electric thrusters largely depends on the mission requirements and constraints. More sophisticated methods for the low-thrust trajectory optimization were implemented such as averaging methods, a Finite Element in

Time (FET) treatment, and combination of gravity assists and weak stability boundaries [31]. Since then, a variety of methods for low-thrust trajectory optimization have been proposed. These methods are well summarized in Ref. [32].

However, all these methods are forced to make assumptions of ideal electric engines due to difficulties of the problem. The simplest approach is taken to assume that the EP thrusters have constant efficiency and constant or linear variation of specific impulse with power. Furthermore, thruster operations at power inputs below the maximum available power are assumed to be possible, which is not generally true for real thrusters. Trajectory designers employ the following relations for thrust and mass flow rate as a function of power given in Equation (1.6) [33].

$$T = 2\eta P / (g_e I_{sp}), \quad \dot{m} = 2\eta P / (g_e I_{sp})^2 \tag{1.6}$$

where, T is the thrust, η is the thruster efficiency, P is the required power, $\dot{m}$ is the propellant mass flow rate, and I_{sp} is the specific impulse. Although there were several researchers accounting for the variable specific impulse or efficiency, their purposes were to investigate the effects of its variation on the low-thrust trajectory optimization [34] - [35]. There was also a demonstration of applying actual thruster performance to the trajectory optimization, but it employed simple polynomial representations for performance and mass flow rate variation with power, and did not incorporate a full operational envelope of the given thruster [36].

Thus, there is also a need to incorporate a more reliable physics-based tool for performance of electric thrusters in preliminary stage of low-thrust trajectory optimization.

1.8 Motivation

As seen in previous sections, current HET design activities and low-thrust trajectory optimizations create a great demand for proper analysis tools for the HET. It is required to obtain more reliable and realistic results in the early conceptual design phase to narrow down a large and uncertain design space. Current HET design does not significantly consider design objectives that are linked to specific missions. Rather its goal is to design HETs for the specified power levels. However, it is clearly meaningful to link the HET design to their associated space missions.

Because any new space mission design begins with finding a feasible trajectory design, it is reasonable that the HET design should be performed along with the low-thrust trajectory design, which involves some mission objectives. Therefore, if these two disciplines were linked and could be simultaneously designed, more optimal results for each mission could be expected for both disciplines, (particularly in the context of high demand missions scenarios, such as transfers to GEO). In addition, the constructed simultaneous design environment could be used for any space mission, which would be a great advantage for future space mission designs involving the HETs.

There have been no systematic studies on the HET Design Space Exploration (DSE) as done in the Aerospace Systems Design Laboratory (ASDL) for other fields [37]-[39]. It is required to overcome the limitations imposed on the current empirical and experimental design procedures using scaling laws. In Figure 1.16, the leftmost S curve is assumed to represent the current technology of HET design based on the HETs which are now being used for actual space missions. When a new design is initiated, the right bottommost technology S curve would be followed if current experimental design process were to be used. It is hoped that the design process would follow the right uppermost

technology *S* curve by implementing the new approach in this thesis to obtain more benefits in design process.
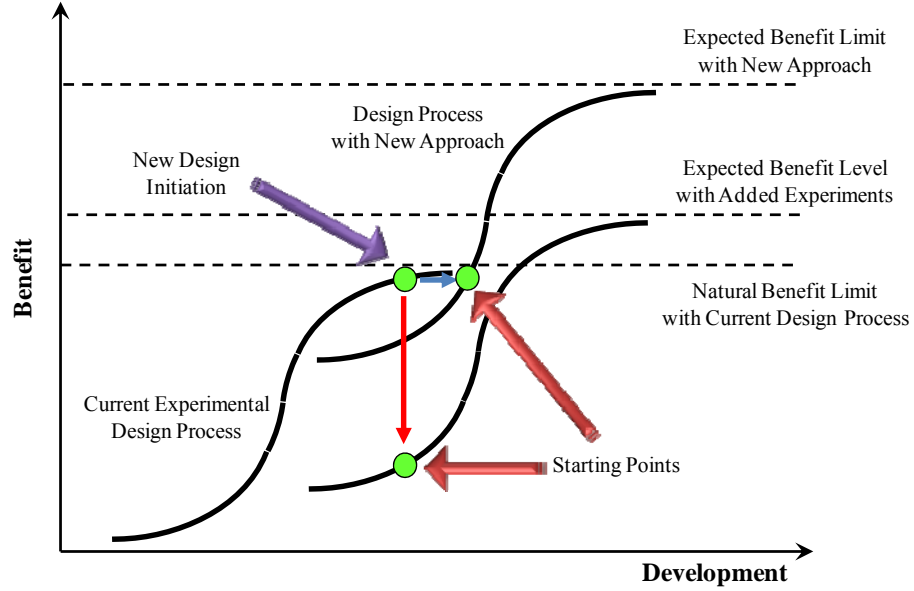
Figure 1.16: Notional Technology *S* Curves on Improvement of HET Design Process

Furthermore, it is also required that performance of real HETs be incorporated in preliminary trajectory optimization in order to clearly understand impacts on global low-thrust trajectory optimization solutions and obtain simultaneous design results.

This research is ultimately motivated by the need for construction of the simultaneous design optimization environment for both HET design and associated optimal low-thrust trajectory design.

1.9 Research Objectives

O1: Identify a proper physics-based analysis tool or methodology for general HET performances among existing methods, which fits at the conceptual design level for HET. Although it could be in either analytical or numerical form, due to very

complicated and nonlinear physical phenomena in HET, there seems to be no analytical method. If an adequate tool or methodology were not identified, develop an appropriate tool or methodology which meets the current research purposes.

O2: Perform conceptual design space exploration for performance metrics with the identified or developed analysis tool. This task is expected to provide more thorough information for a new design of HETs in terms of thruster performance. In addition, a more broad understanding of HET is expected to be gained.

O3: Build the HET performance analysis module based on the identified or developed HET analysis tool and clearly identify the feasible HET design space for the simultaneous design optimization with the low-thrust trajectory optimization.

O4: Construct the simultaneous design optimization environment to design a new HET and associated optimal low-thrust trajectory, which can achieve a specific space mission objective.

O5: Perform the simultaneous design optimization for a selected space mission with a specified goal and investigate the optimum solutions. In addition, demonstrate the capabilities of the simultaneous design optimization environment.

1.10 Research Questions

Based on the motivation, the following research questions arise:

Main Questions

Q1: How can the conceptual design process of HET be improved?

Q2: How can the real thruster performances be infused in preliminary low-thrust trajectory optimization for a specific space mission?

Q3: How can the simultaneous design optimization environment be constructed?

Secondary Questions-1

Q4: Can an appropriate physics-based tool or methodology in conceptual level be found among existing tools or methodologies?

Q5: If not, what is required to develop an appropriate physics-based tool or methodology?

Q6: In case of developing an appropriate tool, can it be validated for a variety of existing HETs?

Q7: Can the appropriate tool be efficiently used for the simultaneous design optimization?

Q8: Can the feasible design space of the HET to be designed be properly specified for the simultaneous design optimization?

The questions 4 and 8 may be interpreted as those incurred from how the main questions can be answered.

Secondary Questions-2

Q9: What unidentified correlations exist between thruster parameters in terms of thruster performance metrics?

Q10: Can the existing scaling laws be improved by a physics-based tool or can new scaling laws be proposed?

Q11: What can be discovered when non-ideal thruster performances are infused in low-thrust trajectory optimization and what are the differences compared to that of an ideal one?

The questions 9 through 11 may be interpreted as those incurred from what contributions can be expected when the main questions are answered.

1.11 Collaboration and Thesis Organization

Based on the research objectives in section 1.9, the current research must cover three major disciplines such as HET physical analysis, conceptual design methodology and preliminary low-thrust trajectory optimization. Therefore, it is expected that a great deal of work would be involved to accomplish the research goals. As a result, it would be a better approach if the research objectives could be accomplished in collaboration with people across research laboratories in the Department of Aerospace Engineering at Georgia Institute of Technology as shown in Figure 1.17.

The issues on HET design and low-thrust trajectory optimization have been reviewed as well as motivation and corresponding research objectives in this chapter. Chapter II provides basic materials on mathematical modeling of HET and low-thrust trajectory optimization to understand the contents of later parts of the thesis. Chapter III deals with previous research efforts on numerical analysis of HETs. It also provides a process to identify an appropriate tool among existing tools or methodologies for the

current research purpose. Chapter IV details how to develop a new HET analysis tool, which is a foundation of the thesis. Chapter V gives intensive validation results with the developed tool. Chapter VI explores the design space of HET using the developed tool. Chapter VII explains how to build surrogate models for the HET module in a simultaneous design optimization environment. Chapter VIII culminates the thesis work by demonstrating the capability of the simultaneous design optimization environment for a specific space mission. Finally, Chapter IX addresses conclusions of the present research, contributions, and future work.
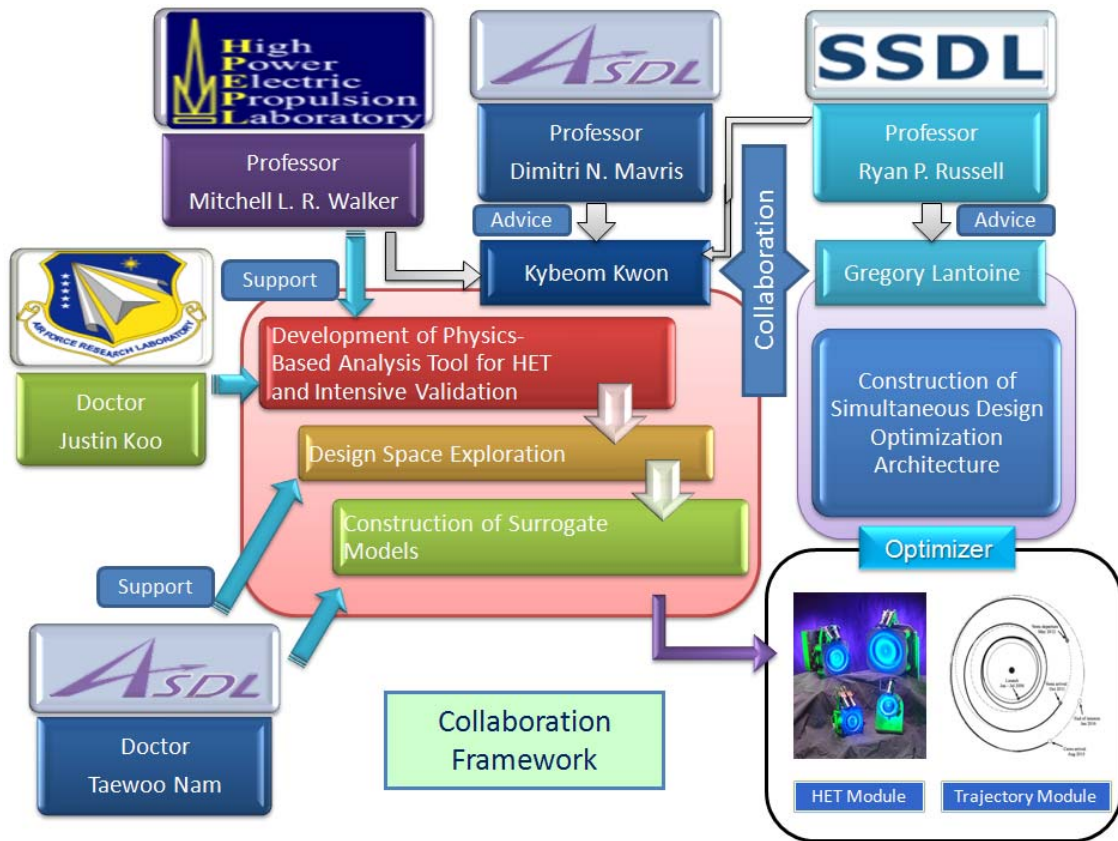
Figure 1.17: Collaboration Framework

CHAPTER 2

THEORETICAL FOUNDATION

2.1 Understanding Basic Mathematical Modeling for HET

In this section, basic solution approaches for plasma modeling are introduced. From the observation of general physical phenomena given in the schematic of HET and the sectional view of Figure 1.3 and Figure 1.4, backgrounds on basic plasma physics, electromagnetism, gas dynamics and other engineering fields are necessary to attempt the analysis of HET. Especially, the basic theories on plasma physics, electromagnetism and gas dynamics are well explained in textbooks [40] - [44].

Since the HET operates in a low density regime for plasma, it is required to consider the Knudsen number (Kn) to find proper mathematical modeling. Appropriate modeling strategies based on Kn are shown in Figure 2.1 [45].
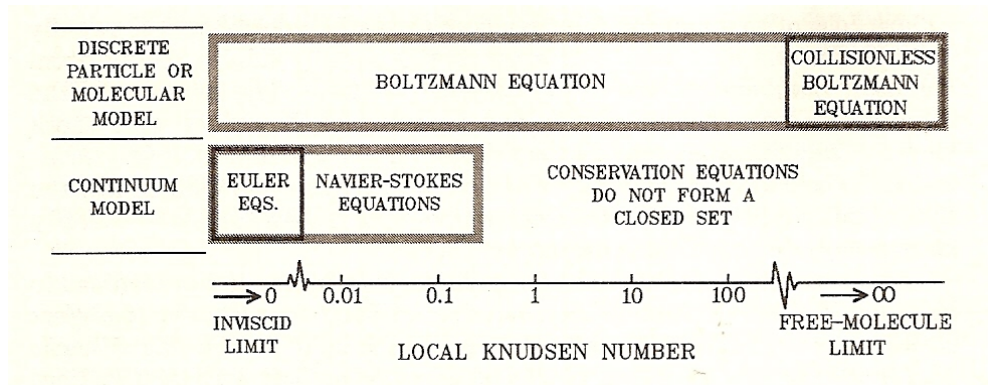
Figure 2.1: Mathematical Modeling based on Kn [45]

As seen in Figure 2.1, the Navier-Stokes equations cannot be applied for the range over $Kn \approx 0.2$, where the Boltzmann equation must be applied. However, the difficulties

arise from the fact that the *Kn's* can be different for each species such as ions and electrons based on associated physical phenomena.

Trapping electrons by a magnetic field can be easily explained by the basic plasma particle motions. Let's consider a simple model for a charged particle motion under constant magnetic fields perpendicular to its plane of motion. The derivation below is taken from Ref. [46]. The equation of motion for a charged particle in a magnetic field is given by

$$m\frac{d\vec{v}}{dt} = \vec{F} = e\vec{v} \times \vec{B} \tag{2.1}$$

The expanded forms of Equation (2.1) with z direction magnetic field ($\vec{B} = B\hat{z}$) are given as

$$m\dot{v}_z = 0, \quad m\dot{v}_x = eBv_y, \quad m\dot{v}_y = -eBv_x \tag{2.2}$$

Equation (2.2) has the solution as

$$\vec{v} = v_{z_0}\vec{n}_z + v_\perp \cos(\omega_c t + \alpha)\vec{n}_x - v_\perp \sin(\omega_c t + \alpha)\vec{n}_y \tag{2.3}$$

The important parameters from the above derivation are cyclotron frequency and cyclotron radius, which are given by

$$\omega_c = \frac{eB}{m}, \quad r_c = \frac{v_\perp}{|\omega_c|} = \frac{mv_\perp}{eB} \approx \frac{mv_{th}}{eB} \text{ where, } v_{th} = \sqrt{\frac{2kT_{cp}}{m}} \tag{2.4}$$

where, ω_c is the cyclotron frequency, r_c is the cyclotron radius, B is the magnetic field strength, m is the charged particle mass, e is the electrical charge, v_{th} is the charged particle thermal velocity, and T_{cp} is the charged particle temperature. The resultant motions for the ion and electron are shown in Figure 2.2.
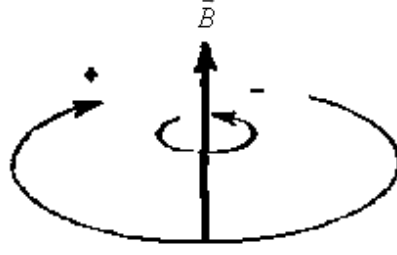
Figure 2.2: Cyclotron Motion of Charged Particles [46]

If there is also an uniform electric field perpendicular to $\vec{B}$, the charged particles will drift in the direction of $\vec{E} \times \vec{B}$ with the resulting cyclotron motions as shown Figure 2.3.
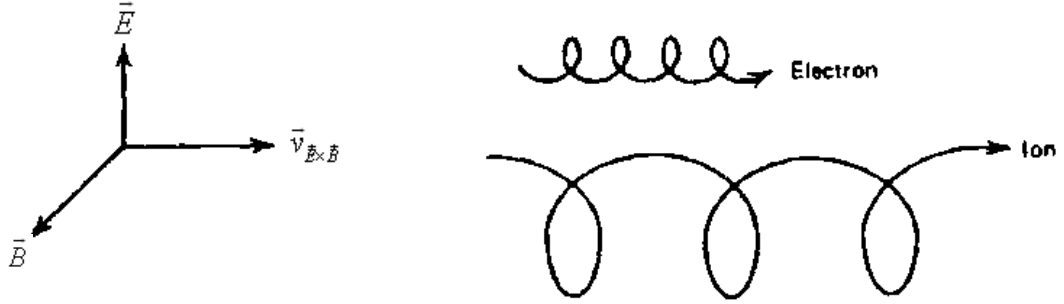
Figure 2.3: $\vec{E} \times \vec{B}$ Drift of Charged Particles [46]

Since the electron mass is very low compared to that of a Xe ion by the order of 10^{-6}, the cyclotron frequency of electrons is much higher than that of ions. Furthermore, the cyclotron radius of electrons is much smaller than that of ions, although the temperature of electrons is usually higher than ions in HET by a factor of 10 to 100. These obvious physical facts actually constitute the basic operation principle of HET which must meet the following criterion.

$$r_e << L << r_i \tag{2.5}$$

where, L is the characteristic device length of the HET, which is usually the length of discharge channel, and r_e and r_i are the electron and ion cyclotron radii respectively.

36

Equation (2.5) demonstrates that in a conventional HET the electrons are magnetized but the ions are not. Therefore, the electrons are trapped by the magnetic field for larger residence times (and more effective ionization) while the ions are not affected by the magnetic field so that they can be accelerated by the applied electric field.

It is expected that the elections are under high collisional states, but ions are not. Subsequently, the Kn of electrons is lower than that of ions. Neutrals are also expected to have higher Kn. Therefore, it seems that the Boltzmann equation should be applied for the neutrals and ions, and the Navier-Stokes equations can be applied for the electrons, which considers the bulk of electrons as a continuum fluid.

Considerable technical papers have been published on the numerical methods to analyze EP devices. The overview on this is well explained in Ref. [47]. The numerical methods fall in three major categories: kinetic, continuum/fluid, and hybrid method which combines the first two modeling approaches.

The kinetic modeling has been used for the high Kn regime in which the physical phenomena are not well represented by the fluid description. This modeling is basically based on the spirit of solving the Boltzmann equation.

The Boltzmann equation is given by

$$\frac{\partial f}{\partial t} + \vec{v} \cdot \frac{\partial f}{\partial \vec{x}} + \frac{\vec{F}}{m} \cdot \frac{\partial f}{\partial \vec{v}} = \left(\frac{\partial f}{\partial t} \right)_{coll} \tag{2.6}$$

where, f is the particle distribution function in phase space, $\vec{x}$ is the space coordinate, $\vec{v}$ is the velocity coordinate, $\vec{F}$ is the force vector in space coordinate, and $\left(\partial f / \partial t \right)_{coll}$ is the time rate of change of the distribution function by collisions. As seen in Equation (2.6), although the differential order of the Boltzmann equation is only 1 in all

independent variables, t, $\vec{x}$ and $\vec{v}$, solving it can be computationally prohibitive for many body systems and very detailed phase space descriptions. Furthermore, a correct mathematical representation of $(\partial f / \partial t)_{coll}$ is not available for most physical situations. For a thermodynamic equilibrium system, $(\partial f / \partial t)_{coll}$ can be considered to be zero. An electron fluid in an HET is rarely in complete thermodynamic equilibrium.

In order to circumvent this difficulty, scientists and engineers especially in the nuclear society have developed methods to solve the Boltzmann equation using particles, i.e., kinetic modeling [48] - [49]. Particle simulations directly deal with particles and solve each individual particle motion under the given forces. The approach is as follows. Since the Boltzmann equation with $(\partial f / \partial t)_{coll} = 0$ merely represents the conservation of the particle distribution function in the phase space, the particle motion can be easily solved simply using Newton's 2nd law with the exerted forces. Then the integrations will provide new velocity and new position for each particle. After moving the particles during a given time step, the collisional effects can be modeled by the collision probabilities as

$$P_{coll} = 1 - e^{-\Delta t \ \nu_{coll}} \tag{2.7}$$

where, P_{coll} is the collision probability, Δt is the time step, and ν_{coll} is the total collision frequency. By comparing this probability with a random number, the occurrence of collision is determined and if a collision occurs, another random number is used to determine what type of collision it would be. Then the collisional interaction is applied according to the determined collision type. This way of dealing with the collisions is an indirect modeling of $(\partial f / \partial t)_{coll}$. The use of random numbers manifests the Monte Carlo

method [50] - [51]. There are various classes of this modeling approach, for example, Monte Carlo Collision (MCC) and Direct Simulation Monte Carlo (DSMC) [52].

Since this approach directly simulates the particle motions, the computational cost are very high at every time step. All the particles must be swept to calculate the interacting forces and collision probabilities. In order to expedite the calculation, nuclear scientists have developed the concept of Particle-Mesh (PM) model, usually called Particle-In-Cell (PIC) methodology [49]. In this methodology, the meshes are used to get macroscopic quantities such as number density, charge density, temperature and so on. In particular, the charge density is input into the Gauss' law, which is one of the Maxwell's equations, to allow for solving the Poisson's equation. Thus, forces are obtained from the resultant field distribution, not the direct calculations by the Coulomb law. In this way, the computational cost to calculate forces can be significantly reduced. In spite of this effort at reducing the computational cost, the kinetic modeling is still impractical for the most HET calculations. There are several factors to make adaption of the kinetic method impractical such as follows.

1) Although the plasma number density is low ($10^{16} - 10^{19} / m^3$) relative to the general flow problem, it is still too high to directly apply the kinetic method. It's obviously impractical to track billions and billions of particles at every time step using current computer capabilities.

2) What makes matters worse is the time step restriction. In order to resolve accurate motion of the charged particles, especially electrons, due to their high

39

mobility, the allowable time step is limited by the plasma frequency, which is one of the basic parameters for plasma and is given by

$$\omega_p = \sqrt{\frac{n_o e^2}{m \varepsilon_0}}$$

(2.8)

where, ω_p is the plasma frequency, n_0 is the plasma number density, e is the electrical charge, m is the mass of charged particle, and ε_0 is the freespace permittivity. Usually the plasma frequency of electrons ($\omega_p \approx 10^{11} \ rad/\sec$) is higher than that of ions due to smaller mass, which yields the time step on the order of $10^{-11} \ \sec$.

3) Another important plasma parameter also makes the implementation difficult, the Debye length, which is given by

$$\lambda = \sqrt{\frac{\varepsilon_0 k T_p}{n_o e^2}}$$

(2.9)

where, λ is the Debye length, k is the Boltzmann constant, and T_p is the plasma temperature. The Debye length is the length over which the charged particles are screened out from the electric fields inside the Debye sphere. This quantity comes from the balance between the energy from electric field and the thermal energy of charged particles. Since the order of the Debye length is μm, several hundred thousand mesh cells may be required for practical devices.

There are several ways of overcoming these impracticalities [52]. The concept of the superparticle has been used to overcome the first difficulty. A superparticle represents many actual particles often up to 1×10^{8} particles per a superparticle and is assumed to have same properties within a superparticle. The size of a superparticle can be determined by several factors to reproduce the correct physics such as distribution functions or some other related reactions. For the HET, the ionization rate is an important factor which must be reproduced correctly.

For getting around the second and third difficulties, the mass ratio between heavy particles such as neutrals and ions, and electrons can be adjusted to be lower than the actual value. In addition, the freespace permittivity can be artificially adjusted to a higher value, which results in lower plasma frequency and higher Debye length.

As a simulation tool, the kinetic approach can resolve the actual physics of HET, but it still involves computational inefficiency and in turn becomes unmanageable without artificial assumptions. In addition, the computational cost can still be very high in spite of these numerical treatments.

The second approach utilizes the fluid description of plasma. In the view of fluid, the relevant properties are the macroscopic ones, not the details from the microscopic view as in kinetic modeling. In the light of complex physics involved in HET, one might be doubtful that the fluid description could accurately represent the correct physics. However, if one is concerned only about macroscopic properties and general features of HET, the fluid approach may be the key.

In the Computational Fluid Dynamics (CFD) and numerical combustion societies, the Navier-Stokes equations are frequently used to obtain solutions. Especially, in

numerical combustion, the source term exists in each species conservation equation to account for chemical reactions. What is usually assumed is mechanical and thermal equilibrium, but chemical non-equilibrium for multi-species fluid is allowed, which is called Local Thermodynamic Equilibrium (LTE). However, from the experimental results for the HET, the plasma might not be in thermodynamic non-equilibrium. In this case, the typical Navier-Stokes equations or those with each species conservation equation incorporating source term cannot be directly applied to the HET. Rather, the classic way of deriving the governing equations must be used to obtain correct mathematical interpretations for fluid description. This can be done by taking moments of the Boltzmann equation in the velocity space. The results of this process produce the conservation of mass, momentum and energy, respectively based on the order of moment.

The generalized moment equation is given as follows [53].

$$\frac{\partial}{\partial t}(n_s \langle \varphi \rangle_s) - n_s \left\langle \frac{\partial \varphi}{\partial t} \right\rangle_s + \nabla \cdot (n_s \langle \varphi \, \vec{v}_s \rangle) - \langle \vec{v}_s \cdot \nabla \varphi \rangle - n_s \left\langle \frac{\vec{F}_s}{m_s} \cdot \nabla_v \varphi \right\rangle = \int \varphi \left(\frac{\partial f_s}{\partial t} \right)_{coll} d^3\vec{v} \quad (2.10)$$

Depending on the expression of ϕ, the following three conservation equations for fluid description can be obtained.

Mass Conservation: $\phi = 1$

$$\frac{\partial}{\partial t}(n_s) + \nabla \circ (n_s \vec{u}_s) = \int_{\vec{v}} \left(\frac{\partial f_s}{\partial t} \right)_{coll} d^3\vec{v} \quad (2.11)$$

where, n_s is the number density of species s, $\vec{u}_s$ is the mean velocity, and $\int_{\vec{v}} (\partial f_s / \partial t)_{coll} d^3\vec{v}$ is the rate of source generation.

Momentum Conservation: $\phi = m\vec{v}$

42

$$\frac{\partial}{\partial t}(m_s n_s \vec{u}_s) + \nabla \circ (m_s n_s \vec{u}_s \vec{u}_s) + \nabla \circ \widetilde{P}_s - n_s q_s (\vec{E} + \vec{u}_s \times \vec{B}) = \int_{\vec{v}} m_s \vec{v}_s \left(\frac{\partial f_s}{\partial t}\right)_{coll} d^3\vec{v} \qquad (2.12)$$

where, $\widetilde{P}_s$ is the stress tensor, $\vec{E}$ is the electric field vector, $\vec{B}$ is magnetic field vector, $\vec{v}_s$ is the velocity vector and $\int_{\vec{v}} m_s \vec{v}_s (\partial f_s / \partial t)_{coll} d^3\vec{v}$ is the momentum transfer rate.

Energy Conservation: $\phi = \dfrac{1}{2} m \vec{v}^2$

$$\frac{\partial}{\partial t}\left[m_s n_s \left(\frac{3}{2}\frac{k}{m_s} T_s + \frac{\vec{u}_s^2}{2}\right)\right] + \nabla \circ \left[m_s n_s \vec{u}_s \left(\frac{3}{2}\frac{k}{m_s} T_s + \frac{\vec{u}_s^2}{2}\right) + \vec{q}_s \right] + \nabla \circ (\widetilde{P}_s \vec{u}_s)$$
$$= n_s q_s \vec{E} \circ \vec{u}_s + \int_{\vec{v}} \frac{1}{2} m_s \vec{v}_s^2 \left(\frac{\partial f_s}{\partial t}\right)_{coll} d^3\vec{v} \qquad (2.13)$$

where, T_s is the temperature, $\vec{q}_s$ is the heat transfer rate vector and $\int_{\vec{v}} \frac{1}{2} m_s \vec{v}_s^2 \left(\frac{\partial f_s}{\partial t}\right)_{coll} d^3\vec{v}$ is the energy transfer rate.

Of course, if the terms containing $(\partial f / \partial t)_{coll}$ were to vanish, the resultant equations would be nothing but the Navier-Stokes equations except for the inclusions of the Lorentz force term in the momentum conservation equation and the Joule heating term in the energy conservation equation for the charged species.

If the term $(\partial f / \partial t)_{coll}$ is not zero, proper mathematical expressions must be given to solve the equations. Approximations for the terms including $(\partial f / \partial t)_{coll}$ for each conservation equation are given as follows.

Mass Conservation: $\int_{\vec{v}} \left(\frac{\partial f_s}{\partial t}\right)_{coll} d^3\vec{v} = n_s n_r \langle \sigma_{sr} v_{sr} \rangle$

Momentum Conservation: $\int_{\vec{v}} m_s \vec{v}_s \left(\frac{\partial f_s}{\partial t}\right)_{coll} d^3\vec{v} = -n_s \sum_r \mu_{sr} v_{sr} (\vec{u}_s - \vec{u}_r)$

Energy Conservation: $\int_{\vec{v}} \frac{1}{2} m_s \vec{v}_s^{\,2} \left(\frac{\partial f_s}{\partial t} \right)_{coll} d^3\vec{v} = n_s \sum_r \nu_{sr} \Delta\varepsilon_{sr}$

where, s represents the concerned species, r represents the species reacting with s species, sr represents the parameters related to reactions between s and r species, σ is the cross section for current reaction, v is the relative velocity between s and r species, μ is the reduced mass, ν is the collision frequency of current reaction, and $\Delta\varepsilon$ is the amount of energy loss required for each reaction. The bracket $\langle \ \rangle$ means the average value.

In order to close the equations, the adequate relations for stress tensor and heat transfer should also be expressed by other known variables. The collision cross section for a specific reaction may be obtained from experimental data.

The fluid approach cannot resolve the sheath on a macroscopic scale. The sheath is the region where quasi-neutrality doesn't hold. Sheath formation has a very similar origin in its role to the Debye length previously explained. The sheath plays a role in producing a smooth transition from the bulk of plasma to the wall. At the edge of the body of plasma, electrons usually have more mobility than ions by the factor of their mass ratio. Furthermore, since the electrons have greater temperature than ions, they move into wall material faster and excess ions are left behind, which results in the positive charge space. As the electrons which hit the wall reduce the wall potential, increasing numbers of ions are attracted to the wall. Equilibrium is then attained when the electron and ion flux going into the wall are exactly the same.

$$\chi = -\frac{eU}{kT_e}$$

Plasma
z<0

Wall
z=0

$-\lambda_D$
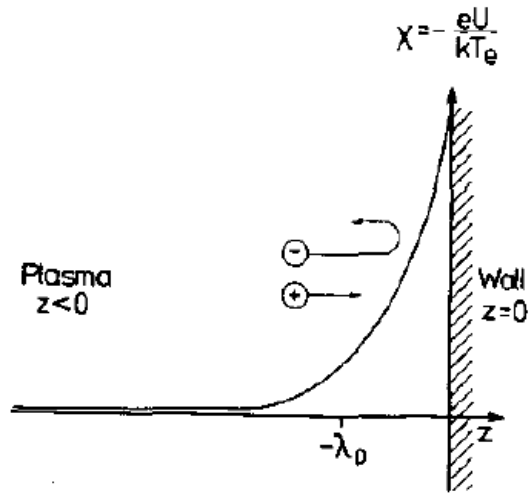
Figure 2.4: Schematic of the Sheath [54]

As seen in Figure 2.4, the plasma can be shielded from wall potential by the sheath formation. The thickness of the sheath is usually on the order of a few Debye lengths (λ), which implies that in order to determine the correct physics of the sheath, the relevant scale should be that of Debye length.
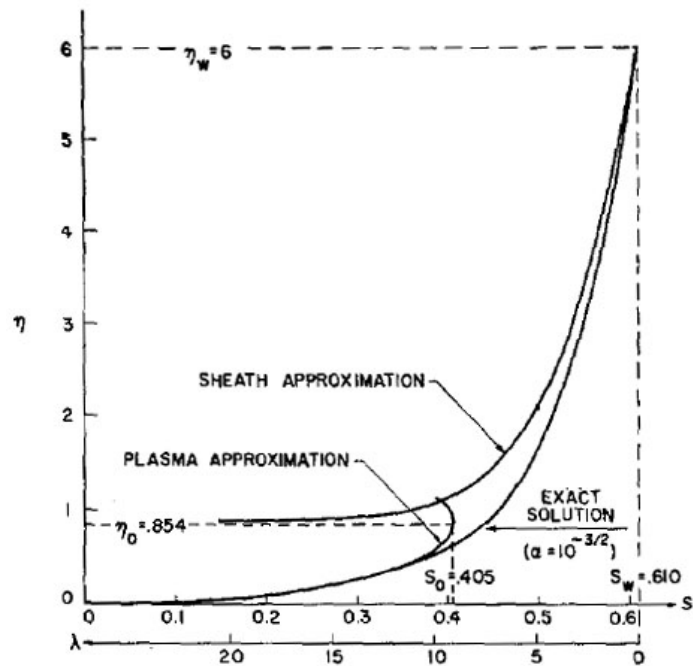
Figure 2.5: Plasma and Sheath Approximation [55]

To incorporate sheath solution into the whole plasma solution using a fluid approach, one must have two scales: microscopic scale on the order of Debye length and macroscopic scale on the order of device length. In reality patching these two scales is difficult mathematically, since the electric field at the sheath edge would be infinity in macroscopic scale when the Bohm criterion is applied. However, there was an effort to overcome this difficulty and an exact solution was provided for this plasma-sheath transition problem as shown in Figure 2.5, which is based on a complex integral equation [55]. In general, for a typical fluid approach, the sheath is not included in the solution domain or the sheath phenomena are neglected.

2.2 Understanding Basic Low-Thrust Trajectory Optimization

Trajectory optimization is an essential part of space mission design. Every mission considers possible transfer trajectories at the early stages. As the mission design progresses, the feasibility of trajectory is identified and optimization is performed to find the best trajectory and associated optimal spacecraft maneuvers.

The characteristics of the trajectory can be different depending on the type of propulsion system. The trajectory resulting from chemical propulsion is ballistic for most of the flight, where the spacecraft coasts. This is because the chemical propulsion system provides a large thrust in a relatively short time and changes spacecraft trajectory at the time of impulse. Therefore, the trajectory optimization is relatively simpler to perform. However, the low-thrust trajectory optimization is a quite challenging problem because it is inherently ill-condition, unstable and computationally expensive [56]. These difficulties originate from highly nonlinear dynamics, a large set of unknowns and parameters, and possible existence of many local optima.

Because of the considerable advantages of EP, numerous approaches have been proposed to overcome the aforementioned difficulties. In spite of these efforts, fundamental difficulties remain. Therefore, the low-thrust trajectory optimization is still an energetic and evolving field.

In the collaboration framework in this thesis, the low-thrust trajectory optimization is accomplished by the collaborator. Thus, in this section, basics of the low-thrust trajectory optimization are reviewed and a brief introduction of a new method proposed by the collaborator is given.

The methods used for the low-thrust trajectory optimization typically fall under two categories: indirect and direct methods. The indirect method is original because it is the same as the one first attempted in typical optimal control theory and it relies on "Calculus of Variations". By applying the Pontryagin Maximum Principle [57], the optimization problem is converted into a Two Point Boundary Value Problem (TPBVP). In this case, the problem has low-dimension since an infinite dimension control problem is reduced to a problem calculating "control law", which is only a function of initial co-states. Co-states are introduced from Hamiltonian formulation when deriving the necessary optimality conditions. Although this method is fast, it is very sensitive to initial guesses of the co-states and difficult to incorporate other constraints such as flybys. In addition, required boundary conditions must be re-derived for each problem type.

Table 2.1 shows the associated formulation of a continuous nonlinear optimal controller, which can be used for this problem as well. In Table 2.1, $\vec{x}$ is the state vector, $\vec{\lambda}$ is the co-state vector, φ is the cost function at the end state, and L is the cost function

associated with states at each time. Some applications of the indirect method to interplanetary trajectories and round trip trajectories are found in Ref. [59] - [60].

Table 2.1: Continuous Nonlinear Optimal Controller [58]

System model: $\qquad \dot{\vec{x}} = \vec{f}(\vec{x},\vec{u},t), \qquad t \geq t_0, \qquad t_0 \ fixed$

Performance index: $\qquad J(t_0) = \varphi(\vec{x}(T),T) + \int_0^T L(\vec{x},\vec{u},t)\,dt$

Final state constraint: $\qquad \vec{\Psi}(\vec{x}(T),T) = 0$

Optimal Controller:

   Hamiltonian: $\qquad H(\vec{x},\vec{u},t) = L(\vec{x},\vec{u},t) + \vec{\lambda}^T \vec{f}(\vec{x},\vec{u},t)$

   State equation: $\qquad \dot{\vec{x}} = \dfrac{\partial H}{\partial \vec{\lambda}} = \vec{f}, \qquad t \geq t_0$

   Costate equation: $\qquad -\dot{\vec{\lambda}} = \dfrac{\partial H}{\partial \vec{x}} = \dfrac{\partial \vec{f}^T}{\partial \vec{x}}\vec{\lambda} + \dfrac{\partial L}{\partial \vec{x}}, \qquad t \leq T$

   Stationarity condition: $\qquad 0 = \dfrac{\partial H}{\partial \vec{u}} = \dfrac{\partial L}{\partial \vec{u}} + \dfrac{\partial \vec{f}^T}{\partial \vec{u}}\vec{\lambda}$

   Boundary condition: $\qquad (\varphi_x + \vec{\Psi}_x^T \vec{v} - \vec{\lambda})^T |_T \, d\vec{x}(T) + (\varphi_t + \vec{\Psi}_t^T \vec{v} + H)|_T \, dT = 0$

$$\vec{x}(t_0) \ given$$

On the other hand, the direct method attempts to directly optimize controls. The entire problem including states, co-states, and time is discretized and the resulting giant parameter optimization problem is solved by using Nonlinear Programming (NLP), which can be considered as a black box. Consequently, the method has large dimensions and a large number of variables to be determined. However, the direct method is more robust and it does not require deriving the necessary conditions for each problem type. Some applications of this method are found in Ref. [61] - [62].

48

Recently, there have been efforts to obtain the advantages of both methods. These are called hybrid methods which combine the indirect and direct methods. The basic idea of the hybrid method is that it first uses the direct method to directly minimize some cost, hit some constraints, and then uses the indirect principles to remove the control dimensions of the problem. Another idea the collaborator proposed is to use Differential Dynamic Programming (DDP), which is based on Bellman's Principle of Optimality of dynamic programming and successive backward quadratic expansions of the objective function [63]. By combining DDP with an efficient discretization scheme, improved convergence properties, and different treatments of hard and soft constraints, he proposed an efficient Hybrid Differential Dynamic Programming (HDDP) algorithm for low-thrust trajectory optimization with an emphasis on robustness and flexibility. For more detail information, refer to Ref. [63].

CHAPTER 3

LITERATURE REVIEW AND PHYSICS-BASED ANALYSIS TOOL IDENTIFICATION FOR HET

3.1 Criteria for Conceptual Physics-Based Analysis Tool for HET

In order to identify a proper physics-based analysis tool or methodology among existing tools and methodologies for conceptual level design, the following criteria are proposed:

C1: Numerical Efficiency

Numerical efficiency is apparently the most important property the conceptual analysis tool must have because a large design space should be explored at the conceptual level of design.

C2: Numerical Robustness

This criterion is chosen because of the highly complex and nonlinear physics involved, which may cause unexpected numerical instabilities. Exploring the design space using a selected tool should be done without execution crash or non-convergence, which means that the tool should provide solutions for all cases attempted in the design space, or at least give the criteria on numerically oscillatory cases and physically impossible cases. In particular, if a tool is highly dependent on the initial guesses, it is not considered as a robust tool.

C3: Self-Consistency

The intended tool should have self-consistency. This criterion is required to cover an arbitrarily defined design space. In order to meet this criterion, the tool should be as self-consistent as possible in solution algorithm. In other words, the number of unknowns which cannot be solved by the tool should be minimized. If this is not the case, the unknowns must be assigned to some arbitrary values to obtain solution, which results in the loss of self-consistency.

C4: Physics Representativeness

This criterion is chosen to ensure that the tool should include as much major physics as possible. The approximate solution provided by the tool should also give reasonable accuracy at a conceptual level.

*Among the 4 criteria, the requirements for the first three should be **high**. **Moderate** requirement for the fourth criterion should be enough at the conceptual level of design.*

3.2 Previous Work on HET Numerical Modeling

3.2.1 Full Kinetic Modeling

Several researchers have attempted this modeling approach to simulate HET. Latocha et al. investigated electron transport in the channel region using PIC-MCC method [64]. Due to inherent computational inefficiency of the kinetic model, they proposed an electron diffusion model and compared it with a kinetic model.

Adam et al. applied 2D (z, θ) full kinetic model to HET [65]. Since their research focus was axial electron transport, no detailed wall effect was included in the domain. Nonetheless, the model is self-consistent and critical physical information could be obtained. The average computational time was a month, which is quite expensive. In order to reduce the constraints on time step and grid spacing, they took cyclotron frequency and radius as constraints, although the plasma frequency and the Debye length should be applied to determine time step and grid spacing respectively. This resulted in a 100 times greater time step than that from the plasma frequency constraint.

Taccogna et al. developed 2D $(r, z) - 3V$ axisymmetric PIC-MCC program for HET [66]. They used artificial heavy particle-electron mass ratio and permittivity ratio to reduce computational cost. They utilized geometrical scaling to lessen computational loads further while maintaining important physical characteristics. Especially, the model revealed the existence of the anode sheath and backflow of ions.

The kinetic model can provide detail physics of HET such as electron distribution function, sheath characteristics, even startup transient characteristics [67] and so on. This modeling approach is expected to show its capability to gain deeper knowledge of physics involved in HET. However, it still has a critical drawback in terms of computational cost even in the current high computer capability environment.

3.2.2 Hybrid Modeling

Hybrid modeling often assumes electrons as a fluid in HET. The first successful implementation of this approach is attributed to Fife [68] - [69]. He applied PIC-MCC modeling to ions and neutrals and solved fluid equations to calculate electron temperature. This method can reduce much of computational cost which was a major obstacle in the

kinetic approach. Since the constraints on time step and grid spacing often come from electron analysis in the kinetic method, if electrons can be treated as fluids, these constraints are basically eliminated. Several researchers simulated HET with a similar approach to that of Fife's method [70] - [72].

However, in spite of the elimination of constraints on time step and grid spacing, this method still suffers from computational inefficiency due to inherent multiple time scale problem of HET. In this method, the time step can be taken as those of ions or neutrals. But, the converged solutions of electron properties must be obtained at every ion and neutral sweep, which also needs considerable computational time.

3.2.3 Full Fluid Modeling

Various researchers have attempted this approach to investigate macroscopic behaviors of HET. In this modeling, all the species are modeled as fluids. From the moments of the Boltzmann equation, mass, momentum and energy conservation equations are obtained. Quasi-neutrality is often assumed and the simplest approach using this method is to take steady state forms of the governing equations and construct a system of ordinary differential equations (ODEs) for dependent variables. The solution domain is usually taken from anode sheath edge to channel exit or cathode or even a farther distance. As explained in section 2.2, to also solve for the anode sheath solution, additional effort and computational cost must be incurred. Currently none of previous methodologies using fluid approach have attempted to include the anode sheath solution.

The most prominent work on solving a system of ODEs is those of Ahedo et al. [73] - [78]. They included the boundary condition at the anode sheath and ion backflow

phenomenon. However, in this formulation, there is a critical problem relating to numerical implementation.

Equation (3.1) shows one of formulations in the form of system of ODEs.

$$
\begin{pmatrix}
\dfrac{du_i}{dz} \\[2mm]
\dfrac{du_e}{dz} \\[2mm]
\dfrac{du_n}{dz} \\[2mm]
\dfrac{dq_e}{dz} \\[2mm]
\dfrac{dT_{eV}}{dz} \\[2mm]
\dfrac{d\varphi_{eV}}{dz} \\[2mm]
\dfrac{dn_e}{dz} \\[2mm]
\dfrac{dn_n}{dz}
\end{pmatrix}
=
\begin{pmatrix}
\dfrac{(rhs1 + rhs4 - n_e rhs6)u_i - rhs3\,T_{eV}}{-n_e(T_{eV} - m_i u_i^2)} \\[3mm]
\dfrac{rhs7}{n_e} + \dfrac{u_e(rhs1 + rhs4 - n_e rhs6 - m_i u_i rhs3)}{-n_e(T_{eV} - m_i u_i^2)} \\[3mm]
rhs5 \\[3mm]
rhs2 - rhs7\,T_{eV} - \dfrac{3}{2}n_e u_e rhs6 + \dfrac{-T_{eV} u_e(rhs1 + rhs4 - n_e rhs6 - m_i u_i rhs3)}{-(T_{eV} - m_i u_i^2)} \\[3mm]
rhs6 \\[3mm]
\dfrac{-rhs4\,T_{eV} - m_i u_i[-rhs3\,T_{eV} + (rhs1 - n_e rhs6)u_i]}{-n_e(T_{eV} - m_i u_i^2)} \\[2mm]
\dfrac{-(rhs1 + rhs4 - n_e rhs6 - m_i u_i rhs3)}{-(T_{eV} - m_i u_i^2)} \\[3mm]
rhs8
\end{pmatrix}
\tag{3.1}
$$

where,

$$
RHS =
\begin{pmatrix}
rhs1 \\
rhs2 \\
rhs3 \\
rhs4 \\
rhs5 \\
rhs6 \\
rhs7 \\
rhs8
\end{pmatrix}
=
\begin{pmatrix}
1: -m_e n_e(\nu_d + \nu_e)u_e + m_e n_e(\nu_{mt}u_n + \nu_{ei}u_i) \\[3mm]
2: m_e n_e(\nu_d + \nu_e)u_e^2 - \varepsilon_i n_e \nu_i - \varepsilon_{ex}n_e \nu_{ex} - \dfrac{3}{2}T_{eV}n_e(\nu_i - \nu_{recom}) \\[3mm]
3: n_e(\nu_i - \nu_{recom}) \\[3mm]
4: m_i n_e(\nu_i - \nu_{recom})(u_n - u_i) \\[3mm]
5: 0 \\[3mm]
6: -\dfrac{2}{5}(\nu_d + \nu_e)\dfrac{m_e}{n_e T_{eV}}q_e \\[3mm]
7: n_e(\nu_i - \nu_{recom}) \\[3mm]
8: -\dfrac{n_e(\nu_i - \nu_{recom})}{u_n}
\end{pmatrix}
$$

As seen in Equation (3.1), one may notice that there might be singular points in the solution domain. Ion Mach number based on ion acoustic velocity is defined as

54

$$M_i = \frac{u_i}{u_{i_a}} = \frac{u_i}{\sqrt{T_{eV}/m_i}}$$

Thus, if the ion velocity is the same as the ion acoustic velocity, i.e., ion Mach number is equal to 1, then singularity occurs in the system of ODEs. This singularity is somewhat similar to that obtained when one derives a system of ODEs from Euler equations for the steady state case. For the current case, the singularity comes from the quasi-neutrality assumption. As in the case of Euler equations, this is not a critical singularity, in other words, a regular or removable singularity. For the removable singularity in the context of ODE, if the denominator approaches a zero value when the trajectory of ODE approaches this singularity, then the numerator also approaches a zero value. Therefore, the derivative there is expected to have some finite value.

However, in the context of numerical analysis, even though it has a removable singularity, one may not integrate the system of ODEs toward a singular point. Rather, one may want to integrate from that singular point, which needs to have a good initial guess for the position. What makes matters worse in a numerical perspective is that if the anode sheath condition, i.e., Bohm condition were to be included in the boundary conditions, an irregular singular point will occur at the anode sheath edge since the Bohm condition itself is the ion velocity, which is a negative value of the ion acoustic velocity. i.e, $M_i = -1$. This fact has a great influence on numerical robustness and very good initial guesses for dependent variables close to solution will be definitely required. Actually, in the perspective of design space exploration where large cases must be covered, it is not easy to find good initial guesses for every case.

Because of this difficulty, some researchers have neglected the anode sheath and assigned arbitrary boundary values at the anode sheath edge, which significantly degraded the self-consistency of the methods [79] - [80]. Other researchers applied even simpler models, for example, constant electron temperature assumption or given electron temperature assumption from experiments [81] - [83].

What should be noted is that although most methods using a fluid approach are based on the SPT-100 thruster, their main purposes were not the validation of their codes with a real thruster, but to demonstrate that the fluid approach works.

3.2.4 Other Methods

Boeuf et al. tried interesting approaches [84]. They basically used fluid approach to obtain plasma behaviors in HET. In Ref. [84], they employed the ion flux tube (ion freefall) equation to calculate plasma density, which had been adapted early in Ref. [86]. The ion flux tube equation is written as

$$n_e(z) = \int_0^z \frac{S(z')dz'}{\left[u_{n_0}^2 + 2\frac{e}{m_i}(\varphi(z') - \varphi(z)) \right]^{1/2}} \tag{3.2}$$

Equation (3.2) masks the assumption that the electric field is always positive or at least the term containing negative potential difference in the denominator must be less than $u_{n_0}^2$ if the electric field is negative. Therefore, the ion backflow cannot be addressed with Equation (3.2). That is why the ion backflow was neglected and arbitrary boundary conditions at the anode sheath edge were used.

In Ref. [85], they used the ion Vlasov equation to calculate plasma density and ion velocity. However, they still neglected the ion backflow phenomenon. Both methods

56

also neglected the electron diffusion term in the electron momentum equation. In spite of simple approximations, the interesting thing about their approach is that their method is found to be numerically robust. They solved each governing equation separately and applied a relaxation method to obtain a convergent solution or time dependent oscillation eliminating singularity problems in their formulation as seen in other methods.

Recently, Keidar et al. developed an analysis program for HET using full fluid description and included radial direction to investigate thruster life time [87]. They utilized an analytical solution for the radial direction to reduce its computational cost to the order of minutes, which is very fast. However, it still assumes the arbitrary boundary values at the anode, which is not self-consistent.

3.3 Tool Identification

Based on the discussion in section 3.2, it should be investigated to see if there is an appropriate tool which meets the criteria proposed in section 3.1.

In Table 3.1, the boldface italicized underlined words in the first row are the required levels for each criterion. The shaded cells indicate the levels for each method which meet the criteria. In order to have an appropriate tool or methodology, all cells in a row must be shaded. However, as can be seen none of the methodologies meet the criteria.

Kinetic and hybrid methods suffer from low computational efficiency. The fluid methods using the formulation of a system of ODEs are identified to have low numerical robustness due to singularities at the anode sheath edge and the internal sonic point. The fluid methods which do not solve the system of ODEs fail to have a self-consistent solution by ignoring anode sheath modeling and incorporating arbitrary boundary conditions.

Table 3.1: Tool Identification based on the Criteria

Researcher	Numerical Efficiency (**_high_**)	Numerical Robustness (**_high_**)	Self-Consistency (**_high_**)	Physics Representativeness (**_middle_**)
Komurasaki et al. (1995)	middle	**_high_**	low	low
Boeuf et al. (1998)	middle	**_high_**	low	low
J. Ashkenazy et al. (1999)	**_high_**	low	low	low
Fruchtman et al. (2000)	**_high_**	low	low	low
Ahedo et al. (2001-2005)	**_high_**	low	**_high_**	**_middle_**
Subrata Roy et al. (2002)	middle	**_high_**	low	low
Avi Cohen-Zur et al. (2002)	**_high_**	low	low	**_middle_**
L. Dorf et al. (2003)	**_high_**	middle	low	low
Keidar et al. (2002-2005)	**_high_**	**_high_**	low	**_middle_**
Fife et al. (1995-1997) Koo et al. (2004) Boeuf et al. (2002-2004)	low	**_high_**	**_high_**	**_high_**
Adam et al. (2004) Taccogna et al. (2005)	very low	**_high_**	**_high_**	**_high_**

As a result, there is a need to develop an appropriate tool for HET at the conceptual level. At this point, other new ideas are required to come up with the criteria.

CHAPTER 4

PHYSICS-BASED ANALYSIS TOOL DEVELOPMENT FOR HET

4.1 Hypotheses for an Intended Tool

In order to develop an appropriate tool, the following hypotheses are proposed.

Hypothesis 1

If the highly detail physics can be properly omitted when providing macroscopic performance metrics, the fluid approach will be a good candidate for improving numerical efficiency.

Hypothesis 2

If the singular form of a system of ODEs occurring in fluid approach can be avoided somehow, numerical robustness will be improved.

Hypothesis 3

If proper modeling near the anode region is included in the fluid approach, a self-consistent model will be constructed and the number of arbitrary boundary conditions will be reduced.

Hypothesis 4

If most of major physical phenomena are included in the model and all the concerned variables are computed by the tool within the range of assumptions, the tool will represent sufficient physical phenomena experimentally observed in HET.

4.2 Ideas to Meet the Criteria

4.2.1 Assurance of Numerical Efficiency

Due to the high computational cost of kinetic and hybrid methods, a continuum/fluid method should be chosen. Furthermore, one-dimensional analysis should suffice for the current purpose. For the governing equations using fluid description, a solution can be attained using a time marching scheme which has been widely used in CFD and numerical combustion societies. On the other hand, if steady state solutions are desired, a solution can be attained by solving the steady state forms of governing equations in terms of TPBVP. One reason why CFD and combustion society usually implement a time marching scheme is that there is no need to consider the internal singular points which arise when the fluid equations are converted to ODE forms. Furthermore, wall time for most of time marching schemes to steady state are reduced significantly thanks to the speed of modern computer capability. However, this is not the case for the current problem. The case is one of multiple time scale problems caused by the fact that electrons have a higher rate of variation in their macroscopic properties by the order of mass ratio, $m_{i\,or\,n}/m_e$, during the course of integration. This fact indicates that when the governing equations of the fluid are solved using the time marching scheme, the convergence for electrons by sub-iterations must be performed at every ion or neutral time step. This brings the solution strategy back to a hybrid-like method, which again

60

costs significant computational time. Thus, the steady state forms of governing equations should be used.

Lastly, the quasi-neutrality should be assumed. This eliminates the calculation step for the Poisson's equation to obtain potential distribution. Thus, the potential distribution must be obtained from one of fluid equations.

4.2.2 Assurance of Numerical Robustness

As seen in Equation (3.1), when the steady state form of governing equations is converted to a system of ODEs with the quasi-neutrality assumption, the regular singular point occurs inside the domain and the irregular singular point occurs at the anode sheath edge for the ion backflow modeling. These singular points cause many numerical difficulties. For example, when the resultant system of ODEs is to be solved in terms of TPBVP with the shooting method, negative density or temperature is often encountered during the course of ODE integration. Furthermore, linearization of the system of ODEs is also required for both anode sheath edge and internal singular point, which must be first guessed.
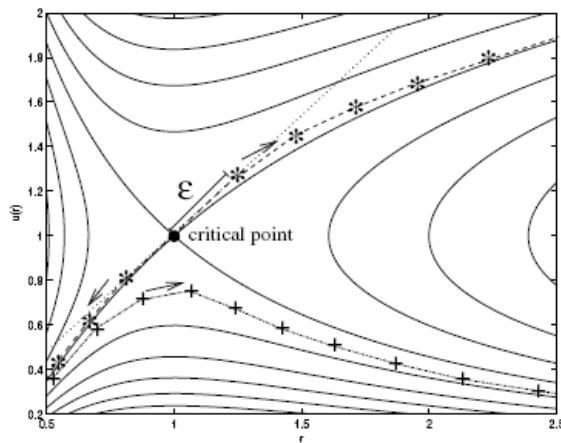
Figure 4.1: Solution Curves for Isothermal Euler Equations [88]

The linearization near the internal singular point is required to have a higher accuracy since this kind of removable singularity usually has a unique solution as in subsonic-supersonic transition flow, which is shown in Figure 4.1. Although a new method using dynamical system formulation to deal with this problem was suggested recently [88], it still requires very good initial guesses for dependent variables and internal singular point location.

Actually, the shooting method is not good for highly nonlinear problems due to breakdown of the code in the course of integration by previously stated reasons. One can think of other methods like multiple shooting [89] or finite difference method [90]. These methods divide the domain into smaller sub-intervals and integrations are performed on each interval. Then the values at each interface between sub-intervals are matched by Newton's method. However, other problems still exist if the singular forms of ODEs are maintained. Multiple shooting method makes the problem more difficult to solve. Since the location of internal singular point is not known in advance, a numerical treatment of moving the internal singular point from one sub-interval to another is definitely required, which might cause slow convergence. Although a finite difference method can deal with the internal singular point by adaptive grid strategy, it still has numerical instability such as gradient blow-up in the vicinity of an internal singular point with poor initial conditions. As a result, the strategy of solving the system of ODEs with a quasi-neutrality assumption should be avoided and a more robust strategy should be found.

In order to avoid the singular formulation, each ODE for a specific variable can be solved sequentially while other variables remain constant. Then the convergence can be obtained by iterations. This is the same method of the so called fixed point iteration in

MDO context [91]. An under-relaxation strategy is applied to enhance numerical robustness. However, there is still a problem with numerical robustness when the ion momentum equation is solved. Equation (4.1) shows the ion momentum equation.

$$\frac{d(m_i n_e u_i^2)}{dz} + n_e \frac{d(e\varphi)}{dz} = m_i n_e (\nu_i - \nu_{recom}) u_n \qquad (4.1)$$

Ion momentum equation can be solved for the ion mean velocity. In order to apply the method of fixed point iteration, the electric field $-\frac{d(e\varphi)}{dz} = eE$ and other variables may be fixed as constants and then Equation (4.1) can be integrated for the ion mean velocity. The resultant equation can be written as

$$\frac{du_i}{dz} = \frac{n_e}{m_i \Gamma_i} eE + \frac{n_e (\nu_i - \nu_{recom})(u_n - u_i)}{\Gamma_i} \qquad (4.2)$$

As seen in Equation (4.2), the ion flux term is in the denominator of the right-hand-side of the equation. If the physics of the ion backflow is included, it is definitely expected that the ion flux term has the range of values from negative at the anode to positive at the cathode, which means there is a point where ion flux must be zero. This also causes another kind of regular singular point and prohibits the analysis from being robust if Equation (4.2) were to be solved for the whole domain. Note that at the point where ion flux is equal to zero, the electric field must approach zero and the neutral mean velocity and the ion mean velocity must approach the same value to have a regular singular point, which is physically correct. The ion flux tube equation in Equation (3.2) cannot be used for the whole domain if physics of the ion backflow were to be incorporated.

Thus, another idea is again required. The idea is to avoid this newly occurring singularity by dividing the solution domain into two regions. This idea is coupled with the topic of next section and will be explained in detail there.

4.2.3 Assurance of Self-Consistency

As seen in Table 3.1, most of previous methods employing fluid description suffer from the loss of self-consistency. Since they neglected physics of the ion backflow, they can't help giving arbitrary boundary values at the anode sheath edge. This can be excused when the general behavior of plasma in HET is intended to be sought and the solvability of the fluid description for this problem needs to be checked. However, inconsistent solutions cannot be used for large design space exploration or approximation of real thruster performance.

In order to come up with the self-consistency of the solution, somehow the physics near the anode region must be modeled. It should be noted that there are two different phenomena possible for anode sheaths; positive and negative anode falls. The word "fall" is attributed to the fact that the plasma potential either increases or drops over a distance on the order of a few Debye lengths toward the anode for positive and negative directions respectively as seen in Figure 4.2. Therefore, the negative anode fall is electron-repelling and the positive anode fall is electron-attracting. HET can have both anode fall phenomena. The type of anode falls is found to be dependent on the cleanliness of the anode by dielectric, discharge voltage, and other operational parameters [92] - [94].
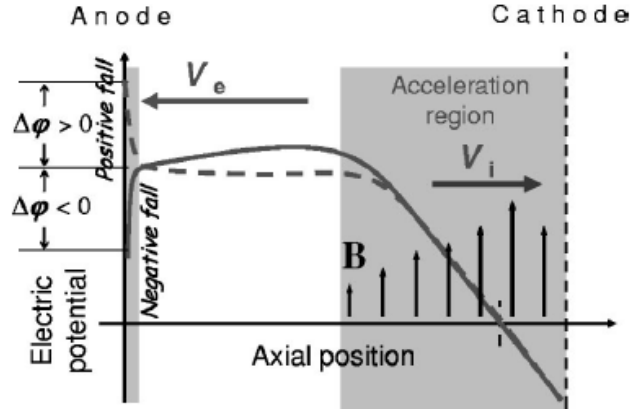
Figure 4.2: Two Types of Anode Fall [94]

Several researchers have noted that positive anode fall can result in discharge extinguishment at low propellant mass flow rate operation [98]. Furthermore, several experimentalists have previously confirmed the existence of negative anode fall as seen in Figure 4.3 [95] - [97]. In addition, several numerical methods successfully solve the HET operational characteristics with the negative anode fall boundary condition [98] - [99]. For the case of the negative anode fall, the ion backflow must be provided to meet the Bohm criterion at the Tonks-Langmuir edge [54]. In the view of current research objectives, the negative anode fall is taken as one of general physical phenomena in HET.
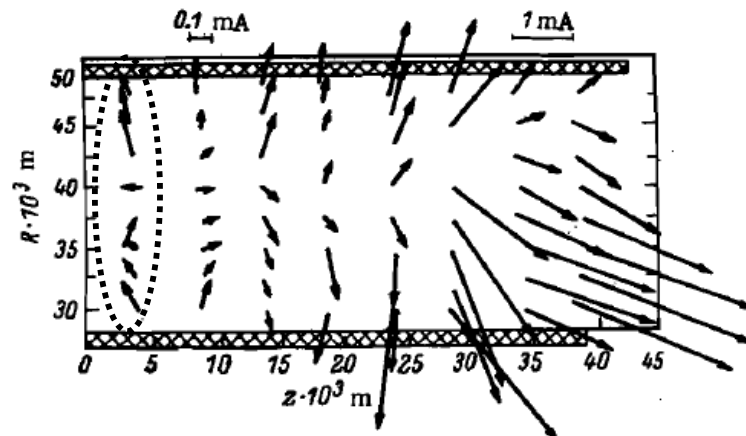
Figure 4.3: Ion Current from Experimental Measurement [96]

As explained in section 4.2.2, the numerical robustness cannot be guaranteed if the whole domain is solved simultaneously even though a fixed point iteration is used. Thus, the solution domain needs to be divided into particular regions to enhance numerical robustness while maintaining the self-consistency as well as representing major physics in HET.

The ultimate idea usually comes from physical observation and intuition. Figure 4.4 shows the general electron trajectories at several thruster channel locations. At the region near the exhaust where the strength of the radial magnetic field is high, the electron trajectory is almost trapped by the strong radial magnetic field. Closer to the anode, the effect of trapping is decreased since the magnetic field is also lower. At the region near the anode where the strength of the radial magnetic field is almost negligible, the electrons are almost purely diffused directly toward the anode.
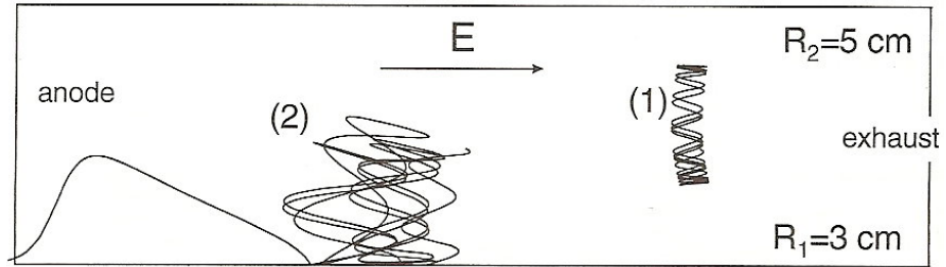
Figure 4.4: Electron Trajectories in Magnetic Field and Uniform Electric Field [84]
(1) Trapped Electron Trajectory (2) Wall-Scattered Electron Trajectory

From the above observations, an appropriate assumption can be made such that the whole solution domain may be divided into two regions; a collisional diffusion dominant region and a pure collisionless diffusion dominant region. The interface linking the two regions should be the point where the ion average velocity is equal to zero. Then the left region of the matching point will contain sheath and presheath regions and the right region of the matching point will contain ionization and acceleration regions. These

two regions are mathematically distinguished mainly by different treatments of the electron momentum equation. The electron momentum equation can be simplified with the assumptions of steady state, neglecting electron inertia terms, reducing stress tensor to pure pressure, and neglecting mean velocities of other species compared to the much higher electron mean velocity. In addition, the azimuthal electron mean velocity obtained from stochastic analysis through the Langevin equation (Appendix A) can be substituted. The resultant equation of these simplifications and substitution is given by Equation (4.3).

$$0 = -\frac{d(n_e kT_e)}{dz} + n_e \frac{d(e\phi)}{dz} - m_e n_e \nu_{e,eff}\left(1 + \frac{\omega_e^2}{\nu_{e,eff}^2}\right)u_e \tag{4.3}$$

Equation (4.3) is actually one type of Ohm's law. This equation is reduced to the different forms for each region given below.

Collisionless Pure Diffusion Region (Left Region)

$$0 = -\frac{d(n_e kT_e)}{dz} + n_e \frac{d(e\varphi)}{dz} \tag{4.4}$$

Collisional Diffusion Dominant Region (Right Region)

$$0 = n_e \frac{d(e\phi)}{dz} - m_e n_e \nu_{e,eff}\left(1 + \frac{\omega_e^2}{\nu_{e,eff}^2}\right)u_e \tag{4.5}$$

In this way, the two regions are solved independently and the properties at the common interface must be matched for all dependent variables. The detailed solution strategy will be discussed later, but the idea of treating the anode sheath/presheath region and the ionization/acceleration region separately ensures both numerical robustness and self-consistency.

4.2.4 Assurance of Physics Representativeness

As compared to previous 1D fluid descriptions, the inclusion of the region near the anode as a sheath/presheath represents an effort to improve major physics models for the HET.

Another straightforward way to improve the physics of this HET model is to directly incorporate the experimental data for the calculation of various cross sections such as ionization, excitation, and momentum collisions between neutrals and electrons, i.e., not using Arrhenius law-like reaction rate representations typically used in previous 1-D fluid researches.

In order to eliminate arbitrary boundary conditions at the thruster exit plane, the plume region is also included in the solution domain. By doing this, more confident boundary conditions at the cathode can be given, which helps the self-consistency of the analysis and physics representativeness.

The actual physical phenomenon to which the most careful attention must be given is regarding electron anomalous diffusion. The electron anomalous diffusion has been a hot topic of controversy among HET researchers since 1960s and it has still not been fully understood. As explained in section 3.2, the electrons exhibit cyclotron motion under a magnetic field and are consequently trapped. In this case, electron cross field conductivity is assumed to be obtained through electron-neutral or Coulomb collisions, which is based on classical collision theory. However, these collisions are not sufficient to explain the experimentally observed electron cross field transport. The collision frequency of electron-neutral and Coulomb collisions is on the order of $10^5 - 10^6 s^{-1}$, but the actual collision frequency is estimated to be on the order of $10^7 - 10^8 s^{-1}$. The

classical cross field mobility of electrons under a magnetic field, neglecting electron pressure is expressed for a high magnetic field region as

$$\mu_{e,\perp} = \frac{e}{m_e \nu_e} \frac{1}{\left(1 + \frac{\omega_e^2}{\nu_e^2}\right)} \approx \frac{e}{m_e} \frac{\nu_e}{\omega_e^2}$$

(4.6)

In Equation (4.6), for a high magnetic field region, collisions actually enhance the electron cross field mobility which is counter to the case often seen in electrical conduction inside the solid wire. For the latter case, the collisions between free electrons and a fixed solid grain reduce the electron mobility. The electron mobility estimated from experiments is much higher than that from Equation (4.6), implying that classical collisions are not sufficient to explain cross-field electron transport.

Morozov et al. first speculated on the mechanism of the anomalous electron cross field diffusion by attributing it to electron-wall collisions [100] - [101]. In subsequent papers using this electron wall conductivity, the electron-wall collision frequency is approximated as

$$\nu_{e,w} = \alpha \nu_{ref}, \quad where, \nu_{ref} = 10^7 s^{-1}$$

where, α is the adjustable constant. However, they apply the magnetic field dependence on electron mobility as $\mu_{e,\perp} \propto 1/B^2$, which is identical to the classical theory.

Other researchers consider azimuthal electric field fluctuation associated with the density fluctuation from the plasma turbulence as a mechanism of the anomalous electron cross field transport [102] - [103]. Gallard et al. numerically investigated this type of anomalous electron diffusion [105]. In this case the electron cross field mobility is simply inversely proportional to magnetic field strength, $\mu_{e,\perp} \propto 1/B$, which is called Bohm-type

cross field conductivity. The papers using this anomalous mobility concept employ the anomalous diffusion collision frequency, which is approximated as

$$\nu_{e,B} = \alpha_{ano} \omega_e, \quad where, \omega_e = electron \;\; cyclotron \;\; frequency$$

where, α_{ano} has the value of $1/16$ for the Bohm diffusion case. Several researchers used different values for their numerical modelings to match experimental data. Fife suggested $\alpha_{ano} = 1/107$ for his hybrid simulation [68]. Ahedo et al. used $\alpha_{ano} = 1/100$ in their 1D fluid approach model [77]. Hofer et al. suggested even a lower value of $\alpha_{ano} = 1/160$ in their hybrid-PIC modeling [105].

Koo et al. compared two types of anomalous mechanisms proposed for the UM/AFRL-P5 Hall thruster [106]. In their results, since the Bohm-type diffusion performed better for thruster performance and electron-wall collision type performed better for potential profile estimation, they could not suggest the preference of one mechanism over the other.

As seen in previous reviews, the electron anomalous cross field transport is still clearly not fully understood. Furthermore, it is impossible to resolve the mechanism for anomalous diffusion using the current approach. Thus both types of anomalous transport mechanisms should be included. For the Bohm type diffusion, the most recent experimentally suggested formula should be used [107]. Although Ref. [107] concluded that the electron-wall collisions play a minor role in the anomalous transport outside the thruster channel, electron-wall collisions must be included to be consistent for electron-wall energy loss rate when solving for electron temperature. The detail implementation will be discussed in next section.

4.3 Development of Physics-based Analysis Tool

4.3.1 Analysis Domain

In order to ensure numerical efficiency, a one-dimensional domain is considered. As seen in Figure 4.5, the analysis domain extends from anode line to cathode line, which includes the entire thruster channel and the part outside the thruster channel up to the cathode location. The region from the anode line to the Tonks-Langmuir edge is analyzed only for potential difference, and not for other solution variables which need to be solved in microscopic scale.
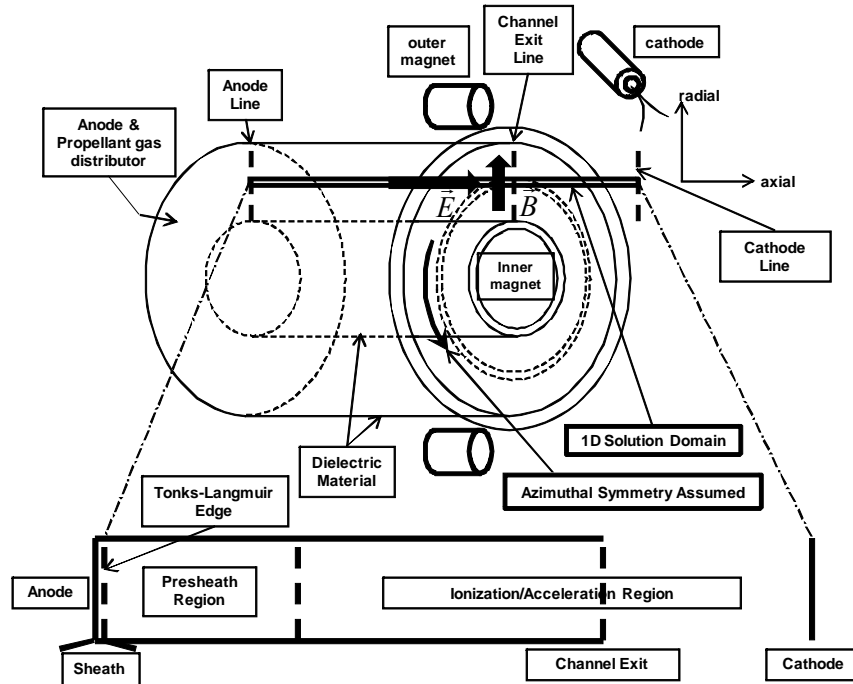
Figure 4.5: Schematic of Analysis Domain

4.3.2 Assumptions

The followings are general assumptions which have been used in most of the previous methods using fluid approach.

1) Cylindrical coordinates are used: (r, θ, z)

2) Steady state solution is sought: $\dfrac{\partial}{\partial t} = 0$

3) Azimuthal symmetry is assumed and radial variations are neglected:

$$\frac{\partial}{\partial r} = \frac{\partial}{\partial \theta} = 0$$

4) Quasi-neutrality is assumed: $n_i \approx n_e$

5) All mean velocities in r and θ are neglected except for electron mean velocity in the θ direction.

6) Neutral and ion temperatures are neglected: $0 \approx T_n, T_i \ll T_e$

7) Electron inertia terms are neglected: $0 \approx m_e \ll m_n \approx m_i$

8) Neutral velocity is constant throughout the domain and calculated from assumed anode temperature: $T_{anode} \approx 1000K$

9) Stress tensor is reduced to pure pressure: $\widetilde{P}_e \approx p_e = n_e k T_e$

10) Only axial direction electric field and radial direction magnetic field are considered: $\vec{E} = E\vec{e}_z, \vec{B} = B\vec{e}_r$

11) The velocity distribution function of electrons is Maxwellian.

12) Neutrals and ions are assumed to be collisionless.

13) The excited neutrals by electron excitation collisions are assumed to immediately give off the excited energy.

The following are the assumptions which are used for developing the current tool based on these ideas.

1) Ion plume expansion is not considered. Thus, the area is assumed to be constant throughout the domain.

2) Only singly charged ions are considered.

3) The presheath region is assumed to be a collisionless region except for the electron-neutral ionization collisions.

4) The electron temperature in the sheath/presheath region is assumed to be constant by assumption 3).

5) The ionization/acceleration region is assumed to be a collision-dominated diffusion region.

6) Azimuthal drift electron kinetic energy is neglected compared to electron internal energy.

7) Electron heat conduction is neglected.

8) The ion recombination at the dielectric wall is not considered.

The analysis is only for approximate plasma behaviors and macroscopic performance parameters. The structural and thermal analysis for a thruster is not the purpose of current research.

4.3.3 Expected Solution Structure for Electric Potential Distribution

Since the negative anode fall is taken as the general behavior near the anode region, the electric potential distribution is expected to be as shown in Figure 4.6. Furthermore, since the ideas suggested the division of the solution domain into two regions, the electric potential should be solved for each region, and matched at the matching point. In order to do this, the potential at the Tonks-Langmuir edge must be

found based on sheath phenomena and DC discharge voltage at the anode. Then, the solution of potential distribution at the presheath region can provide the value of electric potential at the matching point. The value of electric potential at the matching point and cathode boundary condition for electric potential can then be used to solve the potential distribution in the ionization/ acceleration region.
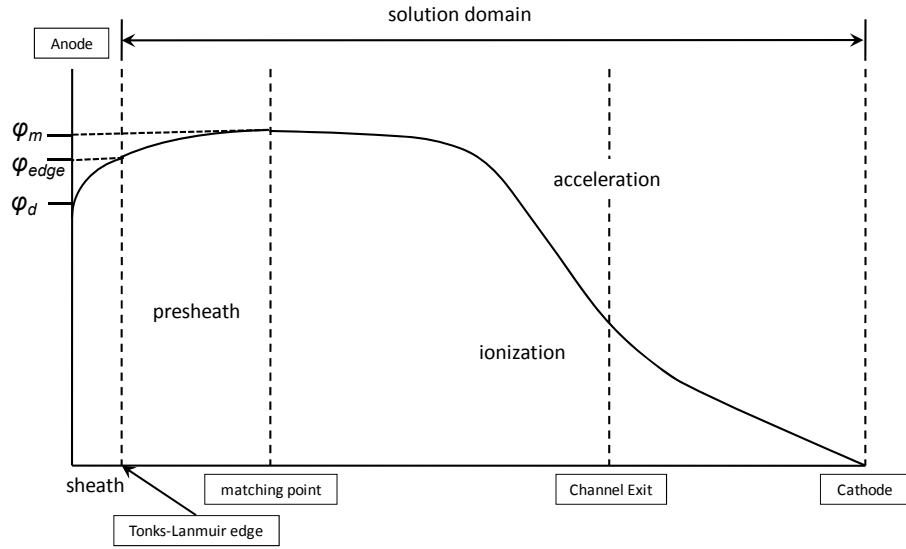
Figure 4.6: Expected Solution Structure for Electric Potential

4.3.4 Anode Sheath Region

In this region, the information on $\varphi_{edge-d} = \varphi_{edge} - \varphi_d$ is only required as shown in Figure 4.7.
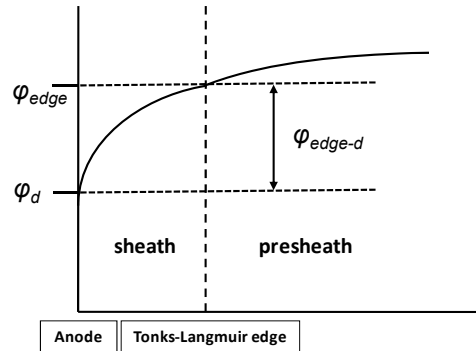
Figure 4.7: Schematic of Electric Potential Distribution in Anode Sheath Region

The current balance relation at the anode is obtained by observing Figure 4.8. The currents involved are discharge current $I_{discharge}$, displacement current $I_{displacement} \propto \dfrac{dE}{dt}$, and the currents from plasma by thermal flux and bulk movements of charged particles $I_{thermal+bulk}$. σ is the surface charge density at the anode.

The current balance relation is simply current continuity around the anode, which is given by

$$I_{discharge} = I_{thermal+bulk} + I_{displacement} \qquad (4.7)$$
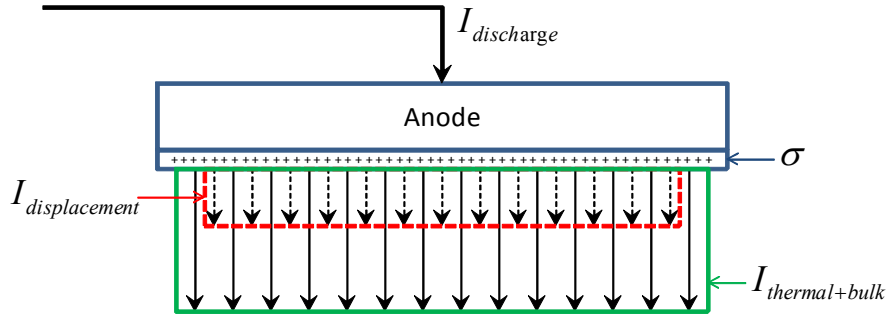
Figure 4.8: Current and Surface Charge at the Anode

When the discharge current is smaller than the thermal and bulk currents from the plasma, the displacement current must be negative and the negative surface charge density is formed [108] - [109]. In this case the relative potential of plasma body to the anode potential at steady state when the displacement current vanishes is given by [110]

$$e\varphi = -kT_e \ln \frac{I_{discharge}}{I_{thermal+bulk}} \qquad (4.8)$$

From Equation (4.8), if the electron temperature, discharge current, and plasma current are known, the value of electric potential at the sheath edge can be calculated. Since most of the currents are carried by electrons at the Tonks-Langmuir edge [92] and the bulk electron velocity must be the same order of magnitude with thermal velocity in

order to have a discharge current, it is easy to see that the plasma current from thermal flux and bulk movement of electrons would be almost twice the discharge current. Therefore, Equation (4.8) is reduced to the following relation.

$$e\varphi_{edge-d} = kT_e \ln 0.5 \approx 0.6931\, kT_e \qquad (4.9)$$

Finally, the potential difference between the anode and the Tonks-Langmuir edge is only a function of electron temperature in this approximation. Since the electron temperature in the sheath/presheath region is assumed to be constant, the electron temperature at the matching point must be calculated from the solutions in the ionization/acceleration region.

4.3.5 Presheath Region

The presheath region is defined technically as the region where an electric field is required to accelerate the ions from zero ion mean velocity at the matching point to the Bohm velocity at the Tonks-Langmuir edge before entering the sheath [54] as shown in Figure 4.9. Based on the assumptions made for this region, similar work was previously done with the assumption of constant ionization frequency throughout the presheath domain [111].
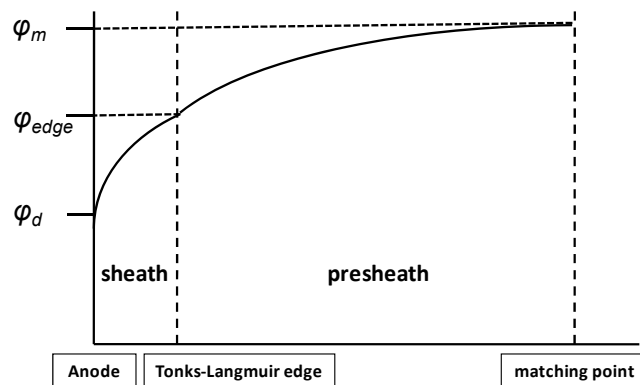
Figure 4.9: Schematic of Sheath/Presheath Region

In order to apply previous work, the assumption of constant ionization frequency is also applied for the current case. What is meant here is that the average ionization frequency in the presheath region may be used to appreciate the previous work. The questions are how this assumption is reasonable and how to calculate the average ionization frequency. The first question can be easily justified noting that the ionization frequency is given by $v_i = n_n \langle \sigma_i v_e \rangle = n_n RR_i(T_e)$, where v_i is the ionization frequency, n_n is the neutral number density, and $\langle \sigma_i v_e \rangle = RR_i(T_e)$ is the ionization reaction rate which is only a function of electron temperature. Since the constant electron temperature in presheath region is already assumed and the neutral number density is almost constant in the region near the anode, it is expected that the ionization frequency has little variation in the presheath region. To be more accurate, the neutral number density variation may be obtained from presheath solutions such as the ion mean velocity and plasma number density by using neutral and ion continuity equations.

The governing equations based on assumptions in section 4.3.2 are as follows.

Continuity equations for neutral, ion, and electron

$$\frac{d\Gamma_n}{dz} = -S \qquad \frac{d\Gamma_i}{dz} = S \qquad \frac{d\Gamma_e}{dz} = S \qquad\qquad (4.10)$$

where, n, i, e represent neutral, ion and electron respectively, $\Gamma = nu$ is the species number flux, and S is ionization source term, which is given by $S = n_e n_n \langle \sigma_i v_e \rangle$. The ionization reaction term, $RR_i = \langle \sigma_i v_e \rangle$, can be calculated as a function of electron energy. Unlike expressions used in most methods using a fluid approach which are the Arrhenius law-like form, the regression equation is generated by numerical integration of experimental data for the ionization cross sections at given electron temperatures with the

Maxwellian velocity distribution for electrons. Note that only first ionization is considered as it is assumed. The experimental cross section data for Xenon first ionization is taken from Ref. [52]. In Ref. [52], the curve fit equation is provided for ionization as well as other cross sections. The original sources are found in Ref. [113] - [118].

Figure 4.10 shows the first ionization cross section for Xenon. It cannot be used directly since the cross section is that for the collision between an electron and a Xenon neutral.
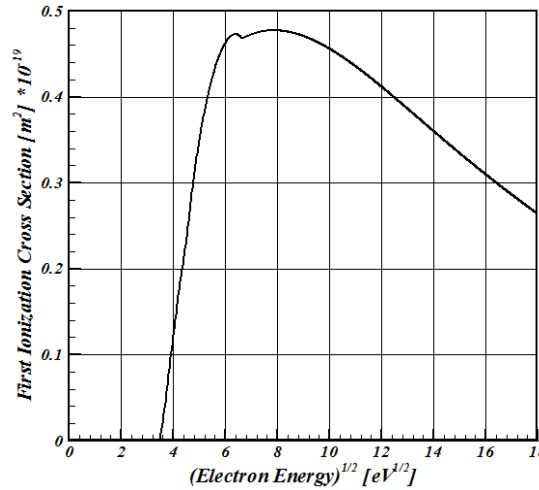
Figure 4.10: First Ionization Cross Section for Xenon [52]

The ionization reaction rate $RR_i = \langle \sigma_i v_e \rangle$ is the macroscopic value and is calculated by averaging $\sigma_i v_e$ in the velocity space. Note that the relative velocity between an electron and a Xenon neutral is assumed to be simply the electron velocity. In order to calculate the ionization reaction rate, electron velocity distribution function must be known. Maxwellian velocity distribution of electrons and further isotropic velocity distribution are assumed. It is more practical to convert the velocity distribution function

to an energy distribution function to calculate reaction rate. The energy distribution

function using the unit of eV is given by

$$f(\varepsilon) = \frac{2}{\sqrt{\pi}} \sqrt{\frac{\varepsilon}{T_{eV}^3}} \exp\left(-\frac{\varepsilon}{T_{eV}}\right)$$ (4.11)

Using Equation (4.11) and recognizing that $v_e = \sqrt{2e/m_e}\sqrt{\varepsilon}$, the ionization

reaction rate can be calculated as

$$\langle \sigma_i v_e \rangle = \int_{E_1}^{+\infty} \sigma_i(\varepsilon) \sqrt{\frac{2e}{m_e}} \sqrt{\varepsilon} f(\varepsilon) d\varepsilon$$ (4.12)

where, E_1 is the threshold of first ionization energy, which is 12.13 eV for Xenon. It is

also assumed that $\langle \sigma_i v_e \rangle \approx \langle \sigma_i \rangle u_{e,th}$, where $u_{e,th} = \sqrt{8eT_{eV}/\pi m_e}$, the mean electron

thermal velocity at a given electron temperature. The energy averaged ionization cross

section $\langle \sigma_i \rangle$ is numerically integrated at the given electron temperature as in Equation

(4.13).

$$\langle \sigma_i \rangle = \int_{E_1}^{+\infty} \sigma_i(\varepsilon) f(\varepsilon) d\varepsilon \cong \sum_{k=1}^{N} \sigma_i(\varepsilon_k) f(\varepsilon_k, T_{eV}) \Delta\varepsilon$$ (4.13)

The upper limit of energy is taken as $E_{upper} = 20 \times T_{eV}$ and the number of energy

bins for numerical integration is 3000.

The resultant $\langle \sigma_i \rangle u_{e,th}$ is shown in Figure 4.11. As seen in Figure 4.11, the

ionization reaction rate is only a function of electron temperature. The curve-fit equation

is then generated for the ionization reaction rate, which is given in Appendix B.
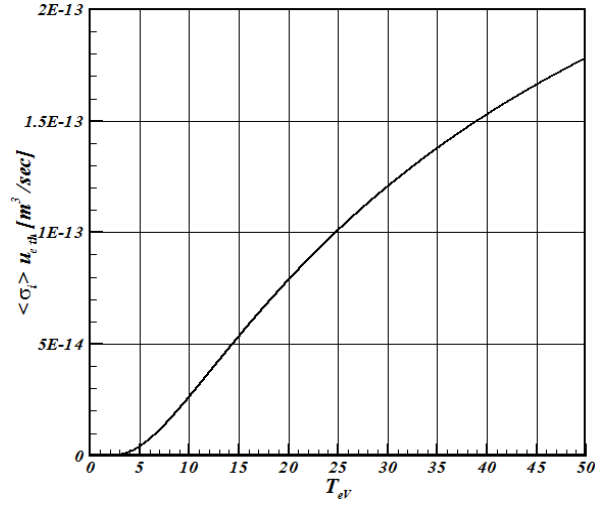
Figure 4.11: First Ionization Reaction Rate for Xenon

If the neutral and ion continuity equations are added and integrated, the resultant equation is called the global continuity equation and is given by

$$m_n n_n u_n + m_i n_e u_i = const. = \frac{\dot{m}}{A}$$
(4.14)

where, m is the species mass, u is the species mean velocity, $\dot{m}$ is the propellant mass flow rate, and A is the thruster channel area.

Another useful relation is obtained by subtracting the electron continuity equation from the ion continuity equation and integrating it. The resultant relation is called the current continuity equation and is given by

$$n_e u_i - n_e u_e = \frac{I_d}{eA}$$
(4.15)

where, I_d is the discharge current, and e is the electric charge. It is important to note that the global and current continuity equations must hold throughout the solution domain, and not restricted to the presheath region as the continuity equations state.

Ion momentum equation

80

$$\frac{d(n_e u_i^2)}{dz} = -\frac{en_e}{m_i}\frac{d\varphi}{dz} \tag{4.16}$$

where, φ is the electric potential. It is assumed in Equation (4.16) that ions are generated at zero velocity unlike the ionization/acceleration region where the ions are generated at neutral velocity. This can be indirectly justified from the experimental results on neutral velocity, where neutral velocity increases from almost 0 near the anode to some value at the exit [71]. However, when the global continuity is applied for the presheath, the constant neutral velocity is used to calculate neutral number density. This is necessary and reasonable by the fact that first if neutral velocity is zero in the presheath, another relation is required to obtain neutral number density and second, since neutral velocity is relatively small compared to ion and electron velocities, the errors from approach above are expected to be very small.

Electron momentum equation

$$0 = -\frac{d}{dz}(n_e kT_e) + en_e\frac{d\phi}{dz} \quad or \quad 0 = -kT_e\frac{dn_e}{dz} + en_e\frac{d\phi}{dz} \tag{4.17}$$

From the assumption of collisionless diffusion in the presheath region, the collision term in electron momentum equation is neglected. Furthermore, since the electron temperature is assumed to be constant, the resultant electron momentum equation has the form of second equation in Equation (4.17).

Equation (4.17) can be easily integrated for plasma number density, which is given by

$$n_e = n_e(0)e^{(e\varphi/kT_e)} \tag{4.18}$$

If $n_e(0)$ is the plasma number density at the matching point, $n_{e,m}$, the plasma number density may be obtained for the whole presheath region once the electric

potential distribution is found. Equation (4.18) is sometimes called the barometric law. It simply implies the balance between electrostatic force and pressure force. It is valid for electrons motion along the magnetic field line and is quite a good approximation across magnetic fields when the magnetic fields are weak.

The neutral momentum equation is not required since neutral mean velocity is assumed to be constant. The energy equations for each species are also not required based on the assumptions in section 4.3.2.

The 6 original unknowns are neutral number density, plasma number density, ion velocity, electron velocity, electron temperature, and electric potential. Since electron temperature is assumed to be constant, now 5 unknowns need to be determined, which is the same as the number of governing equations. Following Kino and Shaw's work [111], the ion velocity and electric potential can be simultaneously obtained using the ion continuity and the ion momentum equations. Then, the plasma number density can be found using Equation (4.18). The neutral number density can be found using global continuity. Finally, the electron velocity can be found using current continuity.

The ion continuity and momentum equations are rewritten below.

$$\frac{d(n_e u_i)}{dz} = n_e \nu_{i,ave} = n_e n_{n,ave} \langle \sigma_i v_e \rangle \qquad \frac{d(n_e u_i^2)}{dz} = -\frac{e n_e}{m_i}\frac{d\varphi}{dz}$$

The above equations are non-dimensionalized using the following non-dimensional variables.

$$s = \nu_{i,ave}\left(\frac{m_i}{2kT_e}\right)^{1/2} z \qquad v_i = \left(\frac{m_i}{2kT_e}\right)^{1/2} u_i \qquad \eta = -\frac{e\varphi}{kT_e}$$

Then the non-dimensionalized governing equations read

$$\frac{d}{ds}(e^{-\eta}v_1) = e^{-\eta} \qquad \frac{dv_1^2}{ds} = \left(v_1^2 + \frac{1}{2}\right)\frac{d\eta}{ds} \qquad (4.19)$$

Equation (4.19) is solved using the coordinates and the boundary conditions shown in Figure 4.12.
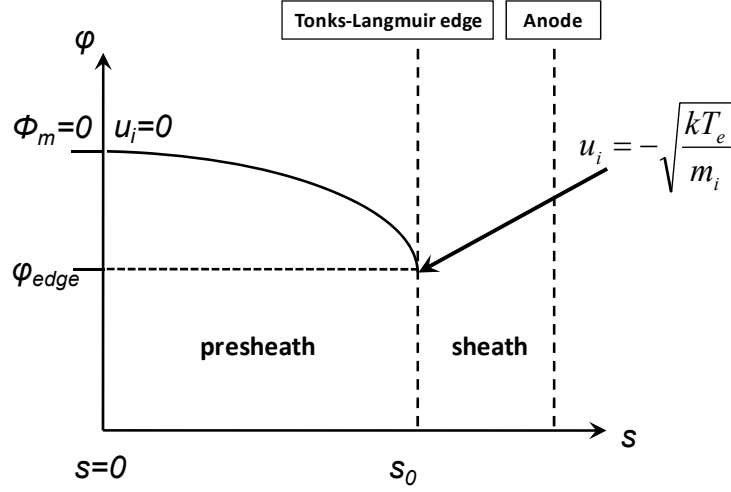
Figure 4.12: Non-dimensional Coordinate for Presheath Solution

The second equation in Equation (4.19) can be integrated with the boundary conditions to give an analytical form of the solution as

$$v_1^2 = \frac{1}{2}(e^{\eta} - 1) \qquad (4.20)$$

Inserting Equation (4.20) into the first equation of Equation (4.19) yields

$$\frac{1}{4}\frac{(1 - 2v_1^2)}{v_1}\frac{d\eta}{ds} = 1 \qquad (4.21)$$

From the observation of Equation (4.21), if $v_1^2 = 1/2$, the electric potential gradient, $d\eta/ds$ goes to infinity at $s = s_0$ and $\eta = \eta_0$. The η_0 can be easily calculated from Equation (4.20), which has the value of $\eta_0 = \ln 2 \approx 0.6931$. Since $v_1^2 = 1/2$ at

$s = s_0$, the Bohm criterion at the Tonks-Langmuir edge is automatically satisfied, which

is $u_i = -\sqrt{kT_e / m_i}$.

Equation (4.21) has an analytical solution with $d\eta / ds$ substituted using Equation

(4.20), which is given by

$$s = -v_1 + \sqrt{2} \tan^{-1}(\sqrt{2}v_1) \tag{4.22}$$

The step by step solution procedure is as follows.

1) Assume plasma number density $n_{e,m}$ and electron temperature $T_{e,m}$ at the

   matching point.

2) Generate a grid for η from 0 to η_0 .

3) Calculate v_1 using Equation (4.20).

4) Calculate s using Equation (4.22).

5) Calculate average ionization collision frequency, $v_{i,ave}$

   a. Calculate plasma number density using η and Equation (4.18).

   b. Calculate neutral number density using the global continuity equation.

   c. Take the average of neutral number density in the presheath domain.

   d. Calculate $v_{i,ave} = n_{n,ave}RR_i(T_e)$

6) Recover dimensional solutions

7) Calculate neutral number density using the global continuity equation again.

8) Calculate electron mean velocity using the current continuity equation.

From the solution procedure, the presheath length is varied depending on the

neutral number density and electron temperature at the matching point as shown in

Equation (4.23). The dependence on neutral number density is weak. However, the electron temperature at the matching point has significant effects on the presheath length.

$$L_{presheath} = \left(\frac{2kT_e}{m_i}\right)^{1/2} \frac{s_0}{v_{i,ave}}$$ (4.23)

If the electron temperature at the matching point increases, the average ionization collision frequency also increases. Although the term $(2kT_e/m_i)^{1/2}$ also increases, the effect of increasing the average ionization collision frequency is greater and this results in a decrease of the presheath length.

By the sheath and presheath solutions, the value of the electric potential at the matching point can be determined, which is higher than the discharge voltage at the anode.

4.3.6 Ionization/Acceleration Region

In this region, 6 unknowns must be determined; neutral number density, plasma number density, ion mean velocity, electron velocity, electron temperature, and electric potential. The governing equations based on assumptions in section 4.3.2 are as follows.

__Continuity equations for neutral, ion, and electron__

Continuity equations are identical to those for the presheath region as well as global and current continuities. The integration is performed only for neutral continuity equation to obtain the neutral number density.

$$\frac{d(n_n u_n)}{dz} = -S \quad or \quad u_n \frac{dn_n}{dz} = -n_e n_n \langle \sigma_i v_e \rangle$$ (4.24)

Equation (4.24) can be integrated with the boundary condition of neutral number density at the matching point. Since the ion velocity is 0 there, the neutral number density

can be directly calculated from the propellant mass flow rate. Consequently, the neutral number density in the left region of the matching point is higher than that from the actually given propellant mass flow rate. This accounts for the ion recombination back to neutrals at the anode due to ion backflow.

Ion flux-tube or freefall equation

$$n_e(z) = \int_0^z \frac{S(z')dz'}{\left[u_{n_0}^2 + 2\frac{e}{m_i}(\phi(z') - \phi(z))\right]^{1/2}} + \frac{n_{e_0}u_{i_0}}{\left[u_{n_0}^2 + 2\frac{e}{m_i}(\phi_0 - \phi(z))\right]^{1/2}}$$
(4.25)

where, the lower integration limit, 0, represents the matching point, u_{n_0} is the neutral mean velocity which is constant, and u_{i_0} is the ion mean velocity at the matching point which is equal to neutral mean velocity. The ion momentum equation is not used to enhance numerical robustness. If it is used, the resultant ordinary differential equation should be solved, which can cause negative plasma number density in the course of integration. The ion flux-tube equation or ion freefall equation simply uses the ion energy relationship and ion continuity with a collisionless assumption. What this means is that ions once created gain energy directly from the electric field and must satisfy the continuity between two points. Equation (4.25) cannot be used for the case stated in Equation (4.26), i.e., the electric potential should continue decreasing from the matching point to the cathode.

$$2\frac{e}{m_i}(\phi(z') - \phi(z)) \le -u_{n_0}^2 \quad and \quad 2\frac{e}{m_i}(\phi_0 - \phi(z)) \le -u_{n_0}^2$$
(4.26)

The second term in Equation (4.25) accounts for the initial ion flux at the matching point [112]. Although the ion mean velocity is zero at the matching point, here the ion mean velocity should have the value of the neutral mean velocity which is a

phenomenological result from numerical experimentations. If it were not included, the plasma number density adjacent to the matching point would have a significantly low value and show discontinuity. The reason why it should be included can also be explained from the ion momentum equation shown in Equation (4.2), where the ion mean velocity must be the neutral mean velocity at the matching point in order to have a regular singular point.

Equation (4.25) is an integral equation with the given information in the context of a fixed point iteration as explained in section 4.2.4. The integration is performed using 4 point Gauss-Legendre quadrature rule to obtain sufficient accuracy [90].

__Electron momentum equation__

$$0 = en_e \frac{d\phi}{dz} - m_e \nu_{e,m} \Gamma_e \quad or \quad \frac{d(e\phi)}{dz} = \frac{m_e \nu_{e,m}}{n_e} \Gamma_e \tag{4.27}$$

To integrate Equation (4.27), Boeuf's method is taken [84] - [85]. Since the two boundary conditions are provided; one at the matching point from the sheath/presheath solutions, and the other at the cathode, which is assumed to be zero potential. Two dependent variables can be determined and the electron flux may be expressed as

$$\Gamma_e(z) = \Gamma_e(c) - \Gamma_n(z) + \Gamma_n(c) \tag{4.28}$$

where, c represents the cathode position. Equation (4.28) is obtained using global and current continuity equations. In this formulation, since neutral flux distribution is calculated from the integration of Equation (4.24), the unknown is $\Gamma_e(c)$. Since $\Gamma_e(c)$ can be considered as a parameter in the ODE to be determined, $\Gamma_e(c)$ can be calculated from the general way of implementing an additional ODE, which should be solved with two boundary conditions.

$v_{e,m}$ represents the classical cross field electron momentum collision frequency including effective electron momentum collision frequency and electron cyclotron frequency and is given by

$$v_{e,m} = v_{e,eff}\left(1 + \frac{\omega_e^2}{v_{e,eff}^2}\right)$$ (4.29)

The effective collision frequency, $v_{e,eff}$, includes the electron-neutral momentum collision, Coulomb collision, electron-wall collision, and anomalous Bohm collision in the form of Equation (4.30).

$$v_{e,eff} = v_{en} + v_{ei} + v_{wall} + \alpha_{ano}\omega_e$$ (4.30)

Electron-neutral momentum collision

The electron-neutral momentum collision reaction rate is calculated the same as was shown for the first ionization reaction rate shown in Figure 4.13. The curve-fit equation for this reaction is also given in Appendix B.
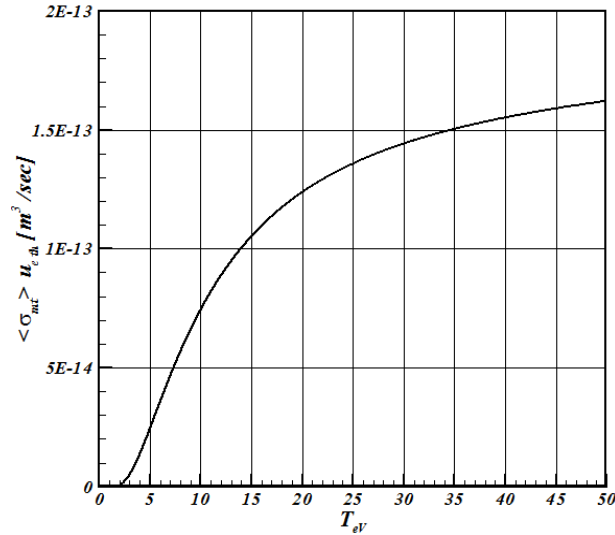
Figure 4.13: Electron-Neutral Momentum Transfer Collision Reaction Rate for Xenon

Then the electron-neutral momentum collision frequency is given by

$v_{en} = n_n RR_{en}$.

Electron-ion Coulomb collision

The reaction rate for electron-ion Coulomb collision is calculated using the formula in Ref. [79], which is given by

$$RR_{ei} = \langle \sigma_{ei} v_e \rangle = \frac{4\sqrt{2\pi}}{3} \left(\frac{m_e}{kT_e} \right)^{3/2} \left(\frac{e^2}{4\pi\varepsilon_0 m_e} \right)^2 \ln\Lambda \qquad (4.31)$$

where, $\ln\Lambda$ is called the Coulomb logarithm, where Λ is given by

$$\Lambda = \sqrt{\frac{\varepsilon_0 kT_e}{n_e e^2}} \frac{12\pi\varepsilon_0 kT_e}{e^2}$$
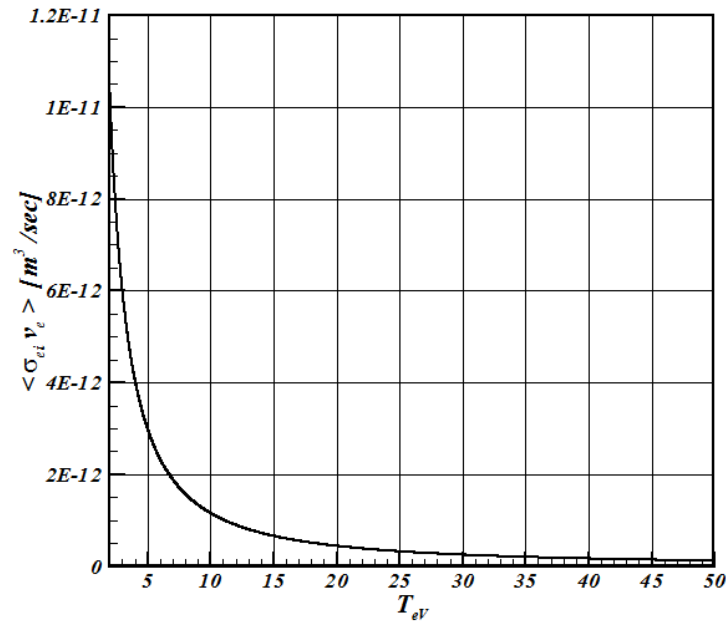
Figure 4.14: Electron-Ion Coulomb Collision Reaction Rate

The reaction rate variation with electron temperature is shown in Figure 4.14. Then the electron-ion Coulomb collision frequency is given by $v_{ei} = n_e RR_{ei}$.

Electron-wall collision frequency

The model of electron-wall collision is taken from Ref. [78]. Ref. [78] analyzed the electron continuity and radial momentum equations and proposed the wall recombination frequency as

$$\nu_w = \frac{\tilde{v}_w}{h_c} \sqrt{\frac{kT_e}{m_i}} \tag{4.32}$$

where, ν_w is the wall recombination frequency, h_c is the channel width, and $\tilde{v}_w$ is governed by the radial presheath plasma dynamics with a value between 0.7 and 1.2 for typical discharge conditions. Here, the value of 1 is taken. Then the electron-wall collision frequency is given by

$$\nu_{wall} = \beta_m \nu_w, \quad where \quad \beta_m = \frac{\delta_w}{1-\delta_w} \tag{4.33}$$

where, δ_w is the effective SEE yield, which is approximated by

$$\delta_w(T_e) = \begin{cases} \sqrt{T_e/T_1}, & T_e \leq T_e^* \\ \delta_w^*, & T_e > T_e^* \end{cases} \tag{4.34}$$

where, $\delta_w^* \cong 0.983$, $T_e^* \cong 0.968T_1$, and $T_1 \sim 0.66E_1$. E_1 is the energy of electron which yields 100% of SEE and its value is 50eV for a Boron Nitride wall material. Equation (4.34) indicates that the effective SEE is limited to δ_w^* at an electron temperature over $T_e = T_e^*$. This means that the electron-repelling sheath at the wall prevents further electron flux to the wall at a higher electron temperature, which is called the Charge Saturation Regime (CSR).

Anomalous Bohm collision frequency

As explained in section 4.2.4, this topic is still not in consensus among HET researchers. Thus, the most recent experimental results are taken to implement it for

current research [107]. In Ref. [107], they claimed that the anomalous diffusion due to plasma turbulence has a dominant effect on electron cross field diffusion compared to electron-wall collision from the conclusion of Fabry-Perot experiments for a 5kW class HET. They compared the experimental results to those of a hybrid numerical model to deduce the wall collision factor, α, and Bohm-type diffusion factor, K, which are given in the following relations.

$$\mu_{\perp,w} \propto \frac{\alpha}{B^2}, \qquad \mu_{\perp,B} \propto \frac{K}{16B} \tag{4.35}$$

where, $\mu_{\perp,w}$ is the electron cross field mobility by wall collision, $\mu_{\perp,B}$ is the electron cross field mobility by Bohm-type diffusion, and B is the magnetic field strength. They varied HET operating conditions and deduced α and K from the numerical model to match experimental results. The result is shown in Figure 4.15.
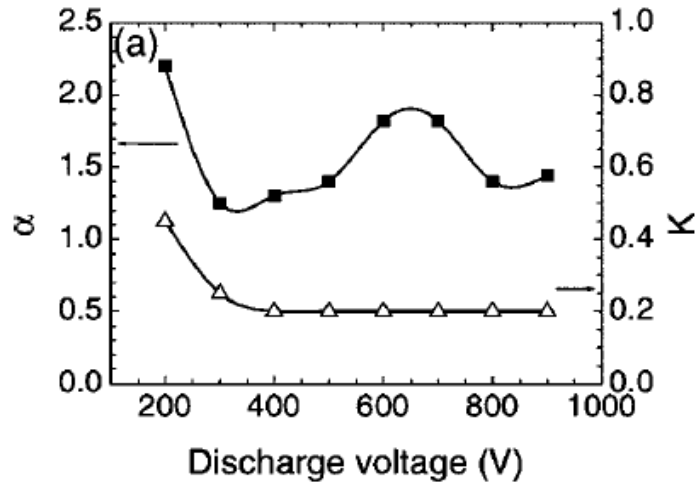
Figure 4.15: Parameter Variation with Applied Discharge Voltage [107]

The main consequence is that the ratio, α/K must be proportional to magnetic field strength based on the experimental evidence, which indicates that the ratio of electron cross field mobility inside and outside the channel is constant as shown in

91

Equation (4.36). This led them to conclude that the same mechanism must hold for the regions inside and outside the channel.

$$\frac{\mu_{\perp,in}}{\mu_{\perp,out}} \propto \frac{\alpha}{K} \frac{1}{B} = const. \tag{4.36}$$

They proposed the same form of mobility expressions for inside and outside the channel and the value of each parameter given by.

$$\mu_{\perp,in} \propto \frac{K_{in}}{16B}, \quad K_{in} = 0.1 \quad \mu_{\perp,out} \propto \frac{K_{out}}{16B} \quad K_{out} = 0.2 \tag{4.37}$$

In order to adapt the results of Figure 4.15 and Equation (4.37) to the current form of $\nu_B = \alpha_{ano}\omega_e$, the following curve fit equations are proposed to cover large discharge voltage variations. By letting $\hat{\alpha}_{ano} = 1/\alpha_{ano}$,

1) Inside the thruster channel

$$\hat{\alpha}_{ano,min} = 100 \quad at \ 150V \ \hat{\alpha}_{ano,max} = 160 \quad over \ 400V$$

$$\hat{\alpha}_{ano} = \hat{\alpha}_{ano,min}\left[1-\exp\left\{A\left(\frac{V_d-400}{400-150}\right)^2\right\}\right] + \hat{\alpha}_{ano,max}, \quad where \ A = \log\left(1+\frac{\hat{\alpha}_{ano,max}-\hat{\alpha}_{ano,min}}{\hat{\alpha}_{ano,min}}\right)$$

2) Outside the thruster channel

The same form as inside the channel but with a different $\hat{\alpha}_{ano,min}$ and $\hat{\alpha}_{ano,max}$.

$$\hat{\alpha}_{ano,min} = 50 \quad at \ 150V \ \hat{\alpha}_{ano,max} = 80 \quad over \ 400V$$

Furthermore in order to have numerical stability, the smooth variation of $\hat{\alpha}_{ano}$ between inside and outside the channel is implemented as shown in Equation(4.38).

$$\hat{\alpha}_{ano}(z) = \begin{cases} \hat{\alpha}_{ano,in} & z \leq L \\ \dfrac{\hat{\alpha}_{ano,in} - \hat{\alpha}_{ano,out}}{2} \cos\left(\dfrac{z-L}{L_s}\pi\right) + \dfrac{\hat{\alpha}_{ano,in} + \hat{\alpha}_{ano,out}}{2} & L \leq z \leq L + L_s \\ \hat{\alpha}_{ano,out} & z \geq L + L_s \end{cases} \qquad (4.38)$$

where, L is the thruster channel length and L_s is the smooth transition distance, which must be less than the distance between the thruster exit to the cathode line. Here, L_s is taken to be half of the distance between the thruster exit to the cathode line.

Electron energy equation

$$\frac{5}{3}\frac{d}{dz}(\varepsilon_e \Gamma_e) = -e\Gamma_e E - n_e \nu_{e,\varepsilon}\varepsilon_e \qquad \varepsilon_e = \frac{3}{2}kT_e \qquad (4.39)$$

Equation (4.39) can be integrated with a boundary condition at the cathode line. The electron temperature at the cathode is usually taken to be 2eV~3eV. Here, 2eV is taken as a boundary condition. Equation (4.39) can be expanded to give the form for $d\varepsilon_e / dz$ as

$$\frac{d\varepsilon_e}{dz} = -\frac{3}{5}eE - \frac{3}{5}\frac{n_e \nu_{e,\varepsilon}}{\Gamma_e}\varepsilon_e - \frac{n_e \nu_i}{\Gamma_e}\varepsilon_e \qquad (4.40)$$

The electron energy loss frequency, $\nu_{e,\varepsilon}$, consists of several loss mechanisms such as ionization, excitation, and wall-collision energy loss.

Ionization and excitation energy loss frequency

The energy loss rate by ionization and excitation is given by

$$\varepsilon_e \nu_{ion/exc} = \varepsilon_{ion}\nu_i + \varepsilon_{exc}\nu_{exc} \qquad (4.41)$$

where, ε_{ion} is the threshold energy of first ionization for Xenon, 12.12984eV, ε_{exc} is the threshold energy of first excitation level for Xenon, 8.32eV, ν_i is the ionization frequency, and ν_{exc} is the excitation collision frequency.

The first ionization reaction rate is given in Figure 4.11. The ionization frequency is then calculated by multiplying the reaction rate by the neutral number density. The excitation reaction rate is obtained in the same manner as the ionization reaction rate, which is shown in Figure 4.16. The curve fit equation is also given in Appendix B.
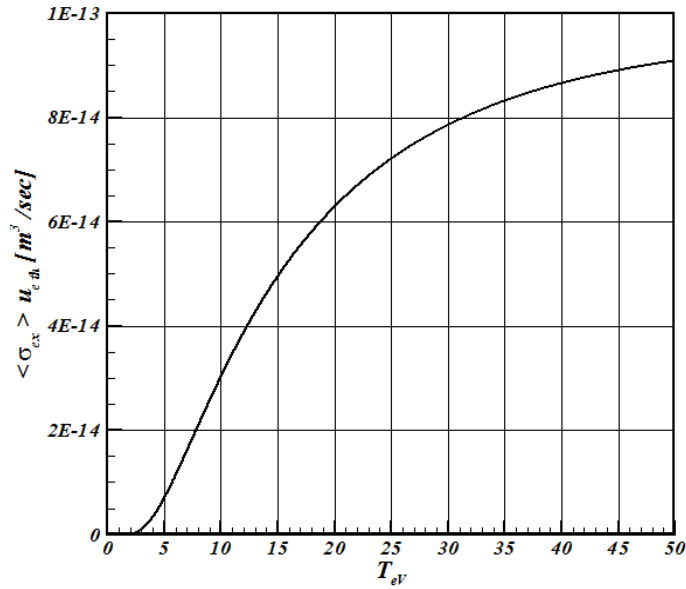
Figure 4.16: Excitation Collision Reaction Rate for Xenon

Excitation collision frequency is then calculated by multiplying the reaction rate by the neutral number density.

Wall-collision energy loss frequency

Again, the model suggested in Ref. [78] is taken and shown in Equation (4.42).

$$\nu_{w,\varepsilon} = \nu_w \beta_e(\delta_w), \quad where \quad \beta_e(\delta_w) \approx 7.77 + 1.65 \frac{\delta_w}{1-\delta_w} \qquad (4.42)$$

94

where, v_w *and* δ_w are given in Equation (4.32) and Equation (4.34), respectively.

4.3.7 Matching Two Solutions

In order to match two solutions, all the values of the unknowns from the presheath and ionization/acceleration regions must be the same at the matching point. Since the unknowns are neutral number density, ion mean velocity, electron mean velocity, electron temperature, plasma number density, and electric potential, proper strategies for these to match must be provided. The strategies are as follows.

1) Neutral number density: Neutral number density is constant and fixed as the one obtained from the given propellant mass flow rate. This is a consequence of global continuity since the ion velocity is zero at the matching point. This value also plays a role of a boundary condition for neutral density integration in the ionization/acceleration region. Neutral number density distribution in the presheath is obtained from global continuity.

2) Ion mean velocity: Ion mean velocity is zero at the matching point. This is a consequence from the assumption of dividing the whole domain into two regions since the presheath region starts from the edge of main plasma body where the ion mean velocity is equal to zero. This value also becomes one of the boundary conditions in the presheath region. Ion mean velocity in the ionization/acceleration region is obtained from global continuity.

3) Electron mean velocity: Electron mean velocity is obtained from the solution of ionization/acceleration region by solving the electron momentum equation. From these solutions, the electron flux at the cathode is obtained and the electron mean velocity is then calculated using current continuity for the

whole domain once the plasma number density and ion mean velocity for the whole domain are known. Another fact is that the current at the matching point comes completely from electron flux and is equal to the discharge current since the ion mean velocity at that point is zero.

4) Electron temperature: Electron temperature at the matching point is calculated by solving the electron energy equation in the ionization/acceleration region. The electron temperature in the presheath is assumed to be constant at the same value as the matching point.

5) Plasma number density: Plasma number density at the matching point is first assumed. After obtaining solutions from the ionization/acceleration region, the electron temperature and discharge current are known. In order to calculate plasma number density at the matching point, the current continuity is employed. Since the total current at the Tonks-Langmuir edge can be calculated, the plasma number density at the matching point is then calculated using the relation in Equation (4.43).

$$\frac{I_d}{eA} = (n_e u_i - n_e u_e)\big|_{edge} = n_{e,m} \exp\left[-\frac{e\phi_{m-edge}}{kT_e}\right]\left[-\sqrt{\frac{kT_e}{m_i}} + \sqrt{\frac{kT_e}{2\pi m_e}}\right] \tag{4.43}$$

Plasma number density in the presheath is obtained using the Boltzmann relation and for the ionization/acceleration region it is obtained using the ion flux-tube equation.

6) Electric potential: Electric potential at the matching point is obtained from the sheath/presheath solution, which also becomes a boundary condition for the electron momentum equation in the ionization/acceleration region.

96

By iteratively applying strategies 1) through 6) to match two solutions, the final converged solution can be obtained. The under-relaxation scheme is implemented to ensure numerical robustness as in Equation (4.44).

$$V^k = \alpha_{relax}V^k + (1-\alpha_{relax})V^{k-1} \tag{4.44}$$

where, k is the iteration step, V is the dependent variables, and α_{relax} is the relaxation coefficient and for under-relaxation it has the value between 0 to 1.

The diagram on implementing stated strategies is shown in Figure 4.17.
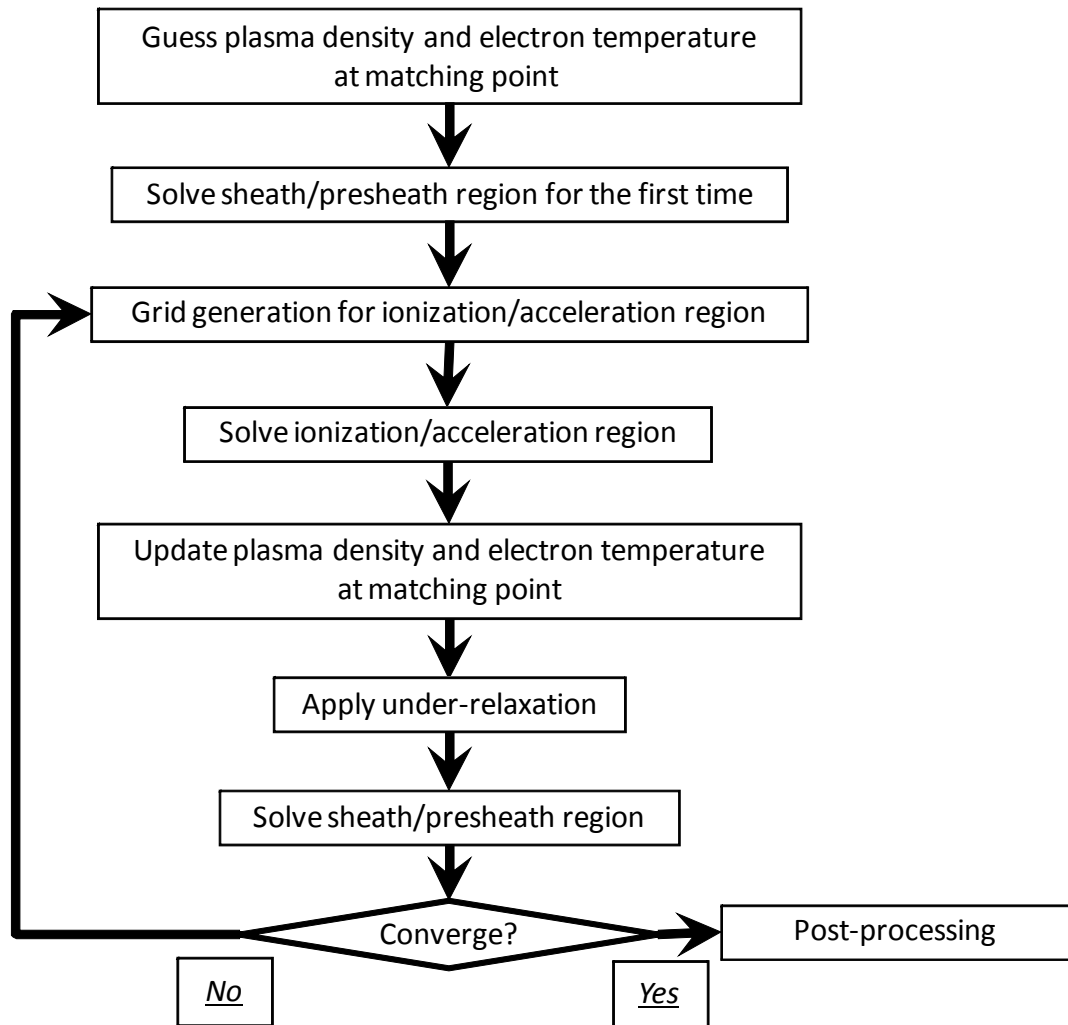
Figure 4.17: Diagram of Implementation of Solution Strategy

4.3.8 Non-Dimensionalization

Before solving the governing equations, they should be properly non-dimensionalized with appropriate reference values. For the current governing equations, the orders of magnitude of the variables are quite different. For example, number density is on the order of 10^{18}, but electron temperature is on the order of 10. Furthermore, the masses of species have considerably low orders of magnitude and the electrical charge quantity is also very low magnitude. Thus, if they are used with original units, it might cause serious numerical errors such as round-off and truncation. The machine precision for calculation must be carefully examined in this regard.

Reference values for proper non-dimensionalizations of each variable are given in Appendix C. These values have been typically used in most of the previous work.

CHAPTER 5

VALIDATION AND TOOL CAPABILITY STUDY

5.1 Point Validation with the SPT-100

5.1.1 SPT-100 Thruster

Considering current research objectives, the validation of concern is regarding the macroscopic performance metrics such as specific impulse, thrust, efficiency and discharge power. In order to validate the developed tool in Chapter IV, the experimental results are taken for the SPT-100 thruster from Ref. [119]. The SPT-100 is a 1.35kW class thruster and it has been well developed and proven for actual satellite applications. A variety of derivatives based on the SPT-100 has been also built and flown. One of derivatives had flown for the Earth-Moon Mission [30]. The picture and sectional view with indication of the computational domain are shown in Figure 5.1.
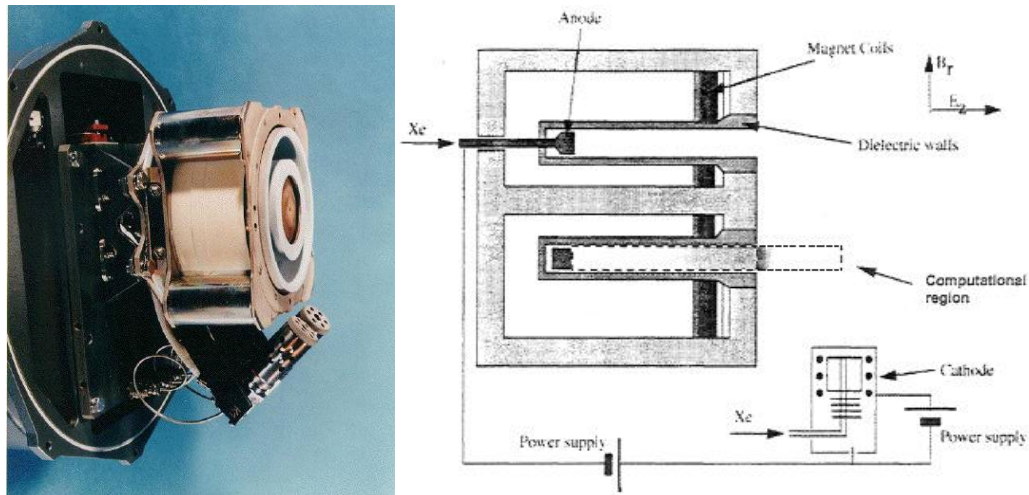
Figure 5.1: Picture of SPT-100 (left) [120] and Computational Domain (right) [119]

The geometry and input parameters of the SPT-100 are shown in Table 5.1.

Table 5.1: Geometry and Input Parameters of SPT-100

Outer radius	5.0 cm	B_{max}	160 G
Inner radius	3.5 cm	Propellant MFR (Xe)	4.9 mg/s
Channel length	4.0 cm	Discharge voltage	300 V
Length from exit to cathode	2.0 cm	Neutral velocity	200 m/s
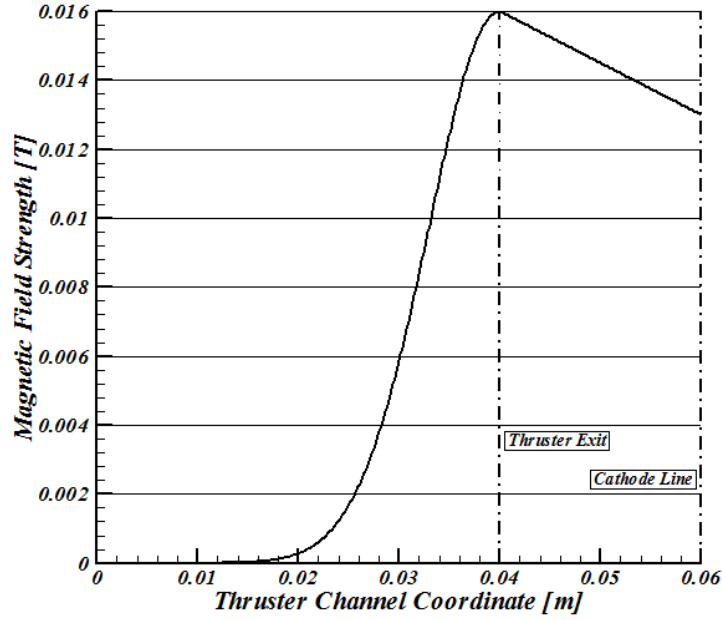
Figure 5.2: Magnetic Field Distribution [119]

Figure 5.2 shows the given magnetic field distribution for the SPT-100. The maximum magnetic field is located at the thruster channel exit line. The magnetic field distribution inside the channel is given in the analytical form as

$$B(z) = B_{max} \exp\left[-K\left(\frac{z}{L}-1\right)^2\right] \qquad (5.1)$$

where, K is the magnetic field shape coefficient. For the SPT-100, K has the value of 16. For the region outside the channel where a significant magnetic field still exists, the linear distribution is assumed as in Ref. [119].

5.1.2 Comparisons of the Performance Metrics

The developed tool can take input parameters such as those shown in Table 5.1. Note that the developed tool has a capability of analyzing the geometric variation such as outer and inner radius and channel length, which is not easily done by experiments.

The metrics to be compared are obtained from plasma macroscopic properties calculated by the developed tool. Those are the unknowns in the developed tool. The metrics are calculated as follows.

Specific impulse

$$I_{sp} = \frac{u_{i,c}}{g_e} \tag{5.2}$$

where, $u_{i,c}$ is the mean ion velocity at the cathode line, and g_e is gravitational acceleration at the Earth's surface.

Thrust

$$T = \dot{m}_{i,c} u_{i,c} \tag{5.3}$$

where, $\dot{m}_{i,c}$ is the ion mass flow rate at the cathode line.

Efficiency

$$\eta = \frac{T^2}{2\dot{m}P_d} \tag{5.4}$$

where, $\dot{m}$ is the given propellant mass flow rate, and P_d is the discharge power, which is then calculated as $P_d = V_d I_d$, where V_d is the discharge voltage. Although all the required

input powers are not included in Equation (5.4), the discharge power is taken as input power because most of power is used for discharge.

Discharge current

$$I_d = e n_e u_e \big|_m A \qquad (5.5)$$

where, $n_e u_e \big|_m$ is the electron flux at the matching point, and A is the thruster channel area. Although the discharge current can be calculated at any point using current continuity, it can be directly obtained at the matching point since the ion mean velocity is zero at the matching point.

The comparisons of the calculated performance metrics with the experimental data as well as with results of Ref. [119] are shown in Table 5.2.

Table 5.2: Comparisons of Calculated Metrics

Metric	Experiment	Ref. [119]	Developed Tool
I_{sp} [sec]	1600	1500 (-6%)	1728 (+8%)
Thrust [mN]	83	90.2 (+9%)	82 (-1%)
Efficiency [%]	50	60 (+20%)	49 (-2%)
I_d [A]	4.5	3.7 (-18%)	4.76 (+6%)
Calculation time ~ 22 seconds			

From Table 5.2, all the differences between calculated performance metrics and those from experiments are less than 10%, which is quite good accuracy. The calculated specific impulse shows the biggest difference and is 8% higher than the experimental result. This might be the result of neglecting ion-wall recombination and plume expansion loss.

The calculation time of 22 seconds indicates that the developed tool could be used as an analysis tool for HET to explore a large design space at a conceptual level of design.

5.1.3 Convergence Characteristics

The condition of convergence is checked with the relative changes of dependent variables between two consecutive iteration steps. The error convergence history is shown in Figure 5.3.
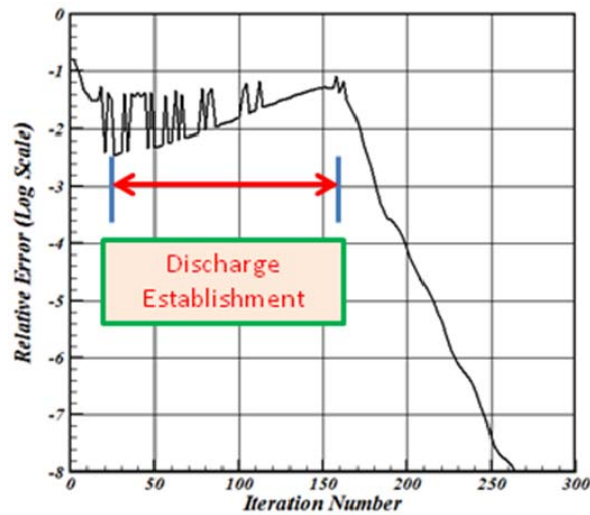
Figure 5.3: Error Convergence History

The initial half part of history shows oscillation and growth. Since the initial guess of electron temperature is quite low, it can be thought that the discharge is established during that part of the history. Once the pseudo-discharge is established, the convergence rate is rapid. The error order in log scale reaches -8 just in about 100 iterations. If this kind of convergence history is not observed, it is expected that the discharge fails and the discharge current and other performance metrics would be very low.

Figure 5.4 shows the convergence history of specific impulse and thrust. After discharge is established, these metrics reach almost constant values until convergence is achieved. The convergence characteristics of the performance metrics can be used in the case that actual error does not decrease further and exhibits oscillation. In this case, the

convergence history of the performance metrics can be used as a convergence criterion. This is usual treatment in CFD when the problem is highly nonlinear and unsteady. Since the HET exhibits a low frequency of discharge oscillation, it should be expected to have the case stated, where the convergence history of performance metrics should be used for the convergence criterion.
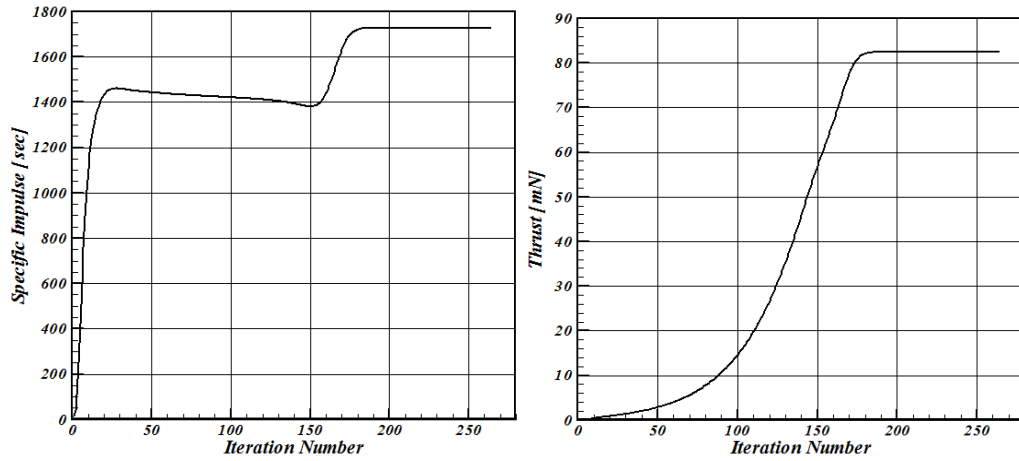
Figure 5.4: Convergence History of I_{sp} (left) and Thrust (right)

5.1.4 Plasma Structures

In this section, plasma structures which are calculated by the developed tool are given. Figure 5.5 shows the neutral number density (left) and plasma number density (right) distributions. It can be seen that many of neutrals are exhausted up to the thruster exit plane. The low values of neutral number density are observed outside the channel.

Plasma number density variation in the presheath is small and after the matching point the increase of plasma number density is quite significant. The peak value of plasma number density is found slightly outside the channel from the thruster exit, and then decreases toward the cathode line.
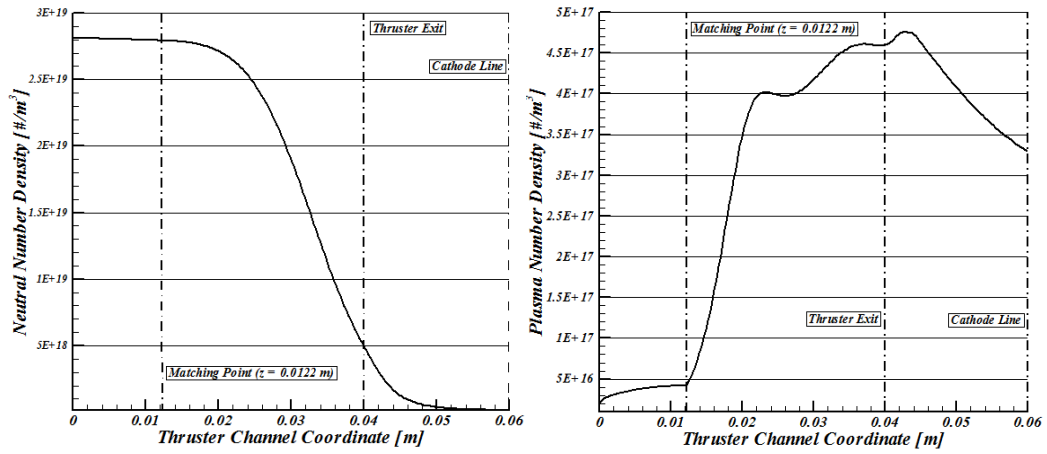
Figure 5.5: Neutral (left) and Plasma (right) Number Density Distributions

Figure 5.6 shows the electric potential (left) and electric field (right) distributions. The electric potential from the anode sheath edge to a portion of the ionization/acceleration region exhibits almost constant values. However the exact shape is convex centered at the matching point. Then it continues to decrease until the cathode line.

Electric field distribution shows that the electric field in the presheath region is negative which makes the ions flow backward and it has a peak value slightly inside the channel from the exit plane.
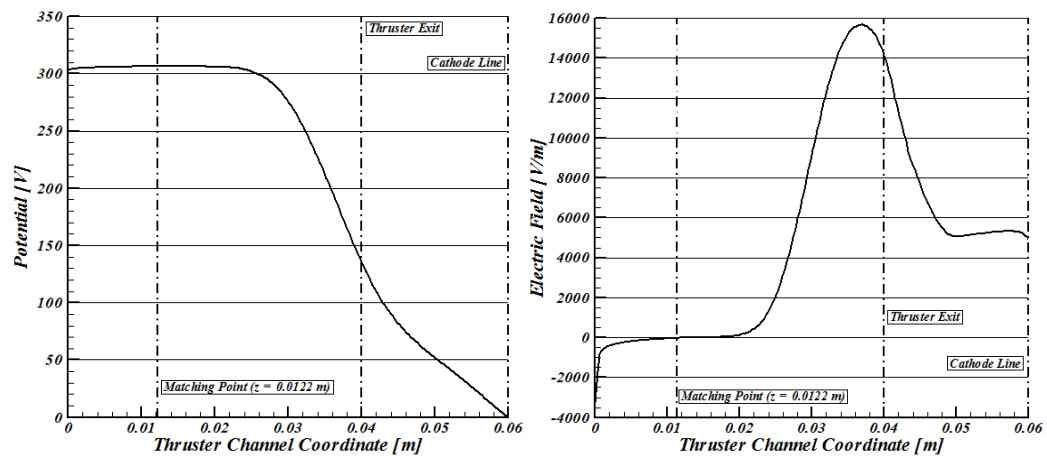
Figure 5.6: Electric Potential (left) and Electric Field (right) Distributions
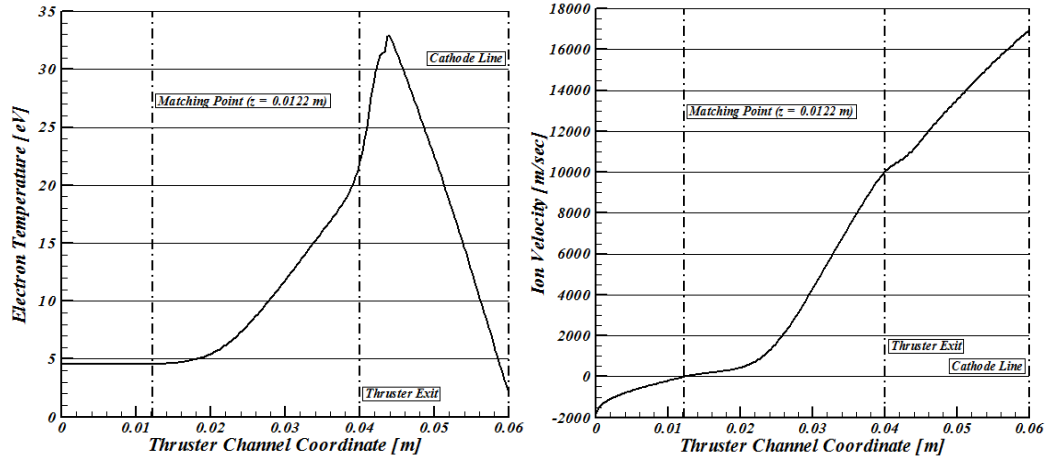
Figure 5.7: Electron Temperature (left) and Ion Mean Velocity (right) Distributions

Figure 5.7 shows the electron temperature (left) and ion mean velocity (right) distributions. The electron temperature has a peak value of about 33 eV slightly outside the channel from the exit line. The ion mean velocity distribution shows negative velocity in the presheath region. In the ionization/acceleration region, it increases due to the electric field.
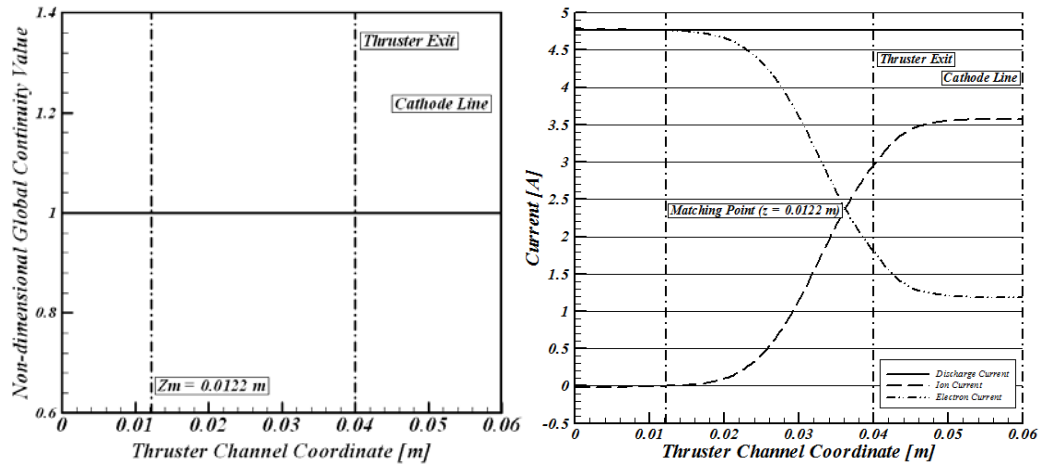
Figure 5.8: Global Continuity (left) and Current Continuity (right)

The global and current continuities are well satisfied for the whole domain as shown in Figure 5.8. The left figure in Figure 5.8 shows the non-dimensional value of the right-hand-side term in global continuity, which is 1. The right figure of Figure 5.8 also

shows the ion and electron current contributions throughout the domain. As expected, almost all the current near anode is carried by electrons. At the cathode line, the electron current still has a value over 1 A, which is the major reason for low total efficiency. The more the ion current at the cathode gains within the total discharge current, the higher the efficiency obtained. The ratio of ion current to discharge current is called acceleration efficiency. In order to have a higher efficiency and higher specific impulse HET, it is required to increase the acceleration efficiency, which is 0.75 in this case.

Figure 5.9 shows the ionization rate (left) and electron hall parameter (right) distributions. As also expected, the ionization rate has the peak value near the maximum magnetic field location. However, since the neutral number density also contributes the ionization rate, the position of peak ionization rate occurs before the location of maximum magnetic field, where the neutral number density is quite low. Electron Hall parameter has the value on the order of 100, which has been usually observed in the experiments.
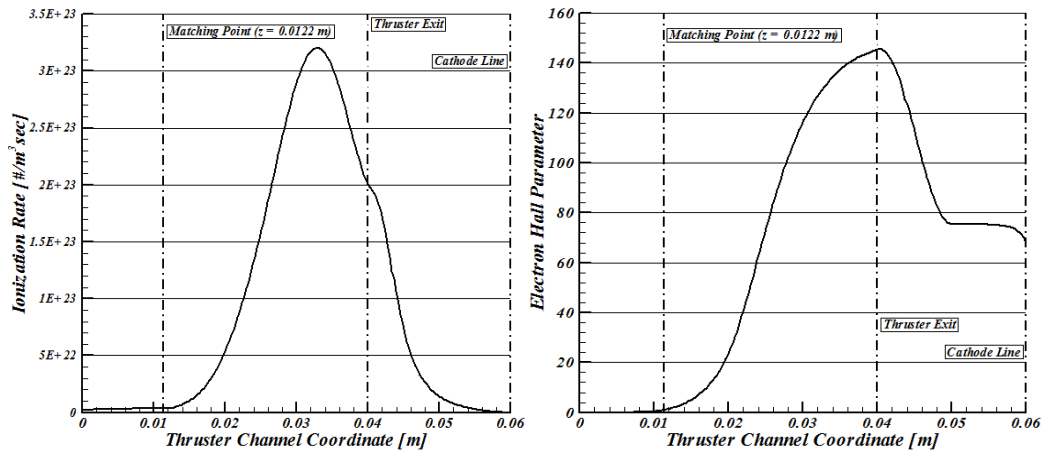
Figure 5.9: Ionization Rate (left) and Electron Hall Parameter (right) Distributions

5.2 Limitations of the Developed Tool

5.2.1 Accuracy of the Plasma Structures

Since two solutions with different assumptions are matched at the matching point, some plasma variables such as plasma number density and electron mean velocity show low accuracies around the matching point.

In Figure 5.10, first derivatives of plasma number density and electron mean velocity seem to be discontinuous at the matching point enclosed by a dotted circle. The division of the solution is necessary to ensure that the method is numerically robust and self-consistent and thus the sacrifice in accuracies of certain plasma variables around the matching point is acceptable. The effect of these discontinuities should not be significant because major performance metrics are given mostly by the plasma properties in the ionization/acceleration region and the plasma number density at the matching point is typically very low compared to that of the ionization/acceleration region. The overall behaviors of plasma number density and electron mean velocity are quite reasonable compared to previous work and experimental data and it does not violate any of continuity equations as seen in Figure 5.8
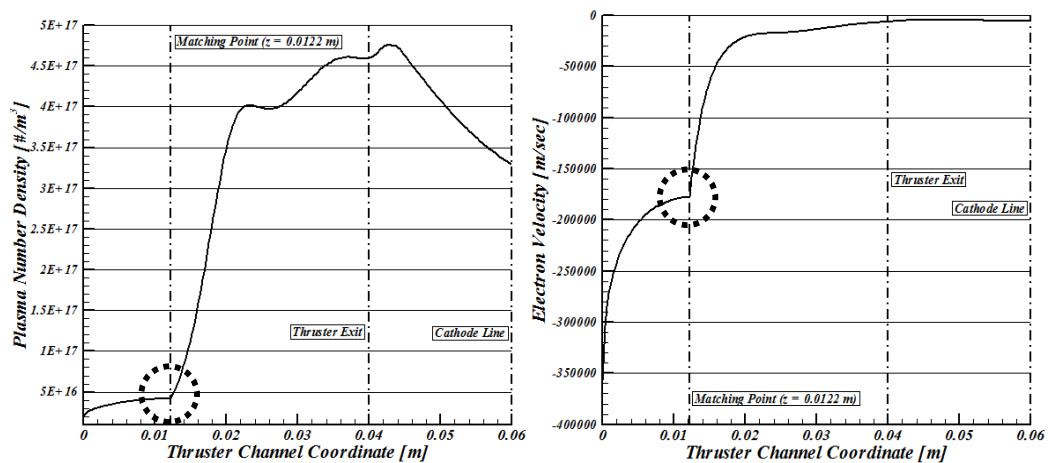
Figure 5.10: Plasma Number Density (left) and Electron Velocity (right) Distributions

5.2.2 Variation of Magnetic Field Distribution

The magnetic field is given in the analytical form as

$$B(z) = B_{max} \exp\left[-K\left(\frac{z}{L} - 1\right)^2 \right]$$

(5.6)

If K decreases, the magnetic field strength at the anode tends to increase as shown in Figure 5.11. For sufficiently small values of K, the developed tool does not converge. As K decreases, the electron temperature at the matching point calculated by solving the electron energy equation in the ionization/acceleration region tends to increase, which results in a decrease of the presheath region length. The decrease of the presheath region length with electron temperature at the plasma body is correct physics since a higher collision phenomenon shortens the collisionless presheath region. The solution tends to be that of a Thruster with Anode Layer (TAL) and the developed tool does not converge, since the presheath region collapses in a very thin region near anode, it cannot be solved in the macroscopic scale of the problem.
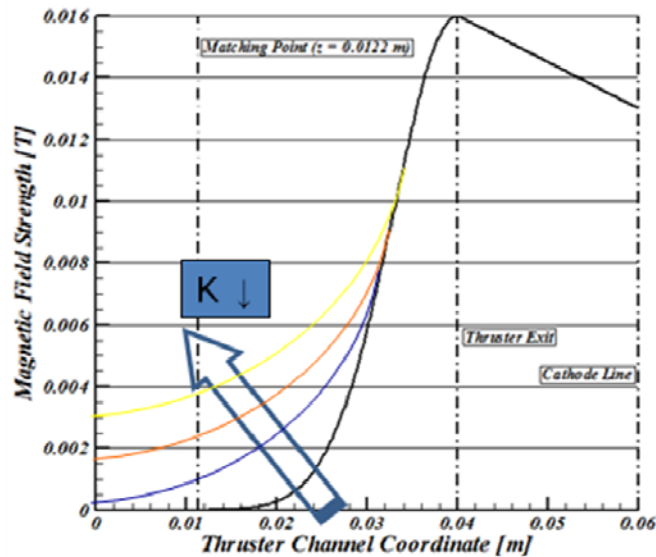
Figure 5.11: Variation of Magnetic Field Distribution with K

However, this should not be a problem since there is no reason why a large magnitude of magnetic field strength is required near the anode region. A large magnitude of magnetic field near the anode region might cause a large performance loss in such a way that a relatively large amount of generated ions near the anode have many chances to recombine at the side dielectric walls and return back to neutrals.

5.3 Validation at Other Operating Points of the SPT-100

5.3.1 Remarks on the Proposed Modeling of the Anomalous Coefficients

The anomalous coefficients for inside and outside the channel are calculated with the proposed formula given in Equation (4.38), and the main equation is repeated here.

$$\hat{\alpha}_{ano} = \hat{\alpha}_{ano,min}\left[1 - \exp\left\{A\left(\frac{V_d - 400}{400 - 150}\right)^2\right\}\right] + \hat{\alpha}_{ano,max}, \ where \ A = \log\left(1 + \frac{\hat{\alpha}_{ano,max} - \hat{\alpha}_{ano,min}}{\hat{\alpha}_{ano,min}}\right)$$

Ref. [107], where the equation above is derived, claims that the role of wall collision to electron cross field transport is minor and the Bohm diffusion effect should be doubled outside of the channel. This can be also partly justified from the experimental data of the electron mobility, as shown in Figure 5.12 [121].
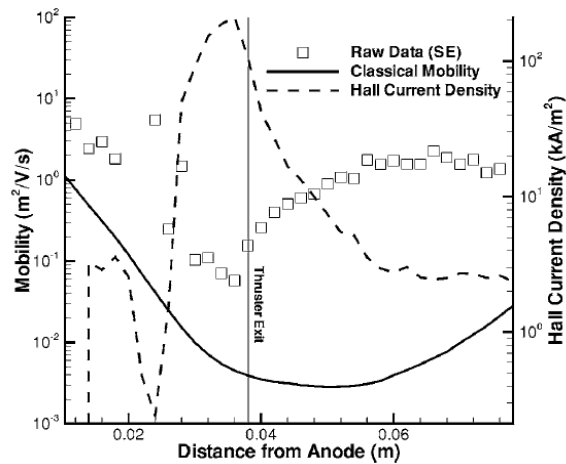
Figure 5.12: UM/AFRL P5 Centerline Properties [121]

Figure 5.12 shows that the difference between experimental mobility and classical mobility outside of the channel is far greater than the difference inside. In the current implementation, the anomalous coefficients are only a function of discharge voltage and those are fixed as $\hat{\alpha}_{ano,in} = 160$ and $\hat{\alpha}_{ano,out} = 80$ over 400 V. Furthermore, the equation is derived based on the experimental results only from the comparison with a 5 kW HET. In order to verify these simple relations, further validation is conducted with the variation of the anode propellant mass flow rate. The experimental data is taken from Table V of Ref. [16] since the lowest facility pressure was achieved in that experiment. The specific impulse and efficiency in the experimental data include the cathode mass flow rate. Therefore, the calculation of performance metrics should be expanded.

5.3.2 Redefinition of Performance Metrics

More thorough definitions for the performance metrics are given below.

Specific Impulse

Specific impulse is given in the same form of Equation (5.2). The total specific impulse incorporates cathode mass flow rate, the form of which will be given later.

Total power required

Total power required to sustain the discharge can be expressed as follows.

$$P_{tot} = P_d + P_{cath} + P_{mag} \tag{5.7}$$

where, P_d is the discharge power and it is the product of the discharge voltage and discharge current, P_{cath} is the power required to operate the cathode and it is usually less than 10% of P_d, although it varies with the cathode type used, and P_{mag} is the power

111

required to produce magnetic field and it would be zero if permanent magnets were to be used.

Anode Efficiency

Anode efficiency is expressed as

$$\eta_{ano} = \frac{T^2}{2\dot{m}_a P_d} \tag{5.8}$$

where, η_{ano} is the anode efficiency, and $\dot{m}_a$ is the anode propellant mass flow rate. The anode efficiency is a function of propellant utilization, ion beam divergence, ionization rate, and the amount of ion recombination. Thus, it can be separated into several efficiency terms characterizing each effect on the resultant anode efficiency. The thrust can be expanded by

$$T = \dot{m}_a u_i = \dot{m}_{i,c} u_{i,c} + \dot{m}_{n,c} u_{n,c} \approx \dot{m}_{i,c} u_{i,c} \tag{5.9}$$

where $\dot{m}_{i,c}$ and $\dot{m}_{n,c}$ are the ion and neutral mass flow rate at the cathode line, respectively. Since $\dot{m}_{n,c}$ is very small at the cathode line, the resultant expression in Equation (5.9) can be safely assumed. If the thrust expression in Equation (5.9) is substituted into Equation (5.8), the anode efficiency can be separated as

$$\eta_{ano} = \frac{\dot{m}_{i,c}^2 \frac{1}{2} u_{i,c}^2}{\dot{m}_n V_d I_d} = \frac{\dot{m}_{i,c}}{\dot{m}_n} \frac{I_b}{I_d} \frac{m_i}{e} \frac{\frac{1}{2} u_{i,c}^2}{V_d} = \eta_e \eta_a \eta_u \tag{5.10}$$

where $\dot{m}_n$ is the same value of $\dot{m}_a$ to emphasize that neutrals only contribute to this mass flow rate term, and I_b is the ion beam current at the cathode line. Note that the relation of

$\dot{m}_{i,c} = m_i \dot{n}_{i,c} = m_i \frac{n_{i,c}}{\Delta t} \frac{e}{e} = \frac{m_i I_b}{e}$ is applied in Equation (5.10). Three efficiency terms at the end of Equation (5.10) are defined in detail below.

112

1) Electrical efficiency, η_e

$$\eta_e = \frac{I_b}{I_d} \tag{5.11}$$

The electrical efficiency is a fraction of the ion beam current to total discharge current at the cathode line. If larger portion of discharge current is used to generate thrust while sustaining the discharge, the overall efficiency of the thruster would be high. Conversely, the electrical efficiency accounts for the minimum electron current necessary to sustain the discharge.

2) Acceleration efficiency (η_a)

$$\eta_a = \frac{\frac{1}{2} m_i u_{i,c}^2}{eV_d} \tag{5.12}$$

The acceleration efficiency is a measure of the mean kinetic energy gained by the ions with the given electrical energy. If all of the ions are generated at the anode and there is no bulk or wall recombination and plume divergence, this efficiency would be one by being accelerated under the maximum potential drop.

3) Propellant utilization efficiency (η_u)

This efficiency can be further expressed as the product of two efficiencies.

$$\eta_u = \frac{\dot{m}_{i,b} \; at \; the \; exit}{\dot{m}_n \; at \; the \; anode} = \eta_i \eta_b \tag{5.13}$$

where,

$$\eta_i \text{ (ionization efficiency)} = \frac{\dot{m}_{i,created}}{\dot{m}_n} \text{ (conversion rate to ion)}$$

$$\eta_b \text{ (beam efficiency)} = \frac{\dot{m}_{i,b}}{\dot{m}_{i,created}} \text{ (exit rate of ion)}$$

113

Based on the definitions above, the actual performance calculations in the developed tool are modified as follows.

Thrust

$$T = \dot{m}_{i,c} u_{i,c} + \dot{m}_{n,c} u_{n,c} \tag{5.14}$$

Anode Specific Impulse

$$I_{sp,ano} = \frac{T}{\dot{m}_a g_e} \tag{5.15}$$

Discharge Power

In the developed tool, the discharge power is only calculated.

$$P_d = I_d V_d \tag{5.16}$$

Anode Efficiency

In the developed tool, the anode efficiency and its components such as electrical, acceleration, and utilization efficiencies are calculated.

$$\eta_{ano} = \frac{T^2}{2\dot{m}_a P_d} \tag{5.17}$$

If the specific impulse and efficiency include the cathode mass flow rate, they are termed as total specific impulse and total efficiency, respectively. For these total quantities as well as total power, additional inputs are required such as

1) Percentage of $\dot{m}_c$ based on $\dot{m}_a$ (%) = pmc (percentage of mass flow rate at the cathode), where $\dot{m}_c$ is the cathode mass flow rate.

2) Percentage of P_{cath} based on P_d (%) = ppc (percentage of power consumed for the cathode)

3) Percentage of P_{mag} based on P_d (%) = ppm (percentage of power consumed for inner and outer electrical magnets)

So, if those inputs are provided, the following total quantities can be calculated.

1) Total specific impulse

$$I_{sp,tot} = \frac{T}{\dot{m}_{tot}g_e} = \frac{T}{(\dot{m}_a + \dot{m}_c)g_e} = \frac{T}{(1+0.01pmc)\dot{m}_a g_e} = \frac{I_{sp,ano}}{(1+0.01pmc)} \tag{5.18}$$

2) Total power

$$P_{tot} = P_d + P_{cath} + P_{mag} = P_d + 0.01(ppc + ppm)P_d = (1+0.01ppc+0.01ppm)P_d \tag{5.19}$$

3) Total efficiency

$$\eta_{tot} = \frac{T^2}{2\dot{m}_{tot}P_{tot}} = \frac{T^2}{(1+0.01pmc)(1+0.01ppc+0.01ppm)2\dot{m}_a P_d}$$
$$= \frac{\eta_{ano}}{(1+0.01pmc)(1+0.01ppc+0.01ppm)} \tag{5.20}$$

5.3.3 Validation with Fixed Anomalous Coefficients

The experimental data in Table V of Ref. [16] is shown in Table 5.3.

Table 5.3: Experimental Performance Data of the SPT-100 [16]

$\dot{m}_a$ [mg/s]	$I_{sp,tot}$ [s]	T [mN]	η_{tot}	I_d [A]	P_d [W]	$\dot{m}_c$ [mg/s]	pmc (%)
3.95	1520	64.4	0.457	3.49	1050	0.38	9.6
4.25	1550	70.1	0.470	3.76	1130	0.38	8.9
4.52	1560	75.1	0.479	4.00	1200	0.38	8.4
4.76	1590	80.0	0.487	4.26	1280	0.38	8.0
4.99	1610	84.9	0.498	4.49	1350	0.38	7.6
5.25	1630	90.1	0.505	4.75	1430	0.38	7.2

The power is taken as the discharge power, and accordingly, ppc and ppm are assumed to be 0. The discharge voltage is 301 V for all experiments, which corresponds to the anomalous coefficients based on Equation (4.38) of

$$\hat{\alpha}_{ano,in} = 152.351 \text{ and } \hat{\alpha}_{ano,out} = 76.176$$

The simulation results based on these anomalous coefficients with the geometry and parameters shown in Table 5.1 are shown in Figure 5.13. All computations are obtained with the same initial conditions. The error bars for the experimental results are based on Ref. [16]. The accuracy of the thrust stand and the flow rate is within both $\pm$ 1% error ranges. The error range of the discharge current is $\pm$ 1.1% at a discharge current of 4.5 A. Based on these error ranges, the errors of the specific impulse and the efficiency are estimated as $\pm$ 1.4% and $\pm$ 2.1%, respectively.
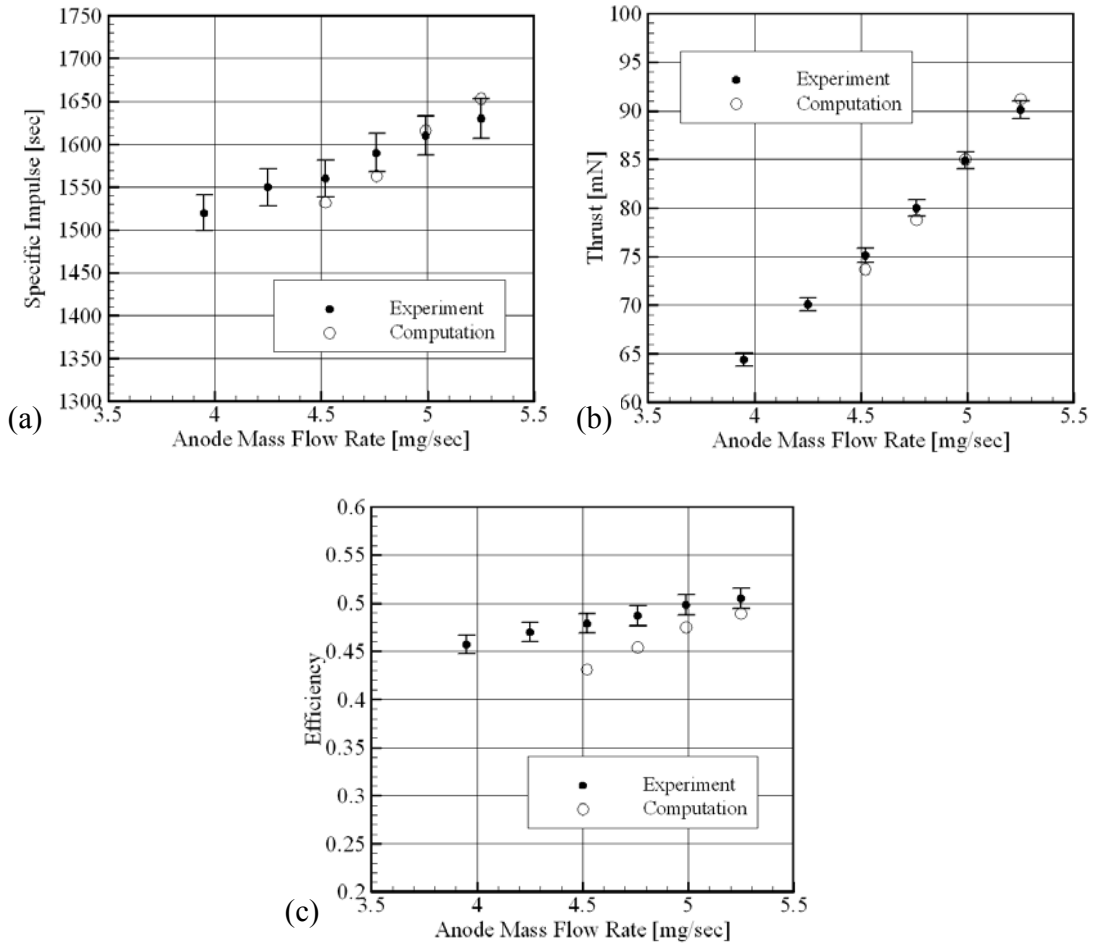
Figure 5.13: Validation results of the SPT-100 with the anode mass flow rate variation
(a) Specific impulse (b) Thrust, and (c) Efficiency.

Figure 5.13 shows that the anomalous coefficients based on the Equation (4.38) give good accuracies for the specific impulse and the thrust near the design operating point of the SPT-100. However, the efficiency is estimated at a slightly lower value. Furthermore, for the mass flow rates lower and higher than the design operating point, the results deviate from experimental data. Even worse, use of fixed anomalous coefficients could not produce solutions for the anode mass flow rates of 3.95 and 4.25 mg/s. This reveals that the anomalous coefficients should also be a function of other parameters such as the anode mass flow rate.

The anomalous diffusion cannot be solved with current 1-D macroscopic models, which requires tuning of the anomalous coefficients to match experimental data. Thus, this calls for further investigation of the characteristics of the anomalous coefficients under various thruster operating conditions as well as geometry variations. To this end, the anomalous coefficients are treated as free parameters and numerical explorations for the range of these coefficient values can be conducted to find the correct values which match experimental data.

5.3.4 Classification of Solutions Obtained from the Developed Tool

In order to conduct the numerical exploration for arbitrary variable ranges, there is a need to classify solutions obtained from the developed tool. Basically, this classification provides criteria for which input variable combination results in the failure of the thruster operation. Subsequently, performance envelope of the given thruster is expected to be determined.

The developed tool has a convergence criterion, i.e., if the normalized sum of relative changes in plasma properties (variable name in the code: ERRORL) is less than

the pre-specified tolerance (variable name in the code: CONV), which is usually a very small value, for example, 1.e-8; then the tool terminates the calculation and the plasma properties at that moment are taken as the solution. The tool also employs the maximum iteration number (variable name in the code: ITMAX) for the case of non-convergent but oscillatory solution.

1) Case 1: ERRORL ≤ CONV – Success

The solution procedure is considered as being successful and the converged solution is obtained. Convergence histories of the usual error and the specific impulse are shown in Figure 5.3 and Figure 5.4

2) Case 2: ERRORL > CONV & ITMAX reached – Success

In this case, the solution procedure is also considered as being successful, but, the error history exhibits oscillatory behavior. Although the relative error does not reach the pre-specified tolerance, CONV, the performance parameters show convergent behavior. These characteristics are shown in Figure 5.14.
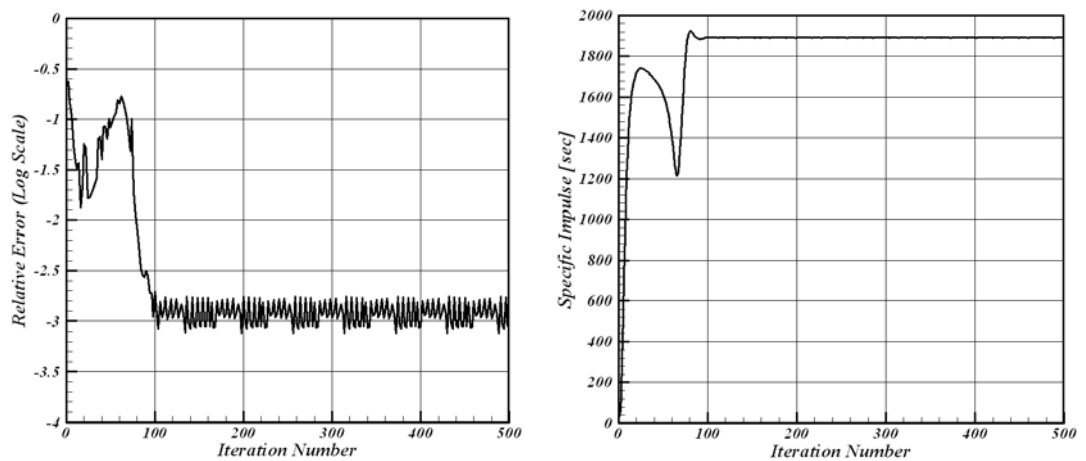
Figure 5.14. Error Behavior (left) and Specific Impulse Convergent Behavior (right)

118

It is a common practice to take it as a convergent solution in the CFD society in case the performance parameters show convergent behaviors even if some plasma parameters in some computational cells show oscillatory behaviors. However, in this case, it is required to take averages on the values of performance parameters during some last iteration steps, for example, about 100 iteration steps.

3) Case 3: Low Plasma Number Density at the Matching Point – Fail

In the section 4.3.7, the plasma number density is updated at each iteration step by means of Equation (4.43). The plasma number density at the matching point is first guessed at a low value, for example, 10^{16} #/ m^3. If the consecutive updates during initial iteration steps yield values lower than the first guessed value, two cases are observed. First, it decreases initially and then increases over the first guessed value. The consequence of this process results in Case 1 or Case 2, which is a successful solution. Second, it keeps decreasing and reaches the negative value. Thus, the tool cannot proceed further and produce no performance outputs. This is considered as a failure case. The reason of this seems to be due to very low propellant mass flow rate, not enough discharge voltage, or insufficient electron diffusion.

4) Case 4: Presheath Region Length < Length of One Grid Cell – Fail

If the calculated presheath region length during iterations is less than the length of one computational cell, the tool also cannot yield any performance output. The reason of this is that the magnetic field in the region near the anode is relatively too high. As explained in the section 5.2.2, solutions tend to be that of the TAL as the presheath region collapses in a very thin region near the anode, which cannot be solved by the current tool.

This case is actually not a failure case. The developed tool simply cannot recognize a noticeable presheath region in the macroscopic scale. However, in this research scope, the noticeable presheath existence in the HETs should be guaranteed. The magnetic field profile should have sufficiently low radial magnetic field strength in the region near the anode. Because the magnetic field profile may be constructed in this way in the view of design, this case is classified as a failure case to avoid a large magnetic field strength near the anode region.

5) Case 5: Positive Electron Mean Velocity at the Cathode – Fail

In this case, the electron mean velocity at the cathode is positive during iteration steps, which means that electrons exit from the thruster. If this happens, the electron temperature in the region near the cathode will be negative, which prevent the tool from proceeding to the solution. There are several possibilities for this occurrence. First, the thruster might require more voltage difference between the anode and the cathode, since the electric potential profile exhibits decreasing and increasing behavior near the cathode. Second, electron mobility might not be enough due to low electron temperature.

6) Case 6: Presheath Region Length > Thruster Device Length – Fail

Basically, the reason seems to be similar to those for the Case 5. Particularly, the fact that electron temperature at the matching point might be too low (cold plasma) causes this failure.

Based on observations of many numerical experiments on the failure cases, Case 3 is the most dominant factor, which clearly indicates that certain input combinations cannot achieve discharge phenomenon for the given thruster. Case 3 through Case 6 stops

the solution procedure. Because these are occurring during the iteration steps, it should be checked whether the exact causes of failure cases are physical or numerical. This requires intensive validation with a variety of existing thrusters.

5.3.5 Construction of Design of Experiment (DOE) Environment

In order to investigate the effects of the anomalous coefficient variation, the environment of design of experiments is created using ModelCenter^{TM}. Figure 5.15 shows the created environment. The left figure is the component tree view, which includes inputs and outputs for each component. The right figure shows actual linkage between components. The "hall1d" component is an actual performance calculation module, which corresponds to the developed tool. Inputs are information on propellant, power, magnetic field profile, geometry, parameters for computation, and other options. Outputs are performance, matching point properties, continuity check, maximum values, and so forth.

The "WidthDelB" component is a simple one where the outer radius is calculated with the given inner radius and the channel width, and maximum magnetic field strength is obtained with the given cathode magnetic field strength and the difference between them. This component is required because the "hall1d" module takes the inner radius and the maximum magnetic field strength as inputs. This component is also necessary to have the channel width and the magnetic field strength difference between the channel exit and the cathode as variables in the design space exploration, which provides the more square-like design space for these variables than using the outer radius, the maximum magnetic field strength, and constraints regarding the inner radius and the cathode magnetic field. The "PerfDetail" component is another simple one where the total performance

properties are calculated with the inputs of pmc, ppc, and ppm, which are explained in the section 5.3.2, and the outputs of anode specific impulse, discharge power, and anode efficiency are calculated from the "hall1d" component.
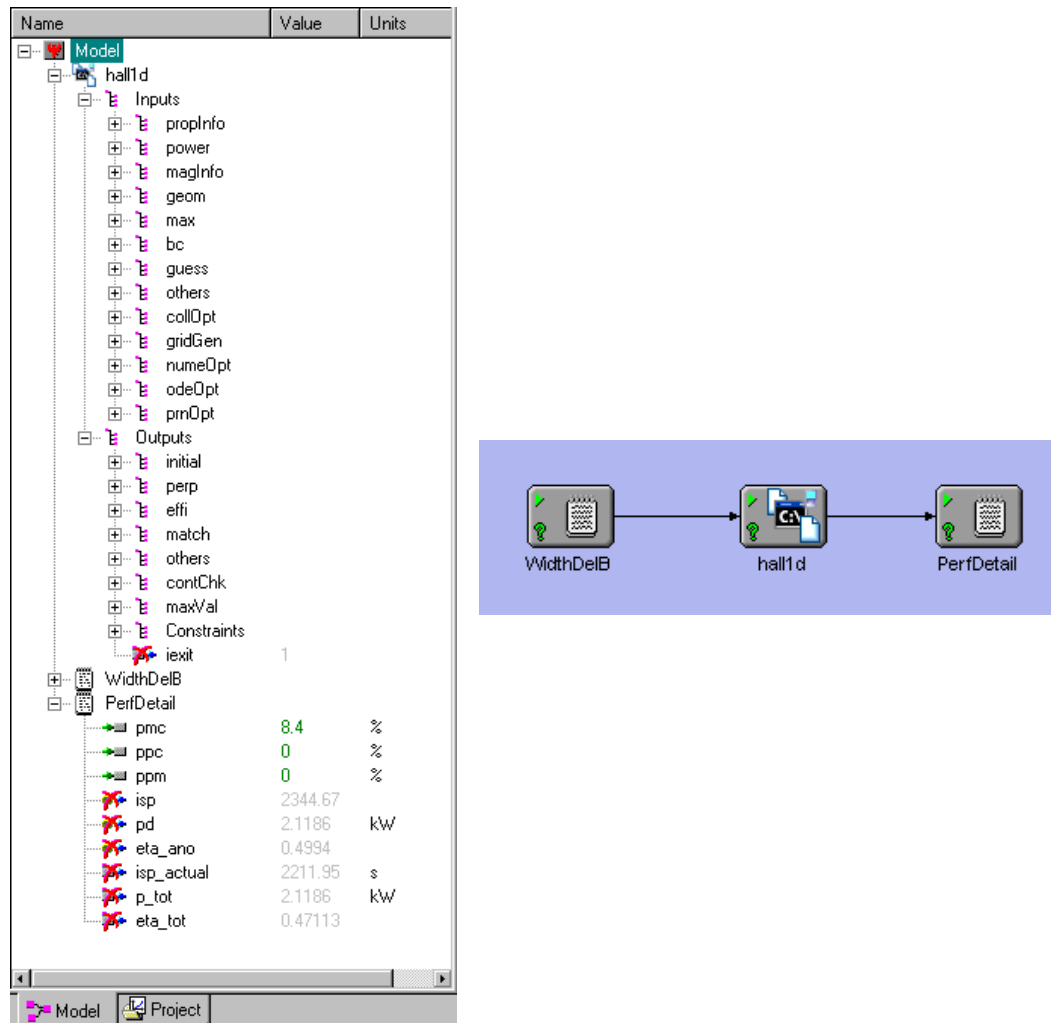
Figure 5.15. Design of Experiments Environment
Component Tree View (left), Component Model Linkage (right)

5.3.6 Numerical Exploration for the Ranges of the Anomalous Coefficients

The specified ranges of the anomalous coefficients are explored by numerical experimentations. Numerical exploration for the anomalous coefficient variation is basically the same as investigating the electron diffusion effects in the

ionization/acceleration region. From the discussion on the proposed method for the anomalous coefficients in Section 4.3.6, the lower bound and the upper bound of $\hat{\alpha}_{ano,in}$ are taken as 100 and 160, respectively. For $\hat{\alpha}_{ano,out}$, 50 and 80 are taken as the lower and upper bounds, respectively. In order to conduct numerical experiments, 6 level full factorial design is used to create an experiment table, which results in a total of 36 runs. This numerical experimentation is conducted in the created environment. Each numerical exploration is performed for each anode mass flow rate shown in Table 5.3. The results are then input to the JMP^{TM} software for statistical analysis. The effects of the anomalous coefficients on performance parameters can be derived through regression testing. The resultant regression coefficients, *t*-ratios, and *p*-values have statistical significance of each anomalous coefficient on each response. In this case, the standard least square method is used to create response surface models.

Figure 5.16 contains grids to visualize the success/fail cases of the solutions as well as the probability of success for each mass flow rate case based on the classification given in Section 5.3.4. As the mass flow rate decreases, more failed cases are observed. In general, the developed tool can produce solutions at higher values of the mass flow rate for the entire range of the anomalous coefficients. In reality, as the mass flow rate increases, the maximum electron temperature would also increase. Thus, it could start to cause thermal and structural problems in the thruster. It can be also inferred from Figure 5.16 that the higher electron diffusion is required for the thruster to work in case of lower values of the anode mass flow rate, which indicates that if the electron diffusion were not enough, the discharge could not be established.

123
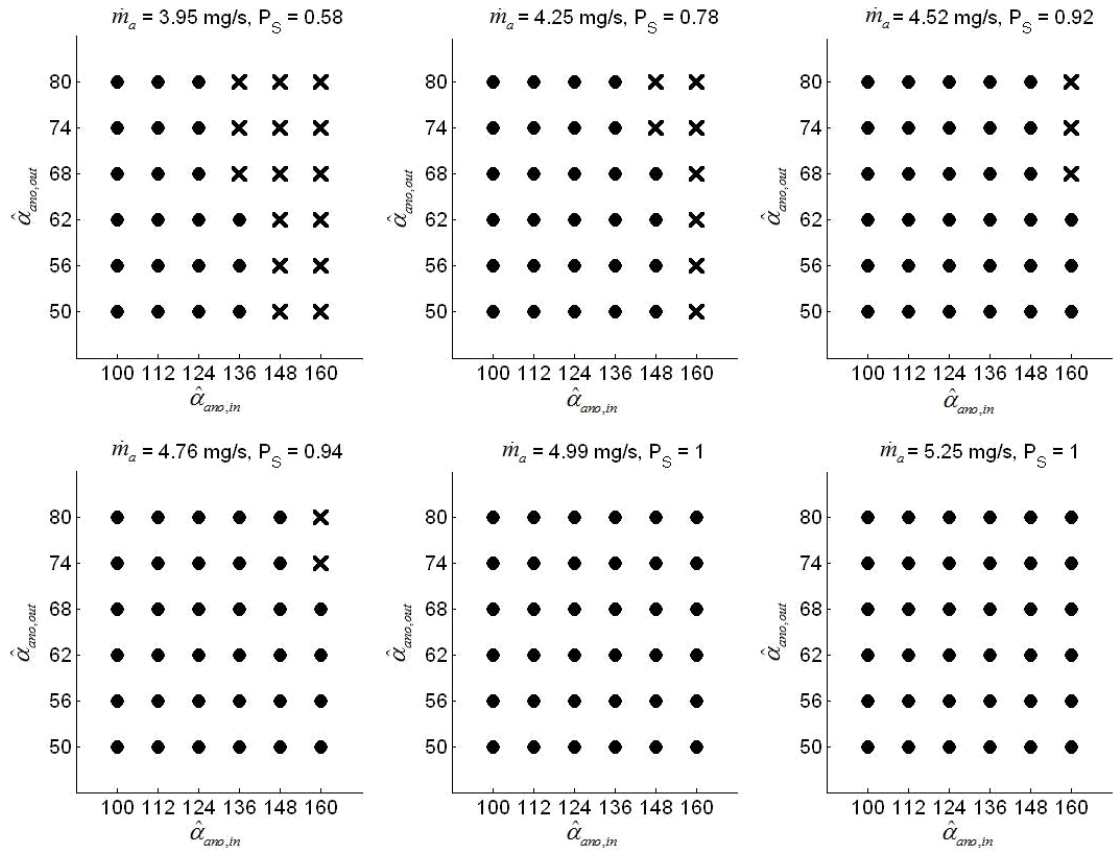
Figure 5.16: Visualization of Solution Success(Dot)/Fail(Cross) and Success Probability ($\hat{\alpha}_{ano,in}$ and $\hat{\alpha}_{ano,out}$ – inverses of the anomalous coefficient inside and outside the channel, respectively)

Let's investigate the regression results of the anode mass flow rate of 5.25 mg/s. The summary of fit for the thrust is given in Table 5.4. An excellent goodness of fit is obtained. The R^2 value is 0.9987, which almost gives a perfect regression. Figure 5.17 also shows that the generated response surface can predict the actual thrust values very well and corresponding errors are very small based on the thrust range.

Table 5.4: Summary of Fit for Thrust

R^2	0.9987	RMSE	0.1321
R^2_{adj}	0.9984	Mean of Response	95.26
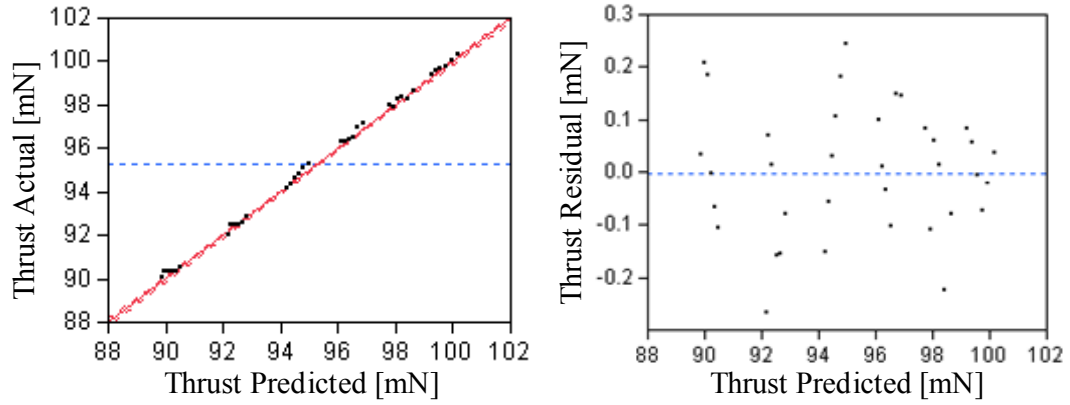
Figure 5.17: Actual by Predicted (left) and Residual by Predicted (right) Plots for Thrust

Table 5.5 shows the parameter estimates and the Pareto plot. The anomalous coefficient inside the channel plays a dominant role for thrust variation. Although the effect of the square term of the inside anomalous coefficient is 10^{-3} times less, it is statistically significant based on the p-value (Prob>|t|). The total specific impulse shows the same trend as the thrust.

Table 5.5: Parameter Estimates and Associated Pareto Plot for Thrust

Term	Estimate	t Ratio	Prob>|t|	Pareto Plot
$\hat{\alpha}_{ano,in}$	-0.1585	-147.5	<.0001*	
$\hat{\alpha}_{ano,out}$	-0.0256	-11.9	<.0001*	
$(\hat{\alpha}_{ano,in}-130)\times(\hat{\alpha}_{ano,in}-130)$	-0.0007	-11.3	<.0001*	
$(\hat{\alpha}_{ano,in}-130)\times(\hat{\alpha}_{ano,out}-65)$	0.00019	1.9	0.0725	
$(\hat{\alpha}_{ano,out}-65)\times(\hat{\alpha}_{ano,out}-65)$	0.00022	0.9	0.3698	

The anomalous coefficients are expected to have a large influence on the discharge current because they basically control the electron cross field transport and accordingly the axial current as seen in Table 5.6. All terms are statistically significant. The total efficiency shows more interesting features. The goodness of fit is not as good as those of other responses as seen in Table 5.7 and Figure 5.18, although it still shows a high R^2 value.

Table 5.6: Parameter Estimates and Associated Pareto Plot for Discharge Current

Term	Estimate	t Ratio	Prob>|t|	Pareto Plot
$\hat{\alpha}_{ano,in}$	-0.0180	-297.0	<.0001*	
$\hat{\alpha}_{ano,out}$	-0.0072	-59.6	<.0001*	
$(\hat{\alpha}_{ano,in}-130)\times(\hat{\alpha}_{ano,in}-130)$	0.00008	24.5	<.0001*	
$(\hat{\alpha}_{ano,in}-130)\times(\hat{\alpha}_{ano,out}-65)$	0.00010	18.2	<.0001*	
$(\hat{\alpha}_{ano,out}-65)\times(\hat{\alpha}_{ano,out}-65)$	4.108e-5	3.0	0.0058*	

Table 5.7: Summary of Fit for Total Efficiency

R^2	0.9824	RMSE	0.0009
R^2_{adj}	0.9795	Mean of Response	0.4897

The trend of the statistical significance of parameters for the total efficiency is much different from others as seen in Table 5.8. The square term of $\hat{\alpha}_{ano,in}$ has the highest absolute t-ratio value. However, all of the t-ratio values have a similar order of magnitude except for the square term of $\hat{\alpha}_{ano,out}$. It can be implied that first the anomalous coefficients alone are not good predictors for the total efficiency. Second, the higher order or some nonlinear terms may be incorporated into the regression model. Third, the total efficiency should be expressed by other internal parameters as well.
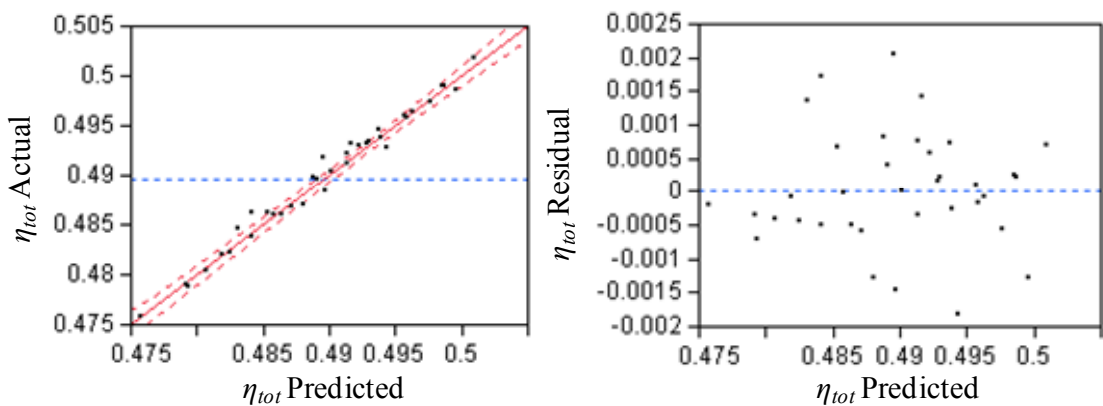
Figure 5.18: Actual by Predicted (left) and Residual by Predicted (right) Plots
for Total Efficiency

Table 5.8: Parameter Estimates and Associated Pareto Plot for Total Efficiency

Term	Estimate	t Ratio	Prob>|t|	Pareto Plot
$(\hat{\alpha}_{ano,in}-130)\times(\hat{\alpha}_{ano,in}-130)$	-1.335e-5	-31.2	<.0001*	
$\hat{\alpha}_{ano,out}$	0.00037	24.9	<.0001*	
$(\hat{\alpha}_{ano,in}-130)\times(\hat{\alpha}_{ano,out}-65)$	-5.867e-6	-8.0	<.0001*	
$\hat{\alpha}_{ano,in}$	-2.854e-5	-3.8	0.0006*	
$(\hat{\alpha}_{ano,out}-65)\times(\hat{\alpha}_{ano,out}-65)$	-8.02e-7	-0.5	0.6426	

Nonetheless, because the goodness of fit for the total efficiency is still acceptable, it can be used to find the values of the best possible anomalous coefficients which can closely match the experimental results. Before getting into this work, it is worth investigating the behavior of each response in the range of the anomalous coefficients. Figure 5.19 shows the prediction profiler for the case of $\dot{m}_a = 5.25\,mg/s$. The profiler is generated based on the regression model in the range of each anomalous coefficient. Thrust, discharge current, and total specific impulse show the same trends such that as $\hat{\alpha}_{ano,in}$ and $\hat{\alpha}_{ano,out}$ increases, they decrease. In addition, it can be easily identified that $\hat{\alpha}_{ano,in}$ has more of an impact on those responses than $\hat{\alpha}_{ano,out}$. The magnitude of electron diffusion is favorable to the thrust and the total specific impulse. The discharge current is simply the result of electron diffusion. The increase of discharge current results in a total power increase. Therefore, there should be a trade-off between performance and power requirements, i.e., the thrust to power ratio.

The impacts of the anomalous coefficients on the total efficiency are quite different from other responses. First of all, the impact of $\hat{\alpha}_{ano,out}$ is opposite, i.e., as $\hat{\alpha}_{ano,out}$ increases, the total efficiency also increases. Furthermore, variation of the total efficiency with $\hat{\alpha}_{ano,in}$ shows a quadratic shape. This indicates that there should be an

optimal magnitude of electron diffusion for this case. The reason of this phenomenon can be explained by examining the profiler for the anode efficiency and its component efficiencies.
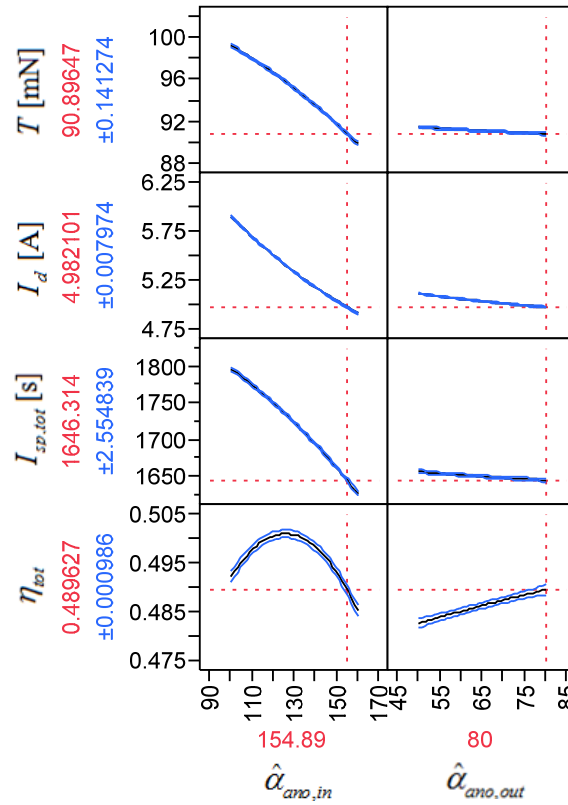
Figure 5.19: Prediction Profiler ($\dot{m}_a = 5.25\,mg\,/\,s$)

Figure 5.20 shows the prediction profiler for the anode efficiency and two of three component efficiencies as defined in Section 4.3.2. The utilization efficiency does not have much variation and it gives the value close to 1 for the most cases. As seen in Figure 5.20, the effects of the anomalous coefficients on the electrical and acceleration efficiencies are exactly opposite, which causes the anode efficiency to have a quadratic profile.

128
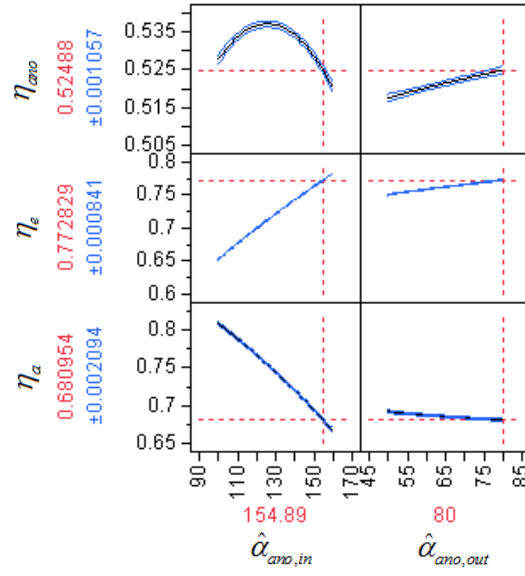
Figure 5.20: Prediction Profiler for Efficiencies ($\dot{m}_a = 5.25 \, mg/s$)

The increase of the electrical efficiency with increasing anomalous coefficients indicates that if the amount of electron diffusion increases, the ion beam current fraction of the discharge current decreases. However, the ions in this case gains more mean kinetic energy at the given electrical energy, which results in an increase of the acceleration efficiency. This might be due to the high electron current ionizing more neutrals at the relatively closer locations to the anode. As a result, the optimal efficiency exists based on the trade-off between these two component efficiencies in view of the electron axial diffusion. Thus, in order for the future HETs to have higher efficiencies, a trade-off between these efficiencies might be a key.

5.3.7 Validation with Optimum Anomalous Coefficients

The response surface equations obtained in Section 5.3.6 can be used to find the values of the anomalous coefficients closely matching the experimental data. In order to find these anomalous coefficients, an optimization strategy is required. The optimization performance index should be the difference between the values from the response surface

equations and the experimental values, which can be expressed as the sum of square differences. Thrust, discharge current, total specific impulse, and total efficiency are taken as the required responses to be matched for this purpose.

Although a rigorous optimization routine may be utilized, the desirability function in the prediction profiler of the JMP^{TM} is used. This is acceptable because the optimization results should be checked with results of the actual tool. The prediction profiler provides a functionality of maximizing desirability based on the given objective of matching the target values. Furthermore, it can provide the visual environment for the variation of the desirability of each response when values of the anomalous coefficients are varied.

Figure 5.21 shows the prediction profiler with the desirability function. The last column of graph matrix is the desirability functions for each response. The rectangles in the desirability graphs indicate target values that need to be matched. The total efficiency shows relatively large deviations from the experimental results for the fixed anomalous coefficient case as shown in Figure 5.13. It is also hard to closely match the experimental data for the total efficiency. When attempting to match the total efficiency, the other three responses start to deviate from the experimental data. Furthermore, the maximum value of the current regression model is lower than that of the experimental data. Thus, the optimization strategy is such that the reasonable values of the anomalous coefficients are obtained by matching the other three responses in their experimental error ranges while enforcing the total efficiency value as close to the experimental value as possible.
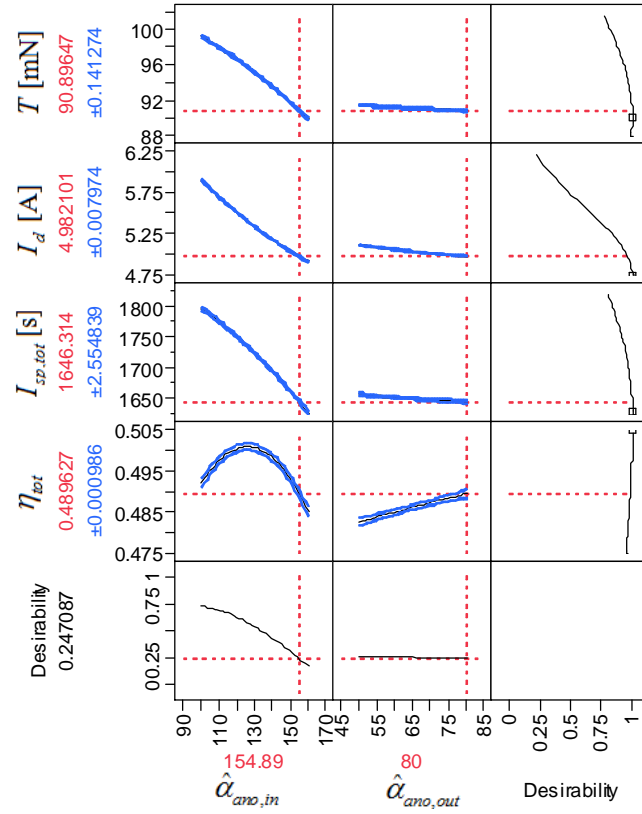
Figure 5.21: Prediction Profiler and Desirability Function ($\dot{m}_a = 5.25\,mg/s$)

The optimization is conducted for all of the anode mass flow rate cases. The results are shown in Table 5.9. Note that the developed tool can also produce solutions for the anode mass flow rates of 3.95 and 4.52 mg/s, which could not be obtained with the fixed values of the anomalous coefficients. This is due to the increase of axial electron diffusion. As seen in Table 5.9, the cathode flow fractions are decreased in the experiments as the anode mass flow rates are increased.

Total specific impulse, thrust, and total efficiency comparisons are also shown in Figure 5.22. Utilizing the optimization strategy yields very accurate predictions for the total specific impulse and the thrust. However, the prediction of the total efficiency still produces a little lower value than the experimental data for all of the anode mass flow rate cases. Nonetheless, it can be concluded that the use of the optimum anomalous

131

coefficients results in successful validation results for all validation points as well as for the cases of low propellant mass flow rate.

Table 5.9: Comparison Results with Fixed and Optimum $\hat{\alpha}_{ano,in\ and\ out}$

	$\dot{m}_a$ [mg/s]	I_{sp} [s]	T [mN]	η	I_d [A]	P_d [W]	pmc[%]	$\hat{\alpha}_{ano,in}$	$\hat{\alpha}_{ano,out}$
Exp.		1520	64.4	0.457	3.49	1050		-	-
Fix.	3.95	Case 5 Failure[*]					9.6	152.35	76.17
Opt.		1528	64.9	0.418	3.86	1164		127.00	80.00
Exp.		1550	70.1	0.470	3.76	1130		-	-
Fix.	4.25	Case 3 Failure[*]					8.9	152.35	76.17
Opt.		1547	70.2	0.430	4.11	1238		136.56	80.00
Exp.		1560	75.1	0.479	4.00	1200		-	-
Fix.	4.52	1532	73.7	0.431	4.27	1285	8.4	152.35	76.17
Opt.		1577	75.8	0.446	4.37	1315		144.22	80.00
Exp.		1590	80.0	0.487	4.26	1280		-	-
Fix.	4.76	1563	78.8	0.454	4.42	1332	8.0	152.35	76.17
Opt.		1594	80.4	0.464	4.50	1355		146.00	80.00
Exp.		1610	84.9	0.498	4.49	1350		-	-
Fix.	4.99	1616	85.0	0.475	4.72	1421	7.6	152.35	76.17
Opt.		1623	85.5	0.478	4.73	1424		150.44	80.00
Exp.		1630	90.1	0.505	4.75	1430		-	-
Fix.	5.25	1653	91.2	0.489	5.02	1512	7.2	152.35	76.17
Opt.		1645	90.8	0.489	4.97	1498		154.89	80.00

[*]: Refer to Section 5.3.4

(a)   (b)
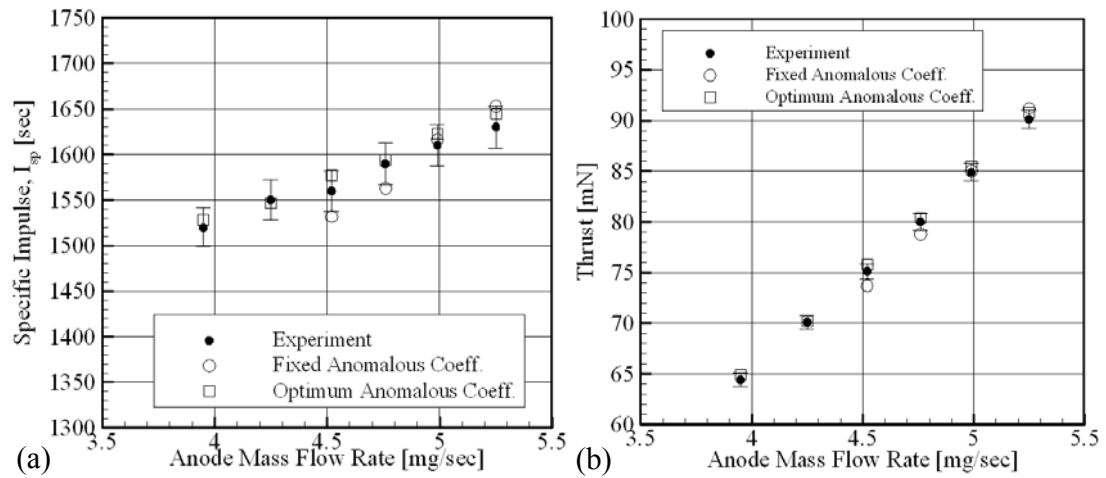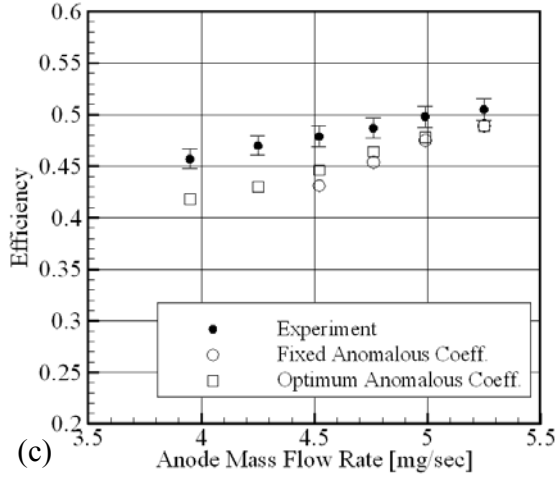
Figure 5.22: Comparisons of Experiments, Fixed and Optimum Anomalous Coefficients (a)Total Specific Impulse (b) Thrust, and (c) Total Efficiency.

An interesting fact is that $\hat{\alpha}_{ano,in}$ increases as the anode propellant mass flow rate increases, while $\hat{\alpha}_{ano,out}$ does not have much impact on the performance parameters. In other words, the anomalous diffusion may be increased as the anode mass flow rate is decreased. The reason for this might be the effect of the cathode propellant mass flow rate fraction. This can be clearly seen in Figure 5.23. The cathode flow rate fraction increases as the anode propellant mass flow rate is decreased, while $\hat{\alpha}_{ano,in}$ is increased. It seems that the anomalous coefficient inside the channel and the cathode mass flow rate fraction are positively correlated.

In view of the actual experiments where the cathode mass flow rate is fixed as $0.38\,mg\,/\,s$ for all cases, it is plausible that this fixed cathode mass flow rate was given based on the lowest anode mass flow rate operation in the experiments with an intention to establish and sustain thruster discharge at the low neutral number density operation. It can be subsequently inferred that the increase of the cathode mass flow rate fraction might cause a higher anomalous diffusion effect.

133
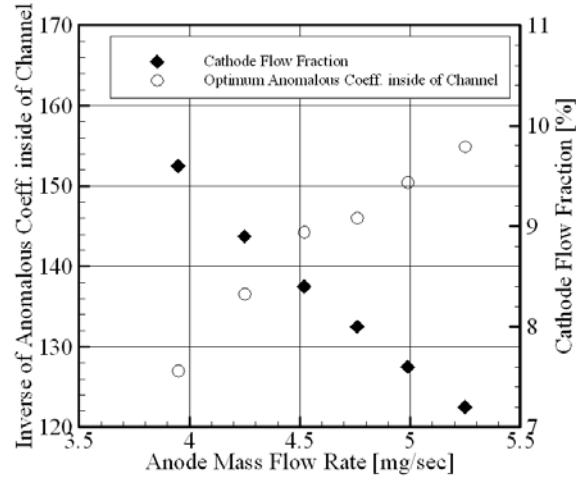
Figure 5.23: Variation of $\hat{\alpha}_{ano,in}$ and Cathode Flow Fraction with Anode Mass Flow Rate

5.4 Pseudo-Validation with the High Power Class HETs

In this section, the developed tool is validated with the experimental data of the high power class HETs. The term "Pseudo" is used because the actual radial magnetic field distribution cannot be obtained due to restrictions imposed by the International Traffic in Arms Regulations (ITAR). The detailed explanation on the pseudo-validation will be given in the following sub-section.

5.4.1 Validation with the T-220 Hall Effect Thruster

As the available power of an on-board spacecraft increases, high power, thrust, and specific impulse HETs become of interest for the reduction of launch vehicle size and application expansion of the HETs to new space missions such as orbit insertion and even primary propulsion in space [122]. NASA launched a high power Hall thruster program under the Advanced Space Transportation Program. The T-220 was designed, built, and tested as one of these efforts led by NASA Glenn Research Center (GRC) [123]. The T-

220 shown in Figure 5.24 is a 10 kW HET and its outer diameter is 220 mm as identified by its name.
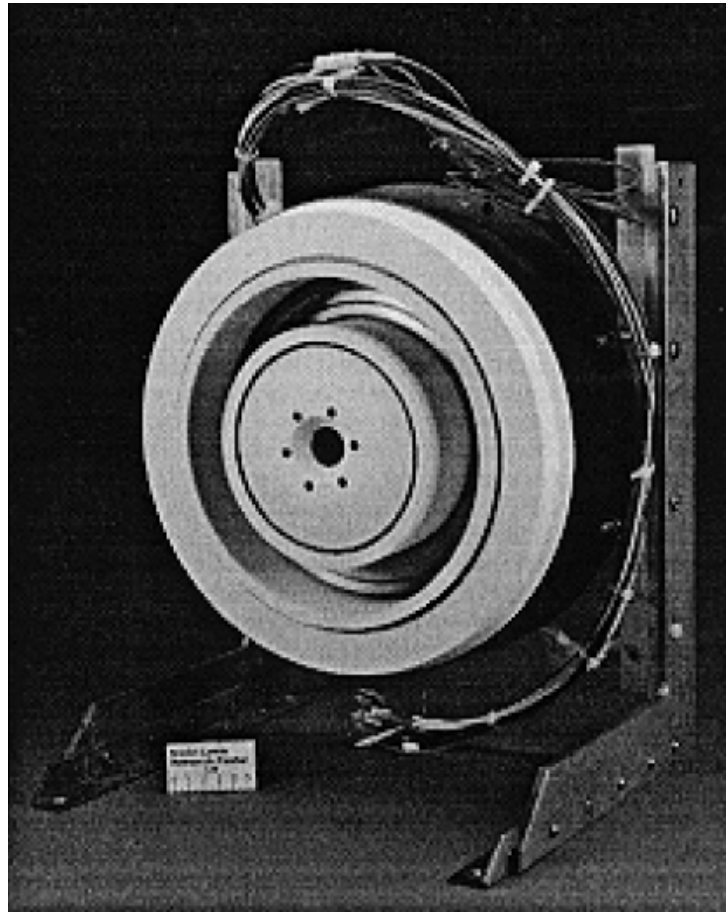
Figure 5.24: T-220 Hall Effect Thruster [124]

The detailed operating conditions and geometry found from literature are summarized in Table 5.10 [123].

Table 5.10: Operation Conditions and Geometry of the T-220

	$\dot{m}_a$ [mg/s]	V_d [V]	Geometry [cm]				
			L	R_1	R_2	W	L_{cath}
Design Point	20	500	5	7.8	11	3.2	4
Range	15.7 ~ 22.1	300 ~ 500					

In order to validate the developed tool with experimental data of the T-220, the radial magnetic field distribution is required. Although it is not available from the literature due to the ITAR Regulations, if the DOE is utilized as done in the previous section, the approximate radial magnetic field distribution can be obtained. The approach is a form of a reverse engineering process and the process can be generalized for other HETs as well. This is the reason why the process is called "Pseudo-Validation."

It is evident that pseudo-validation necessarily increases the number of numerical experiments because parameters characterizing the radial magnetic field distribution should be incorporated in the DOE. The radial magnetic field distribution along the thruster axial coordinate up to the cathode can be completely determined by the three parameters such as B_{max}, B_{cath}, and magnetic field shape coefficient inside the channel which is denoted by K. B_{max} and K completely determine the distribution inside the channel by Equation (5.1). B_{max} and B_{cath} also determine the distribution outside the channel by the assumption of linear distribution as explained in Section 5.1.1. Therefore, variables in the DOE consist of three parameters for the magnetic field distribution and two parameters for the anomalous coefficients.

The ranges of magnetic field variables are given in Table 5.11. In actual numerical experimentation, ΔB is taken instead of B_{max} because B_{max} must be greater than B_{cath}, and it is more preferable to have a square design space in terms of the DOE. The 4 level full factorial design is created, which results in a total of 1024 runs for 5 variables. Because there are 5 variables that have to be adjusted to match the experimental data, the rigorous optimization routine is applied to obtain accurate results.

Table 5.11: Ranges of Magnetic Field Parameters

	B_{max} [T]	ΔB [T]	B_{cath} [T]	K
Lower Limit	0.015	0.005	0.010	12
Upper Limit	0.031	0.013	0.018	20

The experimental data is taken from Ref. [123]. In Ref. [123], there are two sets of data at the design operation condition of the T-220, which differ by the measurement date. Because there is not much difference between two data sets, the average values from the experimental data are taken as a validation set. The results of the DOE are then input into the JMP[TM] to create the response surface equation for each response. The goodness of fit is greater than 0.99 for all of the responses.

In order to find the optimum values for the anomalous coefficients and the magnetic field distribution parameters, the "fmincon" function in MATLAB[TM] is used, which can generally find the minimum of a constrained nonlinear multivariable function. The normalized values in terms of median of each variable range are used and the optimization performance index is chosen to be the sum of square errors, which are the differences between the experimental values and the calculated values. Because the regression equations are all quadratic and the objective function that is the sum of square errors is also quadratic, only one step is required to find optimum values regardless of initial conditions. The optimization results are shown in Table 5.12 with the comparison to the experimental data and corresponding errors. The comparisons show great accuracy and the errors are all within 2%.

The approximate radial magnetic field distribution from the optimization results is also shown in Figure 5.25.

137

Table 5.12: Validation Results for the T-220 Design Operating Point

Parameters	Experimental Results Thrust Error = ±1 %	Numerical Results	Error (%)
T [mN]	512	507	- 0.97
$I_{sp,tot}$ [sec]	2356	2348	- 0.34
η_{ano} [%]	65	64	- 1.54
η_{tot} [%]	57	56	- 1.75
I_d [A]	20	20	0
P_{tot} [kW]	10.39	10.46	+ 0.65
B_{max} [G]	**196**		
B_{cath} [G]	**119**		
K	**12.13**		
$\hat{\alpha}_{ano,in}$	**100.00**		
$\hat{\alpha}_{ano,out}$	**80.00**		
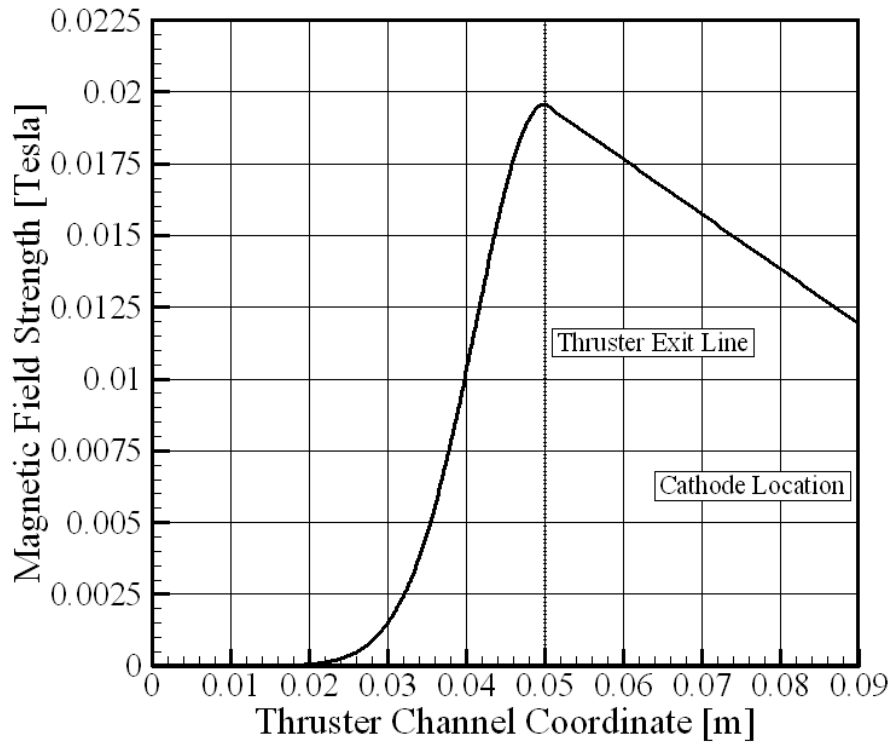
Figure 5.25: Approximate Radial Magnetic Field Distribution for the T-220
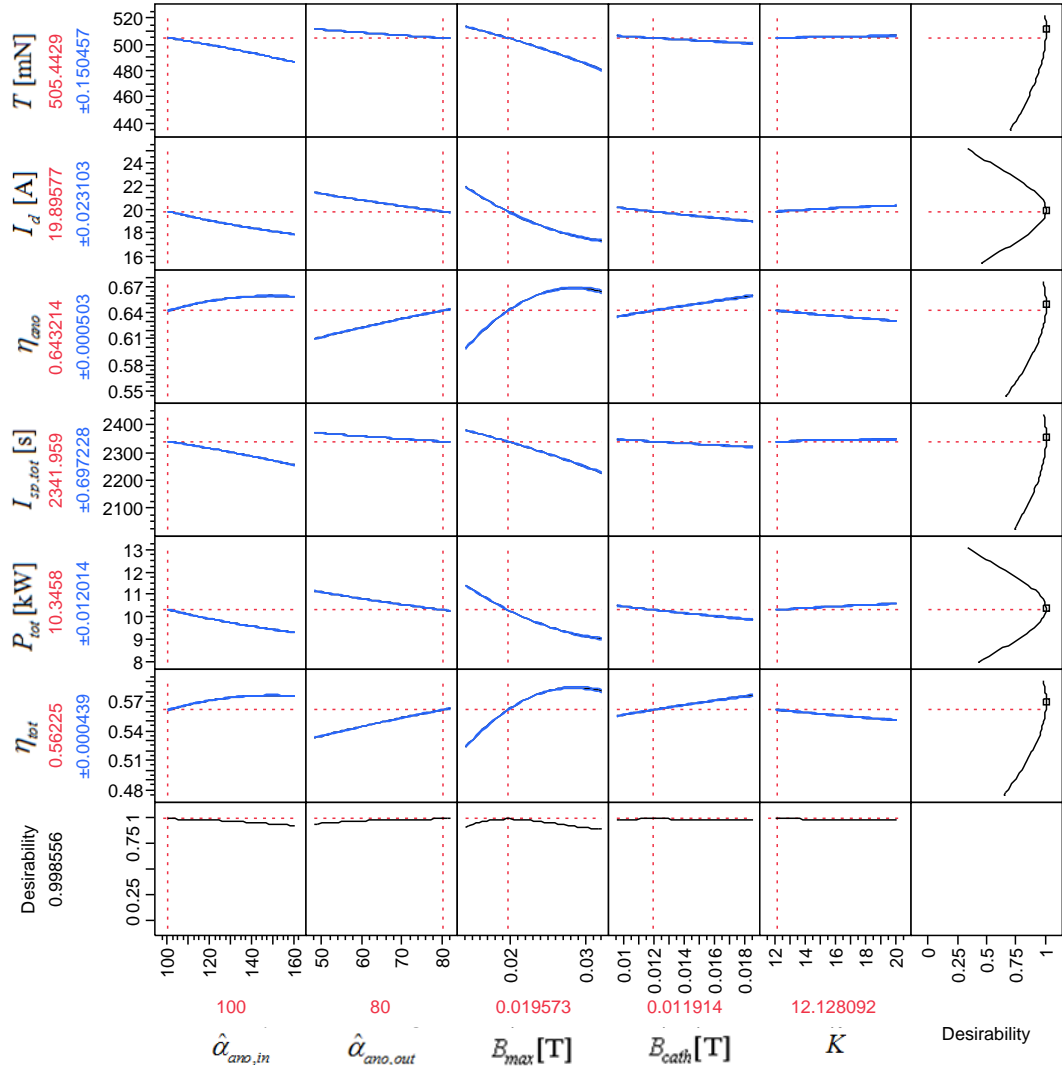
Figure 5.26: Prediction Profiler and Desirability Function for the T-220

Figure 5.26 shows the prediction profiler and the desirability functions. The optimum values are inserted for each parameter to investigate the design operating point of the T-220. B_{max} is the most significant factor, and B_{cath} and K seem to have relatively minor effects on the variation of the responses around the design point. The anomalous coefficients have moderate effects. All of the parameters except for K show the same trends of the effects, i.e., increasing parameter values yields decreases of thrust, discharge

current, total specific impulse, and total power and results in increases of both efficiencies.

Because the optimization results of the anomalous coefficients are still arbitrary, further investigation on the effects of their variations is required. In order to investigate the effects, a Monte Carlo (MC) method is implemented. 100×100 random values for the anomalous coefficients are generated within their ranges. The optimization routine is executed for each anomalous coefficient combination to obtain the optimum radial magnetic field distribution with the given anomalous coefficients. Note again that the optimum means the values of parameters which give the closest match to the experimental data.
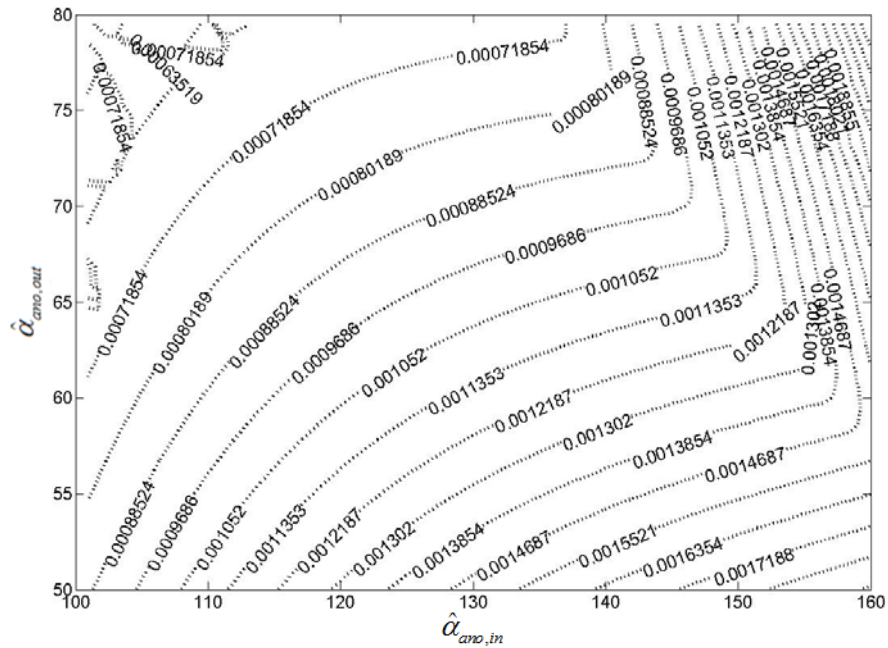
Figure 5.27: Optimization Performance Index Contour

The contour of optimization performance index is shown in Figure 5.27. The range of performance index values is very small, which means that the variation of the responses is not significant. The minimum is identified at the point $(\hat{\alpha}_{ano,in}, \hat{\alpha}_{ano,out}) =$

(100, 80). Figure 5.28 and Figure 5.29 show the contours of B_{max} and B_{cath}. It is clear that they show an almost linear relationship on the anomalous electron axial diffusion except for the small region around the optimum point.
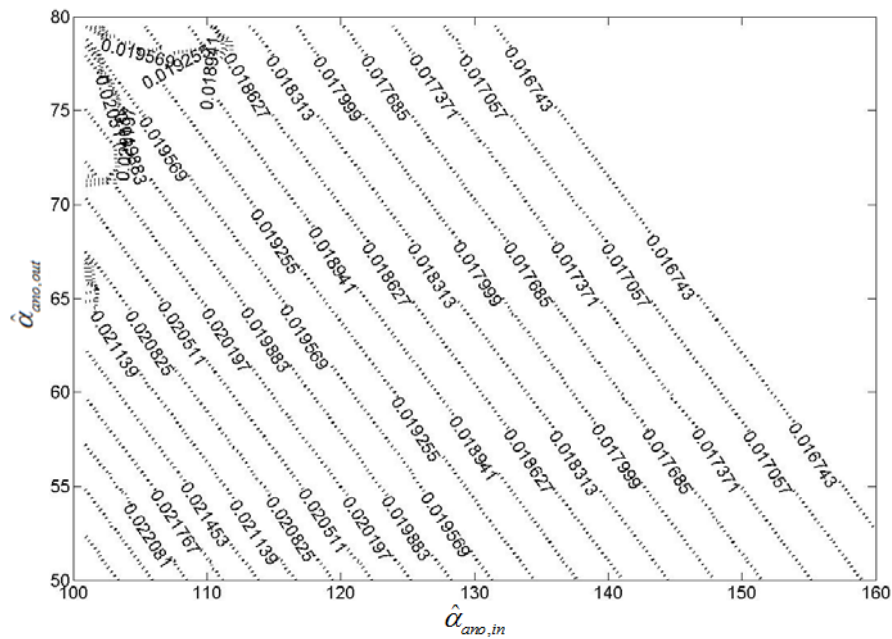
Figure 5.28: Contour of B_{max} [T]
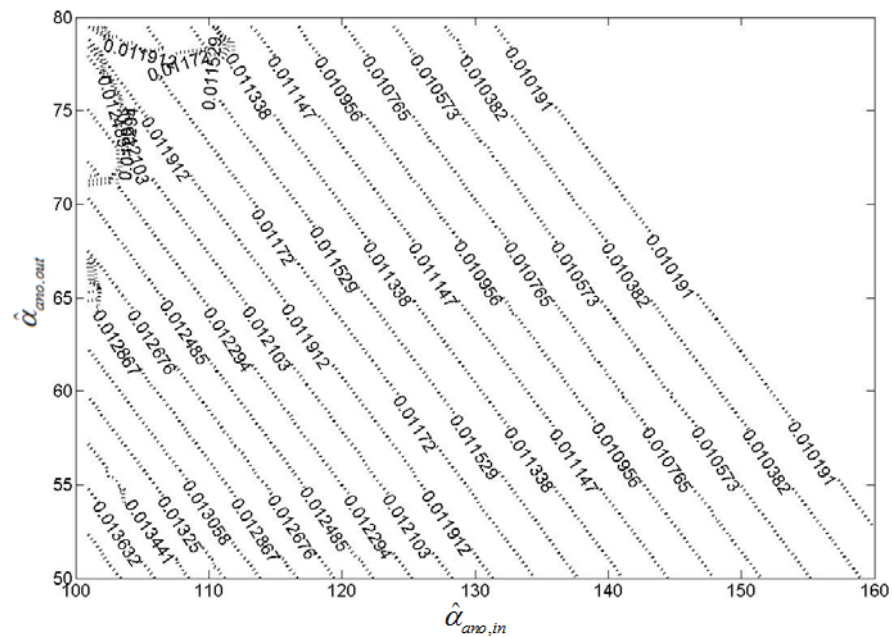
Figure 5.29: Contour of B_{cath} [T]

This reveals that B_{max} and B_{cath} should be increased when the anomalous electron axial diffusion is increased to match the experimental data. In other words, if the anomalous electron diffusion increases, a larger magnetic field strength is required to reduce the axial electron mean velocity to maintain the same discharge current.
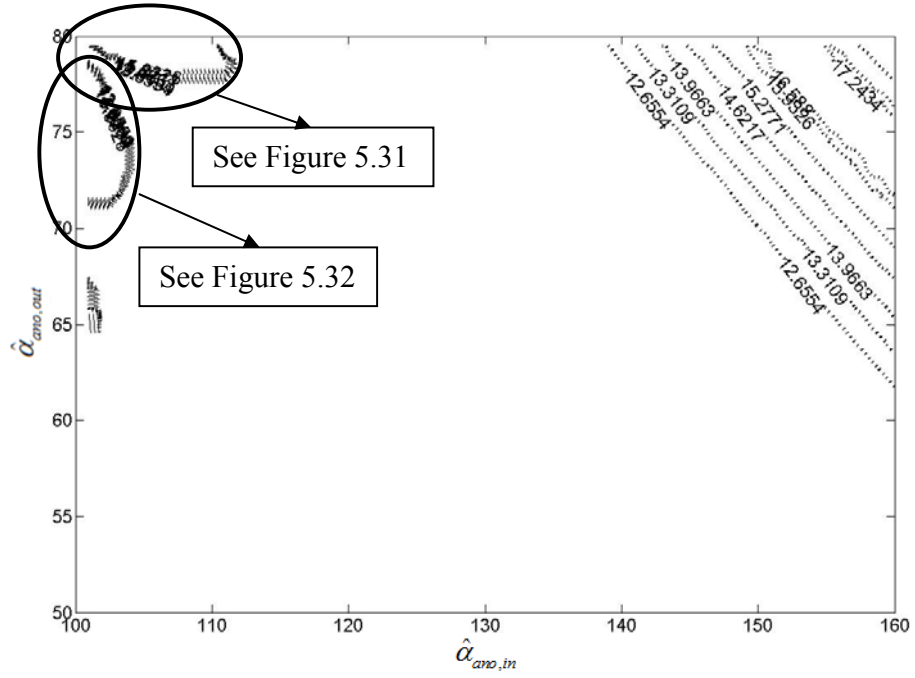
Figure 5.30: Contour of K
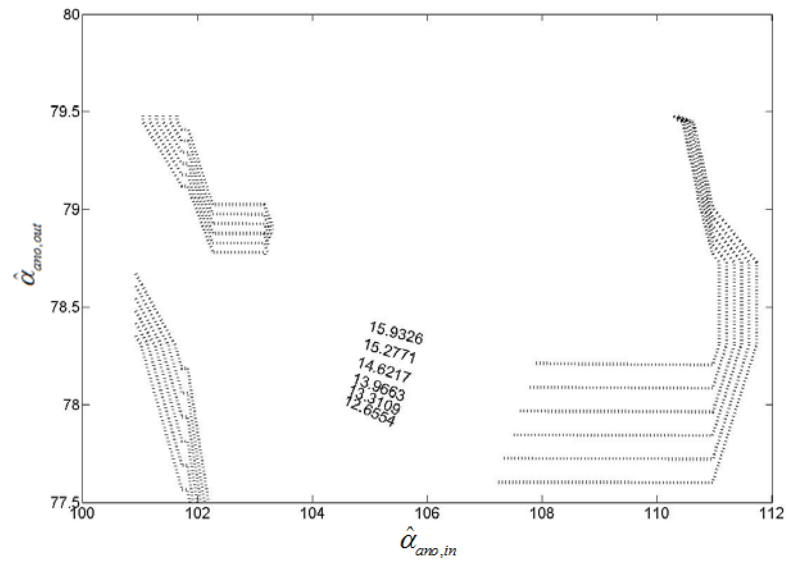
Figure 5.31: Enlarged Contour of K – Upper Side
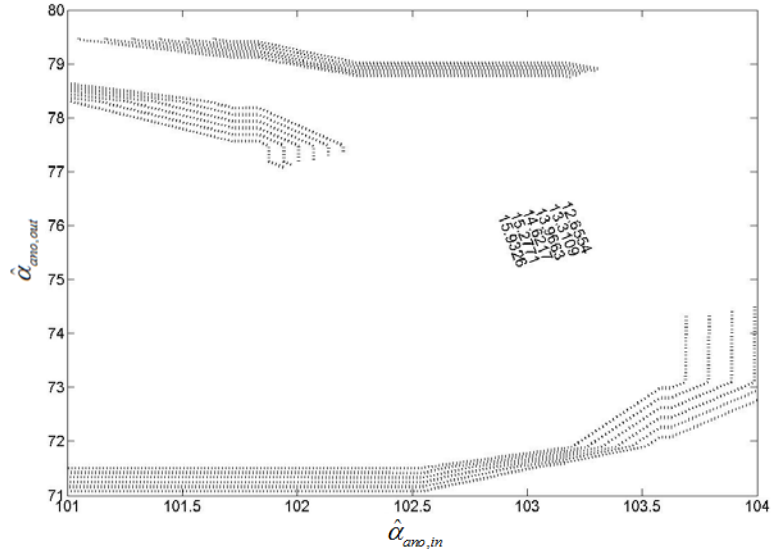
Figure 5.32: Enlarged Contour of K – Left Side

Figure 5.30 shows the magnetic field shape coefficient variation. It has the value of 12 for most of the region, which means that K is not a significant factor compared to B_{max} and B_{cath} for the T-220. A steep variation is observed in the region near the left-upper corner as shown in Figure 5.31 and Figure 5.32. This behavior has been also observed in the previous contours of the optimization performance index, B_{max} and B_{cath}. It seems to come from the small regression errors at the anomalous coefficient range boundaries close to the global optimum and the errors propagate and expand through the optimization routines since there is little or no reason why this should occur at those locations. It is also observed that K linearly increases in the region around the right-upper corner in Figure 5.30. Because the electron diffusion is the smallest in this region, by increasing the axial magnetic field gradient, the electric potential variation with respect to axial coordinate becomes high. This results in the high electric field in the region of high magnetic field gradient to maintain the same performance capabilities.

Table 5.13 shows the performance metric distributions in the whole anomalous coefficient ranges. The plot containing a box above the bar distribution plot is called the Outlier Box Plot and its interpretation is shown in Figure 5.33.
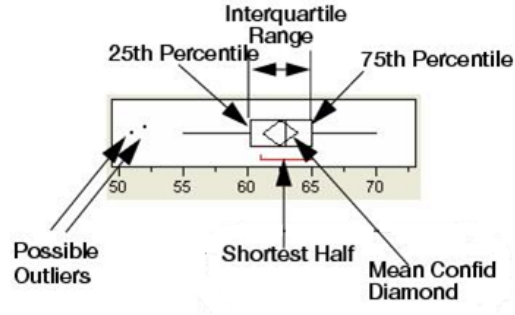
Figure 5.33: Interpretation of Outlier Box Plot [125]
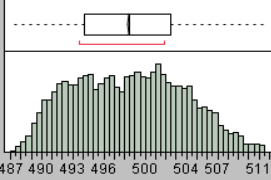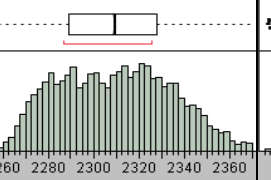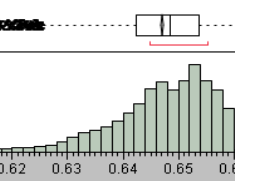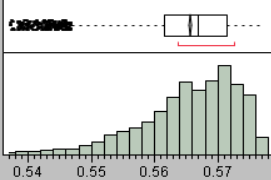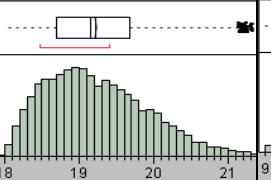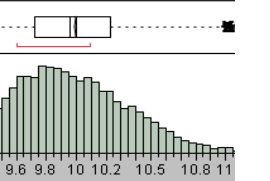
Table 5.13: Performance Metric Distributions

	Thrust [mN]	I_{sp} [sec]	η_{ano}
Distribution			
Mean	503.68	2333.82	0.6395
Standard Deviation	0.902	4.178	0.0018
Upper 95% Mean	503.70	2333.90	0.63954
Lower 95% Mean	503.67	2333.73	0.63947
	η_{tot}	I_d [A]	P_{tot} [kW]
Distribution			
Mean	0.55901	19.8790	10.3371
Standard Deviation	0.0016	0.0428	0.0222
Upper 95% Mean	0.55904	19.8798	10.3375
Lower 95% Mean	0.55898	19.8781	10.3366

The variation ranges of performance metrics are quite small. Thus, it can be inferred that trade-offs between the anomalous coefficients and the magnetic field distributions are possible to obtain nearly the same performance capabilities of the T-220 thruster.

In order to obtain the quantitative confidence level of choosing the optimum values of the magnetic field distribution parameters listed in Table 5.12, another MC simulation is conducted while fixing the optimum magnetic field distribution parameter values.

Table 5.14: Performance Metric Distributions at Optimum Magnetic Field Distribution

	Thrust [mN]	I_{sp} [sec]	η_{ano}
Distribution			
Experiment	512	2356	0.65
Mean	498.42	2309.44	0.647
Standard Deviation	5.27	24.42	0.0086
Range (max. − min.)	24.05 (4.8%)	111.48 (4.8%)	0.0456 (7.0%)
	η_{tot}	I_d [A]	P_{tot} [kW]
Distribution			
Experiment	0.57	20	10.394
Mean	0.566	19.22	10.00
Standard Deviation	0.0075	0.667	0.347
Range (max. − min.)	0.0398 (7.0%)	3.33 (17.3%)	1.73 (17.3%)

The same 100×100 random values for the anomalous coefficients are generated and performance is calculated using performance response surface equations. The results are shown in Table 5.14. The variations with the anomalous coefficients for the thrust, specific impulse and efficiencies are small, less than 7%. The discharge current and power show a little larger variation, about 17%. However, if the mean values and distributions of those metrics and their distributions are considered, the differences are very small. In conclusion, the approximate magnetic field distribution found from the current method could be accepted with favorable confidence.

5.4.2 Validation with the NASA-457M Hall Effect Thruster

The NASA-457M HET succeeded the T-220 for a 50 kW class HET. With advantages of the high power HETs described in the previous section, this class of HETs can be used as a primary propulsion system of missions such as a mission to Mars as a result of the fairly large thrust level, which can lead to moderate transfer times [126]. The development effort was led also by NASA GRC with design efforts from Aerojet Redmond Rocket Center. The development program was under the In-Space Transportation Program funded by the Office of Space Science [127].

The NASA-457M is shown in Figure 5.34 and its outer diameter is 457 mm as also identified by its name. Validation of the developed tool with experimental data of the NASA-457M is a lot more difficult because geometric information is also not available from literature as well as the radial magnetic field distribution due to the ITAR regulations. Thus, because the outer diameter is specified, other required geometries are obtained based on Figure 5.34.
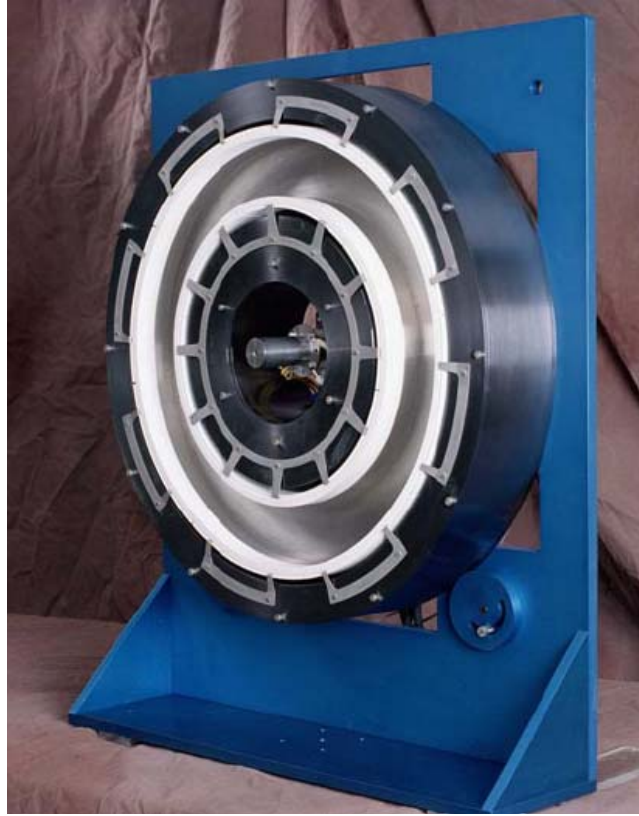
Figure 5.34: NASA-457M Hall Effect Thruster [128]

Since the picture of the NASA-457M in Figure 5.34 was taken with a slant angle to the left, consideration of this effect on geometry estimation is required. The geometries obtained from the picture and operation conditions are listed in Table 5.15.

Table 5.15: Operation Conditions and Geometry of the NASA-457M (est: estimation)

	$\dot{m}_a$ [mg/s]	V_d [V]	Geometry [cm]				
			L (est)	R_1 (est)	R_2	W (est)	L_{cath} (est)
Range	15 ~ 93	300 ~ 650	5.9354	16.56	22.85	6.29	2.284

In order to validate the developed tool with experimental data of the NASA-457M with the estimated geometry, the same approach is taken for "Pseudo-Validation." The variables and their ranges for the DOE are the same as those for the T-220. However, in this case, based on the DOE experiences from the SPT-100 and the T-220, another DOE

strategy is applied to reduce the DOE run time, which is a combination of the Central Composite Design (CCD) and the Latin Hypercube Sampling (LHS) [129]. Their schematics are shown in Figure 5.35.
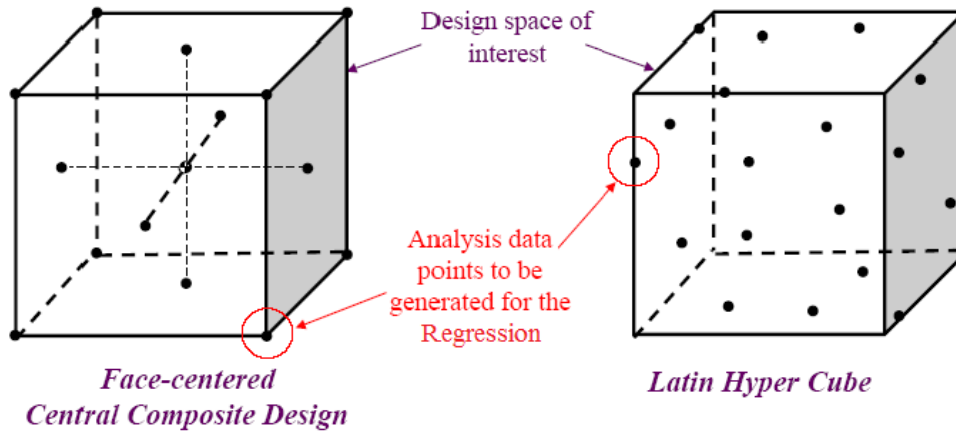
Figure 5.35: Schematics of CCD and LHS

The CCD has advantages of covering the extremes of the concerned space and minimizing the extrapolation. However, as the size of the space becomes large, many experimental cases might not have convergent solutions due to emphasis on the extremes. On the other hand, the LHS has rich samplings on the interior of the space. As a result, higher accuracy can be obtained on the interior design space. This advantage of the LHS reduces the accuracy on the edges of the space. Thus, the combination of these two design methods is expected to yield a reasonable DOE table. For the given 5 variables, the CCD produces 43 runs. Additional 157 runs are created by the LHS, which makes the total of 200 runs.

The experimental data is taken from Ref. [128]. In Ref. [128], the experimental data by varying the anode mass flow rate from 15 to 93 mg/s and the discharge voltage from 300 to 650 V over a range of input powers from 9 to 72 kW is given. Among these data, 4 experimental points are selected for the validation. The anode mass flow rate and

the cathode mass flow rate for all points are 74.3 mg/s and 7.5 mg/s, respectively. The

resultant percentage of the cathode mass flow rate (pmc) is then calculated as 10.09 %.

Other experimental parameters and performance metrics are shown in Table 5.16.

Table 5.16: Experimental Data of the NASA-457M [128] (Thrust Error = $\pm$ 1%)

V_d [V]	T [mN]	$I_{sp,ano}$ [s]	$I_{sp,tot}$ [s]	η_{ano}	η_{tot}	I_d [A]	P_d [kW]	P_{tot} [kW]	$ppm +$ ppc [%]
300	1395.5	1914.5	1739	0.555	0.48	78.5	23.59	24.80	5.14
402	1688	2315	2103	0.60	0.52	80	32.14	33.45	4.05
500	1930	2648	2405	0.62	0.54	81	40.48	41.81	3.27
649	2184	2996	2722	0.62	0.55	80	51.64	52.84	2.32

The results of the DOE for the discharge voltage of 300 V show 116 failure cases

out of a total of 200 cases. For the discharge voltage of 402 V, only 4 failure cases occur.

The DOE for two other discharge voltage cases doesn't have any failure cases. This

somewhat coincides with what's encountered for the SPT-100. For the SPT-100, low

anode mass flow rates with low electron diffusion causes a thruster discharge failure.

Thus, it is observed for the SPT-100 that increasing the cathode mass flow rate fraction

could be one factor causing larger anomalous electron diffusion. For the current case, low

discharge voltage causes the failure. This means that the discharge voltage is also related

to the anomalous electron diffusion, which will be discussed in more detail.

From the DOE results with the developed tool, the resultant response surface

equations for each performance metrics are created using JMP[TM] software as before.

Because the number of runs is reduced for each case compared to the T-220 cases and the

failure cases for the discharge voltage of 300 V are over half of the total runs, the

goodness of fits should be carefully checked. Table 5.17 shows the goodness of fit for

each metric at each discharge voltage. All are over 0.99 of R^2 value except for the

efficiency terms for a 300 V discharge. Because the goodness of fits for the efficiency

terms is still high, the resultant response surface equations for all metrics will be used for

the follow-on analysis.

Table 5.17: Goodness of Fit for the NASA-457M DOEs

V_d [V]	Metric	R^2	R^2_{adj}	RMSE	Mean of Response
300	T [mN]	0.9984	0.9979	2.2205	1362.39
	$I_{sp,ano}$ [s]	0.9984	0.9979	3.0462	1869.15
	$I_{sp,tot}$ [s]	0.9984	0.9979	2.7669	1697.77
	η_{ano}	0.9812	0.9753	0.0017	0.5881
	η_{tot}	0.9812	0.9753	0.0015	0.5080
	I_d [A]	0.9995	0.9993	0.1449	70.92
	P_d [kW]	0.9995	0.9993	0.0435	21.28
	P_{tot} [kW]	0.9995	0.9993	0.0457	22.37
402	T [mN]	0.9989	0.9988	1.7400	1645.26
	$I_{sp,ano}$ [s]	0.9989	0.9988	2.3867	2257.24
	$I_{sp,tot}$ [s]	0.9989	0.9988	2.1679	2050.28
	η_{ano}	0.9962	0.9957	0.0014	0.6256
	η_{tot}	0.9962	0.9957	0.0012	0.5461
	I_d [A]	0.9978	0.9976	0.3228	72.68
	P_d [kW]	0.9978	0.9976	0.1298	29.22
	P_{tot} [kW]	0.9978	0.9976	0.1350	30.40
500	T [mN]	0.9996	0.9995	0.8469	1895.72
	$I_{sp,ano}$ [s]	0.9996	0.9995	1.1622	2600.86
	$I_{sp,tot}$ [s]	0.9996	0.9995	1.0557	2362.39
	η_{ano}	0.9991	0.9990	0.0010	0.6302
	η_{tot}	0.9991	0.9990	0.0009	0.5543
	I_d [A]	0.9971	0.9968	0.4187	77.16
	P_d [kW]	0.9971	0.9968	0.2093	38.58
	P_{tot} [kW]	0.9971	0.9968	0.2162	39.84
649	T [mN]	0.9991	0.9990	0.9159	2211.68
	$I_{sp,ano}$ [s]	0.9991	0.9990	1.2568	3034.34
	$I_{sp,tot}$ [s]	0.9991	0.9990	1.1416	2756.14
	η_{ano}	0.9995	0.9994	0.0010	0.6150
	η_{tot}	0.9995	0.9994	0.0009	0.5460
	I_d [A]	0.9971	0.9968	0.4779	83.06
	P_d [kW]	0.9971	0.9968	0.3101	53.91
	P_{tot} [kW]	0.9971	0.9968	0.3173	55.15

Because there are 4 points for validation, the same procedure to find the optimum

solutions for the anomalous coefficients and the magnetic field distribution parameters is

applied for each discharge voltage validation point. Using the same "fmincon" function

in MATLAB^{TM}, optimum values for the anomalous coefficients and the magnetic field

distribution parameters can be found. The results are shown in Table 5.18, Figure 5.36,

and Figure 5.37. The performance metrics calculated with the optimum values show great

accuracy when compared to the experimental data for all 4 discharge voltage points. The

maximum and the cathode magnetic field strength tend to increase as the discharge

voltage increases. High potential drop between the anode and the cathode entails a

relatively high electric field. This in turn requires higher radial magnetic field strength

sufficient to trap the electrons for the given performance capability.

Table 5.18: Validation Results for the NASA-457M

Parameters	300 V		402 V		500 V		649 V	
	Exp.	Comp.	Exp.	Comp.	Exp.	Comp.	Exp.	Comp.
T [mN]	1395.2	1417.3	1688	1687	1930	1922	2184	2185
$I_{sp,ano}$ [s]	1914.5	1944.5	2315	2314	2648	2637	2996	2998
$I_{sp,tot}$ [s]	1739	1766.2	2103	2102	2405	2395	2722	2723
η_{ano}	0.555	0.58	0.60	0.60	0.62	0.62	0.62	0.62
η_{tot}	0.48	0.50	0.52	0.52	0.54	0.54	0.55	0.55
I_d [A]	78.5	77.8	80	79.4	81	81	80	80
P_d [kW]	23.58	23.34	32.14	31.92	40.48	40.33	51.64	51.69
P_{tot} [kW]	24.80	24.54	33.45	33.21	41.81	41.64	52.84	52.88
B_{max} [G]	174.43		198.32		215.87		240.09	
B_{cath} [G)	100.00		106.27		131.4		120.49	
K	20.00		19.70		16.46		20.00	
$\hat{\alpha}_{ano,in}$	129.40		134.90		119.34		158.05	
$\hat{\alpha}_{ano,out}$	50.00		50.00		63.09		50.00	
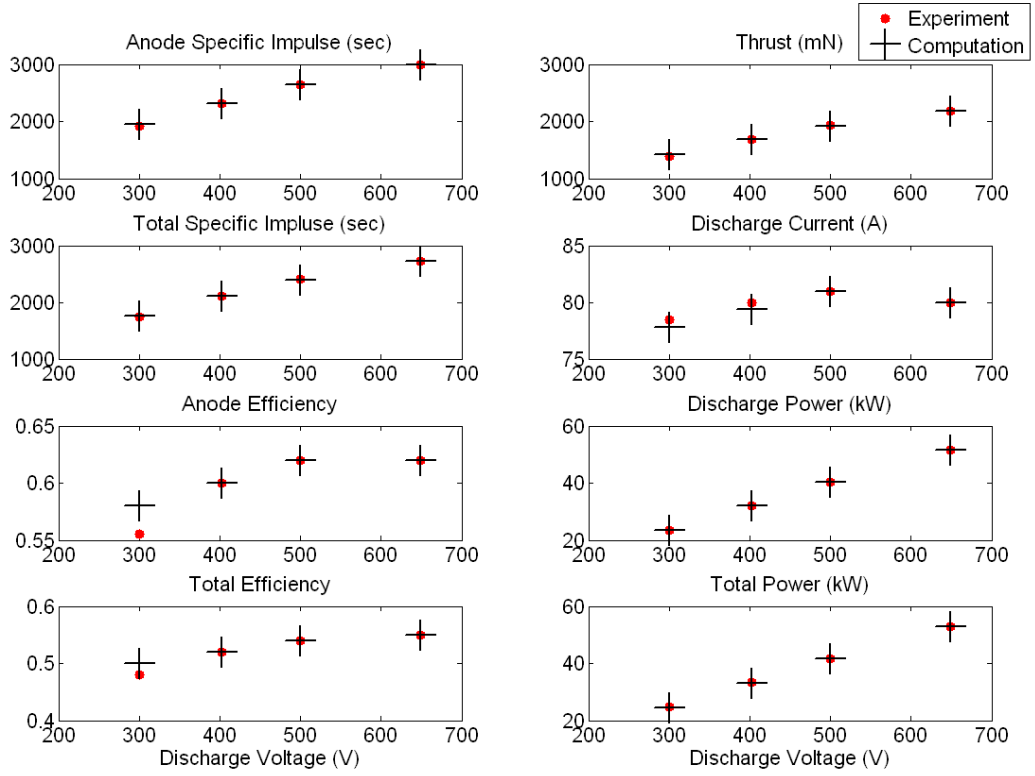
Figure 5.36: Performance Validation of the NASA-457M (Thrust Error of Exp. = ± 1%)
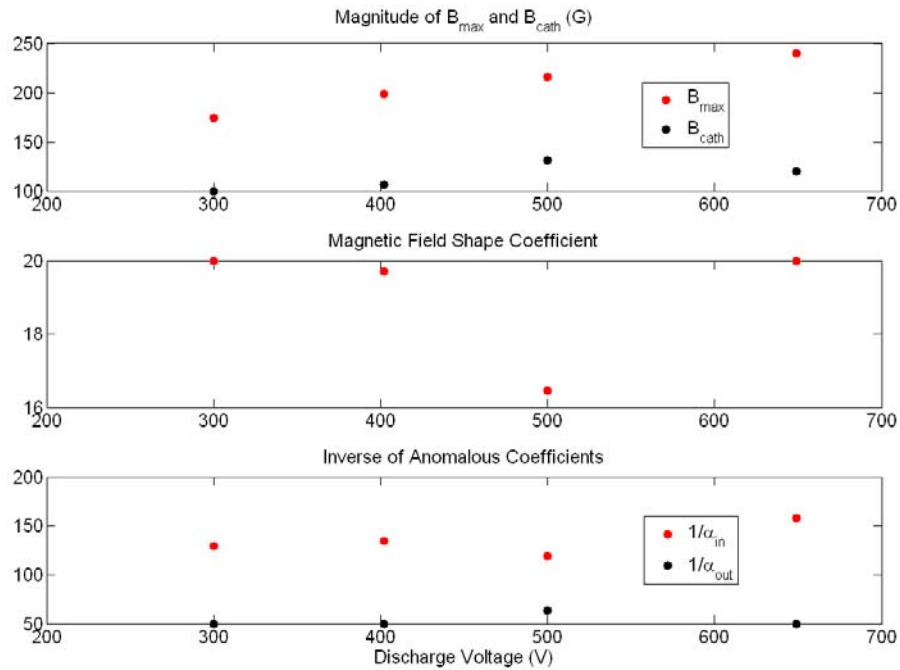
Figure 5.37: Variations of Optimum Magnetic Parameters and Anomalous Coefficients
$(1/\alpha_{in} = \hat{\alpha}_{ano,in}$ and $1/\alpha_{out} = \hat{\alpha}_{ano,out})$

Variation of the magnetic field shape coefficient does not show any consistent trend. The anomalous coefficient outside the channel stays almost the same. The anomalous coefficient inside the channel decreases with the discharge voltage increase except for the case of 500 V. This may partially indicate that the higher anomalous electron diffusion is required for the lower discharge voltage. However, it is not likely to be accepted based on only the results in Table 5.18.

Because the anomalous coefficients are arbitrarily obtained from the optimization process, their values only hold for each discharge voltage. Furthermore, as seen in the T-220 validation results, there are an infinite number of solutions when considering the trade-offs between the anomalous coefficients and the magnetic field distribution parameters. Although the same procedure can be applied as done for the T-220 case and the resultant magnetic field distribution for each discharge voltage case can be accepted with certain confidence, it is worth taking a more rigorous analysis when considering the fact that the same magnetic field distribution is usually used for a specific thruster. This can be also deduced from the experimental data. The powers required for the magnetic field generation and the cathode operation are calculated as 1.196, 1.322, 1.302, and 1.213 kW for 300, 402, 500, and 649 V, respectively based on the data in Table 5.16. It is clear that there is not much difference for these power consumptions.

Thus, it is required to have the same magnetic field distribution for all 4 voltage cases. In the optimization process, this can be done by solving one optimization problem with three global variables for the magnetic field distribution and 8 anomalous coefficients. The performance index is expanded to match all metrics for all voltage cases.

Using this optimization strategy yields the results shown in Table 5.19, Figure 5.38, and Figure 5.39.
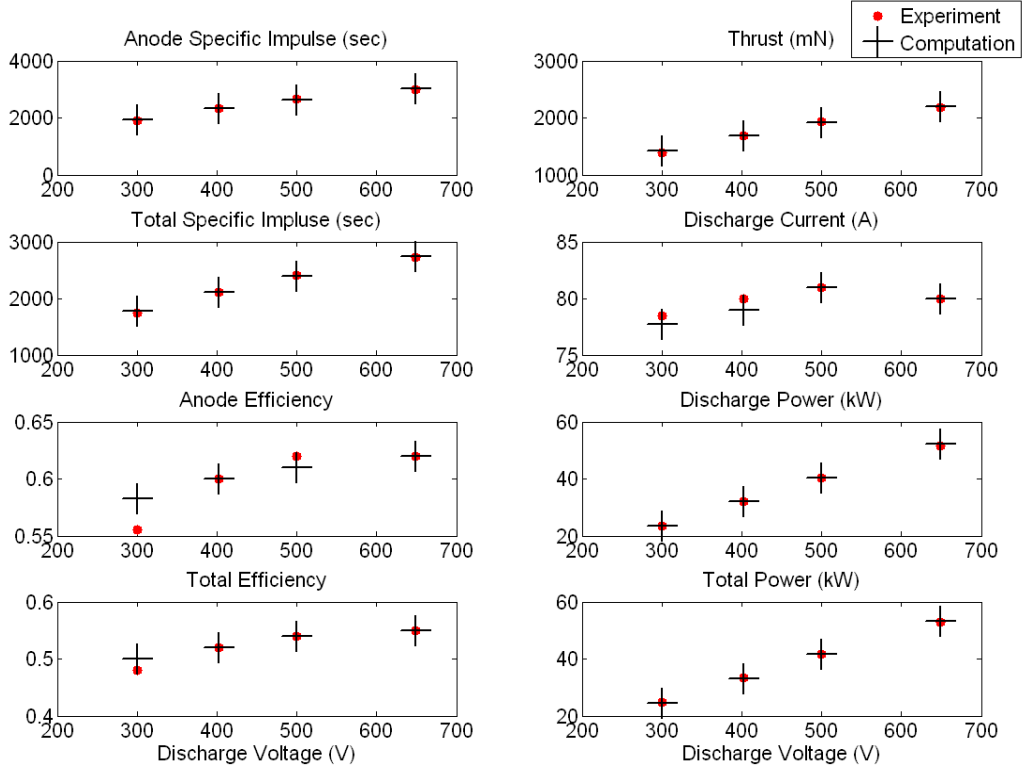
Figure 5.38: Performance Validation of the NASA-457M with One Magnetic Field Distribution (Thrust Error of Exp. = ± 1%)
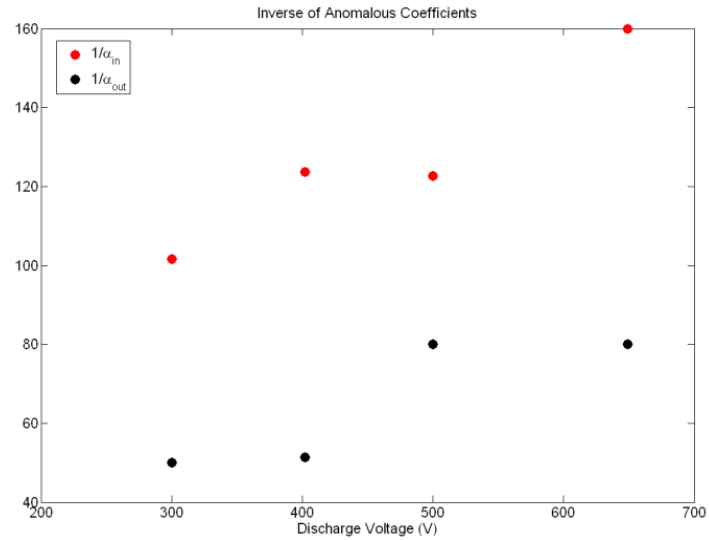
Figure 5.39: Variations of Anomalous Coefficients for One Magnetic Field Distribution $(1/\alpha_{in} = \hat{\alpha}_{ano,in}$ and $1/\alpha_{out} = \hat{\alpha}_{ano,out})$

Table 5.19: Validation Results for the NASA-457M with All 4 Points

Parameters	300 V		402 V		500 V		649 V	
	Exp.	Comp.	Exp.	Comp.	Exp.	Comp.	Exp.	Comp.
T [mN]	1395.2	1421.1	1688	1687	1930	1919	2184	2197
$I_{sp,ano}$ [s]	1914.5	1949.7	2315	2315	2648	2633	2996	3015
$I_{sp,tot}$ [s]	1739	1771	2103	2103	2405	2391	2722	2738
η_{ano}	0.555	0.583	0.60	0.60	0.62	0.61	0.62	0.62
η_{tot}	0.48	0.50	0.52	0.52	0.54	0.54	0.55	0.55
I_d [A]	78.5	77.7	80	79	81	81	80	80
P_d [kW]	23.58	23.31	32.14	31.92	40.48	40.39	51.64	52.14
P_{tot} [kW]	24.80	24.50	33.45	33.21	41.81	41.71	52.84	53.35
B_{max} [G]	213.72							
B_{cath} [G]	100.00							
K	20.00							
$\hat{\alpha}_{ano,in}$	101.68		123.73		122.65		160.00	
$\hat{\alpha}_{ano,out}$	50.00		51.35		80.00		80.00	
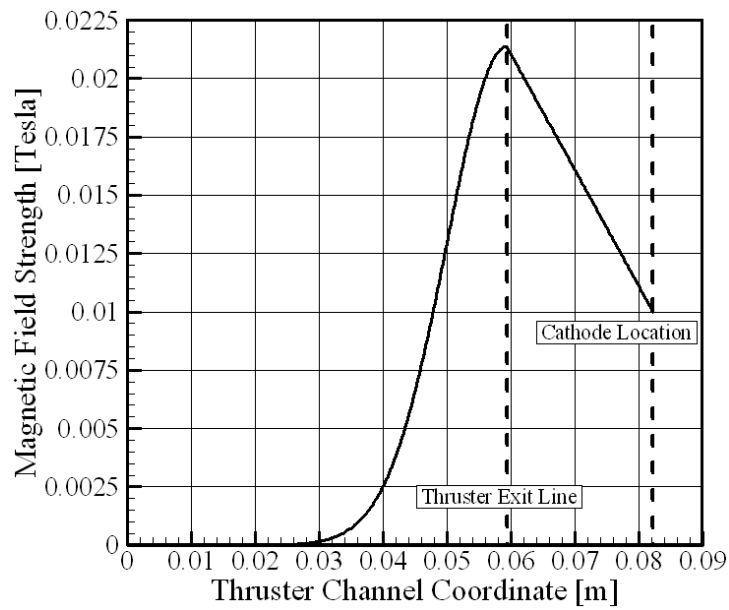
Figure 5.40: Approximate Radial Magnetic Field Distribution for the NASA-457M

The accuracy on the performance metrics is still high and the resultant magnetic field distribution is plotted in Figure 5.40.

Based on the anomalous coefficient variation, it is highly likely that the higher anomalous electron diffusion is required as the discharge voltage decreases with the same magnetic field distribution. This indicates that higher discharge voltage has a negative impact on the anomalous electron diffusion. This behavior of the anomalous electron diffusion is also observed in Ref. [107], which shows that the anomalous coefficient increases as the discharge voltage decreases below 400 V.

Note that the developed method does not incorporate the effect of multiply-charged ions. Ref. [128] suggests that the effect of multiply-charged ions becomes significant for over 20 kW of discharge power or over 30 A of discharge current. Thus, this validation can be thought of as an approximation of the actual thruster with less confidence than the SPT-100 or the T-220.

However, the effect of multiply-charged ions may be incorporated in the developed tool by using the method proposed in the Ref. [25]. In order to prove this possibility, a numerical experiment is done with the experimental data given in Ref. [128]. The experimental data, prediction data by Ref. [25] and the data from the current tool are shown in Table 5.20. For the calculation, the magnetic field distribution and the anomalous coefficients obtained from Figure 5.40 and Table 5.19 are used.

As seen in Table 5.20, approximately on the order of 100 seconds less anode I_{sp} for a singly-charged ion case than that of multiply-charged ion case is observed in the prediction results. The result of the current tool is exactly showing this trend when compared to the experimental data.

Table 5.20: Effect on Multiply-Charged Ions

Parameters	Experimental Data [128]	Prediction [25]		Current Tool
		Multiply-Charged	Singly-Charged	
$\dot{m}_a$ [mg/s]	86.4	88.8	101	86.4
V_d [V]	500	500	500	500
I_d [A]	100	100	100	95.3
$I_{sp,ano}$ [s]	2750	2768	2622	2665

Thus, if the proposed method for the effect of multiply-charged ions in the Ref. [25] were to be incorporated, it would be expected that more confident approximation could be obtained. In conclusion, the developed tool can be still used as an effective tool for even high power class of the HETs.

5.5 Sensitivity Studies for the SPT-100

The purpose of the sensitivity studies for the SPT-100 is to investigate the sensitivities of performance metrics when varying each specific variable while other variables remain fixed. The sensitivity analysis is usually done with a known design point to investigate response variations around that design point. In other words, if a specific input variable is varied by a small amount around the design point, the goal is to investigate what will happen to the responses. As a result, things of interest are the direction of the response variation and how much variation occurs with the variation of a given input variable. In this case, the design operation point of the SPT-100 is taken as a known design point. The variables of concern and their ranges are given in Table 5.21.

The anomalous coefficients inside and outside the channel are assumed to be those obtained in the SPT-100 validation. The variation of each variable is set such that the design operation point is centered. The range of each variable in this sensitivity study

should be low enough, otherwise the assumption of the fixed anomalous coefficient values cannot be guaranteed because they could be also functions of these variables.

Table 5.21: Variables and Ranges of Sensitivity Studies for the SPT-100

Variable	Min.	Max.
Inner Radius [cm]	0.3	0.4
Channel Width [cm]	1	2
Device Length [cm]	3.5	4.5
Cathode Location [cm]	1.5	2.5
Discharge Voltage [V]	251	351
B_{cath} [G]	120	140
ΔB [G]	20	40
K	12	20

The parametric study is done by varying each variable value within the corresponding range and the results are shown in Figure 5.41. The responses of concern are the thrust, the total specific impulse, the total efficiency, and the discharge current.
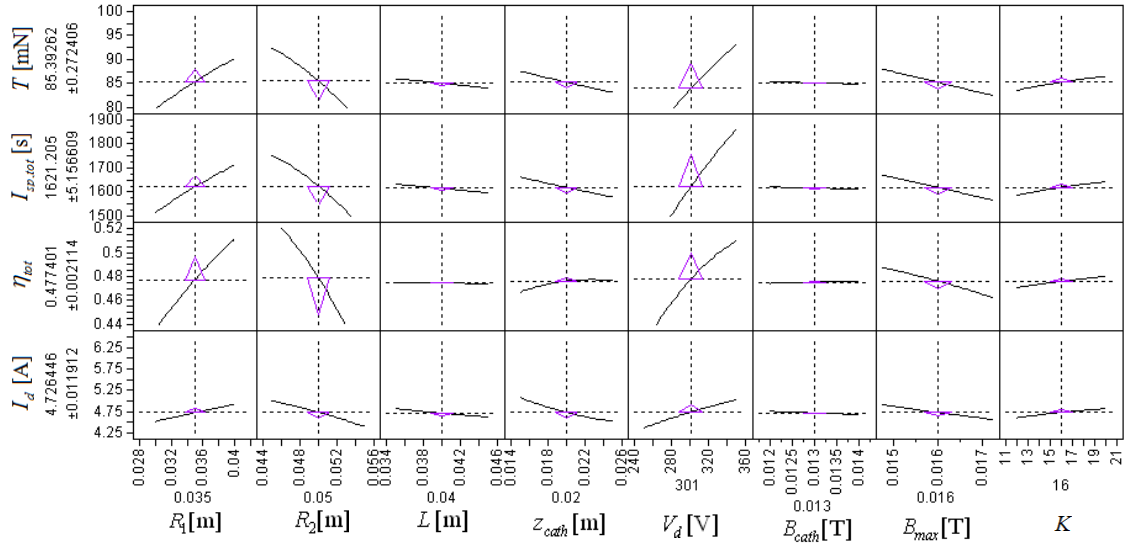
Figure 5.41: Sensitivity Analysis Results around the SPT-100 Design Operation Point

158

The vertical dotted lines correspond to the SPT-100 design operation point for each variable. The triangles shown in Figure 5.41 indicate the sensitivities at the current variable values. That is the value of first derivative of the response with respect to the variable. The direction indicates the sign of the first derivative and the size indicates its magnitude. As seen in Figure 5.41, the most influential variables are the inner radius, the outer radius, and the discharge voltage. The increases of responses with the increase of the inner radius and the decreases with the increase of the outer radius are caused mainly by the reduced thruster channel volume, which increases the neutral number density at the given anode mass flow rate. Increasing the maximum magnetic field strength results in negative effects on the performance metrics, but the discharge current is also reduced. Interestingly enough, the response variations with each variable are in the same direction, increasing or decreasing except for the relatively small variations of the device length, the magnetic field strength at the cathode, and the magnetic field shape coefficient.

5.6 Approximation of the Radial Magnetic Field Distribution with the Given Performance Goals

In this section, how the radial magnetic field distribution can be approximated with the developed tool when the performance goals of a specific HET are given is discussed. In order to show this capability, the P5 Hall thruster is considered. The P5 was first introduced in section 1.6.1. The detail operating conditions and geometry found from literature are summarized in Table 5.22 [21][22].

Because the radial magnetic field distribution of the P5 is not restricted by the ITAR regulations, the precise magnetic field distribution can be obtained. The actual radial magnetic field distribution at the design operation point is shown in Figure 5.42.

For the given radial magnetic field distribution, B_{max} is 107 G and B_{cath} is 39 G. Furthermore, the location of B_{max} does not coincide with the thruster exit line. The location of B_{max} is approximately 2.62 cm from the anode line while the channel length is 3.81 cm as seen in Table 5.22.

Table 5.22: Operation Conditions and Geometry of the P5

	$\dot{m}_a$ [mg/s]	V_d [V]	Geometry [cm]				
			L	R_1	R_2	W	L_{cath}
Design Point	10.248	300	3.810	6.096	8.636	2.540	3
Range	5.66 ~ 10.25	200 ~ 500					

The developed tool also has the capability of dealing with the given radial magnetic field distribution. The analysis of the P5 at the design operation point is attempted. However, the developed tool shows a failure case with the given radial magnetic field distribution. The failure case corresponds to Case 4 in section 5.3.4, which indicates that the presheath region length is smaller than the length of one grid cell. As explained in section 5.3.4, this is because the radial magnetic field strength in the region near the anode is relatively high as indentified in Figure 5.42. This means that the developed tool does not detect the noticeable presheath existence for the P5.
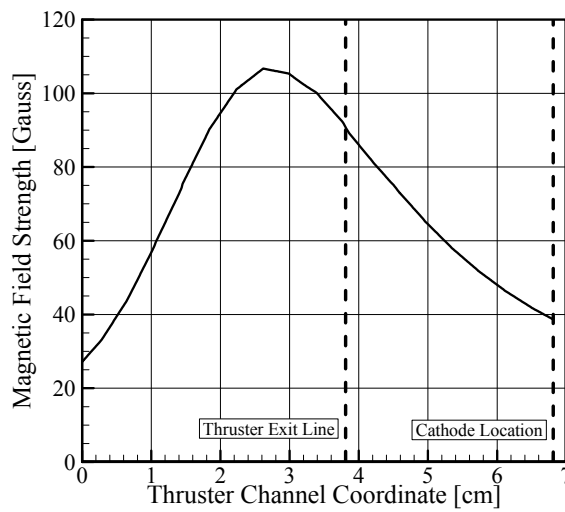
Figure 5.42: Actual Radial Magnetic Field Distribution of the P5

Now a different perspective is considered. A situation is assumed such that there is a given HET geometry and there are also performance goals that designers want to attain for this thruster. The question is what radial magnetic field distribution is required to produce the performance goals with an additional assumption that the structure of the necessary radial magnetic field distribution follows the one assumed in the developed tool. In other words, it is desired to find the required B_{max}, B_{cath}, and K.

Thus, the P5 becomes a given thruster and the experimental data of its performance metrics becomes performance goals. The objective is to find an approximate radial magnetic field distribution which gives the same values of performance metrics from the actual one. In other words, another radial magnetic field distribution which obeys Equation (5.1) inside the channel and is linear outside the channel will be sought in the hope that it exists. The experimental data of the given performance metrics at the operation point is shown in Table 5.23.

Table 5.23: The P5 Performance Metrics at Design Operation Point

T [mN]	$I_{sp,ano}$ [s]	η_{ano}	I_d [A]	P_{tot} [kW]
178	1683	0.51	10.4	3.12

If the same method used for the T-220 is used, the maximum radial magnetic field strength, the magnetic field strength at the cathode, and the magnetic field shape coefficient characterizing the entire radial magnetic field distribution are expected to be found. Since the anomalous coefficients are still arbitrary, those are included as before.

Table 5.24: Ranges of Magnetic Field Parameters for the P5

	B_{max} [T]	ΔB [T]	B_{cath} [T]	K
Lower Limit	0.005	0.005	0.002	1
Upper Limit	0.015	0.013	0.008	16

The ranges for each variable are selected based on power level of the P5, which is shown in Table 5.24. The 4 level factorial design is created for B_{max}, B_{cath}, K, $\hat{\alpha}_{ano,in}$ and $\hat{\alpha}_{ano,out}$. Thus total 1024 runs are executed and those are found using the same method. The results are shown in Table 5.25. The results of performance metrics calculated from the optimization are very close to experimental performance data. B_{max} is calculated as 120 Gauss, which is slightly higher strength than actual one.

Figure 5.43 shows the actual and candidate radial magnetic field distribution. Compared to the actual magnetic field, the candidate distribution has lower magnetic field strength in most of the region inside the channel and higher magnetic field strength outside the channel.

In conclusion, it is expected that the procedure established through the validation can be used effectively to obtain an approximate magnetic field distribution for a specific thruster geometry to achieve the desired performance goals.

Table 5.25: Results of Finding Candidate Radial Magnetic Field Distribution

Parameters	Experimental Results	Numerical Results	Error (%)
T [mN]	178	180	+ 1.12
$I_{sp,tot}$ [sec]	1683	1696	+ 0.77
η_{ano} [%]	51	50	- 1.96
η_{tot} [%]	-	47	-
I_d [A]	10.4	10.6	+1.92
P_{tot} [kW]	3.12	3.18	+ 1.92
B_{max} [G]	120		
B_{cath} [G]	80		
K	7.01		
$\hat{\alpha}_{ano,in}$	114.26		
$\hat{\alpha}_{ano,out}$	79.48		
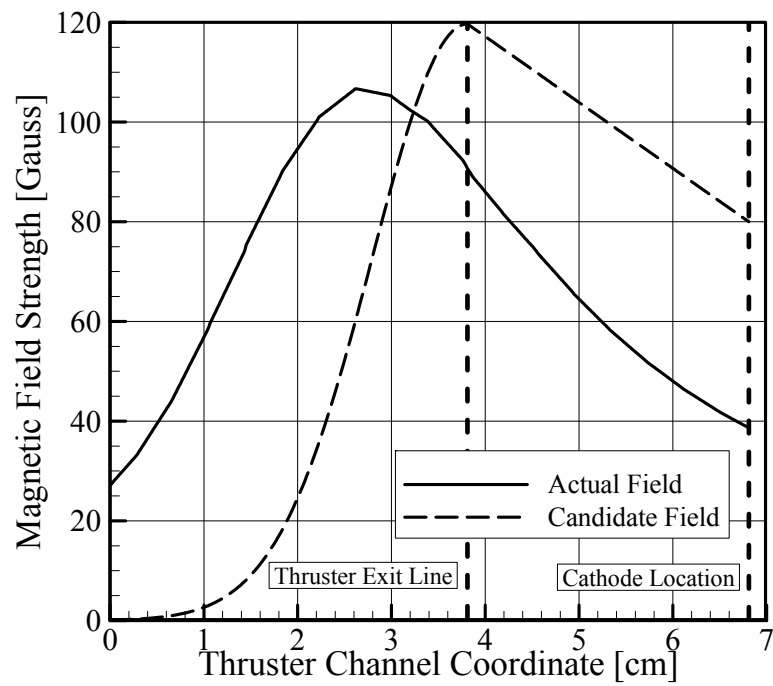
Figure 5.43: Actual and Candidate Radial Magnetic Field Distribution of the P5

CHAPTER 6

DESIGN SPACE EXPLORATION FOR HET

6.1 Need of Design Space Exploration

Based on validations with the HETs from 1 kW to 50 kW classes in the previous chapter, it is expected that the developed tool can, in principle, be effectively used for the design of a new HET in the conceptual design stage. It should be noted that the implementation of the developed tool for design requires additional work as seen in the validation process because the anomalous coefficients are arbitrary and there is currently no way of calculating these coefficients a priori. In order to produce reliable designs, the effects of these coefficients on the design should be incorporated in the design results.

The current method of incorporating the effects of the anomalous coefficients is that they also be treated as design variables. In other words, the variation of the anomalous coefficients also has impacts on the HET performance as other design variables do. By doing this, design results are probabilistic rather than deterministic. This is a reasonable strategy in the conceptual design stage because it can greatly reduce the design space in spite of uncertainties in some variables.

The DSE can be accomplished by generating the data using numerical experiment, which characterizes the entire design space. The advantages of the DSE are in general that: 1) detail correlation information between input variables with respect to each response can be obtained, 2) the feasible region, here the performance envelope, can be

identified, and 3) it could provide an environment for further investigations such as optimization, sensitivity analysis, robust design, and probabilistic design.

6.2 Design Space Exploration for the HET

6.2.1 Selection of the Design Space

Defining the design space can be a quite difficult task due to the fact that: 1) the ranges of variables determine the scope of the output response, 2) the output response scope cannot be known before it is explored, 3) the output response scope should effectively include the response goals, and 4) the DSE is a time-consuming process. Thus, the selection of the design space tends to largely depend on accumulated experiences. Because the DSE for the HET has not been done before, the situation becomes even worse. However, the experiences gained from the validation work in the previous chapter, which covers from 1 kW to 50 kW classes, are expected to aid in determining the HET design space.

The current HET design is intended for near Earth missions. Figure 6.1 shows the electric propulsion spacecraft operating near Earth [131]. Of all HETs on orbit, the SPT-100 class is most common. These thrusters are primarily used for North South Stationkeeping (NSSK) orbit control and momentum management. Their successful daily operations for the geostationary communication satellites are well described in Ref. [132].

Recently, the PPS®-1350-G HET was used for the SMART-1 mission, which is the same power class as the SPT-100 [133]. Although it was used as a primary propulsion system for this mission, it was originally developed for the implementation of the NSKK of the GEO satellites constructed by Snecma.
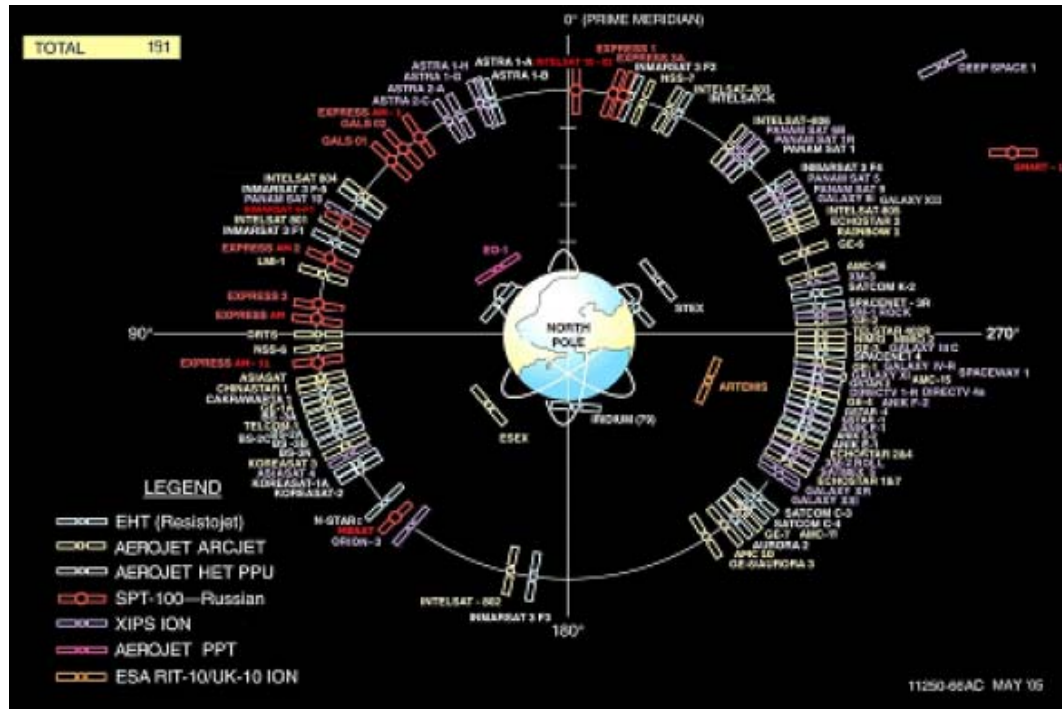
Figure 6.1: Electric Propulsion Spacecraft [131]

In addition, Lockheed Martin Space Systems Company (LMSSC) and General Dynamics Space Propulsion Systems (GD-SPS) developed a 4.5 kW HET propulsion system for applications on the GEO satellites. This HET was designed to perform on-orbit stationkeeping and repositioning maneuvers as well as the Geosynchronous Transfer (GTO-GEO) [134]. Thus, based on these applications, it would be reasonable to explore a design space which covers from 1 kW to about 10 kW if transfer missions are to be included.

Based on validation work for the SPT-100 and the T-220 as well as the P5 radial magnetic field approximation work, the relevant variables and their ranges are chosen as shown in Table 6.1.

Table 6.1: Ranges of Variables

Variable	Lower Limit	Upper Limit
$\hat{\alpha}_{ano,in}$	100	160
$\hat{\alpha}_{ano,out}$	50	80
z_{cath} [m]	0.01	0.03
L [m]	0.03	0.05
R_1 [m]	0.03	0.05
W [m]	0.01	0.03
V_d [V]	200	400
ΔB [T]	0.002	0.008
B_{cath} [T]	0.008	0.015
K	12	20
$\dot{m}_a$ [mg/s]	4	8
pmc [%]	6	10

As explained in section 5.1, the inverse values of anomalous coefficients are included as input variables. The power consumptions by the magnetic field generation and the cathode operation are excluded for the current DSE. The reason for using W and ΔB is to obtain a square-like design space for each variable. If the outer radius were to be used directly, a constraint that the outer radius must be greater than the inner radius should be imposed. The resultant design space from the inner and outer radius and the constraint would produce a triangular region due to the constraint, and this would have a negative effect on the DOE table generation.

6.2.2 Design Space Exploration Strategy

As seen in Table 6.1, there are 4 geometric variables, 3 operational variables, 3 magnetic field variables, and 2 anomalous coefficients. The performance responses of interest are thrust, total specific impulse, total efficiency, discharge current, and discharge power.

In order to establish the DOE table, the same strategy is applied as before, i.e., the use of a combination of the CCD and the LHS. The generated DOE cases are then input into the same ModelCenter^{TM} environment. The DOE cases and results are listed in Table 6.2.

Table 6.2: DOE Cases and Results

Design	# of cases	# of retrieved data from ModelCenter^{TM}	# of success	# of failure
CCD	4121	4113	2167 (52.69%)	1946
LHS	10000	9980	5565 (55.65%)	4415
Total	14121	14093	7732 (54.86%)	6361

The initially generated DOE table contains a total of 14121 cases. The DOE tool in the ModelCenter^{TM} environment produces internal errors for a few cases. Thus, the useful data retrieved from ModelCenter^{TM} totals 14093 cases. Among these retrieved cases, about 54.86 % of design variable combinations are identified as successful cases of thruster operations.

6.2.3 Constraints on Feasible Thruster Operation

As introduced in section 5.3.4, solutions computed by the developed tool can be classified into 6 classes. The first two classes indicate the operation success for the analyzed HET. The rest are the failure cases. The required classification in the DSE is the criteria of whether or not the HET can operate for the given input variable combination. The conditions used for the thruster failure cases can be used as the required criteria.

These conditions could be partially justified by the validation results in previous chapter because the developed tool exhibits the thruster operation success at the experimental operating points. Because the failure cases are determined by monitoring the internal physical variables in the developed tool such as the plasma number density at the matching point, the presheath region length, and the electron mean velocity at the cathode, the constraints on the thruster operation success seem to come from a physically plausible basis. For example, the constraint on the presheath region length for case 4 entails the assumption that the noticeable presheath region is identified and accordingly, the ion backflow region in the presheath exists. This assumption entails very low radial magnetic field strength at the region near the anode. In the design perspective, this should not be a problem because low magnetic field strength can be applied in a designed HET accordingly.

Based on the discussion in section 5.3.4, the constraints can be quantitatively expressed as Equation (6.1).

$$
\begin{aligned}
g_1 &= n_{e,m}\,|_{cal} - n_{e,m}\,|_{initial} \quad \textit{corresponds to Case } 3 \\
g_2 &= z_m\,|_{cal} - dz \qquad\qquad\quad \textit{corresponds to Case } 4 \\
g_3 &= -u_{e,c}\,|_{cal} \qquad\qquad\quad \textit{corresponds to Case } 5 \\
g_4 &= -z_m\,|_{cal} + L \qquad\qquad \textit{corresponds to Case } 6
\end{aligned}
\tag{6.1}
$$

In Equation (6.1), all the variables are in non-dimensional units defined in Appendix C. In constraint 1, the calculated plasma number density at the matching must be greater than the initial guessed value. The initial guessed value is low and set to be 1e-16 $\#/m^3$. In constraint 2, dz is the length of one grid cell. If the presheath region length is less than dz, it is considered that there exists no noticeable presheath and the presheath region collapses in a very thin region near the anode. Thus, all constraints must be greater

than zero for the success of thruster operation. If any one of the constraints is violated, the HET is considered to fail to operate for the given input variable combination.

In the hope that the constraints of $g_1 \sim g_4$ could reveal the performance envelope for the given design space, the values of constraints are recorded during the DSE as well as the required metrics.
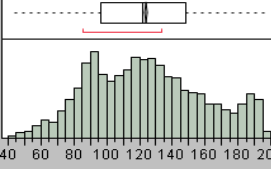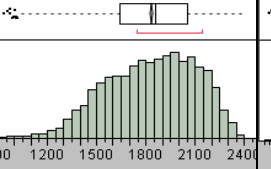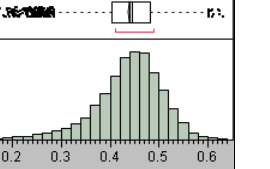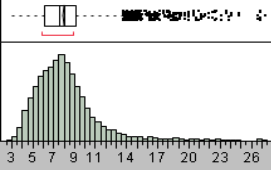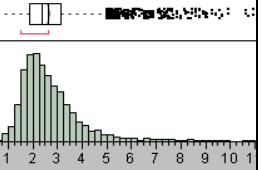
6.2.4 Analysis of the DSE Results

The results of the DSE are retrieved from ModelCenter^{TM} and analyzed in the JMP^{TM} environment. Table 6.3 shows the performance distribution and statistics for each response. Thrust shows the highest standard deviation with variations from about 40 mN to 200 mN.

The average of the total specific impulse is about 1850 sec, which varies from 950 sec to 2400 sec. The total efficiency has a short interquartile range and the maximum value which can be obtained for the current design space is 0.633. The distributions of the discharge current and the discharge power are similar. Their potential outliers are distributed in the high value region and spreads in the wide range. The mean power is 2.65 kW for the current design space, however, the current design space includes the power class from about 700 W to 10 kW, which is the intended power range.

Figure 6.2 shows the scatter plot for the responses, and shows all of the data points and the relations between each pair of responses. Based on Figure 6.2, the envelope of the feasible region can be approximately identified for each response.

Table 6.3: Performance Metric Distributions of the Design Space

	Thrust [mN]	$I_{sp,tot}$ [sec]	η_{tot}
Distribution			
Mean	124.3	1836.5	0.440
Standard Deviation	34.3	266.0	0.066
Min. ~ Max.	42.6 ~ 199.5	936.9 ~ 2398.0	0.139 ~ 0.633
Range (max. – min.)	156.9	1461.1	0.494
	I_d [A]	P_d [kW]	
Distribution			
Mean	8.00	2.65	
Standard Deviation	2.78	1.17	
Min. ~ Max.	3.00 ~ 27.41	0.69 ~ 10.97	
Range (max. – min.)	24.41	10.28	

The clear boundaries seen in the plots of total specific impulse vs. thrust and discharge power vs. discharge current come from the numerical experimental data of the CCD cases because the CCD focuses on the extremes of the design space. The boundaries are almost linear and each point inside the boundaries indicates what values of performance metrics can be obtained for each design variable combination. Because it is somewhat hard to deduce general characteristics of the relationship between performance metrics from Figure 6.2, it is worth investigating the scatter plot with data only from the CCD results to clearly identify the general relationship and which input variable causes major differences in the responses.
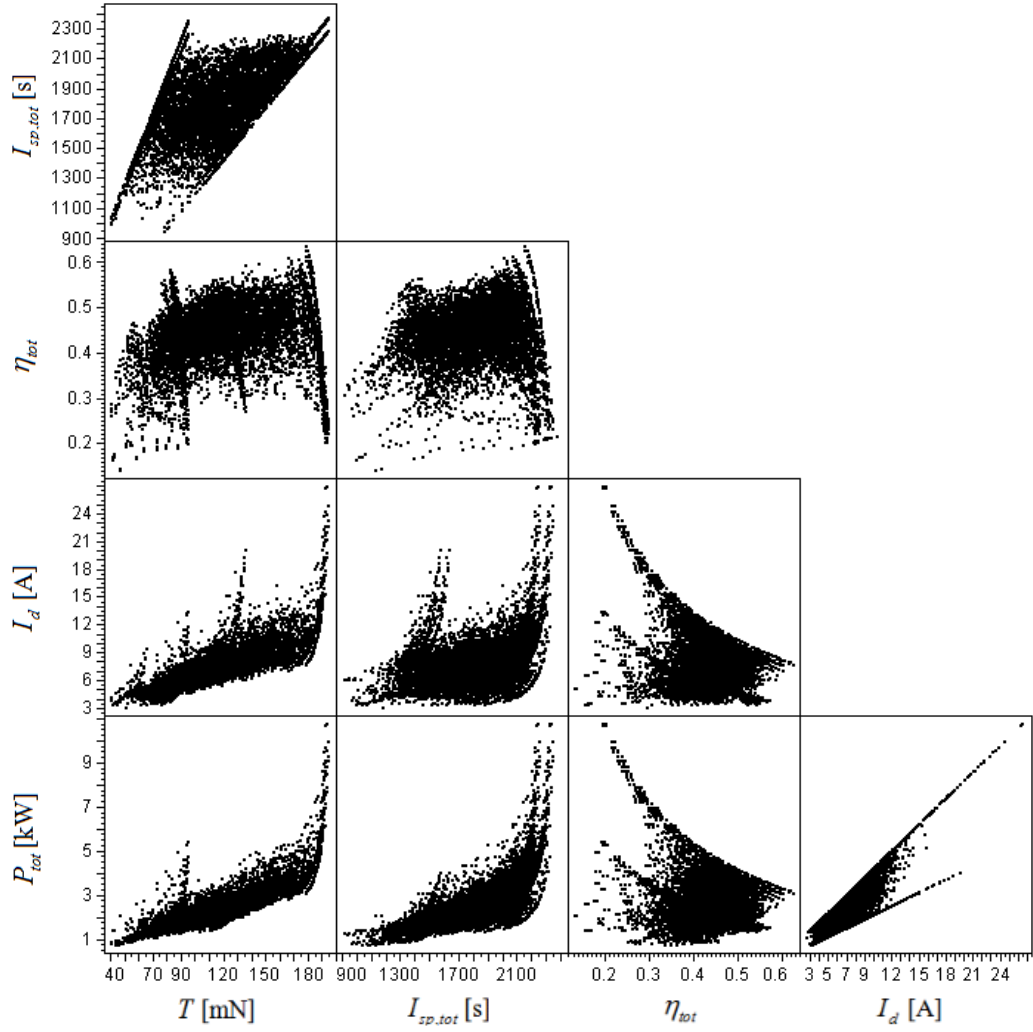
Figure 6.2: Scatter Plot for the Performance Metrics

Figure 6.3 shows the scatter plot for only the CCD cases including the input variables. It is clearly seen that the input variables have mostly extreme values in the design space and some input values are centered in the variable ranges. The two lines of input values around the center of the ranges for the outer radius (R_2) and the maximum radial magnetic field strength (B_{max}) are due to the use of the channel width (W) and the magnetic field strength difference (ΔB) between B_{max} and B_{cath}.
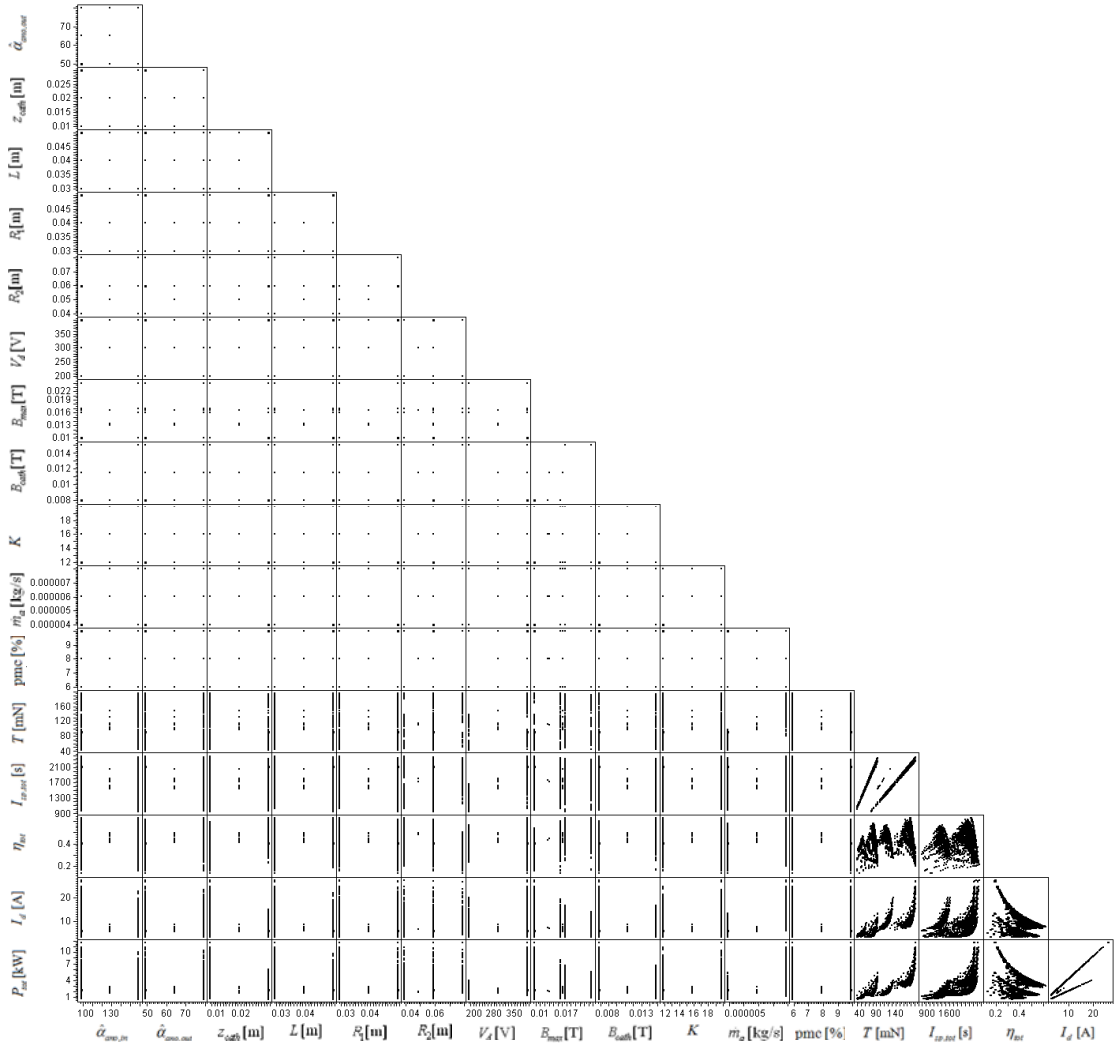
Figure 6.3: Scatter Plot for CCD Cases with Input Variables

Figure 6.4 is the enlarged scatter plot of the responses for the CCD cases. The following general observations can be made from Figure 6.4.

1) The variation of the thrust with respect to the total specific impulse is almost linear. The same relationship holds between the discharge current and the total power.

2) The variation of the total efficiency with respect to the thrust is convex and the maximum total efficiency exists in each convex region. The similar

argument can be made for the total efficiency with respect to the total specific impulse.

3) The variation of the discharge current with respect to the thrust appears to be exponential. The same holds for the discharge current with respect to the total specific impulse.

4) As the discharge current or the total power increases, the total efficiency has a decreasing trend.
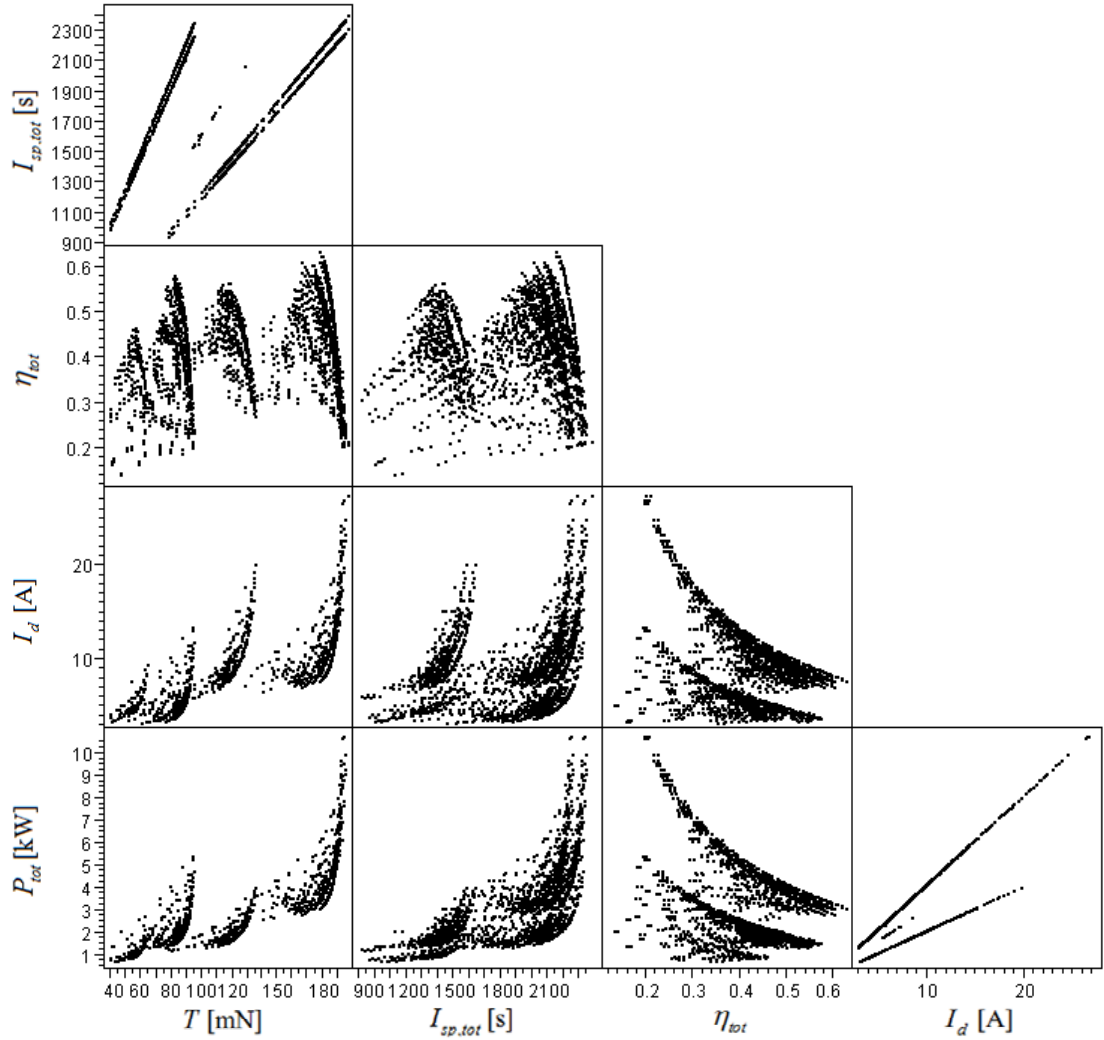
Figure 6.4: Scatter Plot of the Responses for CCD Cases

Several distinctive trends for each individual plot are clearly identified. In order to determine the cause of these distinctions, extreme values for each variable are investigated.

Figure 6.5 shows the effect of the anode mass flow rate on the responses. In the CCD experiments, there are three cases for the anode mass flow rate; 4 mg/s, 6 mg/s, and 8 mg/s. The distinct variation of the anode mass flow rate clearly separate the groups in individual scatter plots except for plots of total specific impulse vs. total efficiency, and discharge current vs. total power.
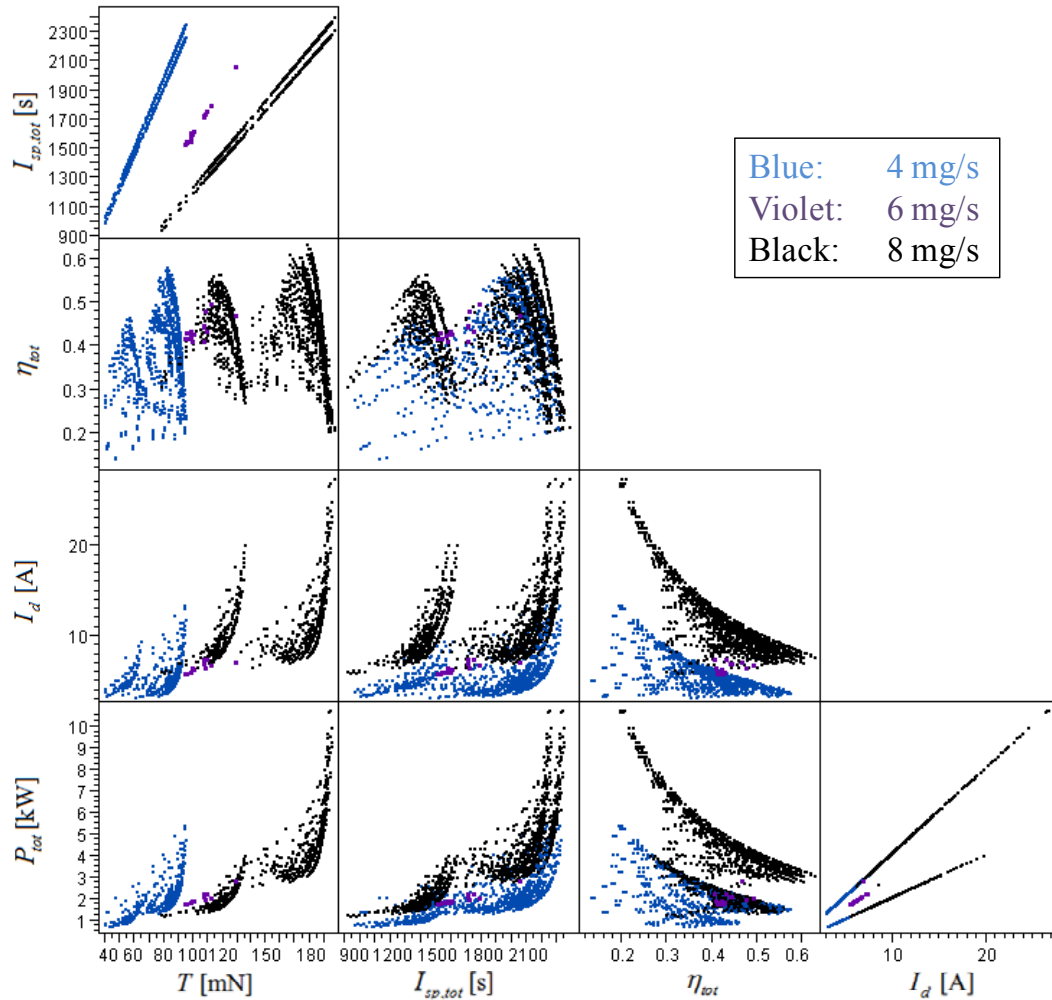
Figure 6.5: Effect of Anode Mass Flow

The following observations can be made based on Figure 6.5.

1) The anode mass flow rate variation has clear effects on the thrust and the discharge current.

2) The magnitude of the anode mass flow rate limits the possible range of the thrust and the discharge current.

3) Each anode mass flow rate follows a different relation between thrust and the total specific impulse.
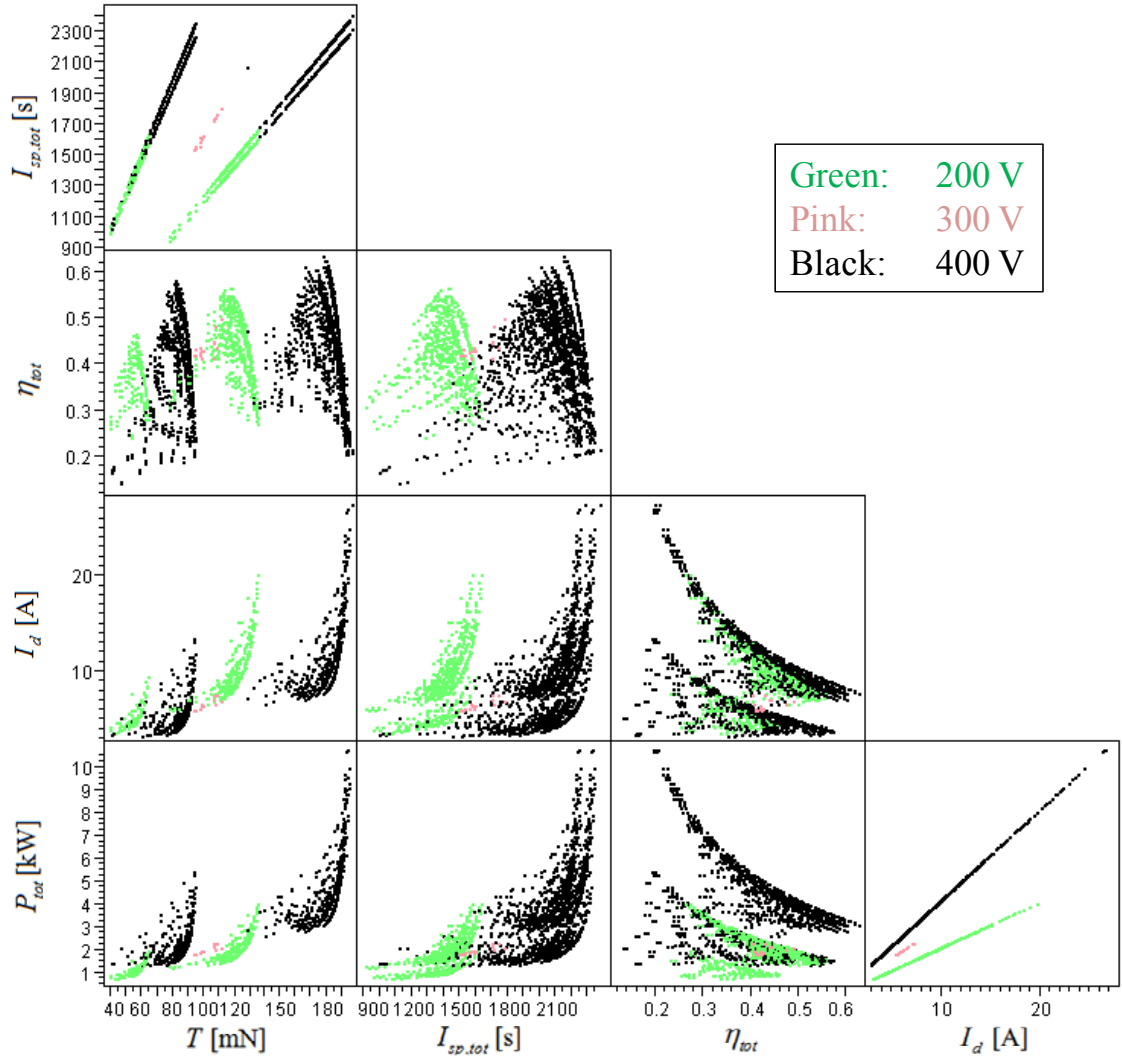
Figure 6.6: Effect of Discharge Voltage

Figure 6.6 shows the effect of the discharge voltage on the responses. There are three cases which are 200 V, 300 V, and 400 V. The distinctive regions are also identified in plots of thrust vs. total efficiency, and total specific impulse vs. total efficiency. The following observations can be made for the discharge voltage variations.

1) The discharge voltage variation has clear effects on the total specific impulse and the total power.

2) The effect of the discharge voltage variation clearly limits the possible ranges of total specific impulse, but weakly limits the total power range.

3) The lower discharge voltage can produce more thrust than higher discharge voltage with the proper values of other parameters.

4) Each discharge voltage follows a different relationship between the discharge current and the total power.

Although the discharge current and the total power are increased, it is interesting to note that the combination of increased discharge voltage and increased anode mass flow rate produces slightly higher maximum attainable total efficiency.

Figure 6.7 shows the effect of the outer radius of the channel on the responses. There are three cases which are 4 cm, 6 cm, and 8 cm. There is no distinctive region identified for the outer radius. However, the effect is given in each group of response. For example, a small radius tends to produce a higher total efficiency, a lower discharge current, and a lower total power in each group for the current design space.

There are not many noticeable effects identified for other input variable variations. One is that a higher maximum magnetic field in the given range provides slightly favorable total efficiency values for a given group.
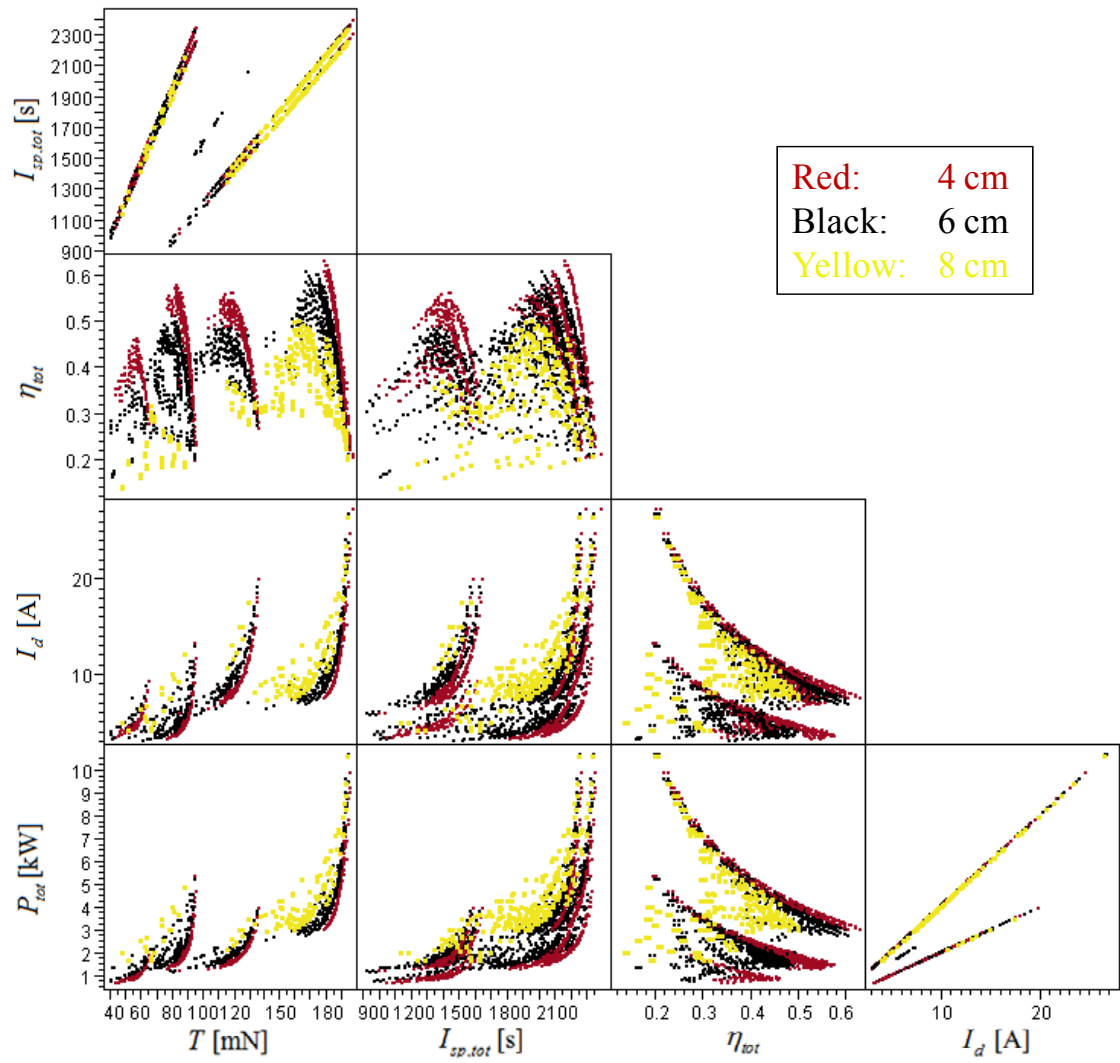
Figure 6.7: Effect of Outer Radius

CHAPTER 7

CONSTRUCTION OF SURROGATE MODELS FOR HET

7.1 Surrogate Models

The current design problem is basically a Multidisciplinary Design Optimization (MDO) with the HET design and the low-thrust trajectory optimization. A specific HET is to be designed simultaneously with the low-thrust trajectory of a spacecraft using the HET. Thus, two analysis modules are required to achieve this MDO which are shown in Figure 7.1.
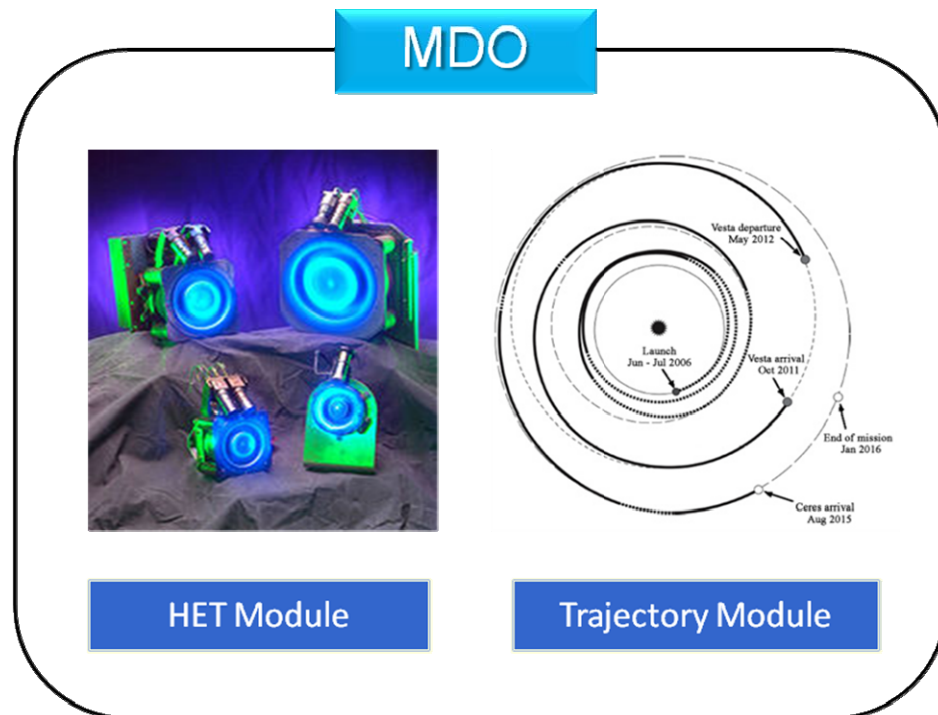
Figure 7.1: HET and Trajectory Modules in the MDO Environment [130], [5]

It is worth noting that the low-thrust trajectory optimization inherently uses optimization algorithms to find the optimal trajectory, and the performance of the electric thruster of interest is required to calculate the trajectory. The general goal of the trajectory optimization is to minimize transfer time or maximize the final spacecraft mass. The traditional low-thrust trajectory optimization has been done with a specifically chosen simple electric thruster performance model as explained in section 1.7. As a result, the thruster performance is fixed during the trajectory optimization except for the thrust. On the other hand, the thruster performance needs to be varied in the current MDO, which means that both the HET and the low-thrust trajectory are to be optimized simultaneously to minimize transfer time or maximize the final spacecraft mass.

For this purpose, the HET performance analysis module and the trajectory analysis module are combined under the global optimization environment and solved simultaneously. Because it is expected that there are potentially thousands of function calls for both modules during the optimization, it is highly desirable to construct proper surrogate models for the HET. Although the developed tool (prior chapters) is numerically efficient, more computationally efficient models, i.e., surrogate models for each performance metric are demanded for the MDO purpose. Furthermore, the surrogate models of the HET must produce performances for the given input variables close to those from the actual developed tool. The acquired data from the DSE can be used to construct the surrogate models of the HET by using a variety of statistical methods.

7.2 Surrogate Models for Performance Metrics using Response Surface Methodology

In order to construct the surrogate models for the performance metrics, only the input variable combinations which guarantee the success of the thruster operation are used because all of the performance metrics are set to zero for the failure cases. The response surface methodology (RSM) is initially used to create the models due to its simplicity. The data regression is done by JMP[TM] as before.
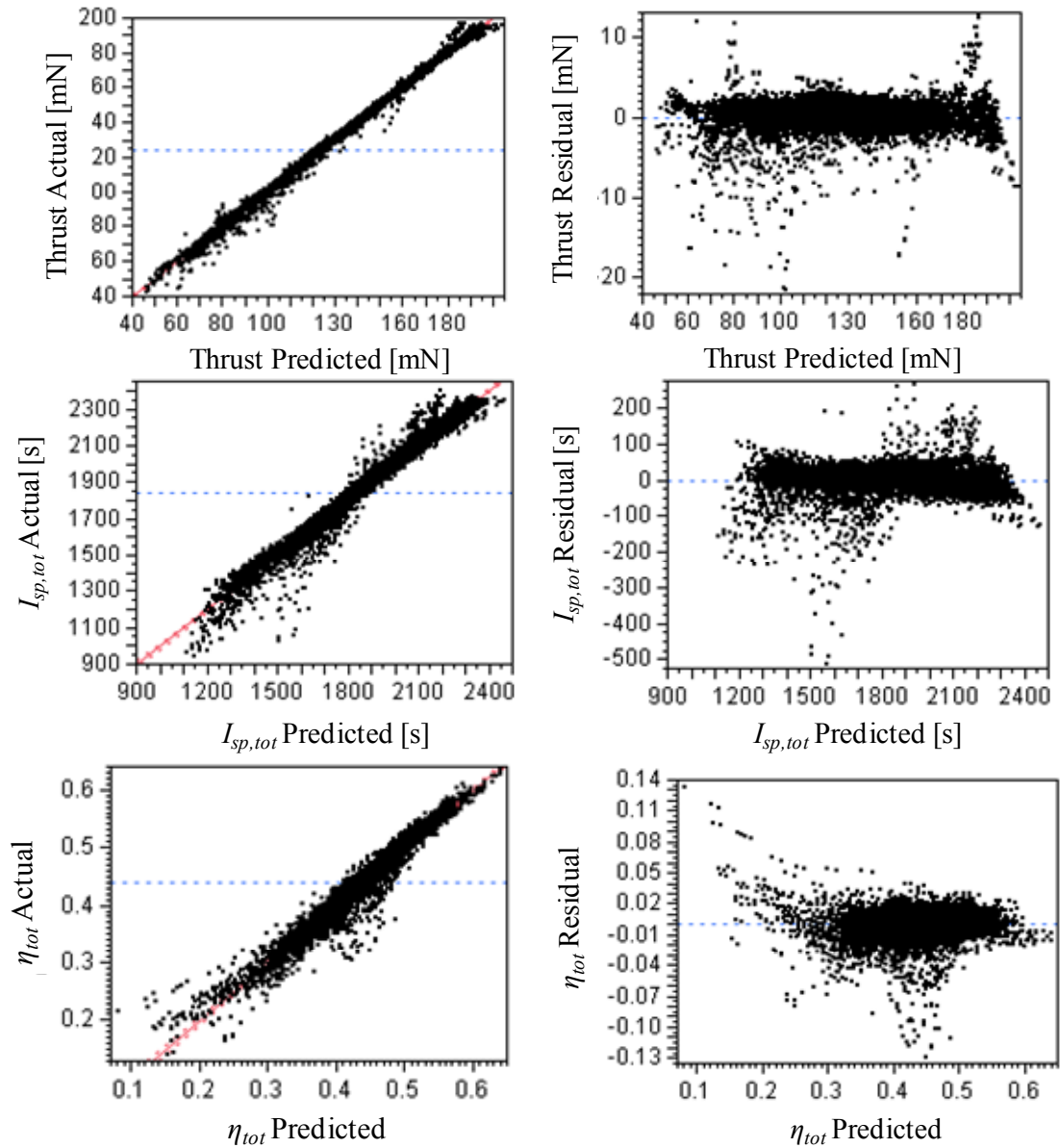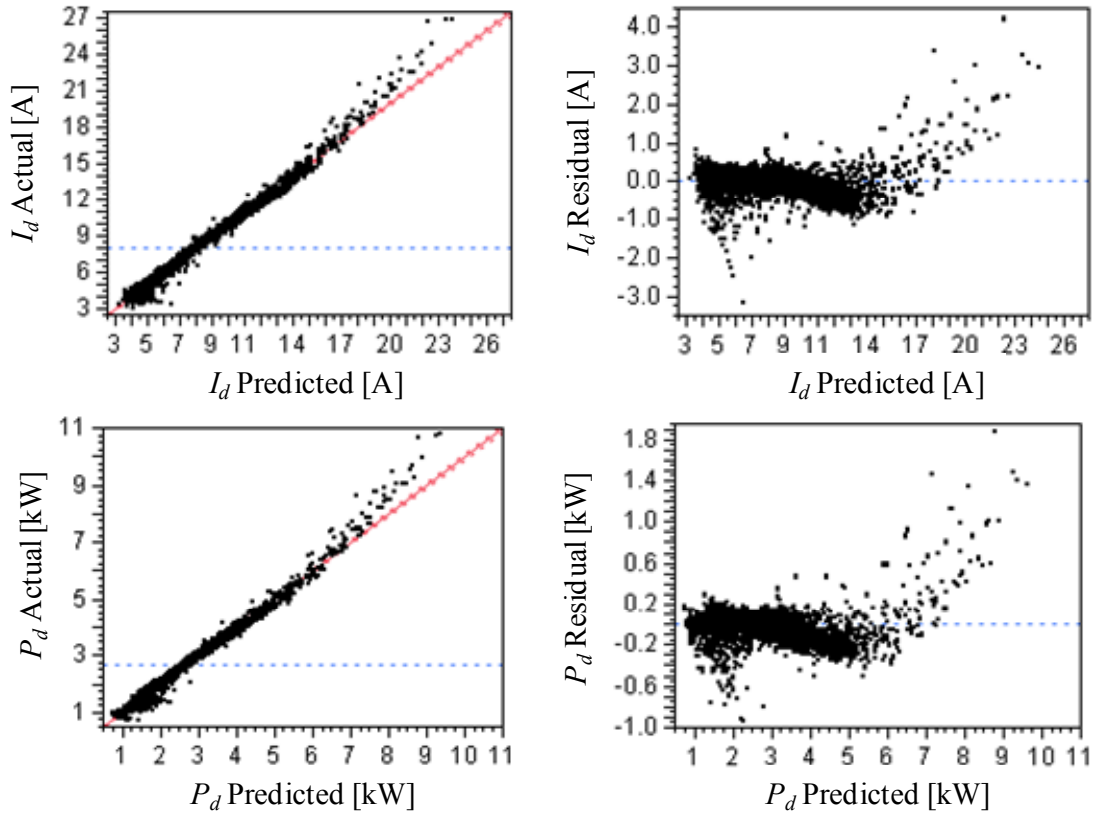
Figure 7.2: Actual by Predicted (left) and Residual by Predicted (right) Plots
For Thrust, I_{sp_tot}, η_{tot}, I_d, P_d from Top

Figure 7.2 shows the actual by predicted and residual by predicted plots for the concerned metrics. Some of figures show chunks and deviations from correct fits, which indicates that higher order regression methods should be recommended.

Table 7.1: Goodness of Fit Results

Metric	R^2	R^2_{adj}	RMSE	Mean of Response
T [mN]	0.9957	0.9957	2.2577	124.3
$I_{sp,tot}$ [s]	0.9755	0.9752	41.8496	1836.5
η_{tot}	0.9493	0.9487	0.0149	0.4395
I_d [A]	0.9852	0.9850	0.3401	8.00
P_d [kW]	0.9855	0.9853	0.1415	2.65

Table 7.1 lists the corresponding goodness of fits. The overall regression results seem to be unsatisfactory although R^2's for all metrics are over 0.9. The goodness of the

total efficiency fit is the lowest. Therefore, a more sophisticated regression method is required to obtain accurate surrogate models.

7.3 Neural Network Implementation for Performance Metric Surrogate Models

The second approach is to use the Neural Networks (NNs) to obtain more accurate surrogate models for the performance metrics. The NN has been used in many different areas of industry, business, science, and engineering since it was inspired by the biological system of human brain functions [135].

The NN basically mimic the human brain cells by something called artificial neurons, the basic structure of which is shown in Figure 7.3.
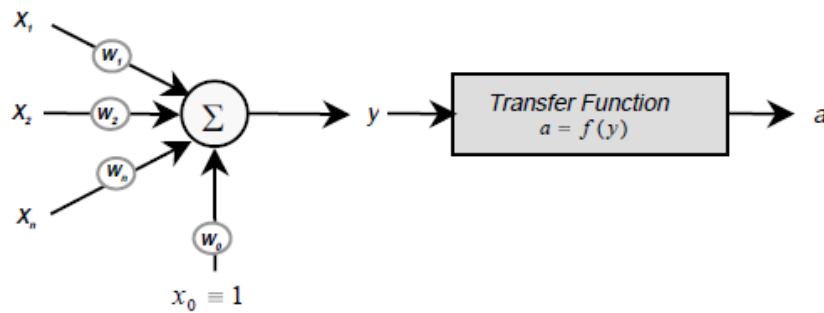
Figure 7.3: Basic Structure of an Artificial Neuron [136]

In principle, any transfer function can be used to produce the outputs. The basic structure of the NNs is shown in Figure 7.4.
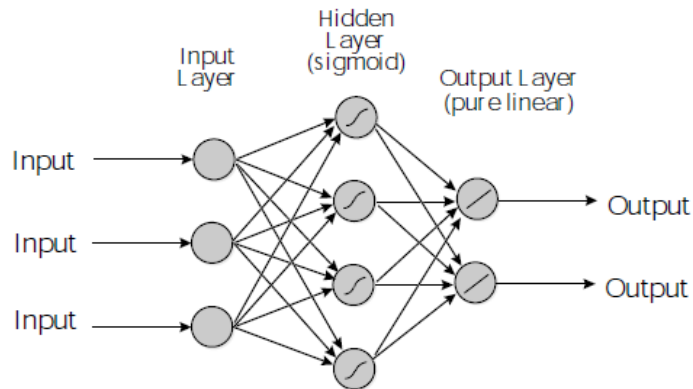
Figure 7.4: Basic Structure of the NNs [136]

When the NNs are used for the regression purpose, several advantages can be gained. They can handle highly nonlinear problems and the final regression equation is given in a closed-form. The NNs can also handle continuous and discrete responses. Although it is relatively more difficult to create and use than the RSM, the advantages are fully appreciated once the corresponding NNs are created.

For the current purpose, the "BRAINN" program, which has been created in the ASDL, is used. The purpose of this program is to provide the users with the automated generation of neural network regressions [137]. The program is written in MATLAB^{TM} language and utilizes the Neural Net Toolbox in MATLAB^{TM}. The snapshot of the program is shown in Figure 7.5.
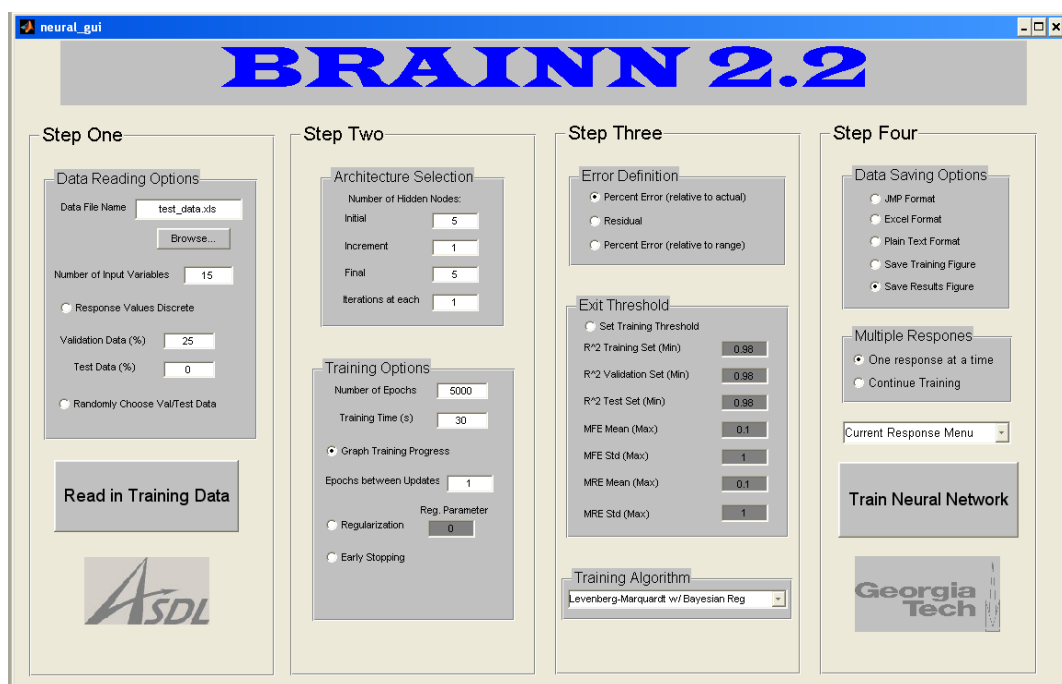
Figure 7.5: Snapshot of BRAINN Program [137]

In order to utilize the "BRAINN", additional data sets are required such as validation data and test data. The original data set is taken as a training data set used to determine the Model Fit Error (MFE) of the resultant network. The validation data set is

used to determine the best network during the training process with the training data set, which has a minimum generalization error known as the Model Representation Error (MRE). As a result, the chosen optimal network is dependent on the validation set. In order to assess the pure generalization error, the independent data set is required and is called the test data set.

The data set which is a combination of the CCD and LHS in Table 6.2 is used as the training data set. Addition DOEs are performed to generate a validation and test data set. The information of these data sets is given in Table 7.2

Table 7.2: Validation and Test Data Sets

Data	Design	# of cases	# of retrieved data from ModelCenter^{TM}	# of success	# of failure
Validation	LHS	2000	1994	1110 (55.67%)	884
Test	LHS	4121	4102	2311 (56.34%)	1791

The initial number of hidden nodes is set to 20. The training algorithm is chosen to be Levenberg-Marquardt with Bayesian Regularization, where the regularization parameter is automatically chosen by a Bayesian approach. This method is known to be the best at providing the best generalization possible. The Levenberg-Marquardt method uses a mix of a quasi-Newton method and a gradient based method. Thus it still requires the calculation of the Jacobian matrix. The regularization method is used to reduce the generalization error of a NN during the training optimization process by changing the objective function.

The cases used to create NN surrogate models total 11153 cases, which are success cases of thruster operation for the given input variable combination. The results are shown in Figure 7.6.

Model Fit Error (MFE)

MFE Mean =0.014076
MFE St Dev =0.91452

Model Representation Error (MRE)

MRE Mean =0.021585
MRE St Dev =0.91246

η_{tot} Actual

Test
Validation
Training
Perfect fit line

Hidden Nodes = 20
R2 Training =0.99529

η_{tot} Predicted

η_{tot} Residual

R2 Validation =0.99244
R2 Test =0.99228

η_{tot} Predicted

Model Fit Error (MFE)

MFE Mean =0.0093585
MFE St Dev =0.21049

Model Representation Error (MRE)

MRE Mean =0.0098111
MRE St Dev =0.17499

I_d Actual [A]

Test
Validation
Training
Perfect fit line

Hidden Nodes = 20
R2 Training =0.99966

I_d Predicted [A]

I_d Residual [A]

R2 Validation =0.99949
R2 Test =0.99945

I_d Predicted [A]

187

Figure 7.6: NN Regression Results For Thrust, I_{sp_tot}, η_{tot}, I_d, and P_d from Top

As seen in Figure 7.6, the NNs work well for the current regression. The resultant number of hidden nodes is 20 for all responses, which is the same as the initial value. The training R^2's are all over 0.995 as well as the test R^2. The MFE and the MSE show considerably low errors. Because the total specific impulse and the total efficiency exhibit relatively larger errors among 5 responses, more investigation on the regression errors is performed. Figure 7.7 shows the percent range errors for both of these responses. The error is relatively large at the lower total specific impulse range and it decreases as the total specific impulse increases. The maximum error is 11.18%, the minimum is 0.01%, and the average range error is 1.37%. For the total efficiency, the errors around $\eta_{tot} = 0.35$ are relatively large and decreases away from that point. The error is very small

at higher total efficiency as in the total specific impulse. The maximum error is 15.01%, the minimum is 0.01%, and the average range error is 2.51%.
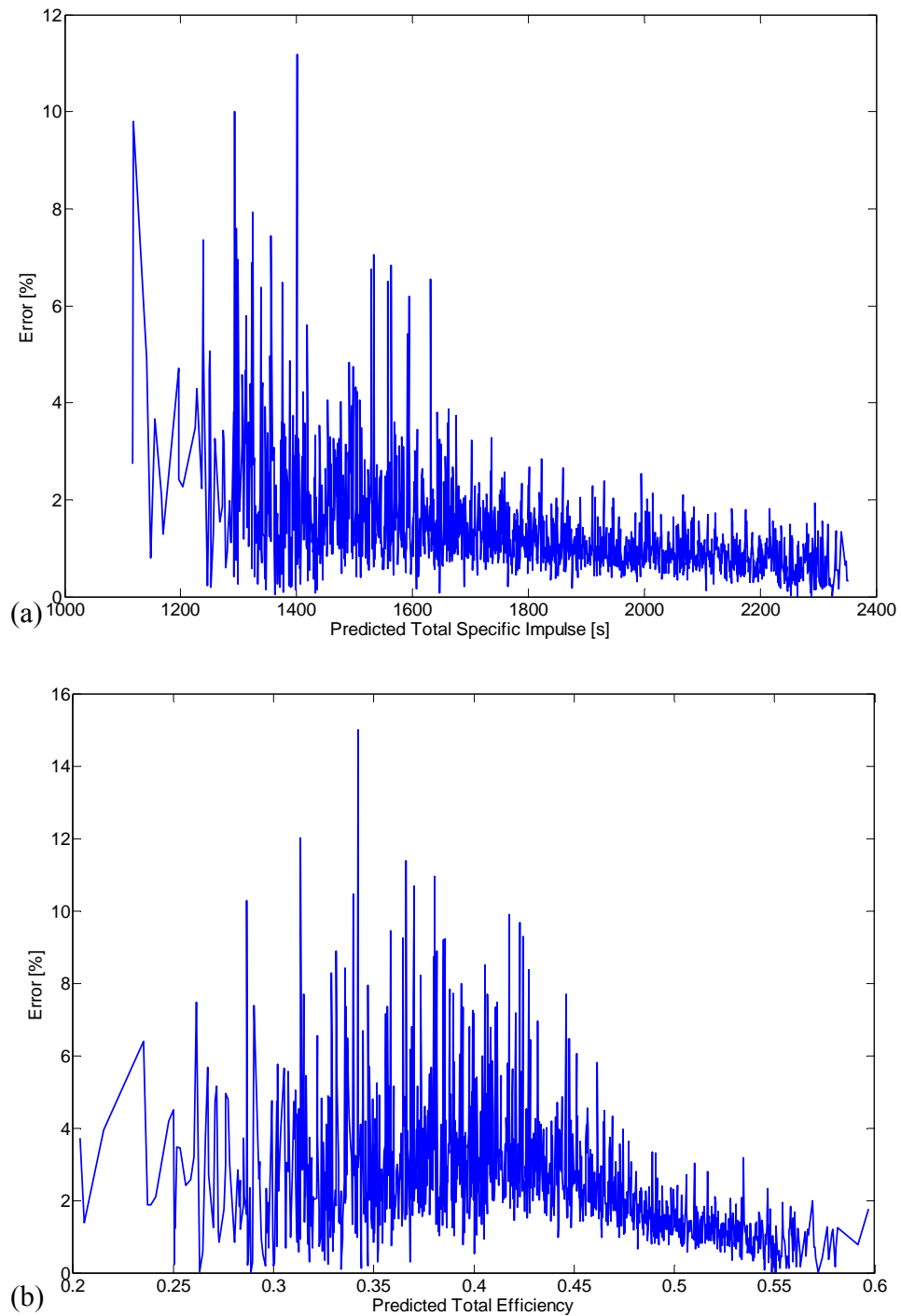
Figure 7.7: Percent Range Errors (a) Total Specific Impulse and (b) Total Efficiency

In conclusion, the surrogate models created by the NNs are taken as a performance response module for the HET in the MDO environment.

7.4 Surrogate Models for Constraints

7.4.1 General Considerations on Constraints

The constraint values from the DOE are given according to Equation (6.1). When trying to obtain the surrogate models for constraints, additional consideration is required. The constraints are basically required to check whether each combination of design variables yields thruster operation failure or not. The important thing about constraints is to find the boundary of these constraints because the optimum solution usually lies in the constraint boundaries as seen in Figure 7.8.
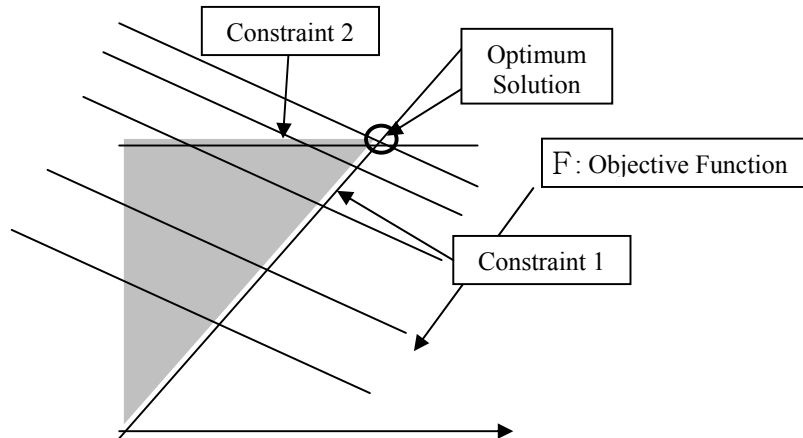
Figure 7.8: General Optimization Problem

Another thing which must be considered is that the existing low-thrust trajectory optimization module in the MDO will be used and it employs a gradient-based optimization algorithm. The gradient based optimization requires that the objective function and the constraints all be continuous functions. Therefore, there are two

objectives when building the surrogate models for the constraints: the constraints must clearly identify the boundary, and the constraint functions must be continuous.

However, the constraint values of the thruster operation failure cases are obtained as intermediate internal physical values because the developed tool cannot proceed to produce the solutions as explained in section 5.3.4. In cases of the thruster operation success, these constraint values, of course, are the converged values based on the plasma number density at the matching point, the presheath region length, and the electron mean velocity at the cathode. Therefore, if the regressions on these constraint values were to be used and include the thruster operation failure cases, it is expected to be very poor. Furthermore, it is also expected that the boundary separating the combinations into operation success and failure is even harder to recognize.

Figure 7.9 shows the entire design space and the feasible region enclosed by the boundary. The optimization in the MDO environment must be done in the feasible thruster operation region.
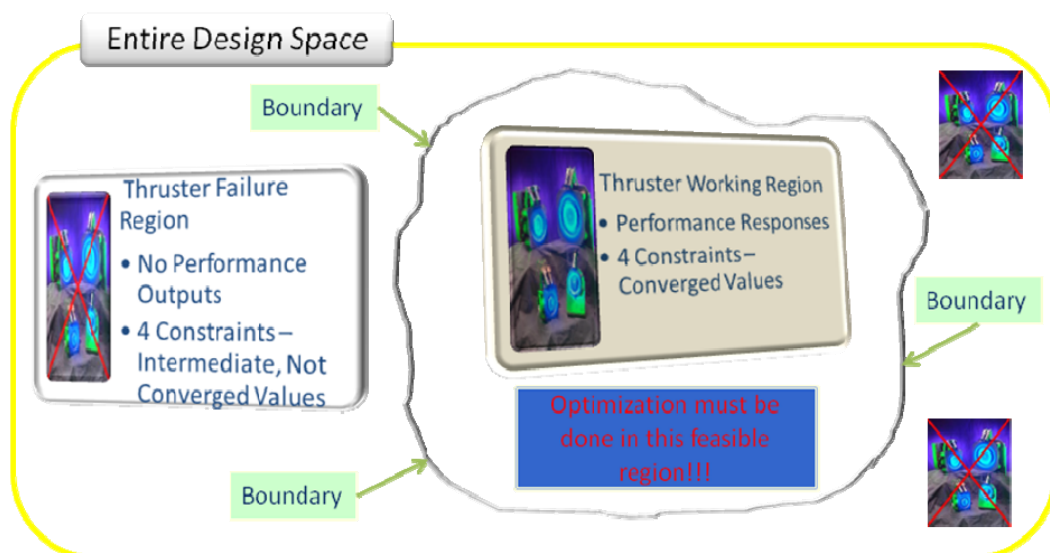
Figure 7.9: Design Space and Feasible Region

7.4.2 Use of Response Surface Methodology

As an initial attempt to obtain continuous constraint functions, the RSM is applied to only the thruster operation success cases of data listed in Table 6.2 as was done with the performance responses. The regression results for 4 constraints are shown in Table 7.3.

Table 7.3: Goodness of Fit for the Constraints

	g_1	g_2	g_3	g_4
R^2	0.9852	0.9871	0.9884	0.9770

All show reasonable goodness of fits. The resultant constraint surrogate models are tested with the original data. The test results are shown in Table 7.4. As seen in Table 7.4, it can be concluded that the resultant constraint surrogate models are not satisfactory because there are numerous cases in which the surrogate models fail to predict actual constraint values. Most prediction failures occur when the actual constraint values less than 0 while predicted constraint values are greater zero. This unsatisfactory regression can be also seen from Figure 7.10, which shows an actual by predicted plot for g_1. The prediction failure region is clearly identified. The success cases are well regressed and aligned to the perfect fit line. The irregular distribution is shown for the failure cases due to non-convergent constraint values.

Table 7.4: Test Results of Constraint Surrogate Models

Case	g_1	g_2	g_3	g_4
$g > 0, g_{pred} > 0$	7732	13972	9204	11402
$g < 0, g_{pred} < 0$	937	0	0	81
$g < 0, g_{pred} > 0$	_**5424**_	_**121**_	_**4889**_	_**856**_
$g > 0, g_{pred} < 0$	_**0**_	_**0**_	_**0**_	_**1754**_
Total	14093	14093	14093	14093
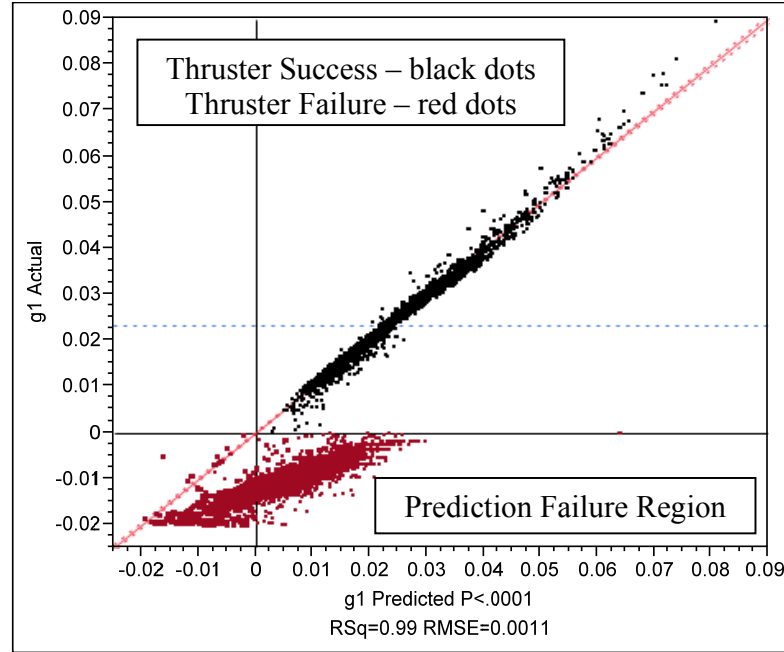
Figure 7.10: Actual by Predicted Plot for g_1

In the hope of further improving the regression, the next attempt is to do the full regression using the same RSM including the thruster operation failure cases. The goodness of fits for this regression is shown in Table 7.5.

Table 7.5: Goodness of Fit with All Cases

	g_1	g_2	g_3	g_4
R^2	0.8521	0.3241	0.5490	0.9342

The goodness of fits is greatly reduced when including the thruster operation failure cases. This is mainly because the constraint values for the failure cases are non-convergent values. The test is also done with the original data and is shown in Table 7.6. It is identified that prediction capability of newly obtained surrogate models is improved. However, there are still many cases that the surrogate models fail to predict correctly.

These observations can be confirmed more clearly in Figure 7.11. The area of the prediction failure region is clearly reduced. However, in this case, another prediction

failure region is identified, which is the left upper quadrant region in Figure 7.11. In this region, the predicted values are less than zero while the actual constraint values are greater than zero.

Table 7.6: Test Results of Constraint Surrogate Models with All Cases

Case	g_1	g_2	g_3	g_4
$g > 0, g_{pred} > 0$	7720	13942	8510	11871
$g < 0, g_{pred} < 0$	4188	0	3721	141
$g < 0, g_{pred} > 0$	_**2173**_	_**121**_	_**1168**_	_**796**_
$g > 0, g_{pred} < 0$	_**12**_	_**30**_	_**694**_	_**1285**_
Total	14093	14093	14093	14093
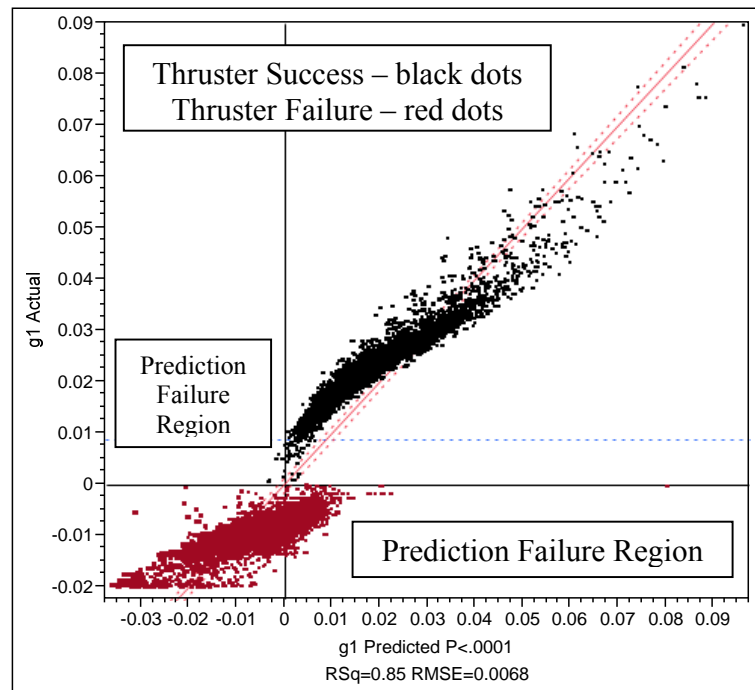
Figure 7.11: Actual by Predicted Plot for g_1 with All Cases

From Figure 7.11, it is also identified that the success cases show some trend while the failure cases show no clear trend. This should not be surprising because constraint values of the failure cases do not come from the converged solution. The

194

success cases show distortion with respected to the perfect fit line compared to the previous case. In conclusion, it is not possible to construct good surrogate models for the failure cases even if the sophisticated regression methodology is used due to intermediate constraint values. In addition, it is expected from the regression experiments that the constraint boundary will also be hard to identify.

7.4.3 Constraints as a Classification

The purpose of the attempts to obtain surrogate models for the constraints is intended to find continuous functions which will be used in the gradient-based optimization. Because the regression does not seem to be a good candidate for finding these boundaries, the view of this problem is changed into a classification problem. Therefore, the current task can be thought to solve a classification problem between the thruster operation success and the thruster operation failure for any given input variable combination.

A typical classification method is the Tree-Based method. In this method, the feature space is partitioned into rectangles. The feature space here is equivalent to the design space of the current problem. The resultant partitions can be ultimately represented by a binary tree, which is why the method is called the Tree-Based method. The schematic of the Tree-Based method is shown in Figure 7.12.

The fit for classification is done independently for each partition. A main issue in this method is tree pruning. For further information, refer to Ref. [138]. Although this method has been well developed for the classification purpose, it is not likely to be a good candidate for the current purpose. Because the method involves partitioning and different fit models for each partition, conditional judgment is required and the

discontinuity may occur at the boundary between partitions. As a result, the classifier from this method will not be a continuous function, which is not a desirable characteristic for the gradient based optimizer.
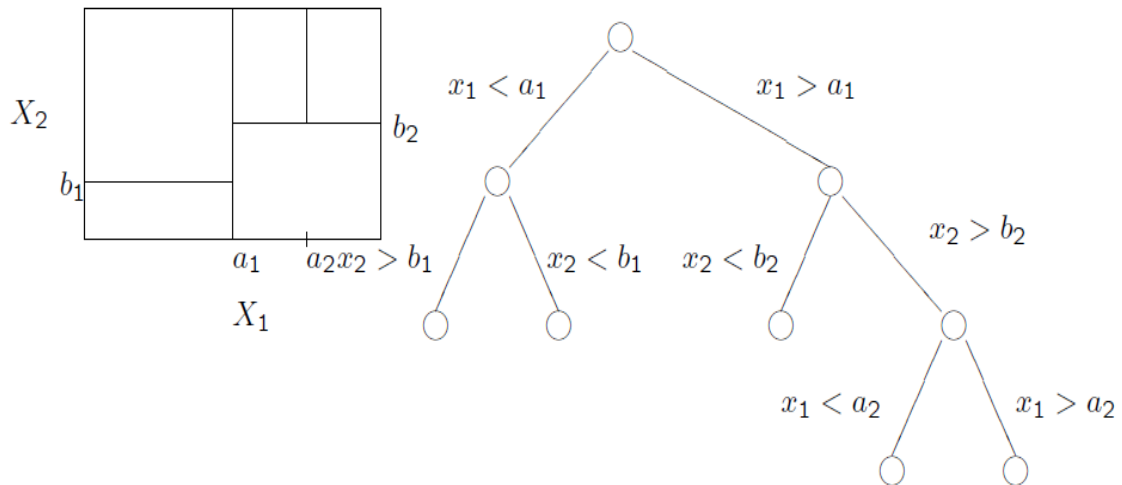
Figure 7.12: Tree-Based Method

The algorithm of the NN classifier is also applied independently for each class of the training data. Although the output from the classifier is continuous due to the continuous activation functions, the classification with the continuous output is not that accurate. Thus, a post-processing compete function is usually used which involves the action of taking the maximum value among the output nodes. This also causes a discontinuity phenomenon.

Two difficulties are identified when dealing with the constraints and finding the feasible region. First, the usual classification algorithm cannot provide the continuous constraint functions due to a conditional statement or taking a maximum value among the output node values for the NN classifier, which makes it impossible to calculate the derivatives of constraint functions. Second, the usual regression methods cannot provide good classification accuracy due to non-convergent constraint values.

196

7.4.4 Support Vector Machine Classifier as a Constraint Function

The idea to resolve these difficulties is to use a Support Vector Machine (SVM) classification algorithm. The SVM is a supervised learning method based on statistical learning theory and its applications are classification and regression. The initial development work is attributed mostly to Vapnik [139]. The SVM has been gaining increasing attention and popularity due to many attractive features, and promising empirical performance [140]. In addition to the basic statistical learning application, areas of application are also increasing throughout science and engineering [141] - [142].

The classification problem in the SVM is to find an optimal hyperplane to separate the data as shown in Figure 7.13. The hyperplane is a general term for separator for any dimensional space. It will be a point for 1-D case, a line for 2-D case, or a plane for 3-D case. The optimal hyperplane is a hyperplane which maximizes the margin. The margin is the distance between the hyperplane and the nearest data point of each class.
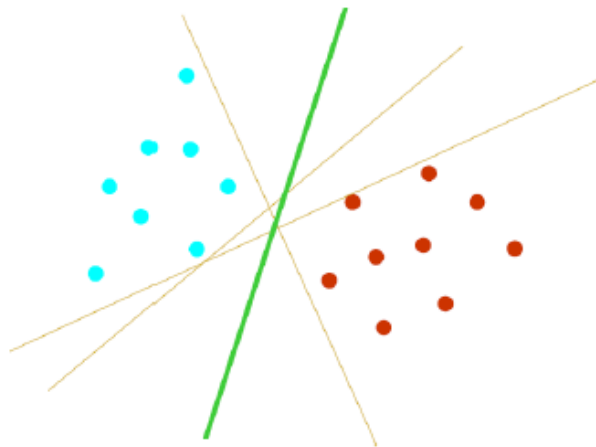
Figure 7.13: Optimal Separating Hyperplane [140]

Thus, calculation of the SVM classifier involves an optimization problem to find the optimal hyperplane. The simple binary classification and the corresponding classifier are shown in the left of Figure 7.14. The nearest points from the optimal hyperplane are

called the Support Vectors. Example of the support vectors and margin are shown on the right of Figure 7.14.
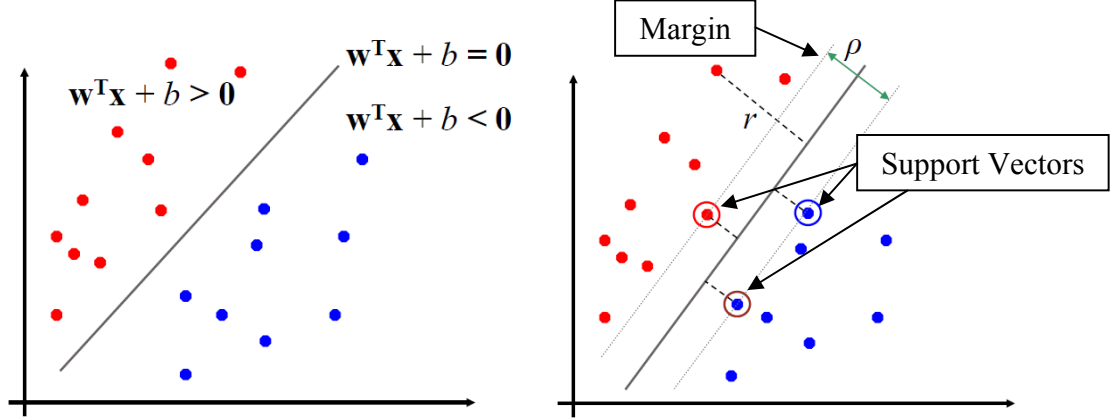
Figure 7.14: Binary Classification (left), Support Vectors and Margin (right) [143]

For the linear SVM case, the quadratic optimization problem can be formed to find the optimal hyperplane as shown in Equation (7.1).

$$
\max_{\vec{w},b} \ \rho = \frac{2}{\| \vec{w} \|}
$$
$$
s.t. \ \ y_i(\vec{w}^T \vec{x}_i + b) \geq 1, \ \ for \ all \ (\vec{x}_i, y_i), i = 1, \ldots, n
$$
(7.1)

where ρ is the margin, $\vec{w}$ is the coefficient vector of the hyperplane, b is the intercept term, $\vec{x}_i$ is the ith point vector, and y_i is the classifier of $\vec{x}_i$ which has the value of -1 or 1. Equation (7.1) can be reformulated as

$$
\min \ \Phi(\vec{w}) = \vec{w}^T \vec{w}
$$
$$
s.t. \ \ y_i(\vec{w}^T \vec{x}_i + b) \geq 1, \ \ for \ all \ (\vec{x}_i, y_i), i = 1, \ldots, n
$$
(7.2)

The usual strategy of solving Equation (7.2) is to convert it to a dual problem using Lagrange multipliers, $\vec{\alpha}$, and the problem can be expressed as

$$\max Q(\vec{\alpha}) = \sum_{i=1}^{n} \alpha_i - \tfrac{1}{2} \sum_{i=1}^{n} \sum_{j=1}^{n} \alpha_i \alpha_j y_i y_j \vec{x}_i^T \vec{x}_j$$

$$s.t. \ \sum_{i=1}^{n} \alpha_i y_i = 0 \ \ and \ \ \alpha_i \geq 0 \ for \ all \ \alpha_i$$

(7.3)

The problem is to find $\vec{\alpha}$ which maximize $Q(\vec{\alpha})$. The solutions are given by

$$\vec{w} = \sum_{i=1}^{n} \alpha_i y_i \vec{x}_i \qquad b = y_k - \sum_{i=1}^{n} \alpha_i y_i \vec{x}_i^T \vec{x}_k \ \ for \ any \ \alpha_i > 0$$

(7.4)

The corresponding classifier is then obtained as

$$f(\vec{x}) = \sum_{i=1}^{n} \alpha_i y_i \vec{x}_i^T \vec{x} + b$$

(7.5)

Note that there is no explicit dependence on $\vec{w}$ in the final classifying function and the classifier depends on the inner product between the given arbitrary point $\vec{x}$ and the support vectors. This inner product dependency is also shown in the optimization formulation. The inner product dependence brings the idea of the kernel for the nonlinear SVM.

The nonlinear SVM uses the kernel to map the original feature space into a higher dimensional feature space. This trick is useful when classification with the original feature space is difficult. Mapping to the higher dimensional feature space can make the classification possible. This is clearly shown in Figure 7.15.

From Figure 7.15, the classification cannot be done with the original 1-D feature space. However, if the data set is mapped into the 2-D feature space, the optimal hyperplane can be effectively found. The kernel functions play a role in mapping to the higher dimensional feature space.
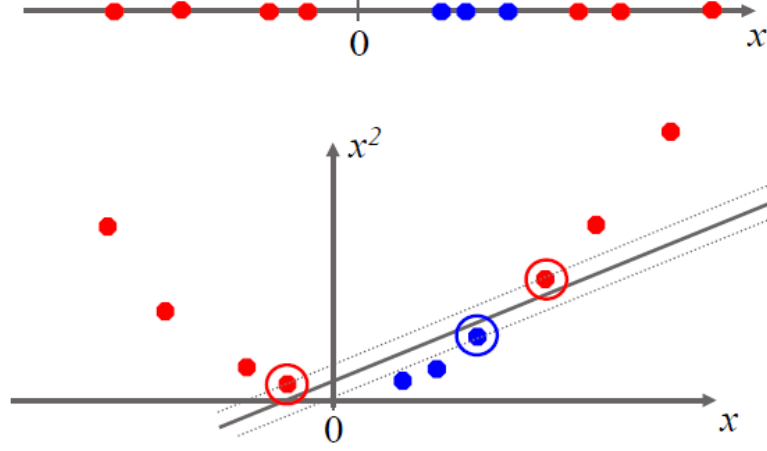
Figure 7.15: Mapping from 1-D to 2-D [143]

Because the SVMs depend on the inner products between data points during the optimization and for the classification with the optimized classifier function, the kernel function may have the form as

$$K(\vec{x}_i, \vec{x}_j) = \varphi(\vec{x}_i)^T \varphi(\vec{x}_j) \tag{7.6}$$

The general SVM dual problem formulation using the kernel function can then be expressed as

$$
\begin{aligned}
&Maximize\ Q(\vec{\alpha}) = \sum_{i=1}^{n} \alpha_i - \tfrac{1}{2} \sum_{i=1}^{n} \sum_{j=1}^{n} \alpha_i \alpha_j y_i y_j K(\vec{x}_i, \vec{x}_j) \\
&s.t,\ \ \sum_{i=1}^{n} \alpha_i y_i = 0 \qquad \alpha_i \ge 0\ for\ all\ \alpha_i
\end{aligned}
\tag{7.7}
$$

The classifier can be expressed accordingly

$$f(\vec{x}) = \sum_{i=1}^{n_s} \alpha_i y_i K(\vec{x}_i, \vec{x}) + b, \quad b = y_k - \sum_{i=1}^{n_s} \alpha_i y_i K(\vec{x}_i, \vec{x}_k)\ for\ any\ \alpha_k > 0 \tag{7.8}$$

where n_s is the number of the support vectors. The function $f(\vec{x})$ produces the distance from the constructed hyperplane to a given point. The sign of $f(\vec{x})$ determines each class. Thus it is actually a continuous function with respect to $\vec{x}$, which is a desirable

200

characteristic for the current problem. Furthermore, because the SVMs are originally intended for classification, it is expected that implementing the SVM to the current problem will resolve the aforementioned two difficulties if the value of the function, $f(\vec{x})$ is directly used without hard and soft classifications.

In order to implement the SVM, the SVM classifier in the Bioinformatics Toolbox$^{\text{TM}}$ of the MATLAB$^{\text{TM}}$ is used. The SVM classifier in this software provides three optimization methods to find the separating hyperplane, which are Quadratic Programming (QP), Least-Squares (LS), and Sequential Minimal Optimization (SMO). Because of high dimensionality and large data set of the current problem, the QP and the LS cannot be used due to computer memory limitations. Thus, the SMO is used for optimization in the SVM.

Before obtaining a desired classifying function, a proper kernel function should be selected. The SVM classifier provides 5 kinds of the kernel functions such as linear, quadratic, Gaussian Radial Basis Function, polynomial, and Multilayer Perceptron. Each kernel functions are given as

$Linear$:
$$K(\vec{x}_i, \vec{x}_j) = \vec{x}_i^T \vec{x}_j$$
$Quadratic$:
$$K(\vec{x}_i, \vec{x}_j) = (1 + \vec{x}_i^T \vec{x}_j)^2$$
$Polynomial$:
$$K(\vec{x}_i, \vec{x}_j) = (1 + \vec{x}_i^T \vec{x}_j)^p, \ p = polynomial \ order \tag{7.9}$$
$Gaussian \ Radial \ Basis \ Function$:
$$K(\vec{x}_i, \vec{x}_j) = e^{-\frac{\|\vec{x}_i - \vec{x}_j\|^2}{2\sigma^2}}, \ \sigma = scaling \ factor$$
$Multilayer \ Perceptron$:
$$K(\vec{x}_i, \vec{x}_j) = \tanh(p_1 \vec{x}_i^T \vec{x}_j + p_2), \ p_1 \& p_2 = scaling \ and \ bias \ parameters$$

The training data to find the hyperplane is taken as the same data listed in Table 6.2. In order to investigate performance of the resultant classifier, an additional data set is required. This test data set is taken from all data listed in Table 7.2. All kernel functions the SVM toolbox provides are tested. Because of the high dimensionality of the current problem, solutions are not obtained for the linear and quadratic kernel functions. For the polynomial kernel functions, solutions are not obtained up to 7th order. The 8th, 9th, and 10th order polynomial cases generate solutions and the resultant classifiers are tested with the test data set as shown in Figure 7.16.

For the Gaussian Radial Basis Function kernel, experiments are done for the scaling factor σ. The results are shown in Figure 7.17 and the correct rate is highest when $\sigma = 3$, which gives 98.33 % of the correct rate. For the Multilayer Perceptron kernel, the scaling and bias are varied, but with the assumption that absolute values of scaling and bias are the same. If the scaling factor is 0.002 and the bias is -0.002, the correct rate is the highest and its value is 96.51% shown in Figure 7.18.
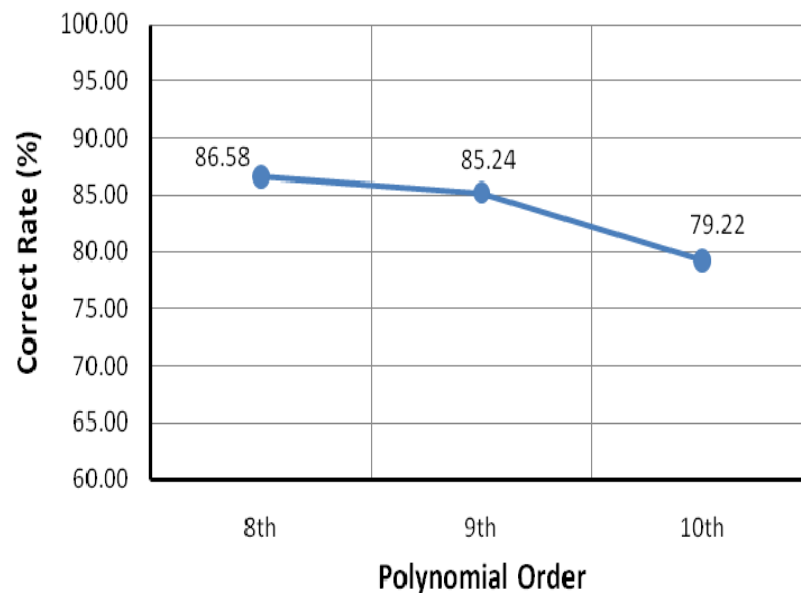
Figure 7.16: Correct Rate for Polynomial Kernel Function
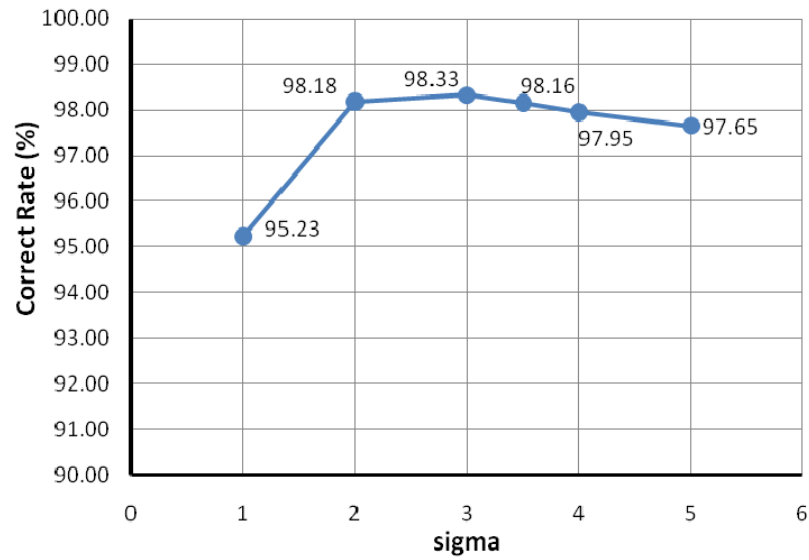
Figure 7.17: Correct Rate for Gaussian Radial Basis Function Kernel
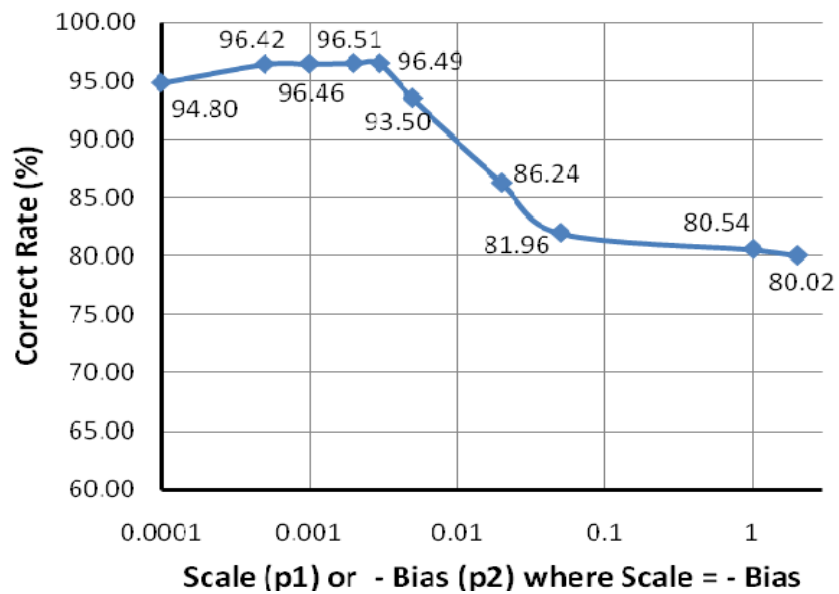
Figure 7.18: Correct Rate for Multilayer Perceptron Kernel

As a result, the Gaussian Radial Basis Function kernel gives the highest correction rate of 98.33 % for a scaling factor of $\sigma = 3$. This kernel is also tested with the training data set and it gives 98.53 % of the correct rate. The optimization using this kernel identifies a total of 2374 support vectors out of 14093 data points. The intercept,

b, is calculated to be 0.0813. The resultant constraint function is given by Equation (7.8) and it can be used as a continuous constraint function in the gradient based MDO environment with the chosen support vectors, the associated Lagrange multipliers, y_i's of the support vectors, and b.

The required constraint function generated by the SVM is set as

$$g_0(\vec{x}) = f(\vec{x}) \geq d_{\text{lower limit}} \qquad (7.10)$$

where $d_{\text{lower limit}}$ is the minimum allowable distance from the hyperplane. The normalized distance from the hyperplane and the support vectors is 1 in the SVM algorithm as seen in Figure 7.19.
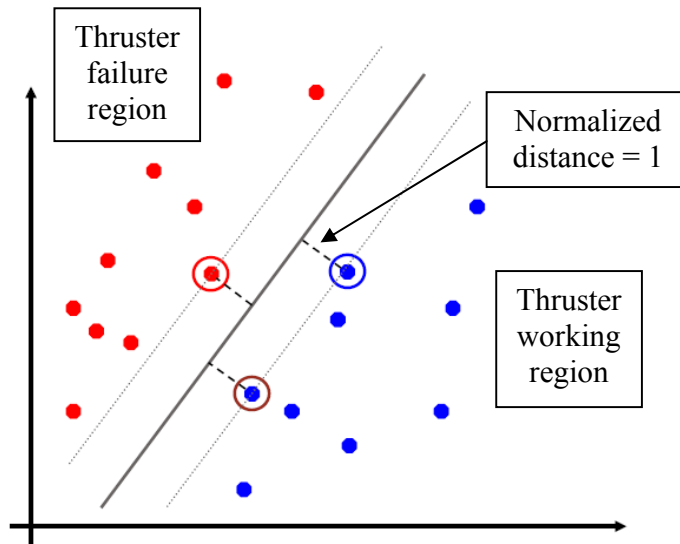
Figure 7.19: Normalized Distance Between Hyperplane and Support Vectors

Although zero can be set for $d_{\text{lower limit}}$ in Equation (7.10), it seems safer to have an increased value of $d_{\text{lower limit}}$ rather than zero to incorporate the anomalous coefficient uncertainty. The $d_{\text{lower limit}}$ can be set to 1, for example, as the lower limit down to the support vectors on the feasible region instead of setting to zero which is down to the hyperplane.

Now that the constraint function by the SVM is constructed, other constraint functions generated by the NNs using only thruster operation success cases are no longer needed. However, it would be useful to check the behavior of those constraint functions in the MDO environment in order to compare them with the performance of the SVM constraint function. All these constraints must be greater than or equal to zero to indicate the feasible region.

CHAPTER 8

SIMULTANEOUS DESIGN OPTIMIZATION FOR AN ELECTRIC

ORBIT RAISING MISSION BY COLLABORATION WORK

8.0 Acknowledgement

It is acknowledged that this chapter is written in part by the efforts of collaborators.

8.1 Mission Selection

The missions with SEP can be applied to such cases where a large acceleration is not required and additional increased time of flight is not a significant factor [144]. Furthermore, as seen in Figure 1.1, SEP increases the possibility of achieving the high ΔV missions to which chemical propulsion is not applicable.

However, if a new HET is considered and designed, near-Earth missions should be the focus because it is not expected that a new HET would be developed for a single mission such as the Discovery class missions nor solar system explorations, or deep space missions due to the large cost of new HET development. The near-Earth missions have benefits in that there is still a high demand for communications satellites worldwide and other near-Earth applications. If the advantages of SEP are fully appreciated with these missions, more performance enhancement and cost-effective satellite operations can be realized.

GEO satellites are now commonly using SEP for stationkeeping purposes. In order to obtain greater mass transportation or extension of satellite lifetime while reducing the launch cost, missions including near-Earth transfers using SEP should be considered for future applications. Especially for the GEO satellites, combinations of transfers and stationkeeping could produce considerable benefits from a systems perspective compared to the present bi-propellant systems for an apogee insertion and stationkeeping scenario, which requires about half of the total mass of the GEO satellites for the propellant in the GTO [145]. Thus, there is a high possibility of increased use of SEP for near-Earth missions and it is expected to increase in the near future.

However, due to long time of transfer with SEP, there are risks involving transfers starting from the LEO such as radiation exposure in the Van Allen Radiation Belts and collision with Earth-orbiting debris. Therefore, the mission considered here is the Orbit Raising Mission (ORM). Generally speaking, the ORM refers to transportation from a transfer orbit to the GEO regardless of the type of propulsion system. The ORM using the electric thruster is termed as Electric Orbit Raising (EOR). The transfer mission from the GTO to the GEO using the EOR has been researched with top-level analysis [146] and found in some low-thruster trajectory optimization papers [147] - [149]. This transfer mission still needs a transfer time on the order of 150 days and the number of revolutions on the order of 200. In addition, a large part of the transfer trajectory is still exposed to a high concentration of radiation. These drawbacks prevent the EOR from being part of commercial applications.

In the low-thrust trajectory optimization perspective, problems with such a large number of revolutions are difficult because the problems are often ill-posed and

numerically difficult to solve. Hence, a mission which is more probable in the near term and numerically easier to solve is considered. David et al. investigated mixed chemical-electric ORMs and showed the analytic results of analysis and optimization as well as an economic benefit analysis [150] - [152]. The research showed that the HET is the most appropriate system due to its operating exhaust velocity which is close to the derived optimal values of their investigation.

The mission costs of the mixed chemical-electric ORMs consist of launch vehicle cost, EOR operating cost, and cost of money. The cost of money is the accumulated interest paid on the program costs at launch until the spacecraft becomes fully operational after final delivery to a desired orbit. The consideration of the cost of money is important due to a long time transfer during the EOR. In Ref. [151], the mixed chemical-electric ORMs can provide a significant cost benefit compared to the pure chemical ORMs. It provides a cost reduction from millions to tens of millions of dollars with reasonable values of the cost of capital. Thus, the mixed chemical-electric ORMs are actually what commercial parties are most interested in. Based on previous discussion, the EOR part of a mixed ORM is taken as a proper mission for the current simultaneous design optimization task.

8.2 Electric Orbit Raising Mission Description

The ultimate purpose is to place more focus on a demonstration of the integrated design environment. Thus, it is intended that the chosen mission should stay as simple as possible. The entire mission scenario consists of three phases; 1) Sea Launch at zero latitude to the intermediate transfer orbit, 2) circularization at the apogee altitude

obtained from the first phase by burn of a chemical apogee kick motor, and 3) EOR to the GEO.

Figure 8.1: One Block DM-SL Burn (Perigee Height ≥ 200 km) [153]

Figure 8.1 shows a GTO injection scheme using a single burn strategy by Sea Launch. Payload capability for transfer to the elliptical GTO varies with the inclination of the GTO and the desired apogee height. The payload capability with the apogee height for zero inclination is shown in Figure 8.2. The perigee height in this case is 200 km.
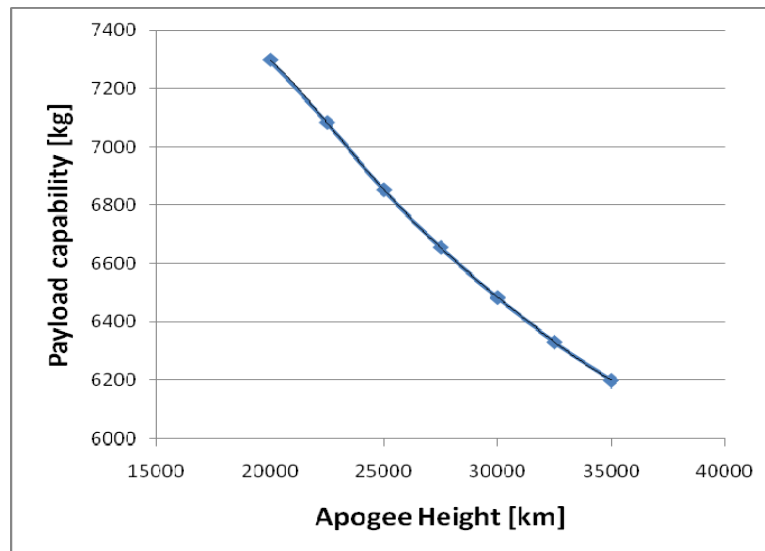
Figure 8.2: Sea Launch Payload Capability – Elliptical GTO [153]

For the current problem, the apogee radius of the intermediate transfer orbit is chosen to be 33000 km. The reason of choosing this radius is that the long time transfer by the EOR can be started approximately at the outer edge of the Van Allen Radiation Outer Belt, which minimizes the radiation exposure during the EOR. Then, it is further assumed that the apogee kick motor, using a bipropellant chemical engine, is used to circularize the orbit. In order to obtain full advantages of the EOR and minimize the propellant for the bipropellant chemical system, the perigee is raised to the apogee radius so that the circle-to-circle EOR can maximize the capability of SEP while minimizing the radiation exposure. Finally, the EOR delivers the spacecraft to the final GEO.

The initial and final orbits of the EOR part are given in Table 8.1.

Table 8.1: Initial and Final Orbits of EOR

	a (km)	e	i (deg)	ω (deg)	Ω (deg)	v (deg)
Initial	33000	0	0	0	0	0
Final	42164	0	0	0	0	free

The spacecraft mass at $t=0$ is assumed to be 700 kg, which is well within the Sea Launch payload capability. It is also assumed that the spacecraft is equipped with two HETs. The objective is a minimum-fuel transfer. In order to make the trajectory optimization easier to solve, it is decided that the time of flight is fixed. The time of flight selected corresponds to the minimum time to accomplish the transfer using two SPT-100 engines, and is equal to 20.034 days. Based on this time of flight, the number of revolutions would be approximately $24\frac{1}{2}$. There are two main reasons for this choice: 1) in practice, it is best to minimize the time of flight to reduce the hazardous effects in the radiation belt during the transfer, and 2) using the physics-based engine model does not allow to switch off the engine during the transfer as will be explained in the next section.

210

8.3 Simultaneous Design Optimization Environment

The overall performance of a spacecraft is a function of both the spacecraft trajectory and the engine design. Further, the engine design will impact the spacecraft trajectory and vice versa. However, as explained before, the impact of simultaneously considering both trajectory and engine design variables has not been previously considered. In fact, the EP design problem is often carried out prior to the low-thrust trajectory optimization problem. Therefore, it can be seen that this limitation might result in a sub-optimal configuration. To improve results during the preliminary design, an 'all-at-a-time' approach is adopted where engine and trajectory problems are optimized together to obtain a solution. Therefore, an efficiently coupled MDO scheme is required to account for the optimization of these two very different disciplines.

Current MDO approaches often involve a multistep sequential optimization procedure. In the current context, this method would consist of a trajectory optimization cycle (inner loop) and an engine design cycle (outer loop). The inner loop uses the data of the outer loop to determine the engine system parameters yielding the optimum performance as long as the departure from the preset design (outer loop) remains small. However, this approach is not efficient for the current problem. Since such a strategy requires many inner loop optimizations given by the number of outer loop iterations, it would be inefficient. Low-thrust trajectory problems are computationally intensive and it is therefore preferable to perform only one optimization per problem.

In this thesis, this issue can be avoided by transforming the MDO problem into a single trajectory problem having both a static and a dynamic aspect. The dynamic aspect involves all the variables that can be varied over time on the trajectory. The static aspect

involves some design decisions (engine dimensions for instance) that are not linked to a time sequence and that are held fixed for a given trajectory. To that end, it is decided to use the unified optimization architecture OPTIFOR that was recently-developed [63]. An important feature of this architecture is its ability to simultaneously optimize both dynamic and static control variables [63][154].

OPTIFOR can be described as a general optimization architecture designed to solve a wide variety of optimization problems. In this framework, the continuous trajectory is discretized into different segments. Each segment is characterized by a transition function that propagates the trajectory, a cost function, and constraint functions that must be met at each segment along the trajectory. In addition, a final constraint function is also present to account for specific conditions at the final states. Figure 8.3 illustrates the general structure of the problems that can be handled by OPTIFOR. Among other solvers, OPTIFOR includes a state-of-the-art NLP optimizer SNOPT [155]. This solver is used for all the optimization problems presented in this thesis. It is noted that the required derivatives of all functions are determined very accurately using the complex variable method described in Ref. [156].
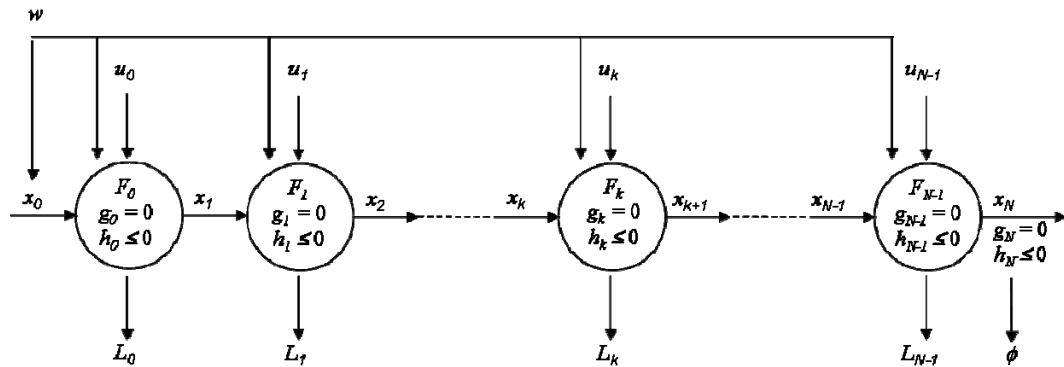
Figure 8.3: Structure of an optimization problem in OPTIFOR

Each element of this structure for our problem of interest is explained in detail.

Types of variables

First, three distinct classes of variables must be defined in OPTIFOR. The goal is to collect all control variables of the trajectory and engine models and incorporate them into different types of control vectors so that they can be manipulated by OPTIFOR. The different control variables of the problem are such that:

-Controls of the trajectory model: spherical angles $\{\theta, \varphi\}$ of the direction of thrust

-Design variables of the engine model: $\{z_{cath}, R_1, R_2, L, B_{max}, B_{cath}, K, \hat{\alpha}_{ano,in}, \hat{\alpha}_{ano,out}, V_d, \dot{m}_a, pmc\}$

The first class of variables is the dynamic control vector u_k that includes all design variables that vary from segment to segment. In this framework, the vector u_k is applied to segment k only and is constant over this segment. It is clear that the two spherical angles $\{\theta, \varphi\}$ characterizing the direction of the applied thrust are in this category since the direction of thrust is time-dependent. Regarding the engine design variables, it is specified that $\hat{\alpha}_{ano,in}, \hat{\alpha}_{ano,out}, V_d, \dot{m}_a$, and *pmc* could be varied along the trajectory. For $V_d, \dot{m}_a$, and *pmc*, it is because they can be changed by modifying the potential difference between the anode and the cathode and modifying the amount of the propellant inputs. For $\hat{\alpha}_{ano,in}$ and $\hat{\alpha}_{ano,out}$, the anomalous coefficients are treated as free parameters along the trajectory because these coefficients are arbitrary and there has been no way of calculating their values from the physical basis. Instead, the effect of their variations on the solution is addressed after obtaining the final design. In summary, at each segment, the dynamic control vector u_k corresponds to $u_k = \{\hat{\alpha}_{ano,in}, \hat{\alpha}_{ano,out}, V_d, \dot{m}_a, pmc, \theta, \varphi\}$.

The second variable class is the static control vector w that encompasses design variables that can have an effect over the whole trajectory and are time-independent. This includes obviously the variables related to the dimensions of the engine $\{z_{cath}, R_1, R_2, L\}$. In addition, it is also decided that B_{max}, B_{cath}, and K should be in this category as it is assumed that changing them along the trajectory would be currently difficult. In summary, the components of the static control vector are defined to be: $w = \{z_{cath}, R_1, R_2, L, B_{max}, B_{cath}, K\}$.

The last variable class is the time-dependent state vector x. It corresponds classically to the position and velocity of the spacecraft, as well as its mass.

Transition function

The representation of Sims and Flanegan is used to propagate the low-thrust trajectory [157] - [158]. Each segment consists of a ΔV impulse followed by a coast period. The impulsive ΔV s approximate the low thrust acceleration over a segment and are computed from the corresponding thrust magnitude. The mass discontinuity due to the impulse is obtained from the rocket equation. Thrust magnitude and I_{sp} are given by the engine model. Figure 8.4 gives the flow diagram for the transition functions of the segments.
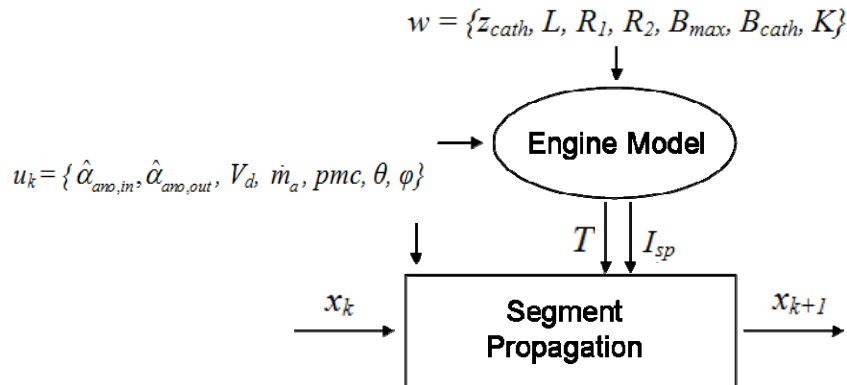
Figure 8.4: Flow diagram of the transition function of a segment

Cost function

The cost function of each segment corresponds to the thrust magnitude, obtained from the engine model.

Segment constraint functions

For feasibility, it should be guaranteed that the SVM constraint g_0 is met at each segment. In addition, to account for the uncertainty in the anomalous coefficients, it is decided that g_0 should be satisfied with some safety margin: $g_0 \geq d_{\text{lower limit}}$. The selection of a proper value for $d_{\text{lower limit}}$ requires some trial-and-errors experiments, which will be shown in the results section.

Moreover, even if other constraint functions g_1, g_2, g_3, and g_4 generated by the NNs using only thruster operation success cases are no longer strictly needed, they are included to provide an extra safety strategy and to check their performance as constraints. It is interesting to compare the behavior of g_1, g_2, g_3, and g_4 with the SVM constraint g_0. All extra constraints must be greater than 0 to indicate the feasible region.

Finally, the power usage required by the engine must not be greater than the power available. In general, the power available is produced by solar arrays. To simplify the problem, it is assumed that the power available is constant along the trajectory, which is a good approximation for geocentric transfers since the distance from the Sun is nearly constant. The corresponding constraint is therefore:

$P_d < P_{available}$, where P_d is output power of the engine model.

The constraints which must be satisfied for each trajectory segment are summarized in Table 8.2.

Table 8.2: Constraints for Each Trajectory Segment

Constraint	Expression	Implication
SVM Classifier	$g_0 \geq d_{\text{lower limit}}$	Guarantee of the feasible region of thruster operation
Available Power	$P_d < P_{available}$	Restriction on required power

8.4 Results and Comparisons

All of the results given in this section use the SNOPT options shown in Table 8.3. The machine used for solutions has an Intel® CoreTM2 CPU 6600, 2.4 GHz clock speed, 2 GB memory, and Microsoft Windows XP operating system.

Table 8.3: SNOPT options

Option	Value	Option	Value
Minor Feasibility Tolerance	10^{-6}	Feasibility Tolerance	10^{-8}
Major Feasibility Tolerance	10^{-6}	Major Optimality Tolerance	10^{-2}

8.4.1 Case of $d_{\text{lower limit}} = 1$ for the SVM Classifier Constraint Limit

As a first solution, $d_{\text{lower limit}}$ is set to 1 for the SVM classifier function constraint in Equation (7.10). This allows the feasible region for the thruster operation to extend down to the support vectors. Table 8.4 shows the simultaneous design results for the geometric and radial magnetic field variables.

Table 8.4: Design Results for $d_{\text{lower limit}} = 1$

Geometric Variable	Solution	Magnetic Field Variable	Solution
R_1 [cm]	3.14	B_{max} [G]	143
R_2 [cm]	4.14	B_{cath} [G]	123
L [cm]	4.93	K	13.56
z_{cath} [cm]	1.77		

Figure 8.5 plots the variations of the anomalous coefficients and operational variables during the time of flight. The anomalous coefficient inside the channel is fixed at the highest value. On the other hand, the anomalous coefficient outside the channel is almost at its minimum value. The discharge voltage shows a bang-bang solution which takes the values of minimum or maximum in its range. The anode and cathode mass flow rates are constants during flight and they take minimum values of their corresponding ranges. This is actually what is expected because the current simultaneous optimization has the objective of minimum fuel.
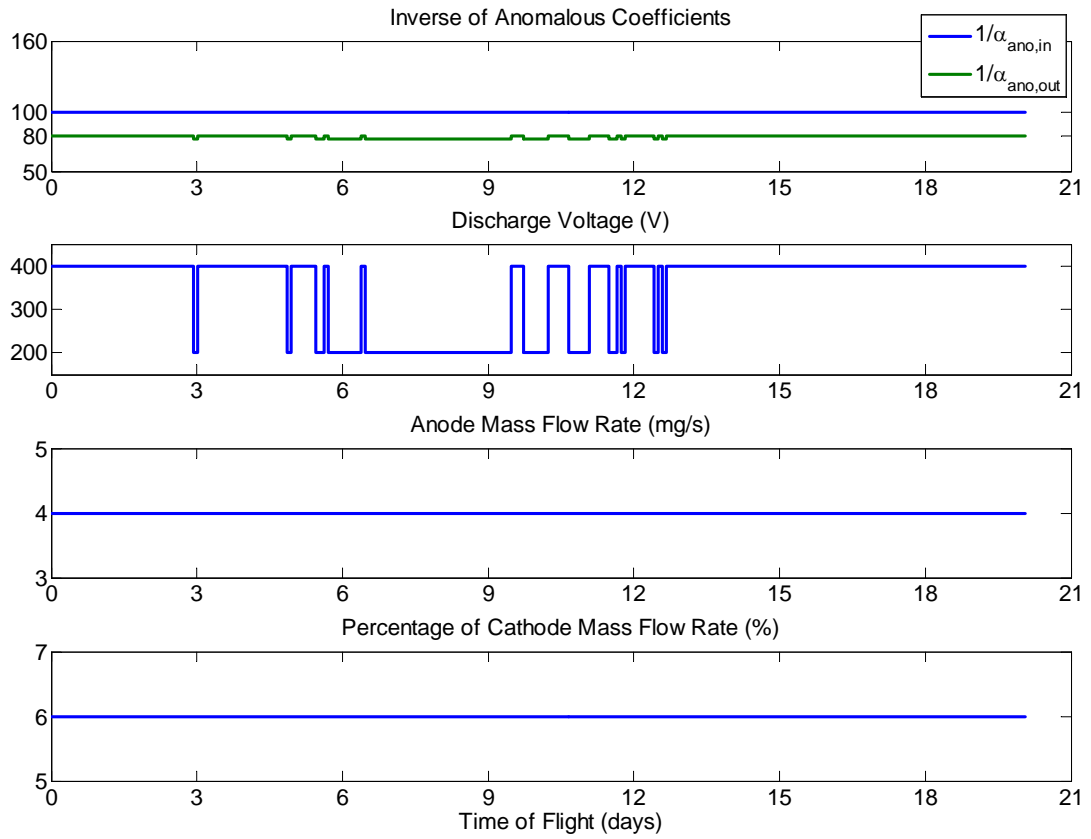
Figure 8.5: Operational Variable Solutions of $d_{\text{lower limit}} = 1$

Figure 8.6 shows the performance histories during the time of flight. The thrust history also indicates a bang-bang solution, which takes a minimum value of about 50

mN and a maximum value of about 90 mN. In general, the minimum-fuel low-thrust trajectory with a constant specific impulse model involves a zero thrust segment during the flight, which is the "coast phase" to minimize fuel usage. However, in this case, there is no coast phase in the entire trajectory. This is because the current HET performance is restricted by the SVM constraint. This actually assumes that the thruster is always working. Thus, if the coasting phase were to be included in the simultaneous optimization architecture, an additional condition should be given.
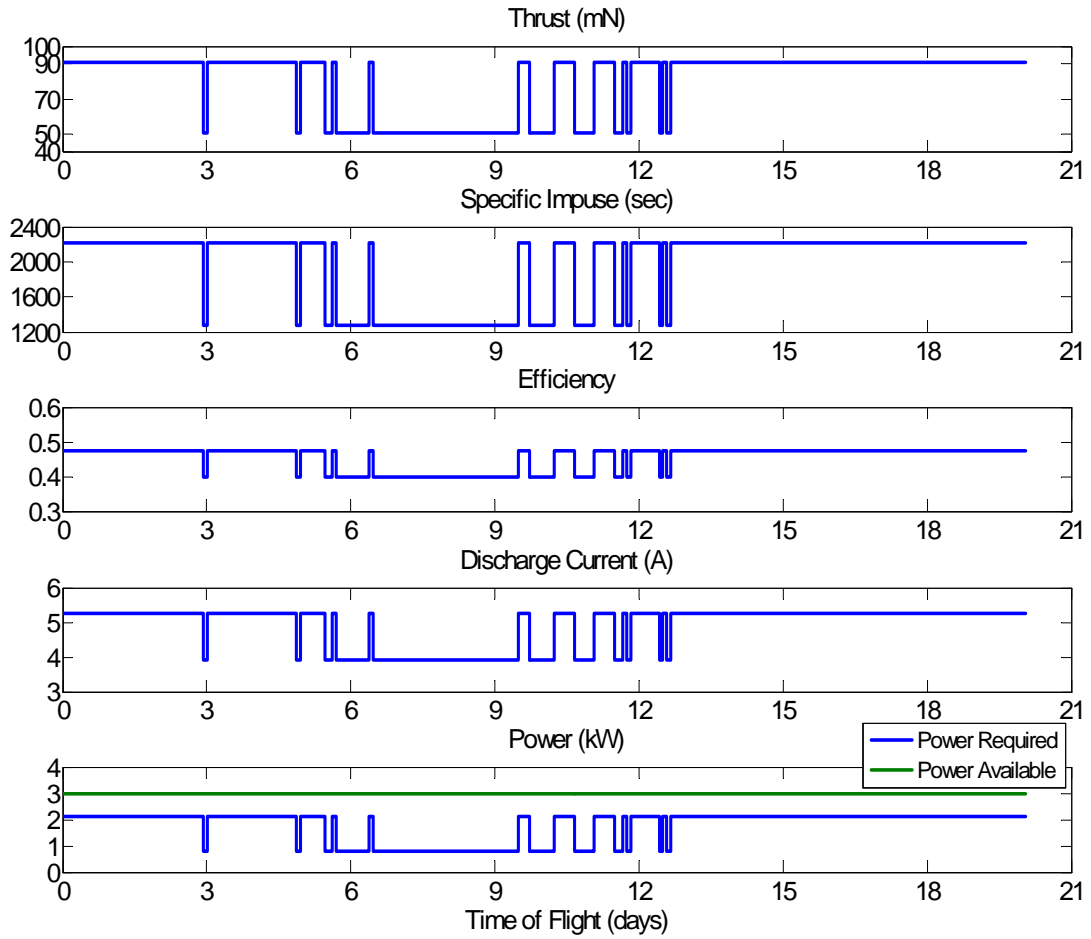
Figure 8.6: Performance Histories of $d_{\text{lower limit}} = 1$

Another remarkable feature is that the specific impulse has bang-bang variations also, with a minimum of about 1200 s and a maximum of about 2200 s. This corresponds

to a range of variation of approximately 1000 s, which is quite impressive for a low-thrust engine. The efficiency variation is between 0.4 and almost 0.5. Most of the segments have the highest efficiency. The discharge current variation is from 4 A to approximately 5.3 A, which yields the variation of power required to be between 1 kW to 2 kW.

The constraint histories are shown in Figure 8.7. It is clear that the SVM classifier constraint is the only active constraint. The constraints from Equation (6.1) do not work very well in finding boundaries of the feasible region due to regressions with only the data of operation success cases. The value of the SVM classifier function hits the lower bound for some segments of the optimum trajectory.
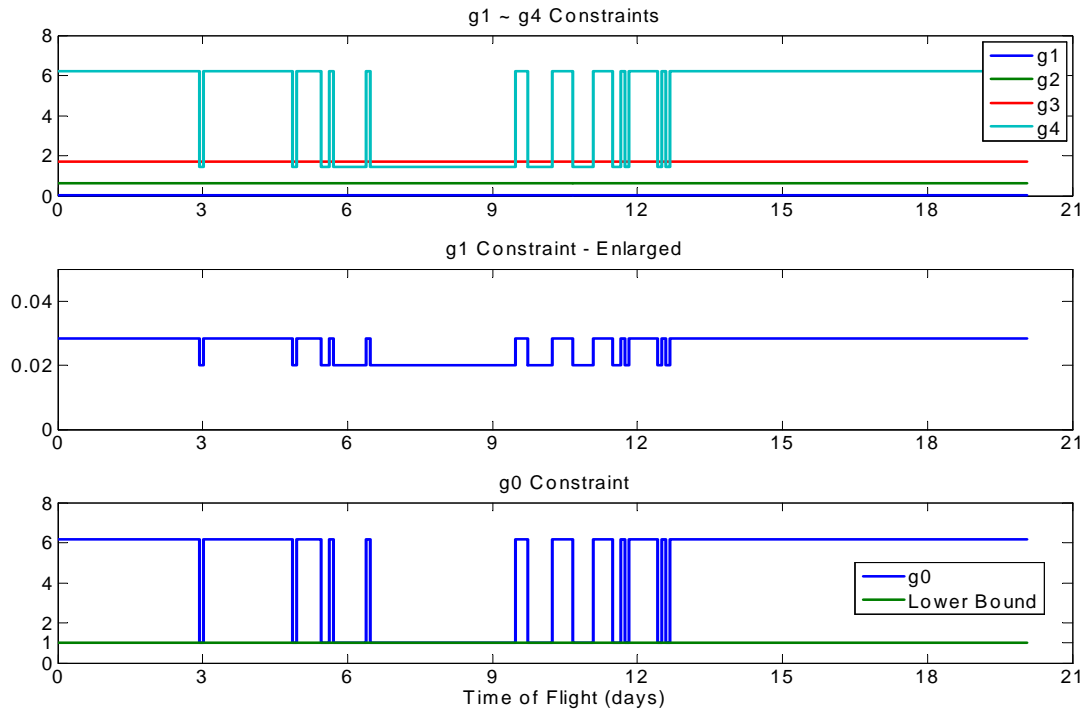
Figure 8.7: Constraint Histories of $d_{\text{lower limit}} = 1$

Figure 8.8 shows the optimum trajectory of $d_{\text{lower limit}} = 1$ case. It requires about $24\frac{1}{2}$ revolutions as expected. The variations of the semi-major axis and eccentricity are shown in Figure 8.9. In Figure 8.9, the semi-major axis is increasing up to that of the

219

final orbit with a slanted S shape. The eccentricity variation shows both short and long period oscillations. This is because the final orbit requires circularization and a larger radius.
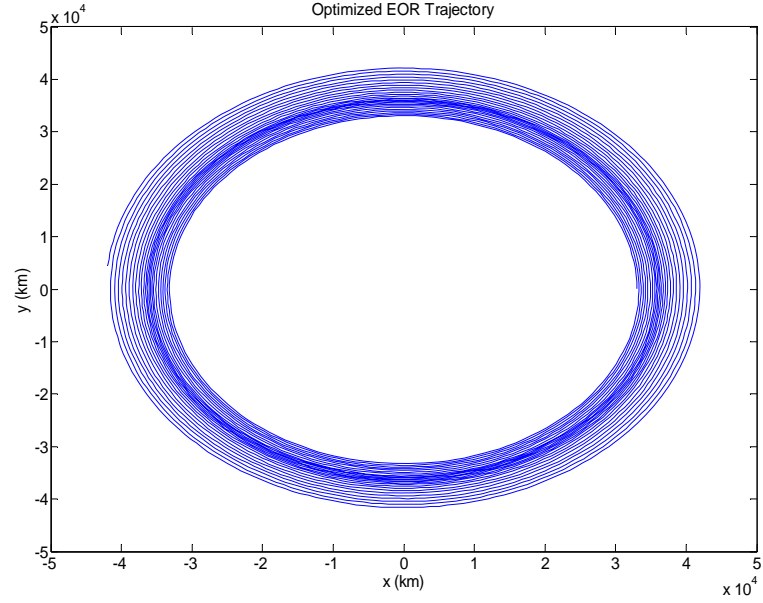
Figure 8.8: Optimum Trajectory of $d_{\text{lower limit}} = 1$
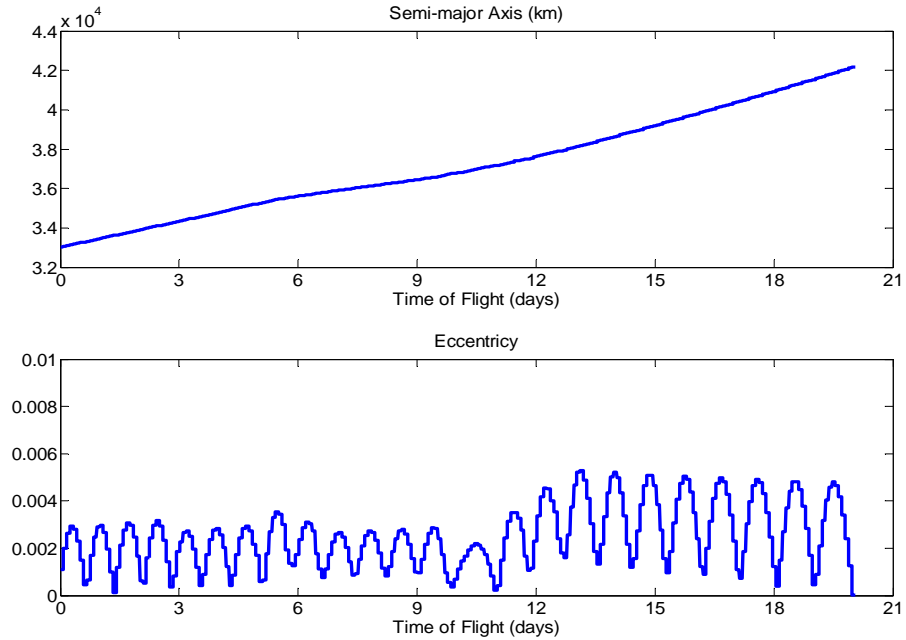
Figure 8.9: Semi-Major Axis and Eccentricity Variations of $d_{\text{lower limit}} = 1$

Based on the eccentricity variation in Figure 8.9, the in-plane steering angle command would show the right and left periodic oscillation in the direction of flight, which is a well known behavior of the problem for transferring from a circular orbit to a larger circular orbit using a constant specific impulse model. The final spacecraft mass is calculated as 685.62 kg, which results in 14.38 kg of propellant usage.

In order to validate that the SVM classifier function represents a feasible space well and that the surrogate models are accurate, comparisons between the performance from the surrogate models and that from the developed tool are conducted. Figure 8.10 shows absolute differences of performance metrics between the values from the actual code and those from the surrogate models. The maximum percent differences for thrust, specific impulse, efficiency, discharge current, and power are 3.39%, 1.07%, 2.40%, 0.95%, and 0.23%, respectively, which are very small.
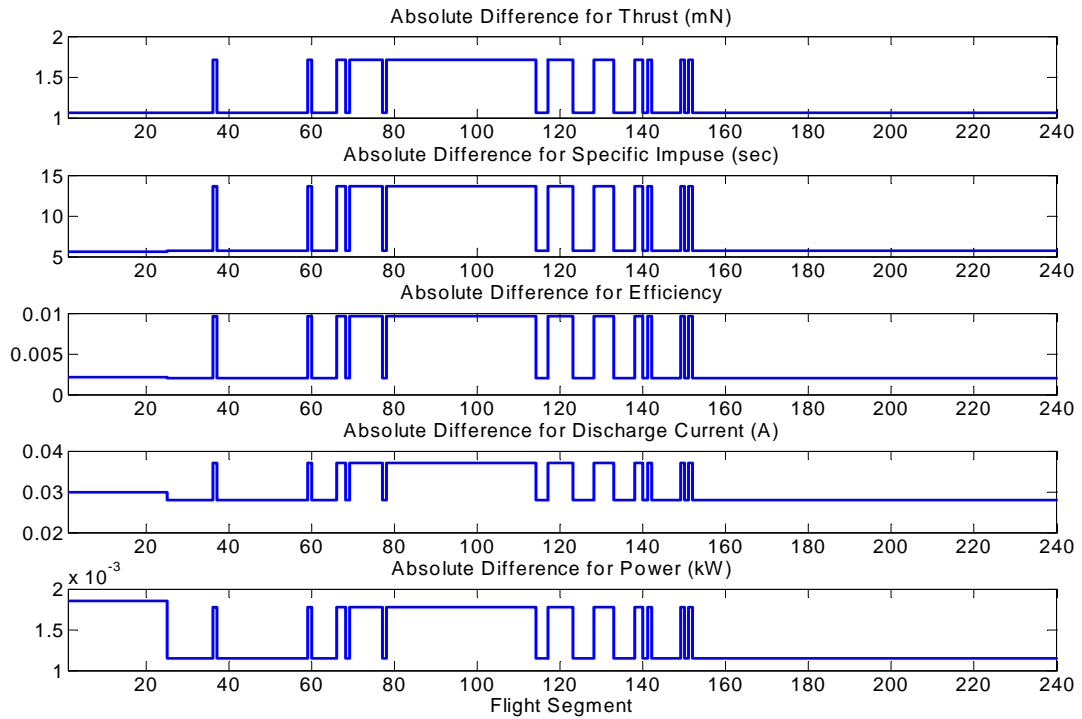
Figure 8.10: Comparisons between Surrogate Models and Actual Code ($d_{\text{lower limit}} = 1$)

As shown in Figure 8.10, the developed tool produces all of the responses for optimum geometry, radial magnetic field parameters, and the variations of operational variables. This indicates that the optimum solutions are within the feasible region. This also confirms that the SVM classifier function constraint is well performing.

Because the anomalous coefficients are arbitrary values, the optimum solutions from the simultaneous design optimization must be given in terms of probability of success and confidence. For this purpose, a Monte Carlo simulation is required for the anomalous coefficients. The strategy is that for each segment of the optimal trajectory 10000 pairs of the anomalous coefficients are randomly generated. The generated pairs for each segment are then checked with the SVM classifier constraint. In this case, $d_{\text{lower limit}}$ is set to zero to cover the entire feasible region. This provides the probability of success (or the success rate) of the obtained optimum solution. The performance values are then calculated with the pairs which do not violate the SVM classifier constraint. Trajectories are integrated with these feasible cases. The required confidence can be given by the distributions of the orbital elements at the end state and the final spacecraft mass.

Unfortunately, results of the Monte Carlo simulation show that the probability of success is 0 for the case of $d_{\text{lower limit}} = 1$. This means that a harder limit should be given to the SVM classifier constraint in order to address the arbitrary variations of the anomalous coefficients. As a result, the harder limit will reduce the feasible region of the thruster operation.

8.4.2 Case of $d_{\text{lower limit}} = 3$ for the SVM Classifier Constraint Limit

The limit for the SVM classifier constraint is now set to 3. This reduces the feasible space for the thruster operation compared to the previous case. The convergence properties are shown in Table 8.5.

Table 8.5: Convergence Property for $d_{\text{lower limit}} = 3$

Iteration	CPU Run Time	Max Constraint Violation
No. of Iteration: 5751 No. of Function Calls: 136	21.35 min.	1.0×10^{-5}

Table 8.6 shows the simultaneous design results for the geometric and radial magnetic field variables.

Table 8.6: Design Results for $d_{\text{lower limit}} = 3$

Geometric Variable	Solution	Magnetic Field Variable	Solution
R_1 [cm]	3.54	B_{max} [Gauss]	157
R_2 [cm]	4.54	B_{cath} [Gauss]	137
L [cm]	5.00	K	13.99
z_{cath} [cm]	1.92		

Both the inner and outer radii are slightly increased. The cathode location is a little farther from the thrust exit line than before. The maximum and the cathode radial magnetic fields are increased by about 15 Gauss. The magnetic field shape coefficient is almost the same as the previous case.

Figure 8.11 plots the variations of the anomalous coefficients and operational variables during the time of flight. The anomalous electron diffusion inside the channel is slightly decreased. Again, the discharge voltage shows more bang-bang behavior. It is also clearly seen that the range of the discharge voltage variation is reduced by 100 V, to between 300 V and 400 V. This is because the feasible design space for the optimization is reduced by the SVM classifier constraint. The anode and cathode mass flow rates still

retain the smallest values of their ranges, which is again indicative of a minimum fuel solution.
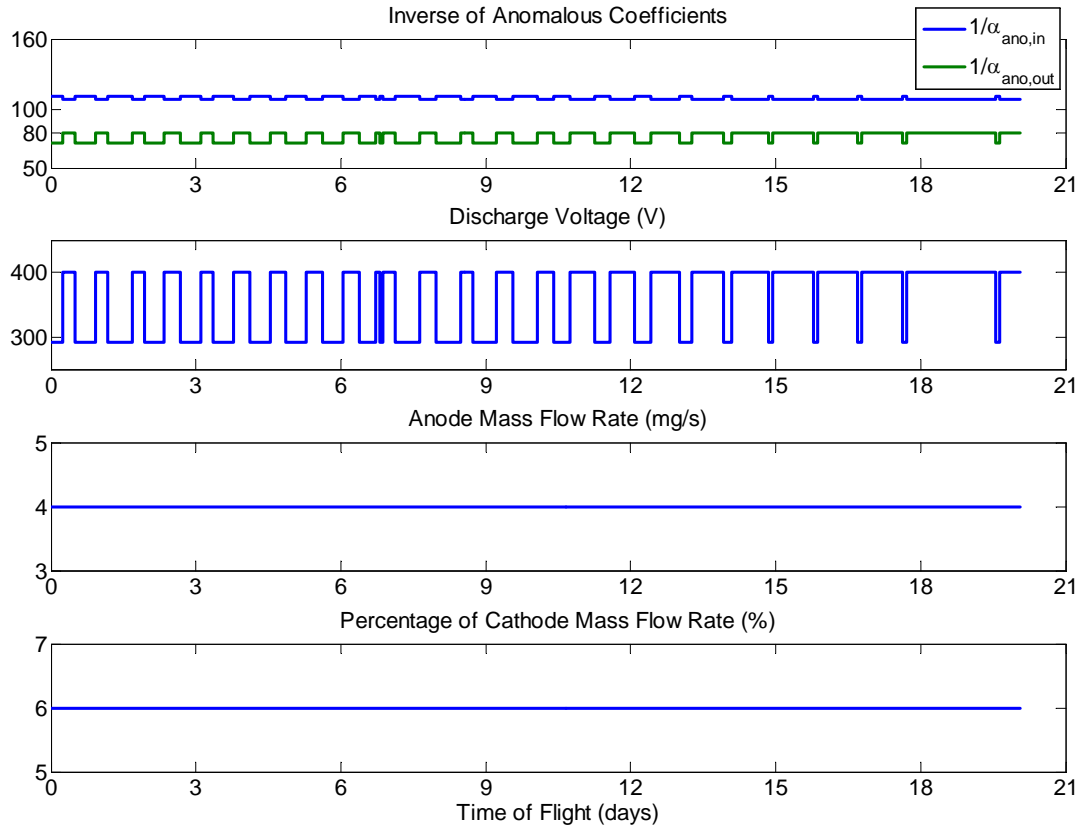
Figure 8.11: Operational Variable Solutions of $d_{\text{lower limit}} = 3$

Figure 8.12 shows the performance histories during the time of flight. The variations of all performances are decreased compared to the previous case. The variation of the thrust becomes smaller by 20 mN. The range of specific impulse variation is decreased by about half, which is approximately 500 s. The efficiency variation stays close to 0.5. The power required decreases somewhat due to the discharge current dropping to a value below 4.8 A for all segments.
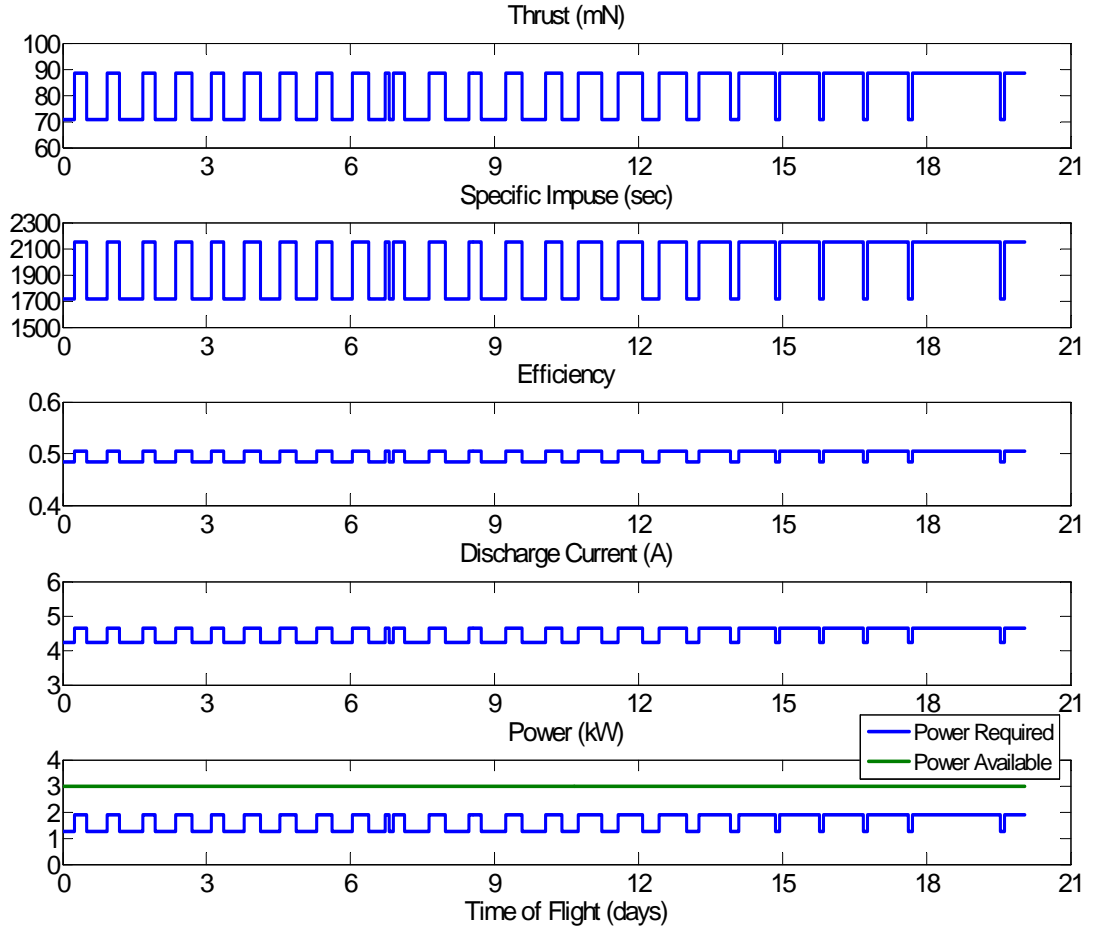
Figure 8.12: Performance Histories of $d_{\text{lower limit}} = 3$

The constraint histories are shown in Figure 8.13. It is again clear that the SVM classifier constraint is the only active constraint even if the feasible region is decreased. The constraints from Equation (6.1) also do not work very well for this case. It is also observed that the value of the SVM classifier function hits the lower bound for a significant part of the optimum trajectory.

Figure 8.14 shows the optimum trajectory of $d_{\text{lower limit}} = 3$ case. It still requires about $24\frac{1}{2}$ revolutions as before.
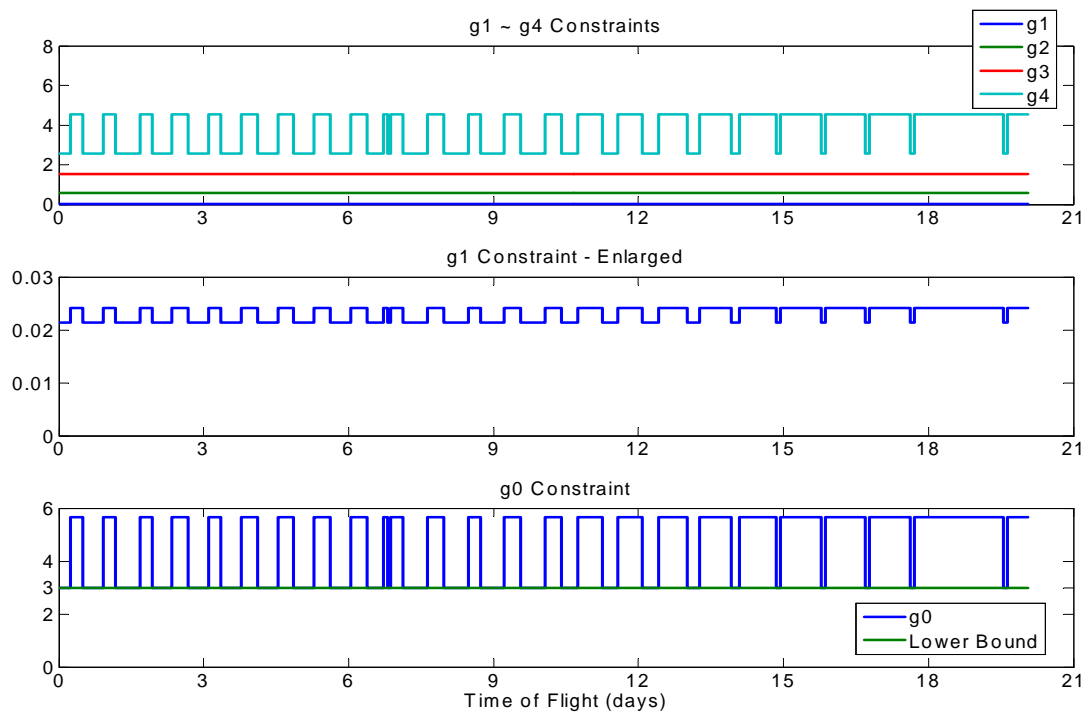
Figure 8.13: Constraint Histories of $d_{\text{lower limit}} = 3$
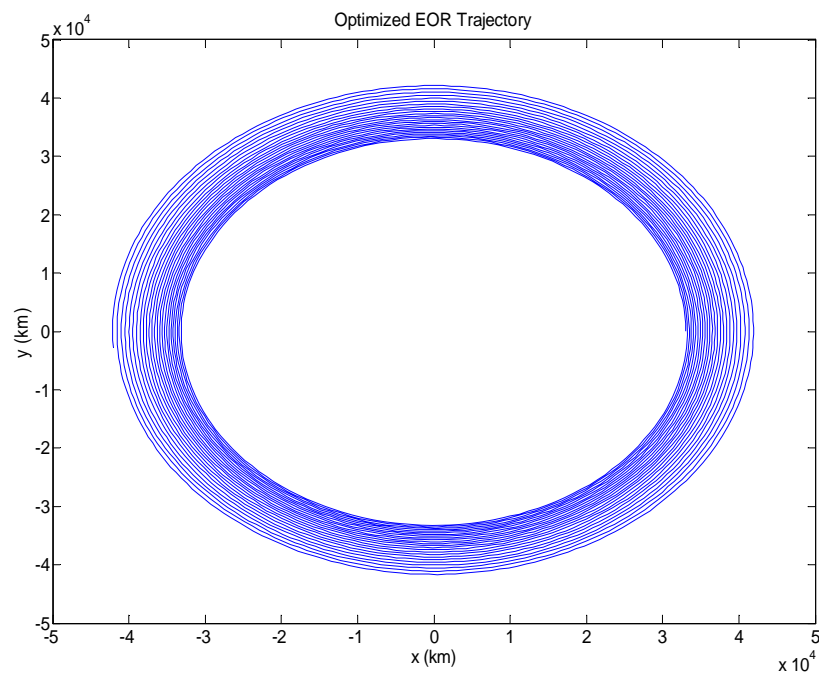
Figure 8.14: Optimum Trajectory of $d_{\text{lower limit}} = 3$
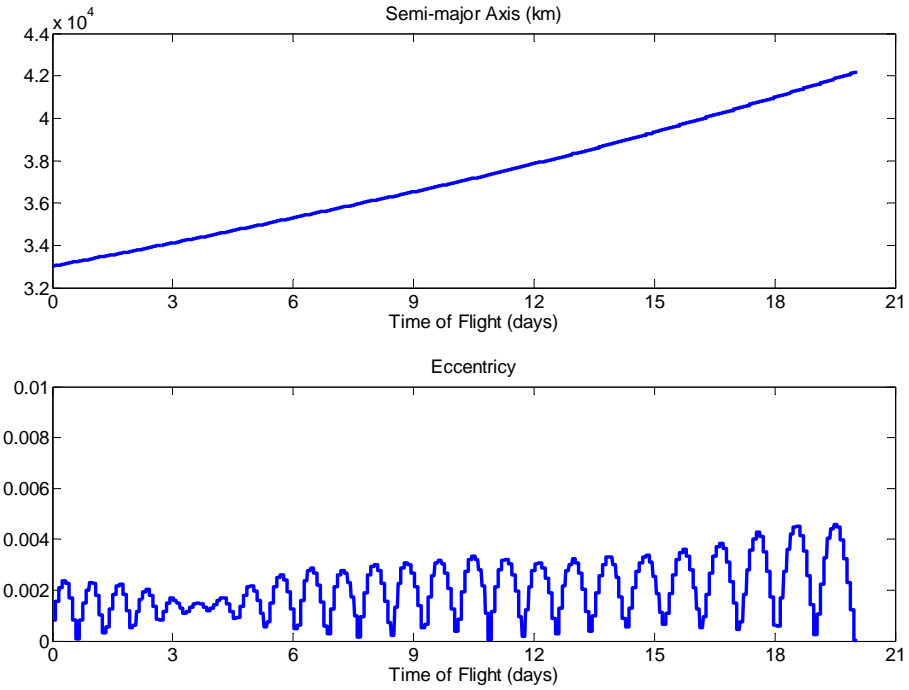
Figure 8.15: Semi-Major Axis and Eccentricity Variations of $d_{\text{lower limit}} = 3$

The variations of the semi-major axis and the eccentricity are shown in Figure 8.15. The behavior of the semi-major axis is almost the same as the previous case, but it shows a more smooth increase. However, the range of the eccentricity variation becomes smaller for the current case. This might be because the higher thrusting strategy is used, where the increasing orbit size and circularization is relatively faster.

The final spacecraft mass is calculated as 685.50 kg, which results in 14.50 kg of propellant usage. Reducing the feasible region causes a slightly increased propellant usage by 120 g.

The comparisons between the performance from the surrogate models and that from the developed tool are also conducted. Figure 8.16 shows absolute differences of performance metrics as before. The maximum percent differences for thrust, specific

impulse, efficiency, discharge current, and power are 1.45%, 0.22%, 0.53%, 1.15%, and 0.36%, respectively, which are further reduced than the previous case.
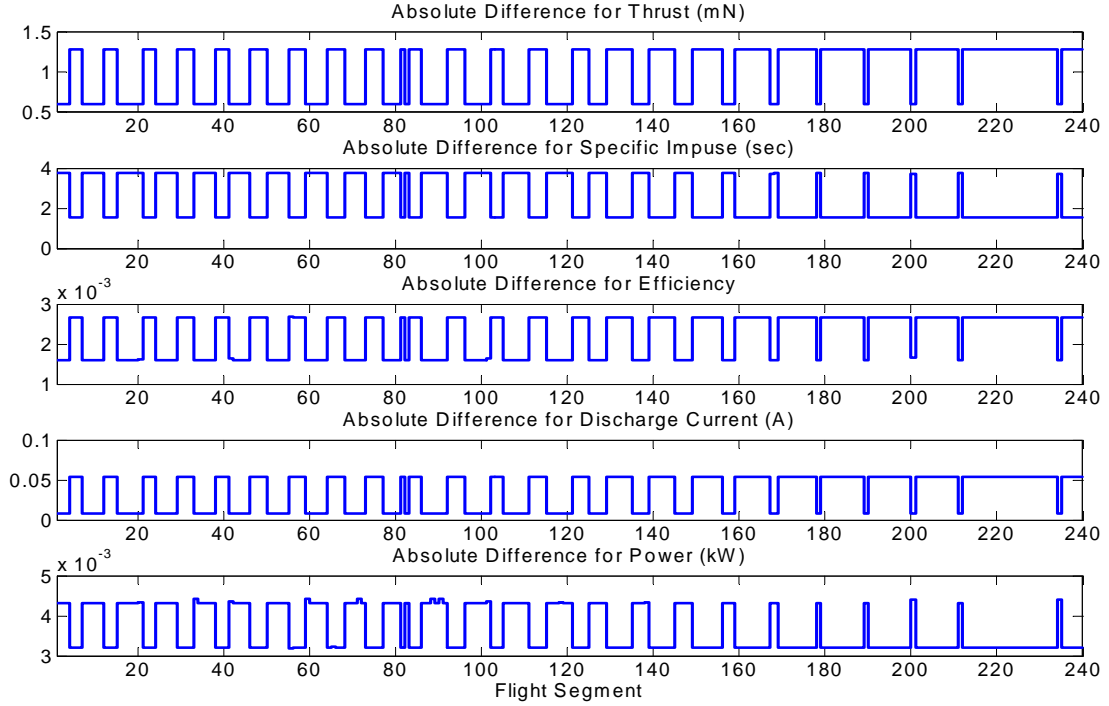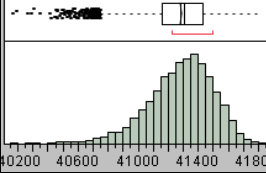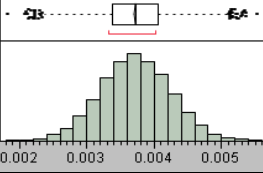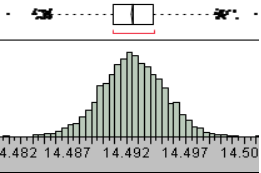
Figure 8.16: Comparisons between Surrogate Models and Actual Code ($d_{\text{lower limit}} = 3$)

From Figure 8.16, it is also clear that the optimum solutions are within the feasible region and the SVM classifier function constraint is well performing.

In order to perform the Monte Carlo simulation for this case, 10000 pairs of the anomalous coefficients for each trajectory segment are randomly generated and checked with the SVM classifier constraint. The probability of success in this case is 1, which means that variations of the anomalous coefficients do not have major impacts on the thruster operation itself (at least within their given ranges). Thus, the trajectory integration is performed for all cases. The distributions of the final semi-major axis, final eccentricity, and required amount of the propellant are shown in Table 8.7. The distribution for the semi-major axis indicates that the final orbit cannot always be reached.

This is because the anomalous coefficients are also used as design variables. The distribution for the eccentricity also deviates from an exact circular orbit. The amount of required propellant is the least sensitive to the variations of the anomalous coefficients.

Table 8.7: Results of Monte Carlo Simulation

	Semi-major axis [km]	Eccentricity	Propellant Used [kg]
Distribution			
Solution	42164	0	14.50
Mean	41285	0.0037	14.49
Standard Deviation	208	0.0005	0.003
Solution - Mean	879	- 0.0037	0.01
Min. ~ Max.	40163 ~ 41816	0.0018 ~ 0.0055	14.48 ~ 14.50

Although uncertainty of the anomalous coefficients makes calculation of an exact optimal trajectory difficult at this conceptual design stage, the uncertainty can be eliminated when the proposed HET is built and the design process becomes mature. Then the exact optimal trajectory can be easily recalculated. In order to transfer from the mean value of the final semi-major axis to the GEO, an additional roughly 2.5 revolutions would be required and an additional amount of required propellant would be approximately 1.4 kg (which results in a total of 15.9 kg.)

It can be concluded that the constructed simultaneous design optimization environment works very well and the anomalous coefficient variations can be also addressed by the Monte Carlo simulation. Furthermore, the established simultaneous design optimization environment can be used at the preliminary design stage for any space mission implementing the HET technology. The design space of the HET can be

dramatically reduced by producing near-optimal geometry and radial magnetic field configuration. If the anomalous coefficient variations were to be clarified through experimental tests of the designed HET, it is expected that the environment would give a very near-optimum solution for the low-thrust trajectory.

8.4.3 Optimal Low-Thrust Trajectory Calculation with the SPT-100 Thruster

In order to compare the results from the simultaneous optimization environment to the results from the existing thruster, the minimum-fuel trajectory optimization is solved with the SPT-100. It is assumed that the maximum thrust and specific impulse are constant throughout the trajectory and are set to be 80.4 mN and 1600 sec, respectively. It is also assumed that spacecraft is equipped with two SPT-100 HETs as before. Other problem statements are the same as in previous cases.

As before, the representation of Sims and Flanegan to propagate the low-thrust trajectory is used. For this problem, there are three dynamic control variables at each segment: the magnitude of the impulse approximating the thrusting, and the two spherical angles of the direction of thrusting. The cost function of each segment corresponds to the ΔV magnitude. For feasibility, it is ensured at each segment that the magnitude of the impulses is less than the maximum ΔV that can be accumulated over the segment. These impulse magnitudes are deduced from the duration of the segment, the current mass of the satellite, and the maximum thrust of the engine.

The convergence properties are shown in Table 8.8.

Table 8.8: Convergence Property for the SPT-100

Iteration	CPU Run Time	Max Constraint Violation
No. of Iteration: 1227 No. of Function Calls: 54	4.13 min.	1.1×10^{-5}

Figure 8.17 shows the thrust history. The thrust takes the maximum value for entire trajectory segments, which indicates a constant maximum thrusting strategy. This strategy is typically observed in minimum time solutions. As explained in section 8.2, the time of flight is fixed as that of the minimum time solution using the SPT-100. When the time of flight is chosen greater than the minimum time of the SPT-100 solution, the minimum fuel solution of the SPT-100 would produce some coasting phases. However, the engine model in the current simultaneous optimization architecture doesn't allow coasting phases due to the SVM constraint, which enforces no coasting phases on the minimum fuel solution of the SPT-100 as well. Therefore, it is clear that the minimum fuel solution of the SPT-100 should be the same as the minimum time solution of the SPT-100.
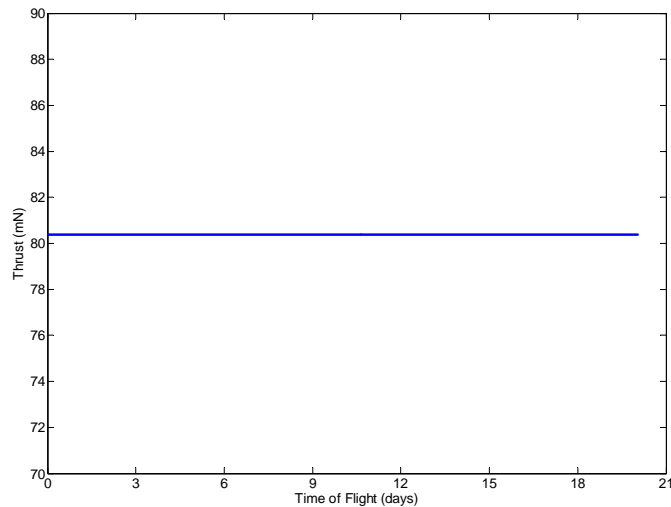
Figure 8.17: Thrust History for the SPT-100

Figure 8.18 shows the optimum EOR trajectory using the SPT-100. The revolution is almost the same as before due to the fixed time of flight. Figure 8.19 shows the semi-major axis and the eccentricity variations with time. The semi-major axis

variation is same as the previous. The eccentricity variation is more regular than previous cases because constant thrust and specific impulse are applied to the entire trajectory.
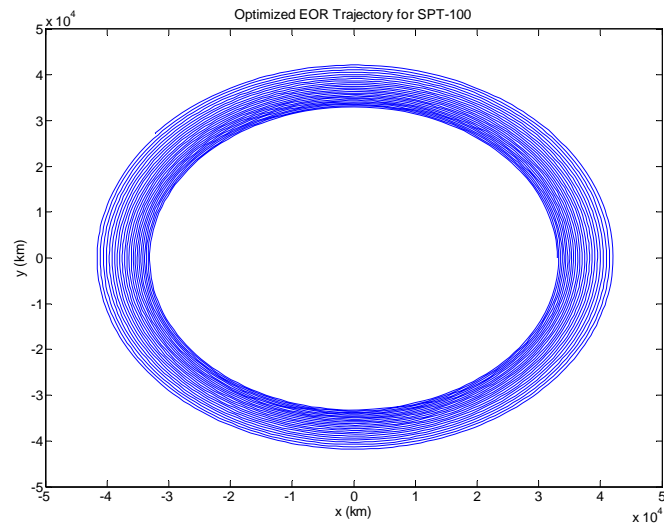
Figure 8.18: Optimum Trajectory for the SPT-100
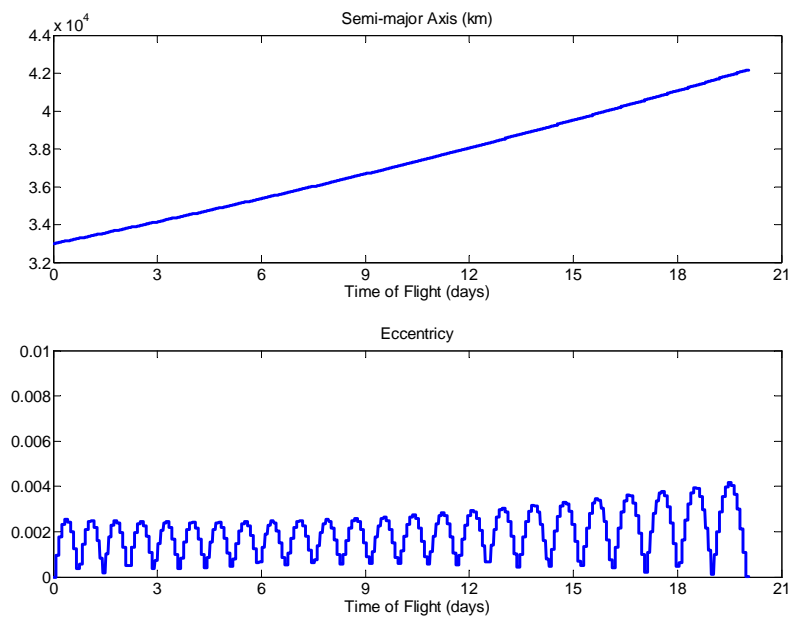
Figure 8.19: Semi-Major Axis and Eccentricity Variations for the SPT-100

The final spacecraft mass is 682.34 kg, which results in 17.66 kg of propellant. When compared with the second case of the simultaneous design environment, 3.16 kg of more propellant is required, which is about a 21.8 % increase in required propellant. In

232

the case of including the variations of the anomalous coefficients, 1.76 kg of more propellant is still required for the SPT-100 case, which is about an 11.1 % increase.

Figure 8.20 shows the comparison of the in-plane thrusting angle variations for all three cases. It is observed that there is not much difference. All show the periodic thrusting angle strategy, which reflects the repeated orbit raising and circularization.

Figure 8.21 shows the comparison of semi-major axis, eccentricity, and spacecraft mass variations. The variations of the semi-major axis are almost similar for all cases. However, it is interesting to note that the variations of the eccentricity are highly dependent on the degree of capability of changing the thrust and specific impulse in the optimal trajectory. The spacecraft mass variations for the designed cases are almost the same. It is clearly seen that more propellant is required for the SPT-100 case where a constant specific impulse model is assumed.
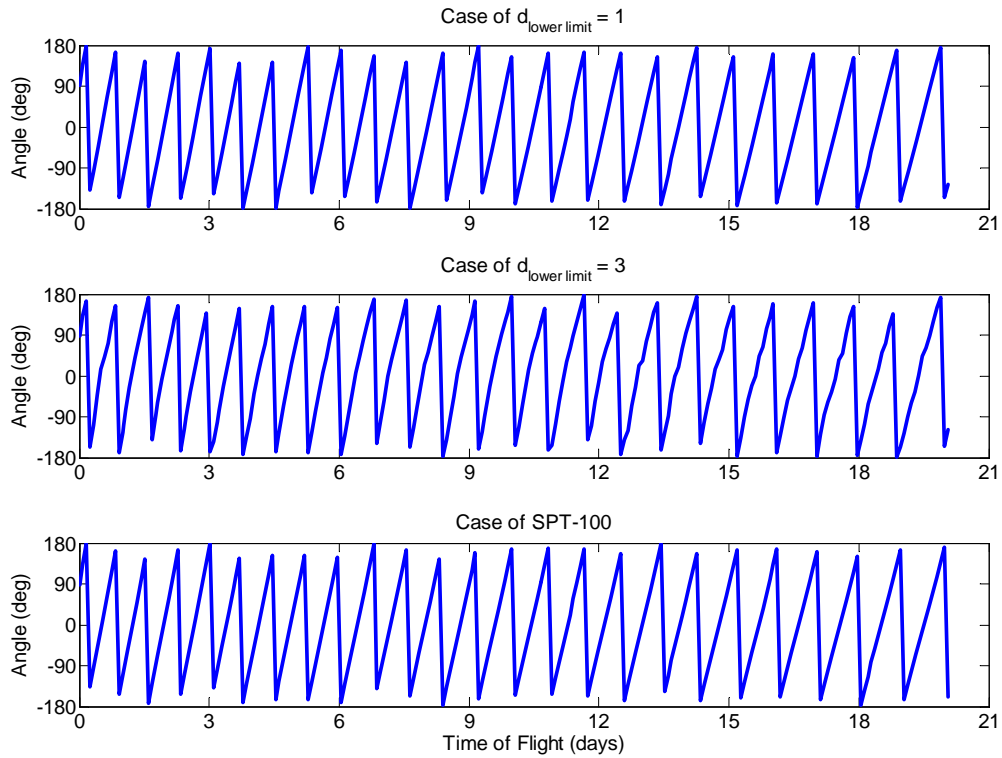
Figure 8.20: Comparison of In-plane Thrusting Angle Variations
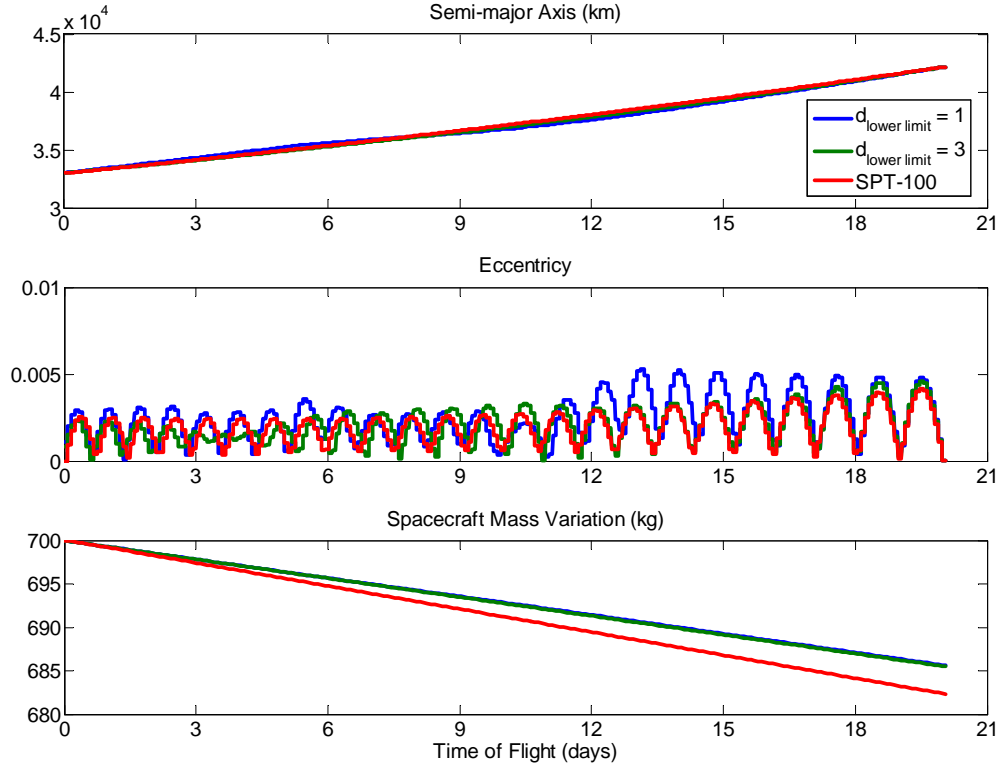
Figure 8.21: Comparisons of Semi-major Axis, Eccentricity and Spacecraft Mass Variations

Table 8.9: Comparison of Design Results with SPT-100

Variable	SPT-100	Designed HET	MC Result
R_1 [cm]	3.5	3.54	
R_2 [cm]	5.0	4.54	
L [cm]	4.0	5.0	
z_{cath} [cm]	2.0	1.92	
B_{max} [G]	160	157	
B_{cath} [G]	130	137	
K	16	13.99	
Spacecraft Final Mass [kg]	682.3	685.5	684.1
Amount of Propellant [kg]	17.7	14.5 (-17.9%)	15.9 (-10.2%)

In conclusion, it is inferred that varying the thrust and the specific impulse could produce more benefit in terms of the propellant used for the minimum-fuel trajectory

optimization. The comparisons of geometry and optimization results between the designed HET and the SPT-100 are summarized in Table 8.9.

Figure 8.22 shows the comparison of the radial magnetic field distributions between the SPT-100 and the designed HET.
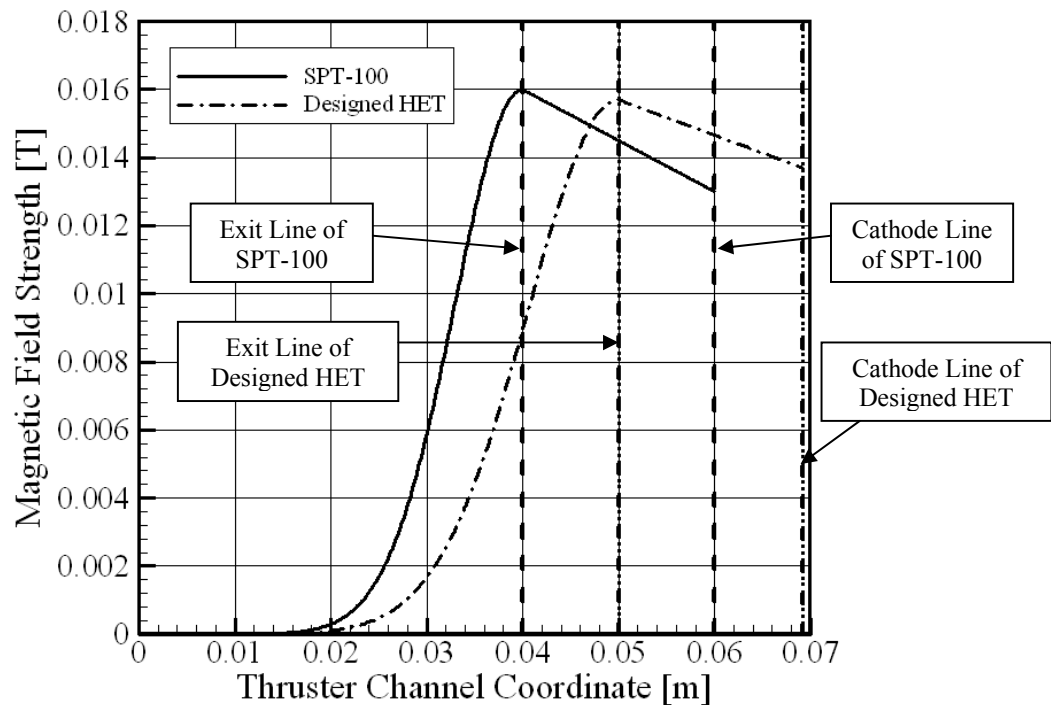
Figure 8.22: Comparison of Magnetic Field Distributions

8.4.4 Comparison with Pure Chemical Transfer

The results of the current EOR problem are compared with chemical transfer to quantitatively investigate the relative advantages of the EOR in terms of fuel saving. As an initial broad comparison, the EOR is replaced with the chemical transfer using the Hohmann transfer.

Table 8.10 shows the spacecraft final mass and the required amount of propellant when a bipropellant liquid rocket is used for the same orbit raising mission. The thrust and the specific impulse for the bipropellant liquid rocket are assumed to be 445 N and

322 s, respectively. The spacecraft final mass and the corresponding amount of propellant used are calculated using Equation (1.2).

Table 8.10: Comparison with Bipropellant Liquid Rocket Transfer for EOR

Variable	SPT-100	Designed HET	Bipropellant Liquid Rocket
Spacecraft Final Mass	682.3 kg	685.5 kg	616.9 kg
Amount of Propellant	17.7 kg	14.5 kg	83.1 kg
Time of Flight	20.05 days	20.05 days	10.07 hrs

As seen in Table 8.10, if the chemical rocket were to be used for this mission, the required fuel would be 83.1 kg. When compared to the EOR by the SPT-100 and the designed HET, an additional 65.4 kg and 68.6 kg of propellant are necessary, respectively. Thus, the EOR can deliver, to the GEO, an increase in payload of about 70 kg. However, since the replacement of the EOR by the chemical transfer used for this comparison is not usually planned for the GEO transfer, a more realistic comparison is performed.

Figure 8.23 shows the GEO transfer mission starting from the LEO (200 km altitude) using pure chemical transfer and mixed Chemical-Electric Orbit Raising (C-EOR).
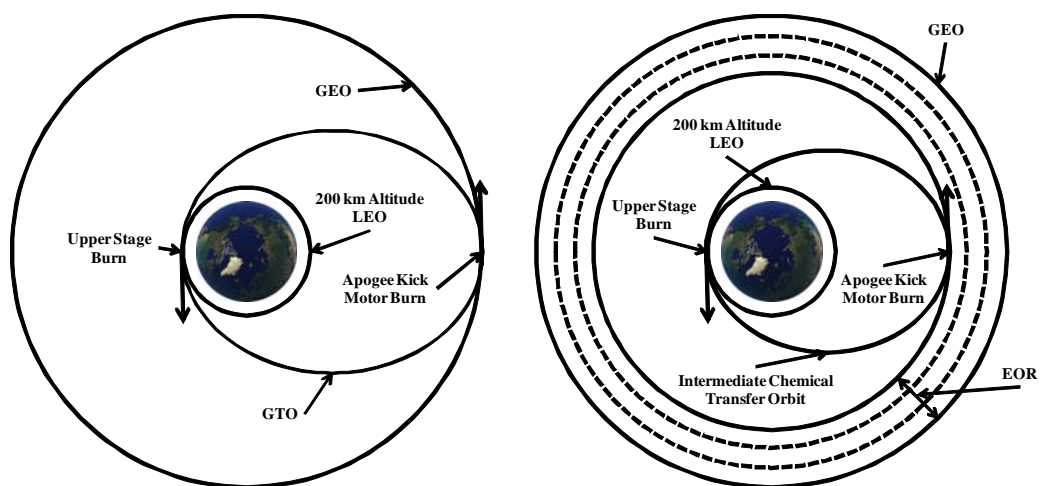
Figure 8.23. Pure Chemical Transfer (left) and C-EOR Transfer (right)

The pure chemical transfer scenario is as follows; 1) the upper stage burn delivers the spacecraft into the GTO, and 2) the apogee kick motor burn inserts the spacecraft to the final GEO. The pure chemical transfer is also using the Hohmann transfer to minimize the required fuel. The upper stage of the Sea Launch is the Block DM-SL, where the propulsive capability is provided by the 11D58M rocket. The rocket uses liquid oxygen and kerosene. The thrust and the specific impulse are assumed to be 80 kN and 353 s, respectively. The C-EOR mission phases are given in section 8.2.

In order to compare these two transfer strategies, the total required fuel for each case is calculated to deliver a given final mass. The given final mass is chosen to be 685.5 kg, which is the final mass for the case of the designed HET. The comparison results are shown in Table 8.11.

Table 8.11: Comparison of Pure Chemical Transfer and C-EOR

Variable	Pure Chemical Transfer	C-EOR
Amount of Propellant	1538.4 kg	1462.5 kg
Spacecraft Initial Mass	2223.9 kg	2148.0 kg
Time of Flight	5.26 hrs	20.21 days

As seen in Table 8.11, the C-EOR can save about 76 kg of fuel, which means that the C-EOR can deliver about 76 kg more payload to the GEO with the same initial spacecraft mass of the pure chemical transfer. Comparing Table 8.11 with Table 8.10, the main advantage of fuel saving results from the EOR. In order to obtain a broad estimate for cost savings, the cost savings per unit of delivered mass is calculated based on data in Ref. [151], which is shown in Table 8.12.

Table 8.12: GEO Delivery Cost Estimation [151]

BOL Mass [kg]	Strategy	Cost [M$]	Cost Savings per Unit Delivered Mass [M$/kg]
3445	Proton M/Breeze M + EOR	82	0.0023
	Sea Launch w/o EOR	90	
4073	Sea Launch + EOR	106	0.0034
	Ariane 5 w/o EOR	120	

If the average value of the cost savings per unit of delivered mass is used, about 0.22 M$ could be saved for this case with the designed HET. It is clear from these comparisons that the advantage of SEP is considerable in terms of fuel savings (mass transportation) and cost, although the transfer time is a lot longer than that of the chemical rocket.

CHAPTER 9

CONCLUSIONS AND FUTURE WORK

9.1 Conclusions

The motivations come from the needs for improving the current expensive experimental design procedure and infusing the actual HET performance envelope in the low-thrust trajectory optimization. The observations on the current design process of the HETs and the low-thrust trajectory optimization are made and the initial main questions are recalled here:

- Observation A.   The design process of the HETs has relied on mostly an experimental and empirical process.

  Q1: How can the conceptual design process of HET be improved?

- Observation B.   The low-thrust trajectory optimization has been performed without consideration of the performance envelope of a real electric thruster.

  Q2: How can the real thruster performance be infused in preliminary low-thrust trajectory optimization for a specific space mission?

- Observation C.   The design of HETs and the associated low-thrust trajectory optimization has been decoupled.

  Q3: How can the simultaneous design optimization environment be constructed?

The main questions guide the direction of the current research. In order to answer the main questions, subsequent secondary questions arise and are as follows:

Q4: Can an appropriate physics-based tool or methodology at the conceptual level be found among existing tools or methodologies?

Q5: If not, what is required to develop an appropriate physics-based tool or methodology?

In order to answer Q4 and Q5, there is a need for a proper physics-based analysis tool or methodology at a conceptual level of design. Thus, addressing this need is the first objective of the thesis, which is recalled here:

O1: Identify a proper physics-based analysis tool or methodology for general HET performances among existing methods, which fits at the conceptual design level for HET. If an adequate tool or methodology were not identified, develop an appropriate tool or methodology which meets the current research purposes.

The first objective requires the proposition of four criteria such as numerical efficiency, numerical robustness, self-consistency, and physics representativeness to evaluate the current tools or methodologies. Based on the evaluation in section 3.3, none are identified as an appropriate tool. Thus, a proper tool is developed with a new approach where the main idea is two-region discharge characterizing the HET physics. The development of a new tool can be achieved by addressing the hypotheses, which are repeated here.

Hypothesis 1. If the highly detail physics can be properly omitted when providing macroscopic performance metrics, the fluid approach will be a good candidate for improving numerical efficiency.

Hypothesis 2. If the singular form of a system of ODEs occurring in fluid approach can be somehow avoided, numerical robustness will be improved.

Hypothesis 3. If proper modeling near the anode region is included in the fluid approach, a self-consistent model will be constructed and the number of arbitrary boundary conditions will be reduced.

Hypothesis 4. If most of the major physical phenomena are included in the model and all concerned variables are computed by the tool within the range of assumptions, the tool will represent sufficient physical phenomena experimentally observed in HET.

The application of the fluid approach ensures the numerical efficiency as proved in the SPT-100 point validation. The idea of the two-region discharge makes it possible to avoid the singular form of the system of ODEs and have no dependence on the initial conditions for solutions, which results in the numerical robustness. The simple anode modeling introduced in section 4.3.4 enables the developed tool to solve all dependent variables without inputting arbitrary values, which guarantees the self-consistency. Finally, as seen in section 5.1, most of major physical phenomena are well reproduced by the developed tool with high accuracy of the performance metrics, which provides the moderate HET physics representativeness. At this point, another secondary question arises.

Q6: In case of developing an appropriate tool, can it be validated for a variety of existing HETs?

Q6 is answered by the intensive validation and additional capability studies which justifies the possibility of its use for new HET designs in spite of uncertainties in the anomalous coefficients. This achievement is largely attributed to careful examination of HET plasma physics from previous researches. This can lead to physical intuitions which give birth to new ideas as well as proofs of the proposed hypotheses.

In order to answer Q2 and Q3, the following secondary questions are invoked:

Q7: Can the appropriate tool be efficiently used for the simultaneous design optimization?

Q8: Can the feasible design space of HET to be designed be properly specified for the simultaneous design optimization.

The second and third objectives are intended to answer these questions by providing an HET performance analysis module that can be used for the simultaneous design environment, which are repeated here:

O2: Perform conceptual design space exploration for performance metrics with the identified or developed analysis tool. This task is expected to provide more thorough information for a new design of HETs in terms of thruster performance. In addition, a more broad understanding of HET is expected to be gained.

O3: Build the HET performance analysis module based on the identified or developed HET analysis tool and clearly identify the feasible HET design space for the simultaneous design optimization with the low-thrust trajectory optimization.

Based on the validation experience, a proper design space for the intended space missions can be defined. Furthermore, the analysis of DSE results provides several important observations on the thruster performance in terms of design variables such as identification of the anode mass flow rate and the discharge voltage as main performance drivers of the HETs. The implementations of the NN and SVM construct a solid HET performance analysis module and a feasible HET design space.

The fourth objective is to construct the simultaneous design optimization environment, which is repeated here:

O4: Construct the simultaneous design optimization environment to design a new HET and associated optimal low-thrust trajectory, which can achieve a specific space mission objective.

The main approach is to divide the HET design variables, based on their time dependence in one trajectory, into two categories; dynamic control and static control. The construction of the simultaneous design optimization environment for HET design and associated optimal low-thrust trajectory interconnects two disciplines which have been studied independently.

The final objective is to demonstrate the capabilities of the simultaneous design optimization environment by performing a simultaneous optimization for a sample orbit raising mission, which is repeated here:

O5: Perform the simultaneous design optimization for a selected space mission with a specified goal and investigate the optimum solutions. In addition, demonstrate the capabilities of the simultaneous design optimization environment.

A demonstration of an orbit raising mission application shows that the environment and its algorithms can be used for any space missions involving HETs. In conclusion, all of the research objectives are successfully accomplished and all of the main questions are answered.

9.2 Contributions

The research questions Q9 through Q11 regard the contributions that can be expected when the main questions are answered. These questions are repeated here:

Q9: What unidentified correlations exist between thruster parameters in terms of thruster performance metrics?

Q10: Can the existing scaling laws be improved by a physics-based tool or can new scaling laws be proposed?

Q11: What can be discovered when non-ideal thruster performances are infused in the low-thrust trajectory optimization and what are the differences compared to that of an ideal one?

By the analysis of the DSE results, the full correlation information between thruster parameters and thruster performance metrics are obtained. Furthermore, the construction of surrogate models for the HET can provide a quick tool to analyze the performance in terms of thruster parameters for a new HET design rather than simple scaling laws. In addition, the low-thrust trajectory optimization with the HET performance envelope provides more design freedom and benefits on the results. These achievements of the current research answer the questions about contributions.

In addition to these contributions from the results of research, development of a new analysis method is one major academic contribution. It overcomes weaknesses of current numerical methods at least in terms of the current purpose. However, because the developed method is expected to be reproduced quite easily by other researchers, it is highly possible that the method will be improved and adopted in other HET applications.

Intensive validations and design space exploration provide a more thorough understanding on HET plasma physics in quantitative ways. The way of identifying the feasible design space for HET is another achievement, and the idea and its use can be further extended to other applications as well.

The construction of a simultaneous optimization environment is another major academic contribution. It can be used for any space mission utilizing HETs. It is expected

that its use in preliminary space mission design stage can greatly reduce design cycles and cost. Practical implementation is also highly possible when designing new HETs for common commercial satellites.

9.3 Future Work

The future work can be enormous based on capabilities of the work presented in this thesis. The first initiative is to look at improvements of the developed tool. The anomalous coefficient needs to be properly physically modeled in order to greatly reduce the uncertainties. Because the electron anomalous diffusion is still a debated topic, it is imperative that a large amount of research effort should be given to understanding this physical phenomenon. Ion recombination at the wall needs to be incorporated in order to obtain more accurate discharge characteristics and address the HET lifetime issue. A method of eliminating the first derivative discontinuities of the plasma number density and electron mean velocity at the matching point should be developed to improve the reliability of the developed tool. The effects of multiply-charged ions also need to be accounted for in order to implement the tool more accurately for high-power HETs. There are still many open problems involving the HET plasma physics such as turbulent diffusion, plasma-wall interaction, electron distribution function and wall erosion. Therefore, the possibility of improvements seems to be unbounded.

However, the improvements should be carefully determined based on the purpose at hand. For example, if the tool is improved to include very detailed physical phenomena it may be necessary to sacrifice numerical efficiency, as in the full kinetic modeling. Thus, in the development procedure, careful decisions on what should be improved must

be made. The proposed criteria presented in section 3.1 can be effectively used for this decision.

Second, more validations with existing HETs are preferable to reveal any major weaknesses of the developed tool. As stated above, the complicated HET plasma physics is a major challenge and there are many phenomena which are yet to be fully understood. Therefore, further validation work will provide excellent guidance with regard to the best direction for improvements.

Third, simultaneous design optimization for a large number of space missions utilizing HETs is worthwhile and it will reveal general characteristics of coupled design and its advantages. The problem of coupled design optimization has not been attempted before, thus, a more thorough understanding is required for practical applications.

APPENDIX A

APPROXIMATION OF AZIMUTHAL ELECTRON MEAN

VELOCITY USING LANGEVIN'S APPROACH

The electron momentum equation based on the assumptions in section 4.3.2 while retaining the azimuthal electron mean velocity can be expressed as:

$$-\frac{d(n_e k T_e)}{dz} + n_e \frac{d(e\phi)}{dz} + e n_e u_{e,\theta} B - m_e n_e v_{e,eff} u_e = 0 \tag{A.1}$$

where $u_{e,\theta}$ is the azimuthal electron mean velocity. In order to eliminate $u_{e,\theta}$ in Equation (A.1), an appropriate physical approximation using other dependent variables for $u_{e,\theta}$ is required. The required approximation is obtained by solving the stochastic differential equations using the Langevin's approach [159].

Paul Langevin modeled the specific force in Newton's 2nd law as a viscous drag plus random fluctuations (often assumed as a normal distribution), which yields the following Langevin equation.

$$dV(t) = -vV(t)dt + \sqrt{\beta^2 dt}\, N(t) \tag{A.2}$$

where $V(t)$ is the random variable representing the particle velocity at time t, v is the effective collision frequency, β is the velocity space diffusion constant, and $N(t)$ represents the unit normal distribution at time t with vanishing mean and unit variance.

The Langevin equation is said to govern the Ornstein-Uhlenbeck process (O-U process) after Ornstein and Uhlenbeck put a solid foundation on the Langevin's approach [160]. The Brownian motion of a charged particle in a plane normal to a uniform,

stationary magnetic field was investigated while incorporating the Lorentz force into an O-U collision model [161]. The formulation here is expanded to incorporate a uniform, stationary electric field normal to the magnetic field as shown in Figure A.1.
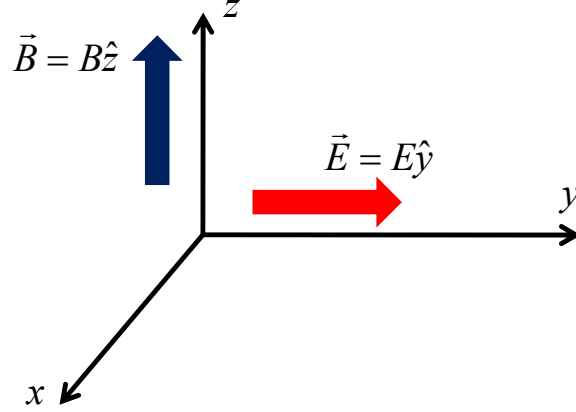
Figure A.1: Uniform, Stationary Magnetic and Electric Fields

The resultant Langevin equations incorporating the Lorentz force for an electron in the $x - y$ plane are given by

$$
\begin{aligned}
dV_x &= -\omega_e V_y dt - \nu_{e,eff} V_x + \sqrt{\beta^2 dt}\, N_{t,x}(0,1) \\
dV_y &= (-\omega_E + \omega_e V_x)dt - \nu_{e,eff} V_y dt + \sqrt{\beta^2 dt}\, N_{t,y}(0,1) \\
dX &= V_x dt \\
dY &= V_y dt
\end{aligned}
\tag{A.3}
$$

where $\omega_E = eE / m_e$. In order to characterize the solutions of Equation (A.3), 14 coupled ordinary differential equations for the time evolution of means and variances must be solved. The required moments include; 1) the mean values, $\langle V_x \rangle$, $\langle V_y \rangle$, $\langle X \rangle$, and $\langle Y \rangle$, 2) the variances, $\mathrm{var}\{V_x\}$, $\mathrm{var}\{V_y\}$, $\mathrm{var}\{X\}$, and $\mathrm{var}\{Y\}$, and 3) the covariances, $\mathrm{cov}\{V_x,V_y\}$, $\mathrm{cov}\{X,V_x\}$, $\mathrm{cov}\{Y,V_y\}$, $\mathrm{cov}\{Y,V_x\}$, $\mathrm{cov}\{X,V_y\}$, and $\mathrm{cov}\{X,Y\}$. Because mean values are of interest and their differential equations are coupled only with these

248

mean values, 4 coupled differential equations are solved with the assumption that sure initial values are given as $V_x(t_0) = v_{x0}$, $V_y(t_0) = v_{y0}$, $X(t_0) = x_0$, and $Y(t_0) = y_0$. By recognizing that the initial values of means are the same as the sure initial values, the solutions are given as:

$$\langle X \rangle = x_0 + \frac{\omega_e \omega_E}{v_{e,eff}^2 + \omega_e^2} t + \frac{1}{v_{e,eff}^2 + \omega_e^2}(v_{x0} v_{e,eff} - v_{y0} \omega_e) - \frac{2 v_{e,eff} \omega_e \omega_E}{(v_{e,eff}^2 + \omega_e^2)^2}$$

$$- e^{-v_{e,eff} t} \left[\frac{1}{v_{e,eff}^2 + \omega_e^2}(v_{x0} v_{e,eff} - v_{y0} \omega_e) - \frac{2 v_{e,eff} \omega_e \omega_E}{(v_{e,eff}^2 + \omega_e^2)^2} \right] \cos(\omega_e t)$$

$$+ e^{-v_{e,eff} t} \left[\frac{1}{v_{e,eff}^2 + \omega_e^2}(v_{x0} \omega_e + v_{y0} v_{e,eff}) + \frac{(v_{e,eff}^2 - \omega_e^2)\omega_E}{(v_{e,eff}^2 + \omega_e^2)^2} \right] \sin(\omega_e t)$$

$$\langle Y \rangle = y_0 - \frac{v_{e,eff} \omega_E}{v_{e,eff}^2 + \omega_e^2} t + \frac{1}{v_{e,eff}^2 + \omega_e^2}(v_{y0} v_{e,eff} + v_{x0} \omega_e) + \frac{(v_{e,eff}^2 - \omega_e^2)\omega_E}{(v_{e,eff}^2 + \omega_e^2)^2}$$

$$- e^{-v_{e,eff} t} \left[\frac{1}{v_{e,eff}^2 + \omega_e^2}(v_{y0} v_{e,eff} + v_{x0} \omega_e) + \frac{(v_{e,eff}^2 - \omega_e^2)\omega_E}{(v_{e,eff}^2 + \omega_e^2)^2} \right] \cos(\omega_e t) \qquad (A.4)$$

$$+ e^{-v_{e,eff} t} \left[\frac{1}{v_{e,eff}^2 + \omega_e^2}(v_{y0} \omega_e - v_{x0} v_{e,eff}) + \frac{2 v_{e,eff} \omega_e \omega_E}{(v_{e,eff}^2 + \omega_e^2)^2} \right] \sin(\omega_e t)$$

$$\langle V_x \rangle = \frac{\omega_e \omega_E}{v_{e,eff}^2 + \omega_e^2} + e^{-v_{e,eff} t} \left[\left(v_{x0} - \frac{\omega_e \omega_E}{v_{e,eff}^2 + \omega_e^2} \right) \cos(\omega_e t) - \left(v_{y0} - \frac{v_{e,eff} \omega_E}{v_{e,eff}^2 + \omega_e^2} \right) \sin(\omega_e t) \right]$$

$$\langle V_y \rangle = -\frac{v_{e,eff} \omega_E}{v_{e,eff}^2 + \omega_e^2} + e^{-v_{e,eff} t} \left[\left(v_{y0} + \frac{v_{e,eff} \omega_E}{v_{e,eff}^2 + \omega_e^2} \right) \cos(\omega_e t) + \left(v_{x0} - \frac{\omega_e \omega_E}{v_{e,eff}^2 + \omega_e^2} \right) \sin(\omega_e t) \right]$$

The relationship at steady-state between $\langle V_x \rangle$ and $\langle V_y \rangle$ is therefore given as:

$$\langle V_x \rangle_{steady\,state} = -\frac{\omega_e}{v_{e,eff}} \langle V_y \rangle_{steady\,state} = -\Omega_e \langle V_y \rangle_{steady\,state} \qquad (A.5)$$

where Ω_e is the electron Hall parameter. If it is assumed that Equation (A.5) locally holds at steady-state, the necessary expression for $u_{e,\theta}$ in Equation (A.1) can be expressed as:

$$u_{e,\theta} = -\frac{\omega_e}{v_{e,eff}} u_e \qquad\qquad (A.6)$$

Finally, substituting Equation (A.6) into Equation (A.1) results in Equation (4.3) in section 4.3.2.

APPENDIX B

CURVE-FIT EQUATIONS FOR REACTION RATES

First ionization reaction rate for Xenon

The following is the FORTRAN routine in double precision for calculating the first ionization reaction rate for Xenon, where TEV is the electron temperature in eV and GET_RC_I_DIM is an approximation of $RR_i = \langle \sigma_i v_e \rangle$ and is given in SI unit.

```
IF( TEV .LE. 0.76D0 ) THEN
 GET_RC_I_DIM = 1.22962468594778D-22 / 0.76D0 * TEV
ELSE IF( TEV .LE. 1.5D0 ) THEN
 GET_RC_I_DIM = 1.D-18 * ( 236.17632992 + 1065.4576546 * TEV**2
- 4963.921454 * TEV * DSQRT( TEV ) + 8518.3433023 * TEV
- 1356.22399 * DSQRT( TEV )
- 5049.120483 * DLOG( 1.D0 + TEV ) )
ELSE IF( TEV .LE. 6.5D0 ) THEN
 GET_RC_I_DIM = 1.D-16 * ( 407.29851331 - 30.76405181 * TEV**2
+ 267.86781003 * TEV * DSQRT(TEV) - 563.5305643 * TEV
- 1243.576261 * DSQRT( TEV )
+ 1678.7433546 * DLOG( 1.D0 + TEV ) )
ELSE IF( TEV .LE. 14.D0 ) THEN
 GET_RC_I_DIM = 1.D-16 * ( 23840.384595 + 47.773442698 * TEV**2
- 1023.557155 * TEV * DSQRT( TEV ) + 9552.3948237 * TEV
```

```
     - 55725.61529 * DSQRT( TEV )

     + 35327.485422 * DLOG( 1.D0 + TEV ) )

     ELSE

      GET_RC_I_DIM = 1.D-16 * ( - 1060.238824 - 0.287349009 * TEV**2

     + 14.890417813 * TEV * DSQRT( TEV ) - 328.0549168 * TEV

     + 4176.1223911 * DSQRT( TEV )

     - 3771.608639 * DLOG( 1.D0 + TEV ) )

     ENDIF
```

First excitation reaction rate for Xenon

The following is the FORTRAN routine in double precision for calculating the first excitation reaction rate, where TEV is the electron temperature in eV and GET_RC_EX_DIM is an approximation of $RR_{exc} = \langle \sigma_{exc} v_e \rangle$ and is given in SI unit.

```
     IF( TEV .LE. 0.69D0 ) THEN

      GET_RC_EX_DIM = 5.08408309542574D-22 / 0.69D0 * TEV

     ELSE IF( TEV .LE. 1.32D0 ) THEN

      GET_RC_EX_DIM = 1.D-18 * ( 384.93301103 + 5906.6945644 * TEV**2

     - 29452.82993 * TEV * DSQRT( TEV ) + 52976.019771 * TEV

     - 4061.78342 * DSQRT( TEV )

     - 37153.48914 * DLOG( 1.D0 + TEV ) )

     ELSE IF( TEV .LE. 4.5D0 ) THEN

      GET_RC_EX_DIM = 1.D-16 * ( 396.15120821 - 72.8269051 * TEV**2
```

+ 559.35258841 * TEV * DSQRT(TEV) - 1206.807152 * TEV

- 1251.468902 * DSQRT(TEV)

+ 2273.5013847 * DLOG(1.D0 + TEV))

ELSE IF(TEV .LE. 14.D0) THEN

 GET_RC_EX_DIM = 1.D-16 * (- 9530.927928 - 12.8807594 * TEV**2

+ 317.4647051 * TEV * DSQRT(TEV) - 3484.270567 * TEV

+ 24038.281055 * DSQRT(TEV)

- 16718.66551 * DLOG(1.D0 + TEV))

ELSE

 GET_RC_EX_DIM = 1.D-16 * (- 1764.678691 - 0.370317143 * TEV**2

+ 14.56036509 * TEV * DSQRT(TEV) - 228.5523671 * TEV

+ 1832.91572 * DSQRT(TEV)

- 783.6626165 * DLOG(1.D0 + TEV))

ENDIF

__Momentum transfer collision reaction rate for Xenon__

The following is the FORTRAN routine in double precision for calculating the momentum transfer collision reaction rate, where TEV is the electron temperature in eV and GET_RC_MT_DIM is an approximation of $RR_{mt} = \langle \sigma_{mt} v_e \rangle$ and is given in SI unit.

IF(TEV .LE. 0.66D0) THEN

 GET_RC_MT_DIM = 2.80018415651284D-021 / 0.66D0 * TEV

ELSE IF(TEV .LE. 0.96D0) THEN

```fortran
      GET_RC_MT_DIM = 1.D-18 * ( 1942.7833599 + 21752.481587 * TEV**2

- 106373.3163 * TEV * DSQRT( TEV ) + 189020.76071 * TEV

- 17006.19333 * DSQRT( TEV )

- 128882.7118 * DLOG( 1.D0 + TEV ) )

ELSE IF( TEV .LE. 1.5D0 ) THEN

 GET_RC_MT_DIM = 1.D-16 * ( 86.367756586 + 340.94984236 * TEV**2

- 1620.465496 * TEV * DSQRT( TEV ) + 2820.6047391 * TEV

- 462.4640629 * DSQRT( TEV )

- 1680.702613 * DLOG( 1.D0 + TEV ) )

ELSE IF( TEV .LE. 14.D0 ) THEN

 GET_RC_MT_DIM = 1.D-16 * ( - 4897.223675 + 23.050024721 * TEV**2

- 182.8462002 * TEV * DSQRT( TEV ) - 632.7605435 * TEV

+ 13942.419088 * DSQRT( TEV )

- 11944.35514 * DLOG( 1.D0 + TEV ) )

ELSE

 GET_RC_MT_DIM = 1.D-16 * ( - 1920.569321 + 0.1200436464 * TEV**2

- 7.301695795 * TEV * DSQRT( TEV ) + 177.65021262 * TEV

- 2572.495579 * DSQRT( TEV )

+ 3848.6613267 * DLOG( 1.D0 + TEV ) )

ENDIF
```

APPENDIX C

REFERENCE VALUES FOR NON-DIMENSIONALIZATION OF

VARIABLES

The followings are the reference values for non-dimemsionalization of the variables. The governing equations are non-dimensionalized with these reference values.

Mass: $m^* = m_n \approx m_i \quad [kg]$

Temperature: $T^* = \dfrac{e\bar{\varepsilon}_i}{k} \quad [K]$

$\Rightarrow \quad \widetilde{T} = \dfrac{T}{T^*} = \dfrac{kT/e}{kT^*/e} = \dfrac{T_{eV}}{T_{eV}^*} \ \& \ T_{eV}^* = \dfrac{kT^*}{e} = \bar{\varepsilon}_i \ (eV)$

Potential: $\varphi^* = \dfrac{kT^*}{e} = T_{eV}^* \quad [eV]$

$\Rightarrow \quad \widetilde{\varphi} = \dfrac{e\varphi}{eT_{eV}^*} = \dfrac{e\varphi}{kT^*}$

Velocity: $u^* = \sqrt{\dfrac{kT^*}{m^*}} \quad \left[\dfrac{m}{\sec}\right] \qquad \Rightarrow \quad m^* u^{*2} = kT^*$

Number density: $n^* = \dfrac{\dot{m}}{m^* u^* A_c} \quad \left[\dfrac{\#}{m^3}\right] \quad$ where, A_c is channel area at the anode.

Cross section: $\sigma^* = \sigma_0 \sqrt{\dfrac{m_i}{m_e}} \quad [m^2] \quad$ where, $\sigma_0 \cong 3.6\times10^{-20} \ m^2 \ for \ Xenon$

Collision frequency: $\nu^* = n^* \sigma^* u^* \quad \left[\dfrac{\#}{\sec}\right]$

Length: $l^* = \dfrac{u^*}{v^*} = \dfrac{1}{n^* \sigma^*}$ $[m]$ $\Rightarrow$ $n^* \sigma^* l^* = 1$

Time: $t^* = \dfrac{1}{v^*} = \dfrac{1}{n^* \sigma^* u^*} = \dfrac{l^*}{u^*}$ $[sec]$

APPENDIX D

DESCRIPTION OF THE DEVELOPED TOOL: HOW-TO-USE

D.1 Introduction

The developed tool is a numerical analysis software for the typical HET configuration. The algorithms are described in Chapter IV. The tool is coded in FORTRAN and consists of the following components:

- A main program

- Readout of input variables and pre-processing

- Calculation of reference variables and non-dimensionalization

- Calculation of miscellaneous required variables, the Gaussian-Legengdre abscissas and weights, and readout of the magnetic field distribution in case it is given

- Iterative solution procedure using relaxation method

- Calculation of anomalous coefficients as a function of discharge voltage

- Calculation of collision frequencies and reaction rates

- Finite difference method for ionization/acceleration region

- Post-processing for plasma structures, performance, and data for plotting

- Miscellaneous routines including spline and grid clustering

D.2 Usage

To use the developed tool, execute "hall1d.exe" with a given input file in the command window or double click the execution file in the directory.

D.2.1 Input

The inputs consist of a total of 13 groups as follows.

1) Group 1: propellant information (limited to Xenon)

   a. AMW_DIM: molecular weight of propellant species [kg/kmole]

   b. EI_DIM: threshold of first ionization energy [eV]

   c. EEXCITE_DIM: first excitation energy [eV]

   d. AMDOT_DIM: propellant (anode) mass flow rate [kg/s]

2) Group 2: power

   a. PHI_D_DIM: discharge voltage [V]

   b. COE_ANO1: inverse of the anomalous coefficient inside the channel

   c. COE_ANO2: inverse of the anomalous coefficient outside the channel

3) Group 3: magnetic field information

   a. BMAX_DIM: maximum radial magnetic field strength [T]

   b. BCATH_DIM: radial magnetic field strength at the cathode [T]

   c. COEMAG: shape coefficient of radial magnetic field strength inside the channel

   d. IMAGOPT: magnetic field option, 1 – analytic expression (no input required), 2 – given in input file (mf.dat file must exist in the same directory as the execution file)

   e. IMAGDISTOPT: When IMAGOPT = 1, option for magnetic field distribution in the plume region, 1 – linear, 2 - quadratic

4) Group 4: geometry information

   a. D_L_DIM: channel length [m]

b. R1_DIM: inner radius [m]

c. R2_DIM: outer radius [m]

d. Z_CATH_DIM: distance from exit plane to the cathode line [m]

5) Group 5: max constraints

a. TE_MAX0_DIM: maximum allowable electron temperature the material can withstand [eV]

6) Group 6: boundary conditions

a. T_A_DIM: anode temperature [K]

b. TE_C_DIM: electron temperature at the cathode line [eV]

c. PHI_C_DIM: electric potential at the cathode line [V]

7) Group 7: guessed values

a. UI_C_GUESS: initial guess for ion mean velocity at the cathode line [m/s]

b. TE_M_GUESS: initial guess for electron temperature at the matching point [eV]

c. NE_M_GUESS: initial guess for plasma number density at the matching point [#/m^3]

8) Group 8: additional parameters

a. IWOPT: option for wall collision model, 1 – constant, 2 – NASA model, 3 – Ahedo's model

b. IMUEOPT: option for electron mobility expression, 1 – classical expression, 2 – expression with the assumption of high electron hall parameter

c. ANODIST: fraction of distance from the thruster exit to the cathode line for smooth transition of the anomalous coefficient between inside and outside the channel

d. WALDIST: fraction of distance from the thruster exit to the cathode line for smooth transition of wall collision effect between inside and outside the channel

9) Group 9: option for collision frequency, 0 – no inclusion, 1 – inclusion

a. IMNCOL: electron-neutral momentum exchange collision

b. IMEICOL: electron-ion Coulomb collision

c. IMWCOL: electron-wall momentum collision

d. IMBCOL: effective Bohm collision

e. IEICOL: ionization energy loss collision

f. IRECOL: recombination collision

g. IEXCOL: excitation energy loss collision

h. IEWCOL: wall energy loss collision

i. IEACOL: additional ionization energy loss collision

10) Group 10: option for grid generation

a. ICLUST: 0 – equal space, else – clustering

b. BETA: degree of clustering (>1), the smaller, the more clustering

c. IPOS1: type of clustering for channel region, negative – start point clustering, 0 – both side clustering, positive – end point clustering

d. IPOS2: type of clustering for outside region with the same options as IPOS1

11) Group 11: general numerical inputs

a. NQ: number of dependent variables to be solved

b. M: number of grid points

c. ITMAX: maximum iteration for global iteration

d. STEP: step size for numerical differentiation

e. CONV: convergence criterion (log scale)

f. OMEGA: relaxation factor

g. NQUAD: number of points used for the Gaussian-Legengdre quadrature rule

12) Group 12: numerical inputs for finite difference ODE solver

a. CONVODE: convergence criterion

b. SLOWODE: factor for convergence rate adjustment

c. ITMAXODE: maximum iteration

13) Group 13: print option, 0 – no print, 1 – print

a. IPREF: reference variable values

b. IPMAG: radial magnetic field distribution

c. IPGRID: generated grid

d. IPINIT: initial guessed values

e. IPPERI: periodic solutions

f. IPSOL: final solutions

g. IPERR: error history

h. IPOUT: performance history

i. NSTO: iteration number interval for saving intermediate solutions

j. NERR: iteration number interval for saving error

k. NAVE: in case of oscillatory solution, average values during last NAVE iterations

D.2.2 Outputs

The outputs consist of an exit mode code and a total of 8 groups as follows.

1) Exit mode code: solution case number explained in section 5.3.4

2) Group 1: constant values

a. COE_ANO1, COE_ANO2: anomalous coefficients inside and outside the channel

b. WE_MAX, Z_WE_MAX: maximum electron gyro frequency [rad/s] and its location [cm]

c. UN0: neutral mean velocity [m/s]

d. NN0: neutral number density at the matching point [#/m^3]

e. TE_C: electron temperature at the cathode [eV]

f. PHI_C: electric potential at the cathode [V]

g. EE_C: electron internal energy at the cathode [eV]

h. A: channel area [m^2]

3) Group 2: performance

a. ISP: anode specific impulse [s]

b. THRUST: thrust [mN]

c. CRT_D: discharge current [A]

d. PD: discharge power [kW]

4) Group 3: efficiencies

a. ETA_ANO: anode efficiency

b. ETA_E: electrical efficiency

c. ETA_A: acceleration efficiency

d. ETA_U: utilization efficiency

5) Group 4: matching point variables

a. Z_M: location of the matching point [cm]

b. TE_M: electron temperature at the matching point [eV]

c. ANE_M: plasma number density at the matching point [#/m^3]

d. PHI_M: electric potential at the matching point [V]

6) Group 5: other parameters

a. ANU_I_AVE: average ionization collision frequency in the presheath region
    [#/s]

b. UE_CATHODE: electron mean velocity at the cathode line [m/s]

7) Group 6: continuity check

a. MDOT_C: total mass flow rate at the cathode line [kg/s]

b. ID_A: discharge current at the anode [A]

8) Group 7: maximum properties

a. TE_MAX, Z_TE_MAX: maximum electron temperature [eV] and its location
    [cm]

b. IR_MAX, Z_IR_MAX: maximum ionization rate [#/m^3-s] and its location
    [cm]

c. EF_MAX, Z_EF_MAX: maximum electric field [V/m] and its location [cm]

d. HP_MAX, Z_HP_MAX: maximum electron Hall parameter and its location
    [cm]

9) Group 8: 4 constraint values explained in section 6.2.3 and maximum electron temperature constraint value for later use

REFERENCES

[1] Dan M. Goebel, and Ira Katz, "Fundamentals of Electric Propulsion," *JPL Space Science and Technology Series*, A John Wiley & Sons, Inc., 2008.

[2] Ronald W. Humble, Gary N. Henry, and Wiley J. Larson, "Space Propulsion Analysis and Design," *Space Technology Series*, The McGraw-Hill Companies, Inc., 1995.

[3] Wiley J. Larson, and James R. Wertz, "Space Mission Analysis and Design," *The Space Technology Library*, Microcosm, Inc., 2004.

[4] Gulczinski, P., and Spores, R., "Analysis of Hall-effect thrusters and ion engines for orbit transfer missions," AIAA-96-2973, 32nd Joint Propulsion Conference, Lake Buena Vista, FL. July 1-3, 1996.

[5] Marc D. Rayman, Thomas C. Fraschetti, Carol A. Raymond, and Christopher T. Russell, "Dawn: A Mission in Development for Exploration of Main Belt Asteroids Vesta and Ceres," *Acta Astronautica*, Vol 58, 2006, pp. 605-616.

[6] E. Y. Choueiri, "A Critical History of Electric Propulsion: The First 50 Years (1906 – 1956)", *Journal of Propulsion and Power*, Vol 20, No 2, Mar.-Apr., 2004, pp. 193-203.

[7] Richard R. Hofer, "Development and Characterization of High-Efficiency, High-Specific Impulse Xenon Hall Thrusters", *NASA/CR-2004-213099.*

[8] E. H. Hall, "On a New Action of the Magnet on Electric Currents," *American Journal of Mathematics*, Vol 2, 1879, pp. 287-292.

[9] Harold R. Kaufman, "Technology of Closed-Drift Thrusters," AIAA Journal, Vol. 23, No. 1, 1983, pp. 78-87.

[10] Raymond S. Robinson, Terry D. Schemmel, and Michael J. Patterson, "Closed-Drift Thruster Investigation," NASA CR-179497, Jun. 1986.

[11] Edgar Y. Choueiri, "Fundamental Difference between the Two Variants of Hall Thrusters: SPT and TAL", AIAA-2001-3504, 37th AIAA Joint Propulsion Conference, Salt Lake City, UT, July 9-11, 2001.

[12] Michelle R. Kirby, "A Methodology for Technology Identification, Evaluation, and Selection in Conceptual and Preliminary Aircraft Design," Ph.D. Thesis, Georgia Institute of Technology, Mar. 2001.

[13] Mavris, D. N., Kirby, M. R., and Qiu, S., "Technology Impact Forecasting for a High Speed Civil Transport," SAE-985547, World Aviation Conference, Sept. 1998, Anaheim, CA.

[14] Mankins, John C., "Technology Readiness Levels: A White Paper," NASA, Office of Space Access and Technology, Advanced Concepts Office, 1995.

[15] Charles E. Garner, James E. Polk, Lewis C. Pless, Keith D. Goodfellow, and John R. Brophy, "Performance Evaluation and Life Testing of the SPT-100," IEPC-93-091, 23rd International Electric Propulsion Conference, Sept. 1993, Seattle, WA, USA.

[16] John M. Sankovic, John A. Hamley, and Thomas W. Haag, "Performance Evaluation of the Russian SPT-100 Thruster at NASA LeRC," IEPC-93-094, 23rd International Electric Propulsion Conference, Sept. 1993, Seattle, WA, USA.

[17] Arhipov B. A., Krochak L. Z., Kudriavcev S. S., Murashko V. M., and Randolph T., "Investigation of the Stationary Plasma Thruster (SPT-100) Characteristics and Thermal Maps at the Raised Discharge Power," AIAA-98-3791, 1998.

[18] N. Gascon, M. Dudeck, and S. Barral, "Wall Material Effects in Stationary Plasma Thrusters. I. Parametric Studies of an SPT-100," Physics of Plasmas, Vol. 10, No. 10, Oct. 2003.

[19] E. E. Barkalov, A. N. Veselovzorov, A. A. Pogorelov, E. B. Svirskii, and V. A. Smirnov, "Composition of the Beam of an SPT-100 Stationary Plasma Thruster," Instruments and Experimental Techniques, Vol. 51, No. 2, 2008, pp. 263-267.

[20] Maslenikov, N. A., Russian Electric Propulsion Seminar, Massachusetts Institute of Technology, 1991.

[21] Haas, J. M., Gulczinski, F. S., Gallimore, A. D, Spanjers, G. G., and Spores, R. A., "Performance Characteristics of a 5kW Laboratory Hall Thruster," AIAA-98-3503, 34th Joint Propulsion Conference, Cleveland, OH, July 1998.

[22] Frank Stanley Gulczinski III, "Examination of the Structure and Evolution of Ion Energy Properties of a 5kW Class Laboratory Hall Effect Thruster at Various Operational Conditions," Ph. D. Dissertation, School of Aerospace Engineering, The University of Michigan, Ann Arbor, MI, 1999.

[23] Brophy, J. R., "Ion Thruster Performance Model," NASA CR-174810, Dec. 1984.

[24] Leonard Biagioni, Massimo Saverdi, and Mariano Andrenucci, "Scaling and Performance Prediction of Hall Effect Thrusters," AIAA 2003-4727, 39th AIAA/ASME/SAE/ASEE Joint Propulsion Conference and Exhibit, 20-23 July 2003, Huntsville, Alabama.

[25] Hofer, R. R., and Jankovsky, R. S., "A Hall Thruster performance Model Incorporating the Effects of a Multiply-Charged Plasma," AIAA 2001-3322, 37th AIAA/ASME/SAE/ASEE Joint Propulsion Conference and Exhibit, Salt Lake city UT, July 2001.

[26] Khayms, V., and Martinez-Sanchez, M., "Design of a Miniaturized Hall Thruster for Microsatellites," AIAA 1996-3291, 32nd AIAA/ASME/SAE/ASEE Joint Propulsion Conference and Exhibit, Lake Buena Vista, FL, July 1-3, 1996.

[27] Yu Daren, Ding Yongjie, and Zeng Zhi, "Improvement on the Scaling Theory of the Stationary Plasma Thruster," Journal of Propulsion and Power, Vol. 21, No. 1., 2005.

[28] Marc D. Rayman, Pamela A. Chadbourne, Jeffery S. Culwell, and Steven N. Williams, "Mission Design for Deep Space 1: A Low-Thrust Technology Validation Mission," Acta Astronautica, Vol. 45, Nos. 4-9, 1999, pp. 381-388.

[29] Marc D. Rayman, Philip Varghese, David H. Lehman, and Leslie L. Livesay, "Results from the Deep Space 1 Technology Validation Mission," Acta Astronautica, Vol. 47, Nos. 2-9, 2000, pp. 475-487.

[30] Racca, G. D., Foing, B. H. and Coradini, M., "SMART-1: The First Time of Europe to the Moon," Earth, Moon and Planets, Vol. 85, 2001.

[31] Giuseppe D. Racca, "New Challenges to Trajectory Design by the Use of Electric Propulsion and Other New Means of Wandering in the Solar System," Celestial Mechanics and Dynamical Astronomy, Vol. 85, 2003, pp. 1-24.

[32] Kristina Alemany, and Robert D. Braun, "Survey of Global Optimization Methods for Low-Thrust, Multiple Asteroid Tour Missions," AAS 07-211.

[33] Damon Landau, Theresa Kowalkowski, Jon Sims, Thomas Randolph, and Paul Timmerman, "Electric Propulsion System Selection Process for Interplanetary Missions," AIAA/AAS Astrodynamics Specialist Conference and Exhibit, 18-21 Aug. 2008, Honolulu, Hawaii.

[34] C. A. Kluever, "Geostationary Orbit Transfers Using Solar Electric Propulsion with Specific Impulse Modulation," Journal of Spacecraft and Rockets, Vol. 41, No. 3, 2004, pp. 461-466.

[35] Giovanni Mengali, and Alessandro A. Quarta, "Fuel-Optimal, Power-Limited Rendezvous with Variable Thruster Efficiency," Journal of Guidance, Control, and Dynamics, Vol. 28, No. 6, 2005, pp. 1194-1199.

[36] David Manzella, David Oh, and Randall Aadland, "Hall Thruster Technology for NASA Science Missions," AIAA-2005-3675, 41st AIAA/ASME/SAE/ASEE Joint Propulsion Conference & Exhibit, 10-13 July, 2005, Tucson, Arizona.

[37] Bucovsky Adrian Eyer, Jesse and Mavris, Dimitri, "Design Space Exploration for Boom Mitigation on a Quiet Supersonic Business Jet," AIAA 3rd Annual Aviation Technology, Integration, and Operation (ATIO) Technology Conference, Denver, Co, Nov. 2003.

[38] Frits, Andrew P. and Mavris, Dimitri N., "A Screening Method for Customizing Designs around Non-Convergent Regions of Design Spaces," 9th AIAA/ISSMO Symposium and Exhibit on Multidisciplinary Analysis and Optimization, Atlanta, GA, Sept. 2002.

[39] Frits, Andrew P., Mavris, N. Dimitri, Kusmik Aldo, and Krol Jr. William, "Examination of a Torpedo Performance Space and its Relation to the System Design Space," 9th AIAA/ISSMO Symposium and Exhibit on Multidisciplinary Analysis and Optimization, Atlanta, GA, Sept. 2002.

[40] Walter G. Vincenti, and Charles H. Kruger, Jr., "Introduction to Physical Gas Dynamics," John Wiley & Sons, Inc., 1965.

[41] Francis F. Chen, "Introduction to Plasma Physics and Controlled Fusion," Plenum Press, NY, 1984.

[42] J. A. Bittencourt, "Fundamentals of Plasma Physics," Springer-Verlag New York, Inc., 2004.

[43] Edward M. Purcell, "Electricity and Magnetism," McGraw-Hill Book Company, 2nd Ed., 1985.

[44] William H. Hayt, Jr., and John A. Buck, "Engineering Electromagnetics," McGraw-Hill Book Company, 7th Ed., 2006.

[45] G. A. Bird, "Molecular Gas dynamics and the Direct Simulation of Gas Flows," Oxford University Press Inc., New York, 1994.

[46] Weston M. Stacey, Jr., "FUSION: An Introduction to the Physics and Technology of Magnetic Confinement Fusion," John Wiley & Sons, Inc., 1984.

[47] Iain D. Boyd, "Numerical Modeling of Spacecraft Electric Propulsion Thrusters," Progress in Aerospace Sciences, Vol. 41, 2005, pp. 669-687.

[48] C. K. Birdsall, and A. B. Landon, "Plasma Physics via Computer Simulation," Taylor & Francis Group, New York, 2005.

[49] R. W. Hockney, and J. W. Eastwood, "Computer Simulation using Particles," Taylor & Francis Group, New York, 1988.

[50] J. P. Boeuf, and E. Marode, "A Monte Carlo Analysis of an Electron Swarm in a Non-Uniform Field: the Cathode Region of a Glow Discharge in Helium," Journal of Physics D: Applied Physics, Vol. 15, 1982, pp. 2169-2187.

[51] Nicholas Metropolis, Arianna W. Rosenbluth, Marshall N. Rosenbluth, and Augusta H. Teller, "Equation of State Calculations by Fast Computing Machines," The Journal of Chemical Physics, Vol. 21, No. 6, 1953, pp. 1087-1092.

[52] James Joseph Szabo, Jr., "Fully Kinetic Numerical Modeling of a Plasma Thruster," Ph.D. Thesis, Massachusetts Institute of Technology, Feb. 2001.

[53] Christopher A. Lentz, "Transient One Dimensional Numerical Simulation of Hall Thrusters," Master Thesis, Massachusetts Institute of Technology, Sept. 1993.

[54] K-U Riemann, "The Bohm Criterion and Sheath Formation," Journal of Physics D: Applied Physics, Vol. 24, 1991, pp. 493-518.

[55] S. A. Self, "Exact Solution of the Collisionless Plasma-Sheath Equation," The Physics of Fluids, Vol. 6, No. 12, Dec. 1963, pp. 1762-1768.

[56] Seungwon Lee, Paul von Allmen, Wolfgang Fink, Anastassios E. Petropoulos, and Richard J. Terrile, "Design and Optimization of Low-thrust Orbit Transfer," IEEEAC paper #2.1204, 2005.

[57] Arthur E. Bryson, Jr., Yu-Chi Ho, "Applied Optimal Control," Taylor & Francis Group, LLC, Revised Edition, 1975.

[58] Frank L. Lewis, "Applied Optimal Control and Estimation," Prentice Hall, 1992.

[59] Lorenzo Casalino, Guido Colasurdo, and Matteo Rosa Sentinella, "Indirect Optimization Method for Low-Thrust Interplanetary Trajectories," IEPC-2007-356, 30th International Electric Propulsion Conference, Sept. 17-20, 2007, Florence, Italy.

[60] Christopher L. Ranieri, and Cesar A. Ocampo, "Optimization of Roundtrip, Tim-Constraintd, Finite Burn Trajectories via an Indirect Method," Journal of Guidance, Control, and Dynamics, Vol. 28, No. 2, 2005, pp. 306-314.

[61] Sean Tang, and Bruce A. Conway, "Optimization of Low-Thrust Interplanetary Trajectories Using Collocation and Nonlinear Programming," Journal of Guidance, Control, and Dynamics, Vol. 18, No. 3, 1995, pp. 599-604.

[62] Matthew A. Vavrina, and Kathleen C. Howell, "Global Low-Thrust Trajectory Optimization through Hybridization of a Genetic Algorithm and a Direct Method," AAS/AIAA Astrodynamics Specialists Conference, Aug. 2008, Honolulu, Hawaii.

[63] Lantoine, G., "A Methodology for Robust Optimization of Low-Thrust Trajectories in Multi-Body Environments," Ph.D. Thesis, Georgia Institute of Technology, 2010 (in completion).

[64] V. Latocha, L. Garrigues, P. Degond, and J. P. Boeuf, "Numerical Simulation of Electron Transport in the Channel Region of a Stationary Plasma Thruster," Plasma Sources Science and Technology, Vol. 11, 2002, pp. 104-114.

[65] J. C. Adam, A. Heron, and G. Laval, "Study of Stationary Plasma Thrusters Using Two-Dimensional Fully Kinetic Simulations," Physics of Plasmas, Vol. 11, No. 1, Jan. 2004, pp. 295-305.

[66] Francesco Taccogna, Savino Longo, Mario Capitelli, and Ralf Schneider, "Plasma Flow in a Hall Thruster," Physics of Plasmas, Vol. 12, 043502, 2005.

[67] F. Taccogna, S. Longo, M. Capitelli, and R. Schneider, "Start-Up Transient in a Hall Thruster," Contributions to Plasma Physics, Vol. 46, No. 10, 2006, pp. 781-786.

[68] John Michael Fife, "Two-Dimensional Hybrid Particle-In-Cell Modeling of Hall Thrusters," Master Thesis, Massachusetts Institute of Technology, May 1995.

[69] John Michael Fife, "Hybrid-PIC Modeling and Electrostatic Probe Survey of Hall Thruster," Ph.D. Thesis, Massachusetts Institute of Technology, Sept. 1998.

[70] Justin W. Koo, and Iain D. Boyd, "Computational Modeling of Stationary Plasma Thrusters," AIAA-2003-10113, 39th AIAA/ASME/SAE/ASEE Joint Propulsion Conference, Huntsville, AL, July 2003.

[71] Michelle K. Scharfe, Nicolas Gascon, Mark A. Cappelli, and Eduardo Fernandez, "Comparison of Hybrid Hall Thruster Model to Experimental Measurements," Physics of Plasmas, Vol. 13, 083505, 2005.

[72] G. Hagelaar, J. Bareilles, L. Garrigues, and J. P. Boeuf, "Two Dimensional Model of a Stationary Plasma Thruster," Journal of Applied Physics, Vol. 91, 2002, pp. 5592-5598.

[73] E. Ahedo, P. Martinez, and M. Martinez-Sanchez, "Steady and Linearly-Unsteady Analysis of a Hall Thruster with and Internal Sonic Point," AIAA-2000-3655, 36th

AIAA/ASME/SAE/ASEE Joint Propulsion Conference & Exhibit, July 2000, Huntsville, Alabama.

[74] E. Ahedo, P. Martinez Cerezo, and M. Martinez-Sanchez, "1-D Performance Analysis of a Hall Thruster," Proceedings of 3rd International Conference on Spacecraft Propulsion, Cannes, Oct. 2003.

[75] E. Ahedo, P. Martinez Cerezo, and M. Martinez-Sanchez, "One-Dimensional Model of the Plasma Flow in a Hall Thruster," Physics of Plasmas, Vol. 8, No. 6, June 2001, pp. 3058-3068.

[76] E. Ahedo, J. M. Gallardo, and M. Martinez-Sanchez, "Effects of the Dielectric Walls on the Axial Discharge of a Hall Thruster," AIAA-2002-4244, 38th /ASME/SAE/ASEE Joint Propulsion Conference & Exhibit, July 2002, Indianapolis, Indiana.

[77] E. Ahedo, J. M. Gallardo, and M. Martinez-Sanchez, "Model of the Plasma Discharge in a Hall Thruster with Heat Conduction," Physics of Plasmas, Vol. 9, No. 9, Sept. 2002, pp. 4061-4070.

[78] E. Ahedo, J. M. Gallardo, and M. Martinez-Sanchez, "Effects of the Radial Plasma-Wall Interaction on the Hall Thruster Discharge," Physics of Plasmas, Vol. 10, No. 8, Aug. 2003, pp. 3397-3409.

[79] Subrata Roy, and B. P. Pandey, "Numerical Investigation of a Hall Thruster Plasma," Physics of Plasmas, Vol. 9, No. 9, Sept. 2002, pp. 4052-4060.

[80] Avi Cohen-Zur, Amnon Fruchtman, Joseph Ashkenazy, and Alon Gany, "Analysis of the Steady-State Axial Flow in the Hall Thruster," Physics of Plasmas, Vol. 9, No. 10, Oct. 2002, pp. 4363-4374.

[81] J. Ashkenazy, A. Fruchtman, Y. Raitses, and N. J. Fisch, "Modeling the Behaviour of a Hall Current Plasma Accelerator," Plasma Physics and Controlled Fusion, Vol. 41, 1999, pp. A357-A364.

[82] A. Fruchtman, N. J. Fisch, and Y. Raitses, "Hall Thruster with Absorbing Electrodes," AIAA 2000-3659, 36th AIAA/ASME/SAE/ASEE Joint Propulsion Conference, 17-19 July 2000, Huntsville, AL.

[83] L. Dorf, and V. Semenov, "Anode Sheath in Hall Thrusters," Applied Physics Letters, Vol. 83, No. 13, Sept. 2003, pp. 2551-2553.

[84] J. P. Boeuf, L. Garrigues, and L. C. Pitchford, "Modeling of a Magnetized Plasma: The Stationary Plasma Thruster," Electron Kinetics and Application of Glow Discharge, 1998, pp. 85-100.

[85] J. P. Boeuf, and L. Garrigues, "Low Frequency Oscillations in a Stationary Plasma Thruster," Journal of Applied Physics, Vol. 84, No. 7, Oct. 1998, pp. 3541-3554.

[86] K. Komurasaki, and Y. Arakawa, "Two-Dimensional Numerical Model of Plasma Flow in a Hall Thruster," Journal of Propulsion and Power, Vol. 11, No. 6, 1995, pp. 1317-1323.

[87] M. Keidar, and I. D. Boyd, "Plasma Flow and Plasma-Wall Transition in Hall Thruster Channel," Physics of Plasmas, Vol. 8, No. 12, Dec. 2001, pp. 5315-5322.

[88] H. De Sterck, "Critical Point Analysis of Transonic Flow Profiles with Heat Conduction," SIAM Journal of Applied Dynamical Systems, Vol. 6, No. 3, pp. 645-662.

[89] D. D. Morrison, J. D. Riley, and J. F. Zancanaro, "Multiple Shooting Method for Two-Point Boundary Value Problems," Communications of the ACM, Vol. 5, No. 12, 1962, pp. 613-614.

[90] W. H. Press, S. A. Teukolsky, W. T. Vetterling, and B. P. Flannery, "Numerical Recipes in FORTRAN," Cambridge University Press, 1992, pp. 745-778.

[91] Laura A. Ledsinger, and John R. Olds, "Multidisciplinary Design Optimization Techniques for Branching Trajectories," AIAA-1998-4713, 7th AIAA/USAF/NASA/ISSMO Symposium on Multidisciplinary Analysis and Optimization, St. Louis, MO, Sept. 1998.

[92] Leonid A. Dorf, Yevgeny F. Raitses, Artem N. Smirnov, and Nathaniel J. Fisch, "Anode Fall Formation in a Hall Thruster," AIAA-2004-3779, 40th AIAA/ASME/SAE/ASEE Joint Propulsion Conference & Exhibit, Jul. 2004, Fort Lauderdale, FL.

[93] L. Dorf, Y. Raitses, N. J. Fisch, and V. Semenov, "Effect of Anode Dielectric Coating on Hall Thruster Operation," Applied Physics Letters, Vol. 84, No. 7, Feb. 2004, pp. 1070-1072.

[94] L. Dorf, Y. Raitses, and N. J. Fisch, "Experimental Studies of Anode Sheath Phenomena in a Hall Thruster Discharge," Journal of Applied Physics, Vol. 97, 103309, 2005.

[95] V. V. Zhurin, H. R. Kaufman, and R. S. Robinson, "Physics of Closed Drift Thrusters," Plasma Sources Science and Technology, Vol. 8, 1999, pp. R1-R20.

[96] A. M. Bishaev, and V. Kim, "Local Plasma Properties in a Hall-Current Accelerator with an Extended Acceleration Zone," Soviet Physics – Technical Physics, Vol. 23, No. 9, Sept. 1978, pp. 1055-1057.

[97] Vladimir Kim, "Main Physical Features and Processes Determining the Performance of Stationary Plasma Thrusters," Journal of Propulsion and Power, Vol. 14, No. 5, 1998, pp. 736-743.

[98] E. Ahedo, and J. Rus, "Vanishing of the Negative Anode Sheath in a Hall Thruster," Journal of Applied Physics, Vol. 98, 043306, 2005.

[99] L. Dorf, V. Semenov, Y. Raitses, and N. J. Fisch, "Hall Thruster Modeling with a Given Temperature Profile," 38th AIAA/ASME/SAE/ASEE Joint Propulsion Conference & Exhibit, Jul. 2002, Indianapolis, Indiana.

[100] A. Morozov, Y. Esipchuk, G. Tilinin, A. Trofimov, Y. Sharov, and G. Y. Shchepkin, "Plasma Accelerator with Closed Electron Drift and Extended Acceleration Zone," Soviet Physics – Technical Physics, Vol. 17, No. 1, 1972, pp. 38-45.

[101] A. I. Morozov, and V. V. Savelyev, Reviews of Plasma Physics, Vol. 21, Kluwer Academic/Plenum Publishers, New York, 2000, pp. 277-299.

[102] G. Janes, and R. Lowder, "Anomalous Electron Diffusion and Ion Acceleration in a Low-Density Plasma,", The Physics of Fluids, Vol. 9, No. 6, 1966, pp. 1115-1123.

[103] E. Choueiri, "Plasma Oscillations in Hall Thrusters," Physics of Plasmas, Vol. 8, No. 4, 2001, pp. 1411-1426.

[104] J. M. Gallardo, and E. Ahedo, "On the Anomalous Diffusion Mechanism in Hall-Effect Thrusters," IEPC-2005-117, 29th International Electric Propulsion Conference, Princeton University, 2005.

[105] Hofer, R. R., Katz, I. Mikellides, I. G., and Gamero-Castano, M., "Heavy Particle Velocity and Electron Mobility Modeling in Hybrid-PIC Hall Thruster Simulations," AIAA 2006-4658, 42th AIAA/ASME/SAE/ASEE Joint Propulsion Conference, Jul. 2004, Ft. Lauderdale, FL.

[106] Justin W. Koo, and Iain D. Boyd, "Computational Model of a Hall Thruster," Computer Physics Communications, Vol. 164, 2004, pp. 442-447.

[107] C. Boniface, L. Garrigues, G. J. M. Hagelaar, J. P. Boeuf, D. Gawron, and S. Mazouffre, "Anomalous Cross Field Electron Transport in a Hall Effect Thruster," Applied Physics Letters, Vol. 89, 161503, 2006.

[108] Luke Uribarri, and E. Y. Choueiri, "The Onset of Voltage Hash and its Relationship to Anode Spots in Magnetoplasmadynamic Thrusters," IEPC-2005-084, 29th International Electric Propulsion Conference, Princeton University, Oct. 2005.

[109] Luke Uribarri, "An Electron-Attracting Anode Sheath," Documentation for Onset in MPD Thrusters, http://www.princeton.edu/~uribarri/research/Onset/anode-sheath. pdf , 2006.

[110] M. Mitchner, and Charles H. Kruger, Jr., "Partially Ionized Gases," John Wiley & Sons, Inc., New York, 1973, pp. 140.

[111] G. S. Kino, and E. K. Shaw, "Two-Dimensional Low-Pressure Discharge Theory," The Physics of Fluids, Vol. 9, No. 3, Mar. 1966, pp. 587-593.

[112] Kimiya Komurasaki, Miharu Hirakawa, and Yoshihiro Arakawa, "Plasma Acceleration Process in a Hall-Current Thruster," IEPC-1991-078, 22nd International Electric Propulsion Conference, Viareggio, Italy, Oct. 1991.

[113] Makoto Hayashi, "Determination of Electron-Xenon Total Excitation Cross-Sections, from Threshold to 100 eV, from Experimental Values of Townsend's α," Journal of Physics D: Applied Physics, Vol. 16, 1983, pp. 581-589.

[114] Rapp, D., and P. Englander-Golden, "Total Cross Sections for Ionization and Attachment in Gases by Electron Impact. I. Positive Ionization," Journal of Chemical Physics, Vol. 43. No. 5, 1965.

[115] Syage, J. A., "Electron-Impact Cross Sections for Multiple Ionization of Kr and Xe," Physical Review A, Vol. 46, No. 9, 1992.

[116] M. Suzuki, T. Taniguchi, N. Yoshimura, and H. Tagashira, "Momentum Transfer Cross Section of Xenon Deduced from Electron Drift Velocity Data," Journal of Physics D: Applied Physics, Vol. 25, 1992, pp. 50-56.

[117] Ramsauer, C., "Ueber den Wirkungsquerschnitt der Gasmolekuele langsamen Elektronen. II. Fortsetzung and Schluss - Effective cross section of gas molecules for slow electrons. II. Continuation and final," Ann. d. Physik - Annals of Physics, 72:345, 1923.

[118] Ramsauer, C., and R. Kollath, "Ueber den Wirkungsquerschnitt der Edelgasmolekuele gegenueber Elektronen unterhalb 1 Volt - Effective cross section of inert gas molecules against electrons below 1 volt," Ann. d. Physik, 3:536, 1929.

[119] I. G. Mikellides, I. Katz, M. J. Mandell, and J. Steven Snyder, "A 1-D Model of the Hall Effect Thruster with an Exhaust Region," AIAA-2001-3505, 37th AIAA/ASME/SAE/ASEE Joint Propulsion Conference and Exhibit, July 2001, Salt Lake City, Utah.

[120] http://www.astronautix.com/engines/spt100.htm

[121] Justin W. Koo, and Iain D. Boyd, "Modeling of Anomalous Electron Mobility in Hall Thrusters," Physics of Plasmas, Vol. 13, 033501, 2006.

[122] Steven R. Oleson, and Roger M. Myers, "Launch Vehicle and Power Level Impacts on Electric GEO Insertion," AIAA-1996-2978, 32nd AIAA/ASME/SAE/ASEE Joint Propulsion Conference and Exhibit, July 1996, Lake Buena Vista, FL.

[123] Lee S. Mason, Robert S. Jankovsky, and David H. Manzella, "1000 Hours of Testing on a 10 Kilowatt Hall Effect Thruster," AIAA-2001-3773, 37th AIAA/ASME/SAE/ASEE Joint Propulsion Conference and Exhibit, July 2001, Salt Lake City, Utah.

[124] Robert S. Jankovsky, and Chris McLean, "Preliminary Evaluation of a 10 kW Hall Thruster," AIAA-99-0456, 37th AIAA Aerospace Sciences Meeting and Exhibit, January 1999, Reno, NV.

[125] JMP® 8.0 Help File, SAS Institute Inc., 2008.

[126] K. Sankaran, L. Cassady, A.D. Kodys, and E. Y. Choueiri, "A Survey of Propulsion Options for Cargo and Piloted Missions to Mars," The Annals of the New York Academy of Science, Vol. 1017, 2004, pp. 450-467.

[127] David T. Jacobson, David H. Manzella, Richard R. Hofer, and Peter Y. Peterson, "NASA's 2004 Hall Thruster Program," AIAA-2004-3600, 40th AIAA/ASME/SAE/ASEE Joint Propulsion Conference and Exhibit, 11-14 July 2004, Fort Lauderdale, FL.

[128] David Manzella, Robert Jankovsky, and Richard Hofer, "Laboratory Model 50 kW Hall Thruster," AIAA-2002-3676, 38th AIAA/ASME/SAE/ASEE Joint Propulsion Conference and Exhibit, 7-10 July 2002, Indianapolis, IN.

[129] C. F. Jeff Wu and Michael Hamada, "Experiment: Planning, Analysis, and Parameter Design Optimization," Wiley-Interscience, ISBN-10 0471255114, 2000.

[130] http://image.absoluteastronomy.com/images/encyclopediaimages/r/ru/russian_stationary_plasma_thrusters.jpg as of 05/08/2010

[131] Danel A. Lichtin, "An Overview of Electric Propulsion Activities in US Industry – 2005," AIAA-2005-3532, 41st AIAA/ASME/SAE/ASEE Joint Propulsion Conference & Exhibit, 10-13 July 2005, Tucson, Arizona.

[132] David J. Pidgeon, Ronald L. Corey, Birgit Sauer, and Michael L. Day, "Two Years On-Orbit Performance of SPT-100 Electric Propulsion," AIAA-2006-5353, 24th AIAA International Communications Satellite Conference (ICSSC) and 4t, 11-14 June 2006, San Diego, California.

[133] D. Milligan, D. Gestal, O. Camino, D. Estublier, and C. Koppel, "SMART-1 Electric Propulsion Operations," AIAA-2004-3436, 40th AIAA/ASME/SAE/ ASEE Joint Propulsion Conference and Exhibit, 11-14 July 2004, Fort Lauderdale, Florida.

[134] Jack Fisher, Alfred Wilson, David King, Steve Meyer, Carl EngelBrecht, Kristi de Grys, and Lance Werthman, "The Development and Qualification of a 4.5 kW Hall Thruster Propulsion System for GEO Satellite Applications," IEPC-01-010, 27th International Electric Propulsion Conference, 15-19 Oct. 2001, Pasadena, California.

[135] Guoqiang Zhang, B. Eddy Patuwo, and Michael Y. Hu, "Forecasting with Artificial Neural Networks: The State of the Art," International Journal of Forecasting, Vol. 14, 1998, pp. 35-62.

[136] Debora D. Daberkow, and Dimitri N. Mavris, "New Approaches to Conceptual and Preliminary Aircraft Design: A Comparative Assessment of a Neural Network Formulation and a Response Surface Methodology," AIAA-98-5509, World Aviation Conference, Sept. 28-30, 1998, Anaheim, CA.

[137] Carl Johnson, and Jeff Schutte, "Basic Regression Analysis for Integrated Neural Networks (BRAINN) Documentation," Users Manual, Version 2.3, Aerospace System Design Laboratory, Georgia Institute of Technology, 2009.

[138] Leo Breiman, Jerome Friedman, Charles J. Stone, and R. A. Olshen, "Classification and Regression Trees," Chapman and Hall/CRC Press, 1998.

[139] V. Vapnik, "The Nature of Statistical Learning Theory," Springer, New York, 1995.

[140] Steve R. Gunn, "Support Vector Machines for Classification and Regression," ISIS Technical Report, 1998.

[141] C. J. C. Burges, "A Tutorial on Support Vector Machines for Pattern Recognition," Data Mining and Knowledge Discovery, Vol. 2, 1998, pp. 121-167.

[142] Ovidiu Ivanciuc, "Applications of Support Vector Machines in Chemistry," Reviews in Computational Chemistry, Vol. 23, 2007, pp. 291-400.

[143] Raymond J. Mooney, "Support Vector Machines," Lecture Note, CS391L Machine Learning, Department of Computer Science, University of Texas at Austin, 2007.

[144] Gordon R. Woodcock, and John Dankanich, "Application of Solar-Electric Propulsion to Robotic Missions in Near-Earth Space," CP880, Space Technology and Applications International Forum – STAIF 2007, Albuquerque, NM.

[145] Gopinath, N. S., and Srinivasamuthy, K. N., "Optimal Low Thrust Orbit Transfer from GTO to Geosynchronous Orbit and Stationkeeping using Electric Propulsion System," IAC-03-A.7.03, 54th International Astronautical Congress of the International Astronautical Federation, the International Academy of Astronautics, and the International Institute of Space Law, Bremen, Germany, Sep. 29 – Oct. 3, 2003.

[146] John W. Dankanich, and Gordon R. Woodcock, "Electric Propulsion Performance from Geo-transfer to Geosynchronous Orbits," IEPC-2007-287, 30th International Electric Propulsion Conference, Sep. 17-20, 2007, Florence, Italy.

[147] Yang Gao, "Linear Feedback Guidance for Low-Thrust Many-Revolution Earth-Orbit Transfers," Journal of Spacecraft and Rockets, Vol. 46, No. 6, 2009, pp. 1320-1325.

[148] C. A. Kluever, "Geostationary Orbit Transfers Using Solar Electric Propulsion with Specific Impulse Modulation," Journal of Spacecraft and Rockets, Vol. 41, No. 3, 2004, pp. 461-466.

[149] Sophie Geffroy and Richard Epenoy, "Optimal Low-Thrust Transfers with Constraints – Generalization of Averaging Techniques," Acta Astronautica, Vol. 4, No.3, 1997, pp. 133-149.

[150] David Y. Oh, "Analytic Optimization of Mixed Chemical-Electric Orbit Raising Missions," IEPC-01-173, 27th International Electric Propulsion Conference, Oct. 15-19, 2001, Pasadena, CA.

[151] Thomas M. Randolph, and David Y. Oh, "Economic Benefit Analysis of Chemical-Electric Orbit Raising Missions," AIAA-2002-1980, 20th AIAA International Communication Satellite Systems Conference and Exhibit, May 12-15, 2002, Montreal, Quebec, Canada.

[152] David Oh, Thomas Randolph, Manuel Martinez-Sanchez and Scott Kimbrel, "End to End Optimization of Two Dimensional Chemical-Electric Orbit Raising Missions," AIAA-2002-3966, 38th AIAA/ASME/SAE/ASEE Joint Propulsion Conference and Exhibit, July 7-10, 2002, Indianapolis, Indiana.

[153] Sea Launch Company, L.L.C., "Sea Launch User's Guide," One World Trade Center, Suite 950, Long Beach, CA, 2008.

[154] Lantoine, G., and Russell, R. P., "A Hybrid Differential Dynamic Programming Algorithm for Robust Low-Thrust Optimization," AIAA-2008-6615, AAS/AIAA Astrodynamics Specialist Conference and Exhibit, Aug. 2008, Honolulu, HI.

[155] Gill, P.E., Murray, W., and Saunders, M. A., "SNOPT: An SQP Algorithm for Large-Scale Constrained Optimization," SIAM Journal on Optimization, Vol.12, No. 4, 2002, pp. 979-1006.

[156] Martins, J. R., Kroo, I. M., and Alonso, J. J., "An Automated Method for Sensitivity Analysis Using Complex Variables," AIAA-2000-0689, 38th Aerospace Sciences Meeting, Jan. 2000, Reno, NV.

[157] Sims, J. A., and Flanagan, S. N., "Preliminary Design of Low-Thrust Interplanetary Missions," AAS-99-338, AAS/AIAA Astrodynamics Specialist Conference, Aug. 1999, Girdwood, Alaska.

[158] Lantoine, G., and Russell, R. P., "A Fast Second-Order Algorithm for Preliminary Design of Low-Thrust Trajectories," IAC-08-C1.2.5, 59th International Astronautical Congress, Sep. 29-Oct. 3, 2008, Glasgow, Scotland.

[159] P. Langevin, "On the Theory of Brownian Motion," C. R. Acad. Sci., Paris, 1908, Vol. 146, pp. 530-533; English translation by D. S. Lemons and A. Gythiel, "Paul Langevin's 1908 paper 'On the Theory of Brownian Motion'," American Journal of Physics, Vol. 65, 1997, pp. 1079-1081.

[160] G. E. Uhlenbeck, and L. S. Ornstein, "On the Theory of Brownian Motion," Physical Review, Vol. 36, 1930, pp. 823-841.

[161] Don S. Lemons, and David L. Kaufman, "Brownian Motion of a Charged Particle in a Magnetic Field," IEEE Transactions on Plasma Science, Vol. 27, No. 5, 1999, pp. 1288-1296.

VITA

Kybeom Kwon was born to Mr. Ohkyo Kwon and Ms. Jaesoon Lee in Daegu, South Korea. He is married to Ms. Insoon Kim and has two sons, Keunhyung Kwon and Uyeol Kwon. His undergraduate degree is in Aerospace engineering from Republic of Korea Air Force (ROKAF) Academy in 1996. After graduating, he had served ROKAF as a strategic intelligence officer for two years. He earned his master degree in Aerospace engineering from Seoul National University in 2000. He studied aircraft design during the master course specializing in CFD and associated design methodology. After the master course, he had taught cadets in ROKAF Academy for 5 years. He received an assistant professor position in 2003. He also served as a medium-size subsonic wind tunnel laboratory researcher. After he joined Georgia Tech in 2005, his main research has been on advanced space propulsion systems. His research interests have expanded to space propulsion system modeling, conceptual design methodology, and space mission trajectory optimization. He has also worked on a variety of systems engineering projects such as space mission design, advanced logistics systems, life cycle cost analysis, advanced vehicle concept modeling, feasibility study for personal air vehicle, and technology evaluation and tradeoff.